2013-3

Design of a Transpired Air Heating Solar Collector with an Inverted Perforated Absorber and Asymmetric Compound Parabolic Concentrator.

Nasif Shams
Technological University Dublin, nasifshams@gmail.com

Recommended Citation

Shams, N. S. M.(2013) *Design of a transpired air heating solar collector with an inverted perforated absorber and asymmetric compound parabolic concentrator.* Doctoral Thesis, Technological University Dublin. doi:10.21427/D7NK67

Design of a Transpired Air Heating Solar Collector with an Inverted Perforated Absorber and Asymmetric Compound Parabolic Concentrator

S. M. NASIF SHAMS, *BSc, MSc*

A thesis submitted in fulfilment of the requirements for the degree of Doctor of Philosophy to the Dublin Institute of Technology

Under the supervision of

Dr. Mick McKeever, Dr. Sarah McCormack and Prof. Brian Norton

School of Electrical Engineering Systems,
Dublin Institute of Technology,
Republic of Ireland

March, 2013

Dedicated to my Parents,

Wife and Brothers

ABSTRACT

A new designed air heating solar collector comprised of an inverted perforated absorber and an asymmetric compound parabolic concentrator was applied to increase the intensity of solar radiation incident on the perforated absorber. A 2D ray tracing model quantified optical efficiency at different incident angles within 27° to 89° incident angles. The beam efficiency was found to vary between 72% and 79% and diffuse efficiency was found to vary between 48.2% and 65%.

The average thermal efficiency was found to be approximately 55%-65% with average radiation above 400 W/m^2 for flow rates in the range of 0.03 kg/s/m^2 to 0.09 kg/s/m^2. Experimental results at air flow rates of 0.03 kg/s/m^2 and 0.09 kg/s/m^2 showed temperature rise of 38°C and 19.6°C respectively at a solar radiation intensity of 1,000 W/m^2. A comparison with a commercially available Unglazed Transpired Collector (UTC) showed that at an air flow rate of 0.03 kg/s/m^2 and solar radiation intensity of 1,000 W/m^2 the air temperature rises were 21°C for the UTC and 38°C for the new system. At an intensity of 500 W/m^2, the air temperature rise was 12°C for the UTC and 19°C with the new system.

Without a glazing cover and tertiary section, reverse flow effects were found to dominate the new system's thermal performance. This problem was resolved by incorporating a 50 mm optically optimised tertiary section that acts as a heat trap. Regular maintenance was found to be necessary in unglazed concentrating collectors with exposure of the high reflectance reflector to outdoor conditions which reduce the lifespan of such collectors. Because the average number of reflections at any incidence angle is > 1, reflector reflectance crucially affects the optical efficiency of the collector.

The estimated indicative cost of the new system was €450/m^2. The designed stationary system has the operational and economic advantages of no moving components. Incorporating a carbon fabric absorber with inherent perforations reduced overall life cycle cost significantly. As the pressure drop in the new system was found to be 10 Pa for an air flow rate of 0.1 kg/s/m^2 between inlet and outlet, the required fan power consumption was very small in comparison to the recovered energy giving operational costs.

A techno-economic analysis of the new system was carried out for a domestic dwelling considering space and water heating demand. The annual CO_2 emission reduced by the new system was calculated as 280 kg/m^2 against an electric heater, 112 kg/m^2 compared to a gas boiler and 147 kg/m^2 against an oil boiler which makes it an attractive air heating system for the residential sector. Considering 8% interest rate the Benefit Cost Ratio (BCR) of the new system was found 1 in year 9 of a 20 year lifespan.

DECLARATION

I certify that this thesis which I now submit for examination for the award of PhD, is entirely my own work and has not been taken from the work of others, save and to the extent that such work has been cited and acknowledged within the text of my work. This thesis was prepared according to the regulations for postgraduate study by research of the Dublin Institute of Technology and has not been submitted in whole or in part for another award in any Institute. The work reported in this thesis conforms to the principles and requirements of the Institute's guidelines for ethics in research.

The Institute has permission to keep, lend or copy this thesis in whole or in part, on condition that any such use of the material of the thesis is duly acknowledged.

Signature ____________________________ Date _________________

ACKNOWLEDGEMENTS

My sincere thanks go to my thesis supervisors Dr. M. McKeever, Dr. S. McCormack and Prof. B. Norton for their excellent guidance and unquantifiable contributions to the completion of this project.

I remain grateful to my colleague and long time friend Dr. L. M. Ayompe for his endless support. I am thankful to my friends and family in Dublin S. Chy, R. Chy, M. Khalek, J. Khalek, S. K. Khadem and L. Mariam. I appreciate the kind contributions and support from my colleagues Dr. M. Kennedy, Dr. M. Hanif, S. Chandra, J. Sarwar and Dr. U. Dwivedi.

I am thankful to my darling wife M. Mostafa for her continued love and support throughout the course of this degree. I am also thankful to my father in-law Mr. K. Uddin and mother in-law Mrs. J. Begum for their love and encouragement. I am thankful to God our creator for my wonderful parents Mr. S. H. Tuku and Mrs L. Begum who have always had a firm commitment in providing my basic needs, love and endless courage since birth. I also appreciate the continued moral encouragement provided by my brothers A. Shams and S. Shams; and their wives B. Shams and L. Shams accordingly.

All glory and honour goes to the Manufacturer of the universe, the Lord Almighty for offering me this unique scholarship opportunity and also for keeping me alive and making my works possible.

LIST OF ABBREVIATIONS

ACPC	Asymmetric Compound Parabolic Collector
BCR	Benefit Cost Ratio
BER	Building Energy Rating
CIF	Present value of cash inflow
COF	Present value of cash outflow
CTAH	Concentrating Transpired Air Heating-collector
CPC	Compound Parabolic Concentrator
CDER	Carbon Dioxide Emission Rate
DSAHC	Double-pass Solar Air Heating Collector
ESTTP	European Solar Thermal Technology Platform
ESTIF	European Solar Thermal Industry Federation
ETC	Evacuated Tube Collector
EU	European Union
EPA	Environmental Protection Agency
EPBD	Energy Performance of Buildings Directive
FPC	Flat Plate Collector
FV	Future value of a cash flow
GSAHC	Glazed Solar Air Heating Collector
GHG	Green House Gas
IEA	International Energy Agency
NREAP	National Renewable Energy Action Plan
NPV	Net Present Value
PBP	Payback Period
RE	Renewable Energy
RET	Renewable Energy Technology

RES	Renewable Energy Sources
SPP	Simple Payback Period
SSAHC	Single-pass Solar Air Heating Collector
TAC	Transpired Air-heating Collector
UNSDC	United Nations Sustainable Development Commission
UTC	Unglazed Transpired Collector
USAHC	Unglazed Solar Air Heating Collector

TABLE OF CONTENT

CHAPTER 1

CHAPTER 2

CHAPTER 3

CHAPTER 4

CHAPTER 5

THERMAL PERFORMANCE ANALYSIS AND EXPERIMENTAL CHARACTERISATION OF CTAH 118

CHAPTER 6

CHAPTER 7

CHAPTER 8

LIST OF FIGURES

LIST OF TABLES

NOMENCLATURE

A_{apt}	Aperture area (m^2)
$B_{equivalent}$	Equivalent benefits (€)
C_{boiler}	Annual fuel cost by boiler (€)
$C_{equivalent}$	Equivalent costs (€)
$CI_{electricity}$	Carbon intensity of grid electricity (kgCO$_2$/kWh)
Cp_{air}	Specific heat capacity of air (J/kgK)
d	Discount rate (%)
D_{h_l}	Hydraulic diameter (m)
E_{a_CTAH}	Total annual thermal energy generated by CTAH (kWh)
EC_{CTAH}	Emitted carbon associated with electricity imported from the grid for CTAH (kgCO$_2$)
$EC_{elc,heater}$	Emitted carbon associated with electricity imported from the grid for electric heater (kgCO$_2$)
E_{imp}	Electricity imported from the grid (kWh)
$E_{consumed}$	Energy consumed by the fan (kWh)
E_{f_air}	Generated energy fraction for space heating (kWh)
E_{f_water}	Generated energy fraction for water heating (kWh)
E_{boiler_CTAH}	Annual thermal energy generation requirement by boiler (kWh)
ED_a	Total annual thermal energy demand (kWh)
F_{boiler}	Unit fuel cost for boiler (€/kWh)
F_{air}	Solar fraction for space heating
F_{water}	Solar fraction for water heating

h_{conv_eff}	Effective convection heat transfer coefficient (W/m^2K)
$h_{operation}$	Total pump hours (hour)
I_{global}	Total solar radiation incident on the aperture (diffuse and direct) (W/m^2)
I_b	Beam radiation (W/m^2)
I_d	Diffuse radiation (W/m^2)
I_g	The ground reflected diffuse radiation (W/m^2)
K_{air}	Thermal conductivity of air (W/mK)
L_{length}	Absorber length (m)
L_{width}	Absorber width (m)
$\dot{m}_{air}$	Air mass flow rate (kg/s)
Nu	Nusselt number (dimensionless)
Pr	Prandtl number (dimensionless)
q_{useful}	Rate of useful energy per unit area (W/m^2)
$\dot{Q}_u$	Rate of useful energy delivered (W)
Q_{rad}	Incident radiation (W/m^2)
Q_h	Quantity of heat generated by CTAH (kWh)
$T_{out,i}$	Outlet air temperature (^oC)
$T_{inlet,i}$	Inlet air temperature (^oC)
T_{abs}	Absorber temperature (^oC)
ε	Emissivity
$\eta_{gas,b}$	Thermal efficiency of condensing gas boiler (%)
$\eta_{elc,heater}$	Thermal efficiency of electric heater (%)

φ_p	Absorber porosity (dimensionless)
$\theta_{incident}$	Incident angle
$\rho_{reflector}$	Reflector reflectance
n_{avg}	Average number of reflection
α_{abs}	Absorptance of the absorber
$\delta_{insulation}$	Thickness of insulation (m)

CHAPTER 1

INTRODUCTION

1.1 Background

The EU has agreed a series of demanding climate and energy targets to be reached by 2020, known as the “20-20-20” targets. As a European Union (EU) member state, Ireland must implement the EU’s ambitious energy policy objectives for 2020 outlined in the European Strategic Energy Technology Plan (Communities, 2007, EPA, 2012). These are:

- A reduction in EU greenhouse gas emissions of at least 20% below 1990 levels
  20% of EU energy consumption to come from renewable resources
- A 20% reduction in primary energy use compared with projected levels, to be achieved by improving energy efficiency

These commitments are enshrined as legally binding targets for each member state in Directive 2009/28/EC in which Ireland is committed to achieve 16% of gross national energy consumption from renewable by 2020.

Solar thermal energy is an extremely convenient source of heating and a technology that does not rely on limited finite energy resources. In the National Renewable Energy Action Plan (NREAP); the government of Ireland has set targets of 40%, 12.5% and 10% of electricity consumption, heating and cooling as well as transport respectively from renewable energy sources by 2020 (DCENR, 2010).

One of the visions 2030 which was developed by the European Solar Thermal Technology Platform (ESTTP) and European Solar Thermal Industry Federation

(ESTIF) is to expand the existing technologies and new technologies should be developed for new sectors like apartment buildings and the industrial sector. Research is needed for new applications (ESTTP, 2008; ESTIF, 2009).

Solar air heating collectors convert solar energy to heat air. Solar Air Heating Systems (SAHS) are well established with applications in space heating and space ventilation, timber seasoning, curing of industrial products and drying.

Conventional solar air heating systems are low efficiency systems due to low thermal capacity of air, low absorber to air heat transfer coefficient and inadequately addressed design. These systems inherit poor convective heat transfer coefficients between the absorber plate and the air flow which results in the absorber temperature being much higher than the air stream temperature. This causes greater heat losses to the surroundings. The heavy metallic absorber also makes air heating systems difficult to integrate in buildings.

In order to overcome the limitations inherent with conventional solar air heating systems, a new type of air heating system has been proposed in this research that integrates a very light and comparatively inexpensive absorber with a concentrator system which ensures high optical and heat transfer efficiency.

The energy efficiency of Irish dwelling can be represented using Carbon Dioxide Emissions Rating (CDER) and Building Energy Rating (BER) of buildings. The integration of a concentrating air heating system in a building is one way to reduce the CDER and improve the BER certification of buildings.

1.2 Problem Statement

The novel design of a transpired inverted absorber integrated with a concentrator is being studied for the first time in this thesis. Optimal design of the proposed air heating system can only be achieved through appropriate optical design optimisation with detailed experimental performance analysis. It is important to develop a combined optical and heat transfer model which represents the performance of the air heating system's output.

One of the vital challenges in conventional space heating systems is to increase air turbulence in order to raise the effective convection heat transfer between absorber surface and air flow to avoid radiative heat loss from the absorber. Most design solutions result in complicated absorber geometry, heavy weight system construction or expensive material selection.

The solution proposed in this thesis is a lightweight collector with simple absorber geometry. Low temperature Unglazed Transpired Collector (UTC) air heating systems became popular in recent years due to their simplicity. However, the design failed to reduce the radiation loss from the absorber surface. The main challenge with solar air heaters is to reduce the radiative heat loss to the sky and conduction loss from the metal absorber.

This research focuses on the design and experimental performance analysis of a stationary novel air heating system which is the integration of a Transpired Air-heating Collector (TAC) and an Asymmetric Compound Parabolic Concentrator (ACPC). This thesis proposes a system to solve the problem in four improvements as shown in Figure 1.1.

1) Inverted perforated absorber: A perforated absorber has been incorporated in the design which faces downward to reduce radiation loss. Perforated surface allows air to flow through the absorber which enhances heat transfer between the absorber and flowing air. Solar air heaters are generally constructed using metal plates as the absorber of the incident solar radiation which introduces conduction

losses. Instead of a heavy metal absorber, a nonconventional low conductive light weight carbon fibre absorber has been used for the first time as the absorber material of the proposed collector.

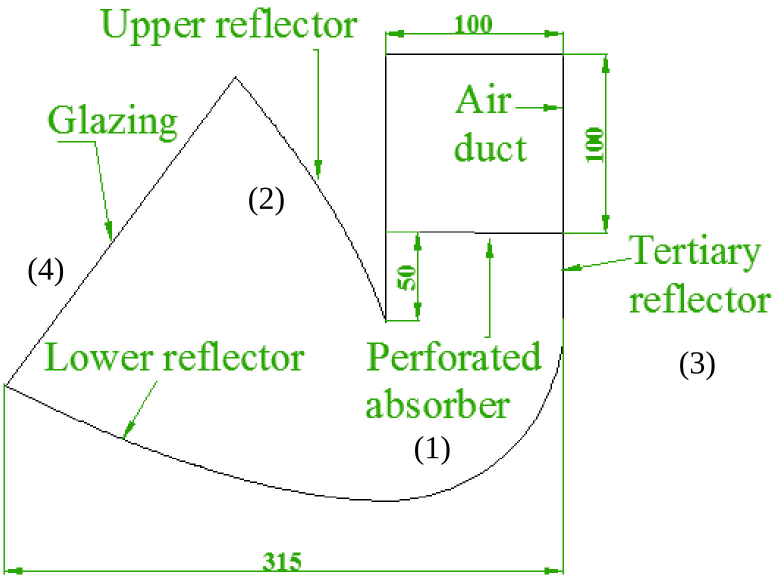

Figure 1.1: Schematic Diagram of the CTAH

2) Concentrator: A concentrator has been introduced with the perforated absorber for the first time to increase the concentration of the incident solar radiation onto the inverted perforated absorber.
3) Tertiary reflector section: A parallel reflector section just below the inverted absorber helps to improve the stratified thermal layer below the absorber which enhances the heat transfer mechanism.
4) Glazing cover: A glazing cover has been introduced which works as the heat trap for the emitted radiation from the absorber surface. However, an optical loss occurs due to the reflection and absorption on the glazing cover. A high transmittance glazing material reduces the optical loss. Also during outdoor

operation a glazing surface is necessary to provide protection from dust deposition, rain and wind. In conventional solar collectors a parallel glazing cover usually orients with absorber surface to reduce the reflection loss. However the design introduces convection loss from the glazing cover and radiation loss from the absorber surface. In the proposed design the absorber is placed at downward facing orientation.

1.3 Aim of this research

The aim of this research is to design, fabricate and optimise a solar air heating collector with a concentrating transpired absorber and evaluate its techno-economic and environmental performance.

1.4 Objectives and Scope

This thesis focuses on the design of a concentrating transpired absorber air heating system, optical and thermal modelling of the air heating system for accurate prediction of the system’s performance, construction and fabrication of the prototype to conduct experimental validation.

Specific objectives of this research are to:

- design a novel air heating collector with an integrated concentrated perforated absorber;
- fabricate a prototype of an integrated concentrated perforated absorber air heating collector;
- undertake field performance characterisation of the air heating collector under typical Irish weather conditions;

- develop and validate a model to predict the thermal performance of an integrated concentrated perforated absorber air heating collector; and
- evaluate the technical, economic and environmental performance of the air heating system.

1.5 Research Methodology

Standard research methodology was followed to achieve the objectives of this research as shown in Figure 1.2 which start with an extensive literature review. That helped to identify the problems to be solved in this thesis. Related topics were read to start with a very good basis using other researcher's published works.

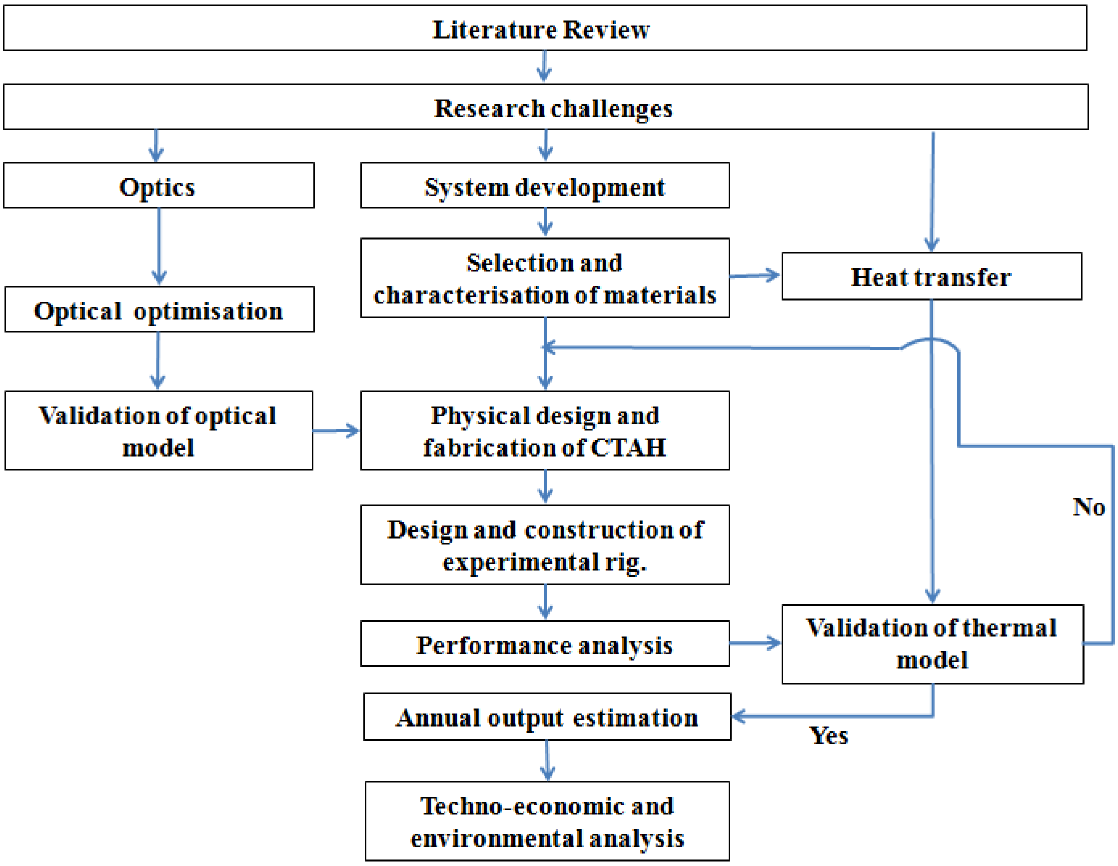

Figure 1.2: Research methodology

The knowledge from literature review lead to design a novel solar air heating system which is affordable, low cost and light weight. In the design stage there were 3 challenges:

1) optical concentrator design,

2) system design and

3) heat transfer design.

In Optical design, optical modelling and optimisation was conducted using ray tracing simulation model of CTAH in Matlab software. Then validation of optical model was carried out using laser experiment. In system design, selection of system materials was done with help of literature review and characterisation was done in DIT lab. A new low cost material was found and was used as absorber material in this new solar collector. Now optimised optical model was used in physical design and fabrication of CTAH.

Design and construction of experimental rig was conducted in DIT. Performance analysis was carried out under outdoor experimental conditions and results were compared with other solar collectors. Heat transfer design was developed with help of literature and using selected system material properties. Validation of the model was done using field trial data and there were few cycles before the expected results were found. The model was used for annual energy output estimation and that was used in techno-economic and environmental analysis.

Main steps of this research methodology has been presented as follows:

- ➢ Review of literature on conventional air heating collectors in order to identify their limitations and develop a novel Concentrating Transpired Air Heating (CTAH) collector that overcomes the shortcomings. Review of existing literature is presented in chapter 2 which includes:

    - Modification and selection of solar air heating system components;
    - Optical concentrator design;
    - Integration of optical concentrator with solar collectors.
- Design of a novel air heating collector includes:
    - Development of an optical concentrator to maximise the concentration of solar radiation on an inverted absorber and validated the optical model;
    - Development of a simulation model to optimise the optical concentrator considering different material properties and position of the incorporated inverted perforated absorber;
    - Development of a perforated inverted absorber solar collector which can absorb the solar radiation and also allow air to flow through the perforation.
- Fabrication and testing the field performance of the prototype includes:
    - Development of the first prototype which was unglazed with locally available perforated metal absorber under typical Irish weather conditions;
    - Fabrication of an improved prototype of the CTAH with glazed aperture, optimised tertiary height and perforation;
    - Characterisation of CTAH's thermal performance and comparison with glazed and unglazed solar air heating collects.
- Development and implementation of a model using Matlab software to predict the thermal performance of the CTAH. The model output was validated using measured data obtained from the field trials.

- The validated thermal model was used to predict the annual energy output from the CTAH collector in order to carry out a techno-economic analysis using the energy output, system characteristics, costs, fuel emission factors. The techno-economic analysis evaluates the thermal, economic and environmental performance of the CTAH collector.

1.6 Thesis Overview

The mentioned methodology in section 1.5 was used in this research. This section presents a short overview of different chapters of the thesis.

Chapter 1 starts by describing the background of the thesis which is followed by the motivation of the research and then establishes the problem statement. It presents the main aim of the research; specific objectives and the methodology used to carry out the research.

Chapter 2 presents an extensive literature review which identifies the state-of-the-art of conventional air heating collectors. It focuses on conventional solar collectors, optical concentrator design and concentrator integrated solar collectors. Two major class of solar air heating collectors: Glazed Air Heating (GAH) systems and Unglazed Transpired air heating Collectors (UTC) were studied to identify proposed modifications to improve system efficiency, outlet temperature and system cost. The drawbacks of conventional air heating systems are taken into consideration during the design process of the concentrating air heating system. Optical concentrator design and concentrator integrated with solar collectors were studied to identify possible ways to concentrate solar radiation on an inverted absorber.

Chapter 3 presents the design of the optical Concentrating Transpired Air Heating (CTAH) system as well as the development and validation of a tool to calculate the optical efficiency of the CTAH system. This chapter presents details of the geometric construction of the CTAH system and a comprehensive development process of a two-dimensional (2D) ray-tracing model. The ray trace technique implemented in Matlab software was used in this research to calculate the energy distribution at the absorber and optical loss due to reflection on the concentrator surface. The effect of tertiary height and reflector reflectivity was analysed using the ray tracing model and optical tertiary height was calculated.

Chapter 4 presents the design of individual components, selection of materials for different components, construction process of each component and fabrication of the CTAH system. This chapter focuses on the material selection and design of vital components of the CTAH system and the fabrication process.

Chapter 5 presents results of the thermal performance of a glazed and unglazed CTAH operating under different air flow rates. The performance of the system depends on wind speed, solar insolation, inlet air temperature and ambient air temperature. The prototypes were constructed and tested in the Dublin Institute of Technology. The temperature of the outlet air and absorber showed significant rise during the experiments. The thermal performance of the CTAH was compared with that of conventional glazed and unglazed solar collectors.

In chapter 6, a model was developed to predict the energy output from the CTAH system. It was validated against field trial data presented in Chapter 5 using statistical methods. The validated model was used to simulate the total energy generated by the CTAH system for different months over an entire year using weather data for Dublin, Ireland. The model was also used to investigate the effect of different air mass flow rates on the maximum outlet air temperature from the CTAH system.

Chapter 7 presents a technological, economic and environmental analysis of the CTAH system for a domestic dwelling. Specific procedures used in this chapter include: accessing the technical and economical performance using a number of investment appraisal techniques under different application scenarios; and evaluating the environmental performance by quantifying the GHG emissions associated with the operation of air heating systems. The performance of the CTAH was compared with that of Flat Plate Collector (FPC) and Evacuated Tube Collector (ETC) which are the most common types of solar thermal system has been integrated in Irish domestic dwellings.

Chapter 8 summarises the main conclusions, presents the contributions to knowledge in the field and then proposes recommendations for future work.

CHAPTER 2

DEVELOPMENTS IN SOLAR AIR HEATING TECHNOLOGY

The integration of a transpired inverted absorber and asymmetric compound parabolic concentrator to develop a novel solar air heating is the main focus of this thesis. An extensive review was carried out to examine:

- state-of-the-art of solar air heating technologies using solar energy to heat air;
- optical concentrator as a method to concentrate solar irradiation; and
- the integration of optical concentrators with solar collectors

2.1 Solar Air Heating Technologies (Glazed and Unglazed)

The main research challenge is to increase the convective heat transfer between the working fluid air and the absorber surface while at the same time minimising the overall heat losses from the system. A wide range of Solar Air Heating Collector (SAHC) designs have been proposed and discussed in the literature in recent years to improve the performance of conventional systems (Alta et al., 2010; Ho et al., 2009; Lin et al., 2006, Tanda, 2011; Ozgen et al., 2009 and Tanda, et al., 2011).

At present, two main types of SAHC exist commercially Unglazed Solar Air Heating Collector (USAHC) and Glazed Solar Air Heating Collector (GSAHC). As illustrated in Figure 2.1, a design from SolarWall (Solarwall, 2011; Shukla et al., 2012; IEA, 1999) is shown in Figure 2.1 (a) as a conventional UTC system (Solarwall, 2011).

Figure 2.1(b)-(d) illustrates different configuration of GSAHC (Duffie & Beckman, 2006; Goswami, 2000).

The basic difference between two main types of solar air collectors is presence of glazing cover and design of absorber surface. UTC collectors do not have glazing cover and contains perforated absorber as shown in Figure 2.1 (a). On other hand glazed collector generally contains non-perforated extended surface absorber Figure 2.1 (b)-(d). Comparatively little experimental research has been carried out (Pramung & Exell, 2005 and Tchinda, 2008) to improve solar air heating system performance using concentrators.

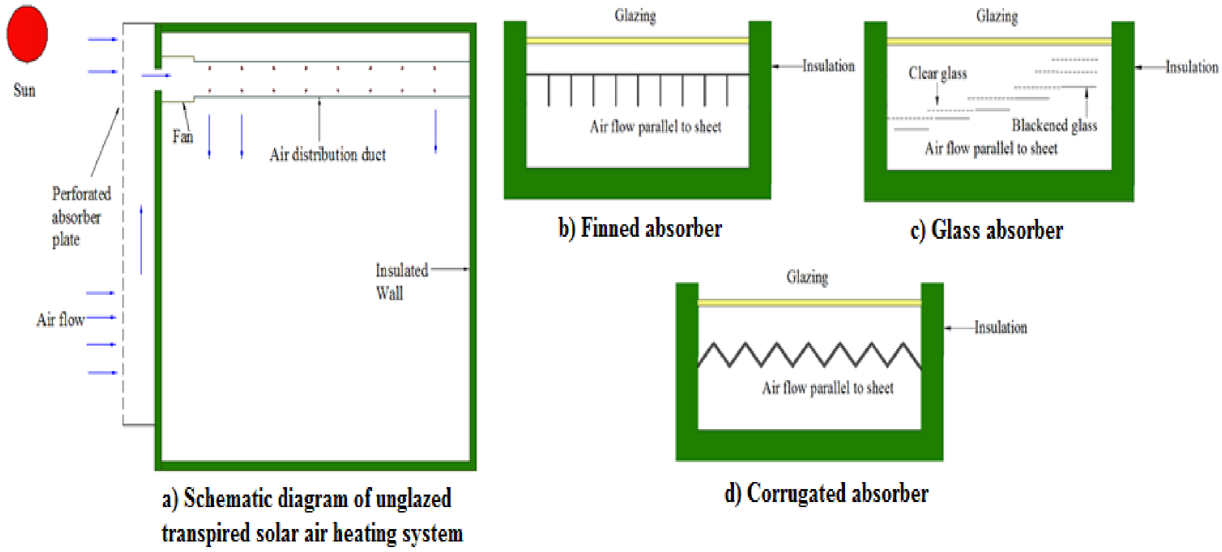

a) Schematic diagram of unglazed transpired solar air heating system

b) Finned absorber

c) Glass absorber

d) Corrugated absorber

Figure 2.1: a) Unglazed transpired collector, b) Glazed collector with finned absorber, c) Glazed collector with glass absorber, d) Glazed collector with corrugated absorber (after Solarwall, 2011; Duffie & Beckman, 2006; Goswami, 2000)

Pramung & Exell (2005) modelled concentrator integrated non-perforated absorber water heating collector. Tchinda (2008) modelled concentrator integrated non-perforated absorber air heating collector. Numerous researches have been carried out on

PV integrated solar air heating systems (Odeh et al., 2006; Athienitis et al., 2011). However, integration of inverted perforated absorber with concentrator for air heating purpose has not been investigated.

2.1.1 Unglazed Solar Air Heating Collector (USAHC)

USAHC generally consists of an absorber plate with a parallel back plate. The space between the absorber and the back plate forms a plenum as illustrated in Figure 2.1 (a). Outside air to be heated is drawn through the perforation and the plenum using extraction fan. There are two types of USAHC: transpired absorber and non transpired absorber (back pass).

The difference between the two systems is the absorber perforation. The most popular type of USAHC presented in Figure 2.1a is the unglazed transpired collector (UTC) well known as the Solar Wall which was invented and patented in the 1990s by John Hollick (Solarwall, 2011; Shukla et al., 2012; IEA, 1999). The research was carried out during Task 14 (IEA, 1999) to better understand of unglazed transpired collectors and to improve the engineering tools for the design of perforated collector systems.

UTC has been the subject of a number of investigations (Dymond & Kutscher, 1997; Gawlik et al., 2005; Keith et al., 2002; Decker et al., 2001). A literature review on transpired solar collectors presented working principle, modelling and comparison of various types of transpired collectors (Shukla et al., 2012). The literature review showed that the most critical factors affecting thermal efficiency of transpired solar collectors were wind velocity, flow rate, absorptivity and porosity.

Continuous improvements to the UTC have focused on the material of the transpired absorber (Gawlik et al., 2005), diameter and pitch of the perforation and thickness of the absorber (Keith et al., 2002; Decker et al., 2001). This technology is an effective low cost option to meet the heating demands in the buildings. However, the temperature rise of the air is comparatively much lower than that for glazed solar collectors at maximum efficiency.

As the UTC system is an open loop system, air flow is directly related to the pressure drop across the absorber plate. A minimum pressure drop of 25 Pa needs to be maintained during the heating operation to avoid reverse flow effects (Charles, 1991; Kutscher et al., 1993; Leon & Kumar, 2007). UTC loses heat from the exposed absorber perforation due to reverse flow and radiation losses cannot be avoided from unglazed absorber.

2.1.2 Glazed Solar Air Heating Collector (GSAHC)

GSAHC generally consists of an absorber plate with a parallel plate below forming a passage of high aspect ratio through which the air to be heated flows. In order to enhance the thermal efficiency of GSAHC, different modifications were suggested and applied to improve the heat transfer between absorber and air (Mittal & Varshney, 2006; Peng et al., 2010). The most important components of GSAHC are: the glazing, absorber, and air flow passage.

Geometry and property of the absorber in a glazed solar air heating collector is different from the UTC systems. Usually heat transfer phenomena occur between air and non-perforated absorber surface. Numerous absorber modifications were suggested to improve the heat transfer between absorber and air flow.

Roughness inducing wires and wavy passage has been used in collector to boost heat transfer (Karim & Hawlader, 2006; Piao et al., 1994). Many kinds of fins such as offset strip fins (Hachemi, 1999; Karsli, 2007) and continuous fins (Moummi et al.,

2004) have been studied extensively. Rough surface and porous media were often used to enhance heat transfer mechanism (Yousef & Adam, 2008).

2.2 Glazed and Unglazed Solar Air Heating Collector design factors

Absorber material and geometry vary significantly for conventional glazed and unglazed solar air heating systems; therefore the optimisation parameters of the absorber in a glazed collector diverge substantially from the latter.

This research investigated four major factors in designing solar air heating collectors (glazed and unglazed) based on previous literature. These are:

1) Absorber modification

2) Glazing modification

3) Airflow and airflow passage modification

4) System modification (Orientation of building integrated solar air heating system components)

2.2.1 Absorber modification for solar air heating collector

2.2.1.1 Unglazed solar collector absorber design factors

For unglazed solar collectors, the absorbers are generally perforated metal plates and optimisation criteria concentrate on the following factors:

1) material of the absorber;
2) porosity of the absorber;
3) air flow rate;
4) thickness of the absorber;

As the air to be heated flows through the perforation of the absorber surface, the heat transfer mechanism between the absorber perforation and air is more intimate compared to the flat plate absorber and as these are low temperature application systems, the maximum operating absorber temperature is much lower.

2.2.1.1.1 Effect of absorber material

Numerous authors have studied transpired absorber materials for UTC (Gawlik et al., 2005; Decker et al., 2001; Gawlik & Kutscher, 2002). It was previously assumed that the high performance of the collector depended on using a highly conductive material. The idea that high conductivity materials were needed was based on the assumption that a significant portion of the energy transfer from the panel to air stream occurs.

It was assumed that decreasing the plate conductivity would reduce the overall energy transfer rate to the airstream. It was also assumed that decreasing the plate conductivity would cause the average plate surface temperature to rise considerably and consequently cause a large increase in the radiant energy loss to the environment (Gawlik et al., 2005; Gawlik & Kutscher, 2002).

The effect of UTC absorber conductance on collector performance was analysed experimentally by Christensen et al. (1997). The absorber materials were aluminium (t = 0.0016 m, k = 216 W/mK) and styrene plastic (t = 0.0016 m, k = 0.16 W/mK) where, k = thermal conductivity and t = thickness. Both plates were spray painted with Krylon brand flat black paint with 0.0135 m triangular pitch and 0.0032 m hole diameter. For mass flux value 0.02 kg/s/m^2, the average heat flux delivered by the plastic absorber increased by 0.2% over the aluminium plate. At mass flux value of 0.04 and 0.06

kg/s/m^2 the average heat flux decreases for the plastic absorber by 0.3% and 6.3% (Christensen et al., 1997).

It was found that the thermal conductance can be very low (less than 1.0×10^{-2} W/K) without significantly affecting the efficiency of the UTC system (Kutscher, 1994). It was stated that the absorber plate of UTC may be formed of rigid or pliable or flexible sheet, foil, film, membrane or fabric (woven and nonwoven) (Christensen et al., 1997).

The material may be either single or multiply layers. Example materials included plastics, polyethylene or styrene, metal foils and porous materials such as open cell foam (Christensen et al., 1997; Keith et al., 2000). One or both of the front and back surfaces of the absorber may be dark colour to absorb solar radiation. Surfaces may be treated or coated to have a low emittance for infrared radiation so that heat loss is reduced.

The local convective heat transfer to the suction air is higher in regions of higher surface temperature and lower in regions of lower surface temperature. The variation of surface temperature may occur due to low conductance. However if the pitch is small enough, this effect can be avoided. Further study showed conductivity of material on the thermal performance of transpired collector was small (Gawlik, 2005). The study concluded that low conductive materials can be used with no thermal performance penalty but a great benefit in cost savings and corrosion resistance.

The performance of thicker absorber UTC (plate thickness 0.6 to 6.5 mm) was investigated (Decker et al., 2001) for a wide range of variables notably: suction velocity (0.028 m/s to 0.083 m/s), wind velocity (0 m/s to 5 m/s), hole pitch (7 mm to 24 mm), hole diameter (0.8 mm to 3.6 mm), thermal conductivity of absorber (0.15 to 200 W/mK).

It was found that the heat exchange effectiveness of the absorber decreases with increasing suction velocity, perforation pitch, hole diameter and thermal conductivity of the absorber. The strongest effects were found to be suction velocity and pitch. The heat exchange effectiveness was found to be very weakly dependent on plate thermal conductivity (Decker et al., 2001).

2.2.1.1.2 Effect of absorber porosity

Gawlik and Kutscher (2002) conducted experiments for UTC absorbers of low porosity ranging from 1.0 to 5.1 percent. They found that an increase in porosity decreases the effective conductivity of the material. Also lower porosity increases thermal performance due to increase in the heat transfer between absorber perforation and the air flow. However below 5% perforation of the absorber surface, the effect of porosity on thermal performance is insignificant (Christensen et al., 1997).

Simulation showed that the perforation diameter and pitch in a UTC affects performance significantly (Leon & Kumar, 2007). Analysis revealed that for a constant solar insolation and airflow, changing the pitch from 12 to 24 mm with a corresponding change in perforation diameter from 0.8 to 1.55 mm resulted in a drop of 5.5^{o}C in the air temperature rise.

Thus a decrease in pitch and hole combination from higher (24 mm pitch and 1.55 mm hole) to a lower combination (12 mm pitch and 0.80 mm hole) increases the temperature rise by 5.5^{o}C. The study also explained that the efficiency and effectiveness decrease with increase in pitch. However, pitch has a stronger influence on heat exchange effectiveness than on efficiency.

2.2.1.1.3 Effect of flow rate

For a combination of 1.6 mm thick, 3.2 mm hole, 13.5 mm pitch with 5% porosity of an aluminium absorber, if mass flux varies from 0.02-0.06 kg/s/m^2, efficiency of UTC increases from 63% to 82% (Christensen et al., 1997). At the same time, temperature rise decreases from 26.4^{o}C to 10.7^{o}C. However for 1.6 mm hole and 27 mm pitch with much lower porosity of 0.3%, for same air flow the efficiency increases from 63% to 84%. The difference in maximum efficiency was only 2%. It may be considered that above 1.6mm of diameter, the effect becomes insignificant.

Van Decker et al. (2001) predicted the collector efficiency was 68% at a mass flux of 0.02 kg/s/m^2. Most recently Badache et al. (2010) characterized unglazed transpired collectors where experimental results showed good agreement with previous study as the efficiency decreases with increasing absorber temperature with radiation.

The increase of the mass flow rate from 0.01 kg/s/m^2 to 0.03 kg/s/m^2, induces a decrease in surface temperature and consequently, an increase in efficiency from 30% to 70% for 1.5 mm perforation diameter, 24.5 mm pitch with triangular pattern (Christensen et al., 1997). The lower pitch and hole combination increases the heat transfer between absorber and the air flow and hence improves thermal performance.

In this case the outside air is drawn straight from ambient, uniformly through the whole surface of a perforated blackened absorber plate. The plates were assumed to be isothermal. The problem of defining effectiveness for a non-isothermal collector was addressed in a previous study (Gawlik, 1995).

2.2.1.1.4 Effect of absorber thickness

The effect of thickness of the absorber is insignificant when the absorber is thin ($0.794 \text{ mm} \geq t \leq 1.5 \text{ mm}$) (Kutscher, 1994). However, for thick absorbers ($1.6 \text{ mm} \geq t$

≤ 3.6 mm) the heat transfer varies between different area of the perforation which affect the thermal performance of the collector. For a thick absorber plate under typical operating conditions, ~ 62% of the ultimate temperature rise of the air occurred on the front surface, 28% in the hole and 10% on the back of the plate (Decker et al., 2001).

2.2.1.2 Glazed solar collector absorber design factors

The absorber in glazed solar collectors is entirely different from the UTC systems. For glazed solar collector, the absorbers are generally metal plates and optimisation criteria concentrate on following factors:

1) Material of the absorber

2) Geometry of the absorber

3) Selective coating on the absorber

4) Porous media in air passage

5) Absorber surface area alteration

2.2.1.2.1 Material of the absorber

Most popular absorber materials used for glazed solar collectors include: aluminium (Koyuncu, 2006); steel (Kurtbas & Durmus, 2004) and copper (El-Sebaii et. al., 2011a, 2011b; Karsli, 2007). However, these absorber materials are quite expensive and heavy in weight. Again the prices of these materials are closely related to the price of crude oil due to their production, fabrication and transport. The most common forms of modified absorber plates used in GSAHC are shown in Figure 2.1 (b), (c), (d) are finned absorber, glass absorber and corrugated absorber. Development of critical absorber plate designs were necessary to overcome the inherent shortcomings of metal absorber.

2.2.1.2.2 Geometry of the absorber

The purpose of the absorber is to absorb as much of the incident solar radiation as possible, re-emit as little as possible and allow efficient transfer of heat to a working fluid. Modification of the absorber involves increasing the absorber's heat transfer area by using different types of absorber configurations such as finned type, box type or V-corrugated type as presented in Figure 2.1 (b), (c), (d).

To extract the maximum amount of heat from the absorber, one solution is to introduce obstacles in the air stream to increase the absorber surface area (Kurtbas & Durmus, 2004). And at the same time increase the heat transfer co-efficient. The objective of using these obstacles is to increase the output temperature of the solar air heater. These obstacles can be fixed either to the internal face of the absorber or on the back plate or as a combination.

Several experiments were conducted on extending the heat transfer area of the absorber by attaching fins to the absorber of the solar air heater (Yeh, 1999; Yeh & Ting, 1986; Yeh & Hou, 2002). A solar collector of pin-fin integrated absorber was designed (Peng et al., 2002) to increase the thermal efficiency of the GSAHC. The average efficiency of pin-fin arrays collector reached 50% to 74%.

A single-pass Solar Air Heating Collector (SSAHC) was developed with offset rectangular plate fins (Moummi et al., 2004) which reached the maximum efficiency of ~ 75% during indoor experimental investigation for air flow 0.075 kg/s with a selective absorber (coppersun plate). A significant improvement is to use fins at 70^{o} to 75^{o} angle which increases the performance of the collector significantly (Karsli, 2007). However, the complicated absorber design increases collector weight and manufacturing cost.

2.2.1.2.3 Effect of selective coatings on absorber

In order to increase the absorption of solar radiation and reduce emission of long wave radiation from the absorber, metallic absorber surfaces are painted or coated with black paint. A selective coating can also be added to improve absorption of the absorber plate.

Selective coatings have high absorptance in the visible range of solar spectrum (0.3 to 3.0 µm) (Goswami et al., 2000). They have a low emittance coefficient beyond a wavelength of 2µm. Thus sunlight is absorbed well by a selective surface and because of its low emittance ($\epsilon = 0.02$ for infrared) the thermal energy is retained (Palz, 1978).

The properties of popular selective coatings for solar applications are presented in Appendix 1.1 and they are effective technique to enhance thermal performance. However, addition of these coatings increases the production cost of the collector absorber.

2.2.1.2.4 Effect of porous media in air passage

Incorporation of porous media within the air flow passage increases the heat transfer area between the absorber and the flowing air. However, due to complicated absorber geometry in GSAHC may result in elevated cost and construction difficulties. It may also reduce integration capability with the building façade.

The investigation by (Yousef and Adam, 2008) showed that the use of porous media in the lower channel of Double-pass Solar Air Heating Collector (DSAHC) increased the thermal efficiency by 8%. Air flows over and under the absorber surface in double pass solar air heating collectors. Porous materials are suitable for applications where higher temperatures are desirable.

The increased effectiveness of the heat exchange is mainly due to the intimate contact between the air and the porous plate. The idea of using a black porous matrix as an absorber of solar radiation has been used for many years.

The most common types of porous media in GSAHC are wire meshes, slit and expanded metals and transpired honeycomb absorbers (Tiwari & Suneja, 1997). Inexpensive porous materials such as crushed glass, wool, glass wool (Yousef and Adam, 2008) and metal wool (Yildiz et al., 2002) have been used to improve the performance of Single-pass Solar Air Heating Collectors (SSAHC). Air flows only over or under the absorber surface in single pass solar air heating collectors.

The thermal efficiency of a double pass solar collector with porous media is significantly higher than the thermal efficiency of conventional single pass air heaters, exceeding 75% under normal operating conditions (Ramadan et al., 2007; Sopian et al., 2009). However, porous media may reduce thermo-hydraulic performance of the collector as it increases the pressure drop which may cause higher operating cost.

2.2.2 Glazing modifications of solar air heating collector

A solar air heating collector has to allow insolation to reach the absorber plate while preventing rain, snow, wind and outside temperatures from reducing energy reaching the plate surface. The simplest improvement is to glaze the absorber plate with a transparent material capable of transmitting sunlight and retaining that transmitted energy within the collector.

Three transparent materials commonly used are glass, plastic and fibreglass with the challenge being to find a material with good transmissivity, low thermal conductivity and the required mechanical properties for building integrated glazing systems.

A glazing cover transmits shorter wavelength solar radiation but block the longer wavelength solar radiation from re-radiating from the absorber plate (Palz, 1978). The heat trap phenomenon is more generally known as the greenhouse effect. Glass for this application fulfils the requirements of transmission and toughness and is almost totally opaque to thermal radiation (5.0 – 50 µm) (Cheremisinoff & Regino, 1978; Kalogirou, 2009).

Primarily it may sound like a disadvantage, but most of the long wave radiation can be trapped from the absorber plate after conversion to heat. Thus glass prevents the collector from moisture and convective heat loss. As a result the cavity works as a long wave heat trap which helps the collector to operate at high efficiency.

Most common types of GSAHC are designed with one glazing cover (Karsli, 2007; Koyuncu, 2006; Kurtbas & Durmus, 2004; Romdhane, 2007). In order to minimize the upward heat loss from the collector, more than one transparent glazing may be used (El-Khawajah et al., 2011; El-Sebaii et al., 2011a, 2011b; Sopian et al., 2009; Wazed et al., 2010; Yeh et al., 2002). However, transmittance decreases due to the increased number of glazing covers (Duffie & Deckman, 2006).

Glass is also very resistant to scratching, high temperatures and practically impervious to the damaging effects of ultraviolet exposure. The incident sunlight transmitted through glass depends on the iron content of the glass, between 85% to 92%, at normal incidence (Cheremisinoff & Regino, 1978). While low iron content increases the transmittance of glass, low iron glass is more expensive. Glass can be easily broken; this disadvantage is usually minimized by using tempered glass which adds a further additional cost.

Glass is the most common glazing material used in (El-Khawajah et al., 2011; El-Sebaii et al., 2011a, 2011b; Karsli, 2007; Kurtbas & Durmus, 2004; Sopian et al., 2009; Wazed et al., 2010; Yeh et al., 2002). Spectral transmittance of 6 mm thick glass with different iron oxide content for incident radiation at normal incidence is shown in Figure 2.2. The content of iron oxide varies from 0.02% to 0.5% depending on the quality of the glass. Water white, standard and heat absorbing glass contains accordingly 0.02%, 0.1% and 0.05% iron oxide. Water white glass shows transmittance approximately 90% between 0.3 and 2.8 μm.

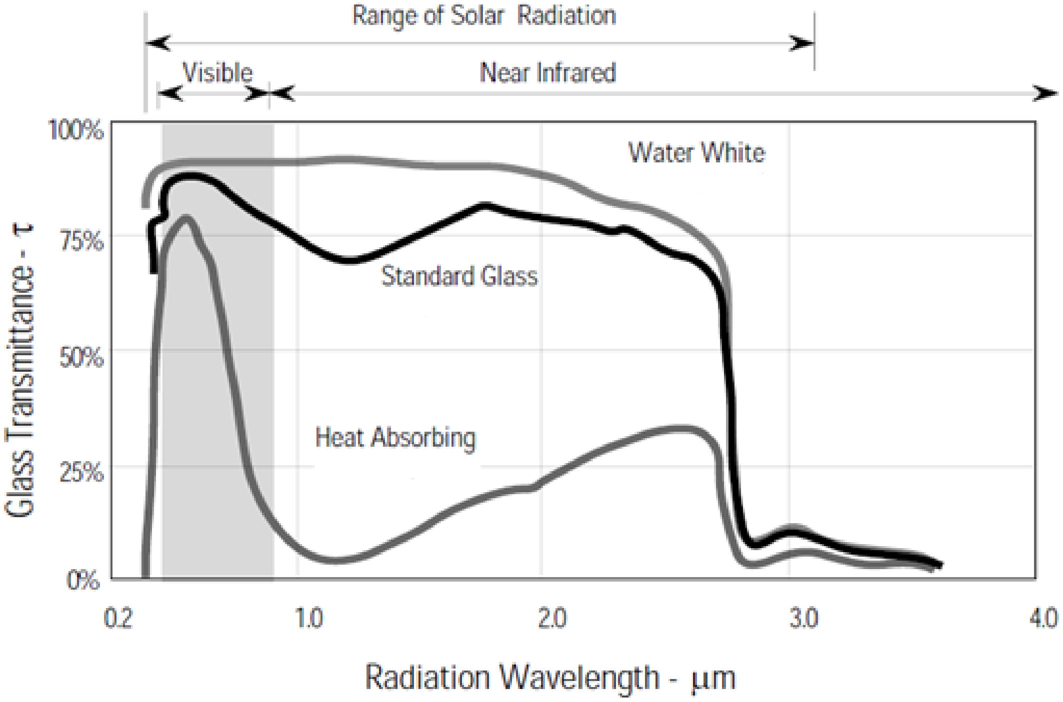

Figure 2.2: Spectral transmittance of 6 mm thick glass with various iron oxide content for solar radiation at normal incidence. Adapted from Duffie and Beckman (2006) as referred by Wasley & Utzinger (1996)

Standard glass shows transmittance more than 75% within visible range. However the spectral transmittance declines after visible range. Glass transmittance shows worst performance for higher iron oxide content. Transparent plastics, such as polycarbonates (Cansolar; Goswami et al., 2000; Palsun, 2011; Romdhane, 2007), polyethylene (Koyuncu, 2006) (Koyuncu, 2006) and acrylics (Acrylite, 2011) have been used as glazing materials.

Their main advantages are resistance to breakage and light weight. The main disadvantages of plastics are: their high transmittance in the longer wavelength and deterioration over a period of time due to ultraviolet solar radiation (Goswami et al., 2000; Duffie & Beckman, 2006). Additionally, plastics are generally limited in the temperatures they can sustain without deteriorating or undergoing dimensional changes.

Appendix 1.2 shows the properties of currently commercially available enhanced glazing materials. Enerconcept Technologies (STW, 2012), a Canadian company recently used perforated plastic (polycarbonate) as glazing material for their new transpired 'Lubi Wall' glazed air collector.

As shown in the Appendix 1.2, the transmittance of low iron glass with antireflective coating can reach 96%. A tempered glass with high transmittance (96%) with antireflection coating cost €125/m^2. Polycarbonate with antireflecting coating can reach such transmittance and available with €70/m^2 which is much cheaper than glass. Polyethylene terephthalate (PET) costs only €5/m^2. A glazing of 0.15 mm thick PET was used by Koyuncu (2006) as listed in Table 2.2.

However, glass still seems best option as glazing material of the collector considering 20 years life span of the collector. Product life span, quality and cost are three critical factors in selecting system component. PET with low thickness may be the cheapest option in selecting glazing material of solar air heating system. However, this can only be feasible for prototype designing which cannot be used for longer life span. Polycarbonate is better than PET as the glazing material considering strength and durability.

Yellowing effect due to UV was reduced in commercial brands of polycarbonate. However, this material can only be appropriate if the solar air heating collector life span in less than 5-7 years. If the weight is an issue, commercial brands of clear polycarbonate (example: Plexiglass) has very low density (1.19 g/cm^3) compare to low iron glass (2.5 g/cm^3). Though glass is an expensive option when considering 20 years collector life span, this is the best option as the glazing material.

Reflection losses of the glazing surface depend on the refractive index of the cover material and structural orientation of the glazing. The lowest reflection losses can be achieved if an antireflective coating with a refractive index between the air and the cover material is used (Duffie & Deckman, 2006). The effect of dirt and dust on collector glazing may be quite small, and the cleansing effect of an occasional rainfall is usually adequate to maintain the transmittance loss within 2-4% of its maximum value (Duffie & Beckman, 2006; Kalogirou, 2009).

2.2.3 Air flow passage modifications of glazed solar air heating collector

Double pass systems are 10-15% more efficient than SSAHC (Tiwari & Suneja, 1997). An improvement in the efficiency of DSAHC is obtained with very little additional material and construction cost in the design of the air passage. Experiments (Wazed et al., 2010) showed that the maximum efficiency is much higher for double flow solar air heating collector with forced draft (62.2%) compared to natural draft (24.8%).

Solar air heating collectors require a fully developed turbulent flow for better thermal conversion (Moummi et al., 2004; Youcef-Ali, 2005). This increases the thermal heat transfer between the absorber plate and air. It was reported that the effect of recycling enhances the efficiency. Numerous investigators proposed two or multi-pass operation with internal or external recycle included (Duffie & Beckman, 2006; Kalogirou, 2009; Yeh & Hsieh, 2005; Yeh et al., 2002; Yeh et al., 1999).

2.2.4 System modifications of glazed solar air heating collector

Research on system modification approved by the committee of the International Energy Agency (IEA) and funded by nine countries under ‘Task 19’ suggested six types of solar air systems (Hastings & Morck, 2000). Details of the six models are shown in Figure 2.3. The models are:

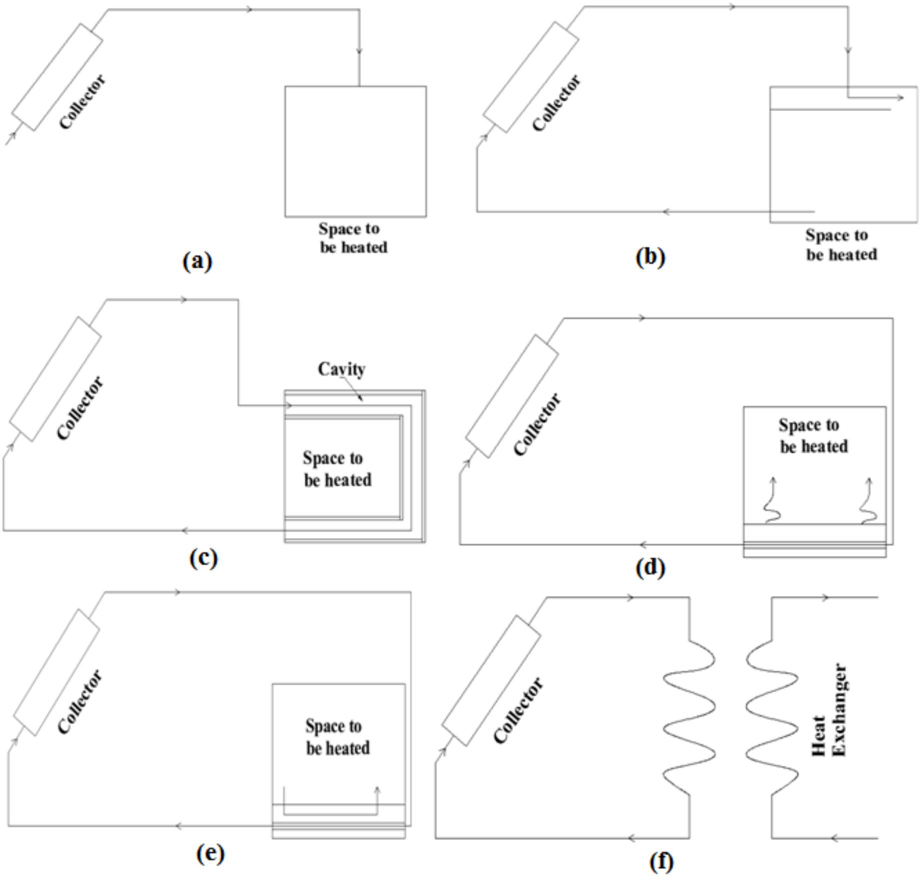

Figure 2.3: a) Solar heating of ventilation air; b) Collector/room/collector; c) Collector-heated air circulated through cavity in the building envelope; d) Closed loop collector/storage and radiant discharge to building spaces; e) Open single loop collector to the building spaces; f) Collector heated air transferred to water via an air/water heat exchanger.

a) **Solar heating of ventilation air:**

Figure 2.3 (a) shows the solar heating of ventilation air. This is an open loop heating system. This is the most economical design which draws outside air through the collector directly into the space to be ventilated and heated. This system can achieve very high efficiencies because cool air is supplied to the collector. Appropriate applications range from keeping unoccupied vacation cottages from becoming damp and musty to ventilating schools, offices and large industry halls. The type-a air heating system appropriate for ventilating schools, offices and large industry halls and keeping unoccupied vacation cottages from becoming damp and musty.

b) **Collector/Room/Collector:**

Figure 2.3 (b) shows a closed loop solar heating system. In this model room air is circulated into the collector where it is heated, rises and returns via a thermal storage ceiling back into the room, all by natural convection. The storage radiates heat after sunset. This system has been used mostly for apartment buildings. Type-b system was used for apartment buildings.

c) Collector-heated air circulated through cavity in the building envelope:

Figure 2.3 (c) shows a solar heating collector with air circulated through cavity in the building envelope. Heat losses through the hollow building envelope can be drastically reduced by circulating warm air through a hollow building envelope. The air is warmed by a SAH collector. Type-c is especially appropriate for retrofitting poorly insulated existing apartment buildings. The air returns to the collector from the building envelope. A bypass from the collector directly to an air to water heat exchanger can allow heating of domestic hot water as well. The system is especially appropriate for retrofitting poorly insulated existing apartment buildings.

d) Closed loop collector/storage and radiant discharge to building spaces:

Figure 2.3 (d) shows a closed loop collector and storage system. In this type of solar air heating collector, warm air is circulated through channels in a floor or wall which then radiates the heat into the room four to six hours later. This system has the advantage of large radiating surfaces providing comfort. Fan-forced circulation provides the best overall system efficiency and output. Applications include all building types which have large surfaces available for the radiant surfaces. Application of type-d includes all building types which have large surfaces available for the radiant surfaces.

e) Open single loop collector to the building spaces:

Figure 2.3 (e) shows an orientation of heating system with separate collector and heating discharge unit. This system is similar to (d) however; separate channels in the storage allow a controlled active discharge.

The storage is insulated so it can be charged to higher temperatures and not discharged until heat is desired. An additional advantage of this system is the storage can be located remotely from the rooms to be heated. The type-e can be used for rooms to be heated with remotely located storage. Relatively few buildings exist with this system because of the expense involved.

f) Collector heated air transferred to water via an air/water heat exchanger:

Figure 2.3 (f) shows a heating system integrated with a heat exchanger. In this system, the hot air from the collectors passes over an air to water heat exchanger. The hot water can then be circulated to conventional radiators, radiant floors or walls or to a domestic hot water tank. Type-f can be used for the applications where the heat must be transported over a distance are particularly suited for this system. Retrofit of existing buildings is simplified in this SAH system.

2.3 Experimental results on glazed air heating collectors

Research relating to glazed solar air heating collectors has mostly focused on double pass and single pass solar air heating collectors to enhance the heat transfer mechanism, to reduce radiation and convection losses from the glazing aperture, to improve thermo-physical performance and to improve thermal efficiency. The performance of the air heating systems varies with system dimension, climate conditions and the location of the experiment.

Table 2.1 presents a summary of various research results on the performance of double-pass and single-pass solar air heating collectors which are two major types of glazed air heating collectors considering flow criteria. The applied air flow rate varied between 0.0107 kg/s/m^2 and 0.04 kg/s/m^2. The maximum radiation level during experiment varied between 880 W/m^2 and 1100 W/m^2.

The maximum outlet temperature rise varied between 55^{o}C and 67^{o}C. The maximum outlet temperature with single pass air heating collector was 67^{o}C at very low air flow rate (0.012 kg/s/m^2). The maximum outlet air temperature with double pass air heating collector was 64.5^{o}C at air flow rate 0.0203kg/s/m^2. The thermal efficiency varied between 55.7% and 70.8%.

The highest thermal efficiency was 70.8% for double pass flow collector with flow rate 0.0214 kg/s/m^2 at 1100 W/m^2 radiation level during indoor experiment with modified absorber with finned attached over and under the metal absorber plate. The lowest thermal efficiency was 55.7% for double pass flow collector 0.04 kg/s/m^2 at radiation level 977 W/m^2. In outdoor experiments the maximum temperature rise was 28.5^{o}C at 0.0203 kg/s/m^2 flow rate with v-corrugated copper absorber and 0.3 cm two window glass glazing. The lowest temperature rise was 21.7 ^{o}C with plane aluminium absorber and single glass cover glazing.

Table 2.1: Reported performance of GSAHC

Type	Air mass flow at max. temp. rise (kg/s/m^2)	Air mass flow at max. efficiency (kg/s/m^2)	Max. temp. rise (ΔT) (^{o}C)	Max. amb. temp. (^{o}C)	Max. air temp. at outlet (^{o}C)	Radiation at max. temp. rise (W/m^2)	Max. thermal η (%)	Reference
DSAHC	0.020	0.04	28.50	36.0	64.5	978	65.3	(El-Sebaii et al., 2011a)
DSAHC	0.020	0.04	24.00	34.5	58.5	977	55.7	(El-Sebaii et al., 2011b)
DSAHC	0.037	0.07	×	33.5	×	624	70.0	(Sopian et al., 2009)
DSAHC	0.011	0.02	×	30.0	×	1100	70.8	(Yeh et al., 2002)
DSAHC	×	×	21.75	33.3	55.0	1000	62.1	(Wazed et al., 2010)
SSAHC	0.012	0.03	×	×	67.0	880	64.0	(Kurtbas & Durmus, 2004)

Table 2.2 details the selection of the system component, incorporated modification, location and weather condition of the experiment of recent research initiatives. The most of the experiments were carried out under prevailing weather condition. The modification of the collector were double flow/single flow, 2/4/6 fins with wire mesh incorporated absorber surface, V-corrugated absorber plate, finned absorber plate, porous media in the air channel, fins attached over and under the absorber plate, baffles between the absorber and insulation, zigzag plate absorber and special construction of absorber surface.

The glazing material used in experimental prototype varied in material type, number of glazing and thickness. The material of the glazing in experiments varied within glass, polycarbonate and polyethylene etc. Glass was the most common glazing used in experiments which vary in quality and thickness. Glass was used from 3 mm to 5 mm and quality varied from low iron glass to general window glass. The number of glazing was used one or two. Polyethylene was the thinnest with 150µm. Window glass of 0.4 cm was the thickest glazing.

The absorber materials used in the experimental solar air collectors were black painted copper, aluminium and galvanized steel. The absorber of 1mm thickness was the most commonly used absorber. The lowest absorber thickness was 0.4 mm and the highest thickness was 1 mm. The insulation materials used in experimental solar air collectors were: styrofoam, polystyrene, wood, foam, glass wool and hardboard etc. The highest thickness was 5 cm of polystyrene and the 2 cm of Styrofoam and hardboard.

Table 2.2: Experimental details of glazed air heating collectors

Type	Location	Condition	Date	Insulation	Dimensions	Glazing	Modification	Reference
DSAHC	Cyprus	Clear Sky	May to Aug. 2010	External 2 cm thick Styrofoam	2 cm thick plywood frame internally black painted	0.4 cm thick window glass	2/4/6 fins with wire mesh was used as absorber	(El-Khawajah, 2011)
DSAHC	Tanta, Egypt	Prevailing weather	July 2009	4 cm thick foam at the back and sides	0.1 cm thick copper absorber of $1m^2$ area	0.3 cm two window glass	V-corrugated absorber plate	(El-Sebaii et al., 2011a)
DSAHC	Tanta, Egypt	Clear Days	July 2009	4 cm thick foam	0.1 cm thick copper absorber of $1m^2$ area	0.3 cm thick two window glass	Finned absorber plate	(El-Sebaii et al., 2011b)
DSAHC	Selangor, Malaysia	Indoor	2009	Insulated	Black painted aluminium absorber. 120 cm x 240 cm collector	Glass covers	Porous media in the second channel	(Sopian et al., 2009)
DSAHC	Taipei, Taiwan	Indoor	2002	Insulated	$30\times2.75\times30$ cm^3 collector	Glass covers	Fins attached over and under the absorber plate	(Yeh et al., 2002)
SSAHC	France	Indoor	2006	5 cm thick polystyrene insulation	2 m^2 collector area, 1 mm black painted absorber	5 mm double polycarbonate	Baffles between insulator and the absorber	(Romdhane, 2007)
DSAHC	Bangladesh	Outdoor	August	×	Black painted metal absorber	Single glass cover	Forced and natural draft	(Wazed et al., 2010)
SSAHC	Erzurum, Turkey,	Clear sky	15 June 2004	Backs and sides with 5 cm and 2.5 cm of glass wool	Dull black painted copper absorber of 1 mm thickness and 0.405 m^2 absorber area	Normal window glass of 4 mm thickness	Finned at different angles to the absorber and the back plate	(Karsli, 2007)
SSAHC	Samsun, Turkey.	Outdoor	Summer, 2001	20 mm hardboard thickness (conductivity 0.15 W/mK)	Black painted 0.4 mm thickness aluminium sheet.	Normal polyethylene of 0.15 mm thickness	Zigzag black painted plate was used as absorber	(Koyuncu, 2006)
SSAHC	Elazig, Turkey.	Outdoor	June, July and August	Glass wool (conductivity 0.038 W/mK)	Black painted galvanized sheet 0.8 mm thick.	Single glass cover	Special construction of absorber surface	(Kurtbas & Durmus, 2004)

2.4 Optical concentrator

Compound Parabolic Concentrator (CPC) is a non-imaging optical concentrator which does not produce an image of the light source. It is designed to concentrate radiation at a density as high as theoretically possible. Originally it was invented in 1965 for the reflection of Cerenkov radiation onto a sensor, and it took more than a decade for it to become the state of the art of solar thermal energy collection (Leutz & Suzuki, 2001). CPC reflectors were introduced by Winston (1974) to improve the performance of low concentration solar collectors having the ability to reflect all of the incident radiation on the aperture to the receiver over ranges of incidence angles within acceptance angle.

2.4.1 Design of CPC as an optical concentrator

A basic CPC for solar energy applications consists of the combination of two parabolic reflectors. These reflectors can reflect both direct and a fraction of the diffuse incident radiation at the entrance aperture onto the absorber. The axis of the parabola makes an angle $\pm\theta_a$ with the collector mid plane. The geometry of CPC is a combination of two parabolas. A basic parabola can be generated using the x-y coordinate system of the Equation 2.1.

$$y = \frac{x^2}{2b\left(1+\sin\theta_a\right)} \qquad 2.1$$

The focal length is given as:

$$f_{parabola} = \frac{b}{2}\left(1+\sin\theta_a\right) \qquad 2.2$$

The height,

$$h = \frac{f\cos\theta_c}{\sin^2\theta_c} \qquad 2.3$$

where

b = absorber width, θ_a = half acceptance angle

f = focal length, h = height of the CPC

The geometry of a two-dimensional CPC is shown in Figure 2.4. The concentrator consists of two segments AC and BD which are parts of two parabolas 1 and 2.

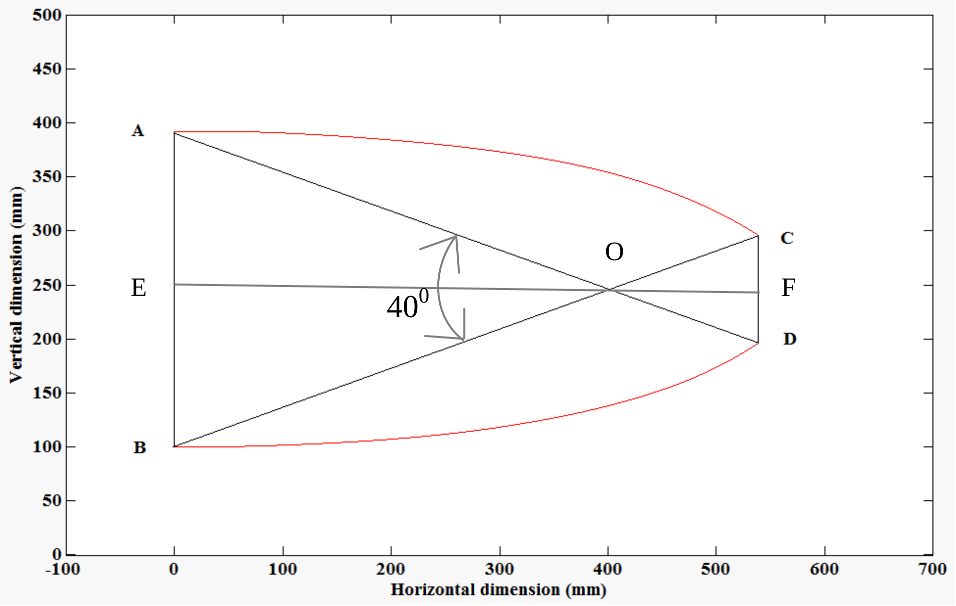

Figure 2.4: Symmetric CPC

AB is the aperture of width w and CD is the absorber surface of width b. The axes of the two parabolas are oriented to each other at an angle such that point C is the focus of parabola 2 and point D is the focus of parabola 1. Tangents drawn to the parabolas at points A and B are parallel to the axis of the CPC, EF.

The acceptance angle of the CPC is the angle AOB (2θa), made by the lines obtained by joining each focus to the opposite aperture edge. The geometric concentration ratio is given by (w/b).

2.4.2 Concentration Ratio of the optical concentrator

The geometric concentration ratio of a concentrator system is defined as the ratio between the entry aperture and the exit aperture:

$$C = \frac{A_1}{A_2} \qquad 2.4$$

Where, C = concentration ratio, A_1 is the area of the entry aperture and A_2 is the area of the exit aperture.

Concentrators can be divided into two groups:

1) two dimensional concentrators (2D); and

2) three dimensional concentrators (3D)

The principal non tracking collector types are flat plates, flat plates enhanced by side reflectors or V-troughs, tubular collectors, and compound parabolic concentrators (CPC). Concentrators that reach the thermodynamic limit of concentration for an acceptance half-angle θ_a have been called ideal concentrators because of their optical properties (Nilsson, 2005).

$$C = \frac{1}{\sin\theta_a} \text{ in two dimensions,} \qquad 2.5$$

$$C = \frac{1}{\sin^2\theta_a} \text{ in three dimensions,} \qquad 2.6$$

2.4.3 The Equation of a CPC with a Flat Absorber

The equation for a meridian section of CPC reflector was presented by Welford and Winston (1978). In Figure 2.5, CPC using the equation has been shown.

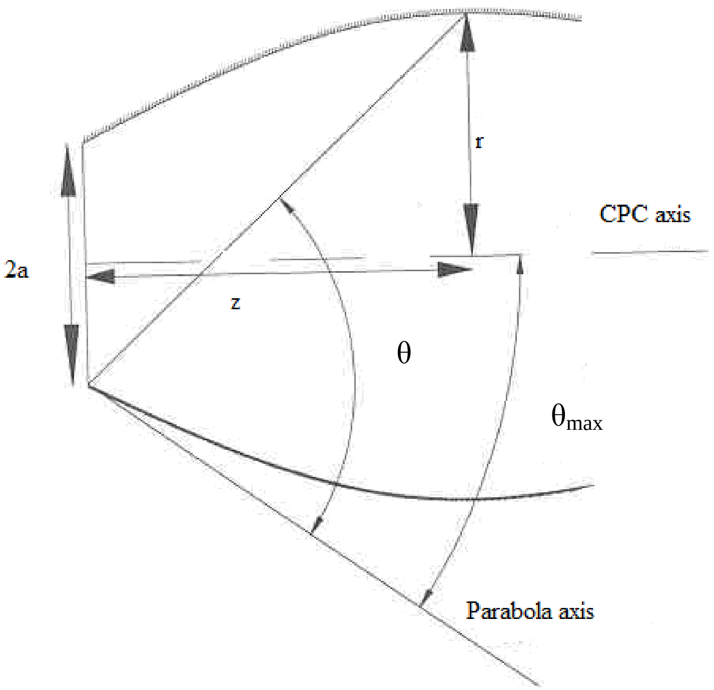

Figure 2.5: The angle used in the parametric equations of the CPC
(Welford & Winston, 1978)

This is drawn by rotation of the axis and translation of the origin in terms of diameter (2a) and the acceptance angle (θ_{max}). The CPC profile was expressed in polar coordinates (r, φ) (Welford & Winton, 1978).

$$\left(r\cos\theta_{max} + y\sin\theta_{max}\right)^2 + 2a\left(1+\sin\theta_{max}\right)^2 r - \\ 2a\cos\theta_{max}\left(2+\sin\theta_{max}\right)z - a^2\left(1+\sin\theta_{max}\right)\left(3+\sin\theta_{max}\right) = 0 \qquad 2.7$$

Where,

2a = receiver width

θ_{max} = maximum acceptance angle (This is the maximum possible concentration for the acceptance angle 2θa).

CPC can be optimised considering location and application. Lowering the CPC geometric concentration ratio results in a higher proportion of the diffuse component of incident solar radiation being accepted. This CPC with a high angular acceptance can operate efficiently without the need for the additional capital and maintenance cost of solar tracking mechanisms.

CPC is very deep and requires a large concentrator area for a given aperture. However, large portions of the top of the CPC can be removed with negligible loss in performance. Thus, CPC is generally truncated by about 50 % in order to reduce its cost. A detailed study on the effects of truncation has also been carried out by (Rabl, 1976a).

The height and surface area of the CPC can also be calculated with help of Equation 2.12 from (Rabl, 1976a, Rabl, 1976b).

The height to aperture ratio of the concentrator is given by

$$\frac{H}{W} = \frac{1}{2}\left(1 + \frac{1}{\sin\theta_a}\right)\cos\theta_a = \frac{1}{2}(1+C)\left(1 - \frac{1}{C^2}\right)^{\frac{1}{2}} \qquad 2.8$$

Where,

H = Height of the concentrator, θ_a = half acceptance angle

C = Concentration ratio, W = Width of the aperture

The surface area of the concentrator is obtained by integrating along the parabolic arc and the ratio of the surface area of the concentrator to the area of the aperture is given by the expression as:

$$\frac{A_{con}}{WL} = \sin\theta_a\left(1+\sin\theta_a\right)\left[\frac{\cos\theta_a}{\sin^2\theta_a} + \ln\left\{\frac{\left(1+\sin\theta_a\right)\left(1+\cos\theta_a\right)}{\sin\theta_a\left[\cos\theta_a + \left(2+2\sin\theta_a\right)^{1/2}\right]}\right\} - \frac{\sqrt{2}\cos\theta_a}{\left(1+\sin\theta_a\right)^{3/2}}\right] \qquad 2.9$$

Where,

A_{con} = Area of the concentrator, L = Length of the concentrator

The calculation of average number of reflection (n_{avg}) for a symmetric CPC is as follows.

$$n_{avg} = \frac{1}{2\sin^2\theta_a}\left(\frac{A_{con}}{WL}\right) - \frac{(1-\sin\theta_a)(1+2\sin\theta_a)}{2\sin^2\theta_a} \qquad 2.10$$

Height and aperture of truncated CPC can be calculated as (Welford and Winston, 1978)

$$h_T = \frac{f\cos(\phi_T - \theta_c)}{\sin^2\left(\phi_T/2\right)} \qquad 2.11$$

$$a_T = \frac{f\sin(\phi_T - \theta_c)}{\sin^2\left(\phi_T/2\right)} - a_{absorber} \qquad 2.12$$

Where,

f = focal length, h_T = truncated height of the concentrator,

a_T = aperture of the truncated collector

Average number of reflections for either a truncated CPC can be calculated as (Rabl, 1976b)

$$n_{avg} = \max\left[C\frac{A_{T\mathrm{con}}}{a_{Taperture}} - \frac{x^2-\cos^2\theta}{2(1+\sin\theta)}, 1-\frac{1}{C}\right] \qquad 2.13$$

$$x = \left(\frac{1+\sin\theta}{\cos\theta}\right)\left\{-\sin\theta + \left(1+\frac{h_T}{h}\cot^2\theta\right)^{\frac{1}{2}}\right\} \qquad 2.14$$

An approximate value of the average number of reflection for symmetric CPC has been used for CPC design (Pramuang & Exell, 2005; Rabl, 1985)

$$n_{avg} = 1 + 0.07C \qquad 2.15$$

Where,

n_{avg} = average number of reflection, C = concentration ratio

Mallick (2003), demonstrated the performance of an asymmetric CPC (ACPC) for building-integrated façades. ACPCs with geometric concentration ratios of 2 and 2.45 were developed (Mallick & Eames, 2007; Mallick et al., 2006). A reduction of 40% in cost per W_p, compared to a reference non-concentrating panel utilizing the same solar cells, is estimated for the CPC panel with an acceptance half angle of 37° (Mallick et al, 2007).

For this research a detailed ray tracing was necessary to estimate the optical efficiency of this novel SAH collector. The average number of reflections was calculated for each degree incident angle of radiation on the aperture. The symmetric un-truncated CPC of 20^o acceptance angle is shown in Figure 2.6, AB is the aperture and CD is the absorber of the concentrator.

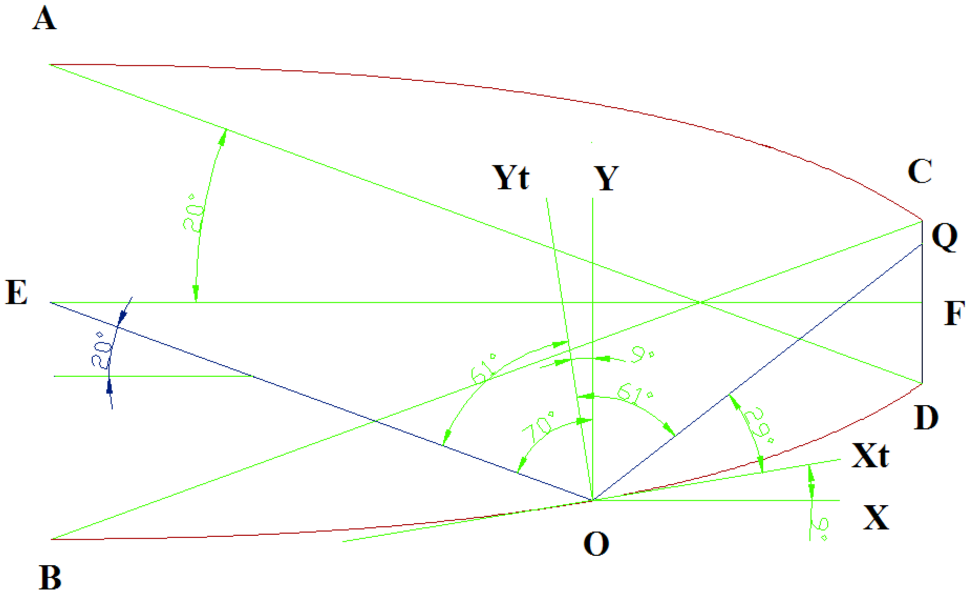

Figure 2.6: Solar radiation concentrated at 20^o incident angle

A ray EO incident at point O at an angle 20^o on the lower reflector surface and reaches absorber after one reflection. The related angles are shown in Figure 2.6.

2.5 CPC Integrated with Solar Collectors

The usefulness of the CPC for solar energy collection was noted by numerous researchers (Rabl, 1985, Welford & Winston, 1978; Winston, 1974; Norton et al., 1989; Norton et al., 1991; Eames et al., 1995).

A numerical simulation model was developed by (Eames and Norton, 1993a) for the prediction of the combined optical and thermo-fluid behaviour of line axis concentrating solar energy collectors which combines two-dimensional steady state finite element analysis of convective heat transfer and ray trace techniques. A detailed parametric analysis of heat transfer in CPC integrated solar energy collectors was performed using unified model for their optical and thermophysical behaviour (Eames & Norton, 1993b). The effects of angular inclination and collector acceptance angles on free convection within the cavity were presented.

A theoretical and experimental investigation into the modifications in optical and thermal performance resulting from the introduction of a baffle into the cavity of a CPC integrated solar energy collector was presented (Eames & Norton, 1995). It was showed that by the introduction of a baffle into the cavity of a non evacuated CPC the total collector efficiency can be increased.

A design and thermal performance of modified CPC integrated solar energy collector were descried by Norton et al., (1989) which incorporated a curved inverted-Vee absorber fin which allows a reflector of simple geometry. The CPC collector showed a superior optical efficiency and heat removal factor to that of a conventional cusp reflector CPC design. An extensive review on the optical and thermal characteristics of line axis concentrating solar energy collectors was presented by Norton et al., (1991) which details the thermal and optical aspects of symmetric and asymmetric CPC integrated solar energy collectors.

Several researchers (Adsten, 2002; Mallick, 2003; Nilsson, 2005) suggested that the concentrator design should be highly asymmetric at high latitude. The ACPC is a transformed form of a non-imaging CPC. The foci and end points of the two parabolas of an ACPC make different angles with the absorber surface. Truncation of the reflectors of an ACPC reduces the size and cost of a system but results in a loss of concentration (Mallick, 2003).

Mallick (2003) has demonstrated different ACPC implementation for building-integrated wall façade. The asymmetric CPC designed by Mallick et al. (2006) is shown in Figure 2.7, based on a detailed optical and heat transfer analysis (Mallick, 2003). This research showed the feasibility of asymmetric CPC integration with building façade. An integrated Collector storage (ICS) solar system with ACPC is shown in Figure 2.8 (Tripanagnostopoulos & Souliotis, 2004). The systems were developed to absorb solar radiation directly and after concentration on the absorber for heating water. The irradiation in MaReCo concentrator (Nilsson, 2005) reaches the absorber on both sides due to the circular section inserted between the endpoints of the two parabolas. The circular section reflects all incoming irradiation onto the absorber.

Two stage ACPC systems with an inverted absorber were developed to heat water through tubular absorber. The system showed reduced convection loss due to the inverted absorber (Eames, 2002; Eames et al., 2001; Smyth et al., 2005). Increasing the CPC concentration ratio leads to higher working fluid temperatures but reduced utilization of available insolation. The junction section of primary and secondary concentrator creates a non-uniform surface in the two stage concentrator structure. An absorber placed horizontally, facing downward was presented in a previous study (Rabl, 1976a) which showed a lower radiation loss compare to absorber surface facing sky.

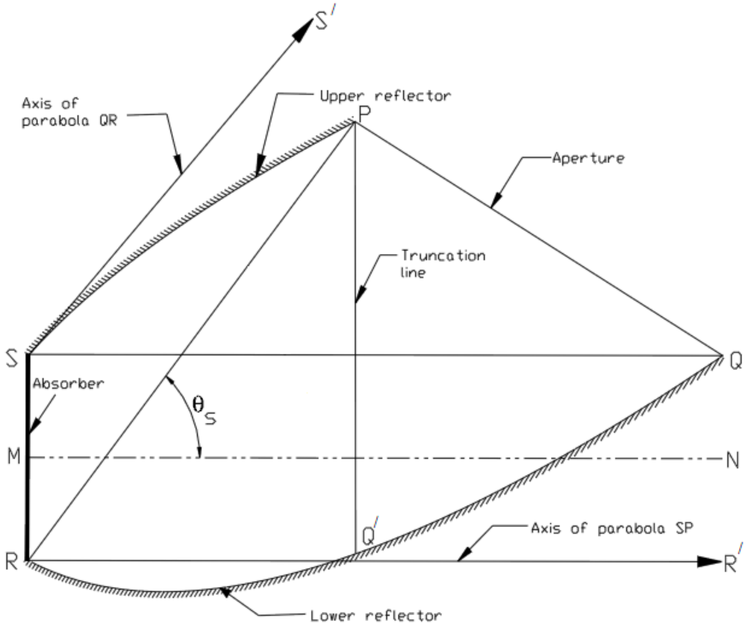

Figure 2.7: ACPC for building integration (Mallick, 2003; Mallick et al., 2006)

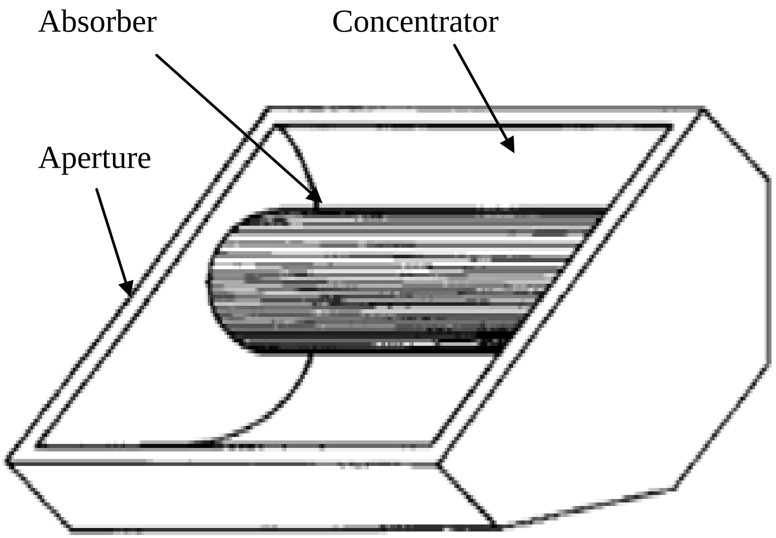

Figure 2.8: Integrated Collector storage (ICS) solar systems with asymmetric CPC (Tripanagnostopoulos & Souliotis, 2004)

A concentrating system employing inverted flat plate absorbers was demonstrated (Kienzlen et al., 1988) in which radiation was reflected from below onto the downward facing absorber. Kothdiwala et al. (1995) conducted optical parametric analysis on asymmetric line-axis Inverted ACPC. Optical efficiency of an inverted absorber was estimated highest at the lowest height of the tertiary reflector. This phenomenon is due to reduction of reflection loss at the tertiary section.

However, the research suggested a tertiary section to improve thermal efficiency of the collector. This is mostly due to convection suppression at the absorber due to the formation of a pocket of hot air at tertiary section (Eames et al., 1993a; Eames et al., 1993b; Eames et al., 1996; Kothdiwala et al., 1995; Kothdiwala et al., 1996; Kothdiwala et al., 1999; Norton, 1994). It also stabilise the thermal layer below absorber surface from the interference of the air flow.

2.6 Why integration of transpired absorber and CPC

Low convective heat transfer coefficients arising from low thermo-physical properties of air i.e. low density, volumetric heat capacity and heat conductivity are the vital reason for the poor thermal heat transfer performances of flat plate solar air collectors (Esen, 2008; Ma et al., 2011; Moummi et al., 2004). Poor heat removal gives high absorber plate temperatures, leading to high heat losses to the environment resulting in low thermal efficiency.

Glazing design has to consider the best way to allow the sunshine to reach the absorber plate while preventing external weather conditions from harming the plate surface and stealing away collected heat. However, optical loss due to reflection at the glazing surface is another factor for stationary solar collectors. The improvement of these drawbacks is a trade-off with manufacturing cost. UTC system design solved some of these issues. UTC is an unglazed solar air heating collector which avoids optical loss due to glazing and provides intimate heat exchange between flowing air and absorber surface as air flows through the perforated absorber surface (Dymond & Kutscher, 1997; Kutscher, 1994).

The cost of the UTC was minimised compared to glazed solar collectors due to absence of the glazing surface. However, the surface area of UTC has to be significantly large because the typical range of mass suction flow rates is 0.006 to 0.04 kg/s/m^2. At a stable radiation level of 700 W/m^2, the corresponding temperature rise was 36^{o}C at low flow rate (0.006 kg/s/m^2) range and 12^o C at high flow range (0.04 kg/s/m^2) (Kutscher, 1994; Kutscher et al., 1993).

Basically UTC system may look very simple without a glazing surface. However, it is not possible to avoid radiation loss from the large uncovered absorber surface. The performance of UTC can be affected due to reverse flow effect, high wind speed effect, rain effect as it is exposed to the environment. Also at low air flow range the efficiency of the system is poor because the amount of air to be heated is very low.

Integration of a concentrator in a transpired collector can increase the radiation concentration onto the absorber surface. However, it may enhance radiation loss due to a higher absorber temperature, conduction loss from the metal absorber, convection loss from the glazing and back plate. These critical issues of optical loss, heat transfer loss, absorber size reduction, system weight reduction and cost reduction aspects were considered during CTAH design.

Integration of transpired absorber with asymmetric CPC for air heating purposes has been investigated in this thesis for the first time. However, there have been numerous researches reported on CPC integration with solar collectors (Kienzlen et al., 1988; Kothdiwala et al., 1995; Kothdiwala et al., 1997; Kothdiwala, 1999; Mallick et al., 2006; Nilsson, 2005; Rabl, 1976a; Tripanagnostopoulos & Souliotis, 2004). Also, very few analyses reported on CPC integrated solar air heating collectors (Pramuang & Exell, 2005; Tchinda, 2008). The previous research presented feasible designs of solar thermal collectors. This research presents Concentrating Transpired Air Heating-collector (CTAH) which is integration of an inverted transpired absorber and asymmetric CPC.

2.7 Design issues of Concentrating Transpired Air Heating-collector

Schematic diagram of the CTAH system is presented in Figure 2.9 which is a combination of transpired absorber and Asymmetric Compound Parabolic Concentrator (ACPC). ACPC in CTAH has been designed with upper and lower reflectors of identical reflectance. Upper reflector is a combination of primary parabolic and straight tertiary reflector.

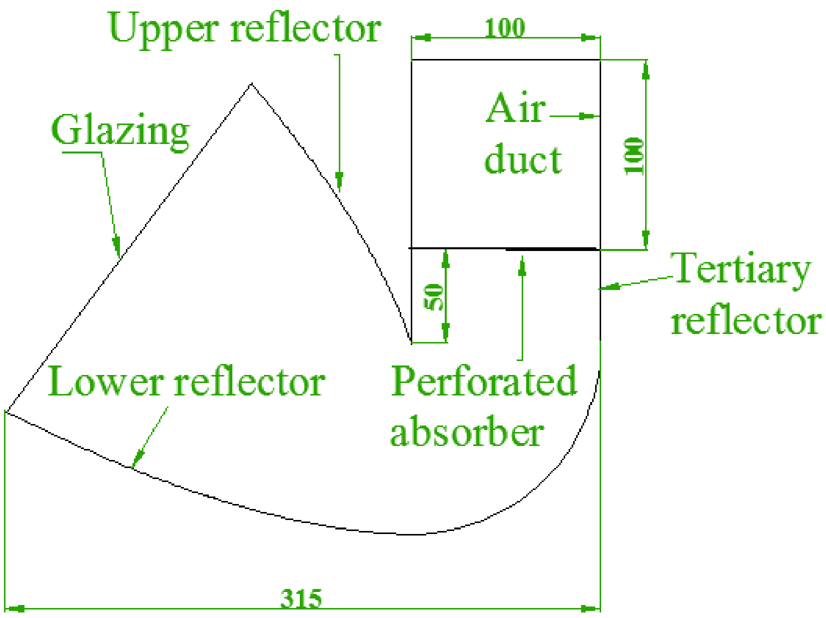

Figure 2.9: Schematic diagram of the CTAH

Lower reflector is a combination of parabolic primary, circular secondary and straight tertiary reflectors. The secondary circular part of the concentrator in CTAH concentrates all incident radiation on the inverted absorber. The concentration ratio between inlet and outlet of the secondary circular reflector is 1.

Concentration of solar radiation becomes necessary when higher temperatures are desired. Heat losses from the collector are proportional to the absorber area. Concentration ratio is the ratio of aperture area to absorber area. So, heat losses are inversely proportional to the concentration.

A perforated absorber is placed at the end of the tertiary reflector. Air flows through the inlet to the secondary and tertiary reflector. A fan is placed at the end of the air duct to extract air through the perforated absorber. The input of the system is insolation at the aperture. The available insolation varies for local climate and orientation of the aperture. The concentrator of the system works as an amplifier which increases the amount of solar radiation on a decreased absorber area. Aperture geometry, reflector properties, tilt angle, position of the absorber, and properties of the absorber are to be considered to reduce energy loss.

The basic optimisation factors considered in designing the CTAH system were to:

- enhance the optical efficiency of the collector using a low concentration ratio concentrator;
- minimise the radiation and convection heat loss from absorber to ambient which can be achieved by using an inverted absorber facing downward;
- maximise convection heat transfer from absorber to inward airflow by using a perforated absorber and tertiary section to maintain a stable thermal layer in the

concentrator cavity and applying low conductive absorber material to reduce conduction loss and enhance convection heat transfer;

- minimise weight of the heating system by using a low weight perforated absorber; and
- minimise cost of the system by using unconventional low cost absorber material to avoid expensive selective coated metal absorber.

2.8 Summary

In this chapter, a review of published research on conventional glazed and unglazed solar air heating collectors, optical concentrators and concentrator integrated solar collectors was undertaken. Four important factors that influence the design of solar air heating collectors (glazed and unglazed) were investigated. They include: absorber modification; glazing modification; airflow and airflow passage modification; system modification (Orientation of building integrated solar air heating system components).

Depending on the absorber characteristics and existence of a glazing cover, major types of solar air heating collectors are: glazed flat plate collector and Unglazed Transpired Collector (UTC). Flat plate collectors are constructed with metal absorber and glazing surface. UTCs are constructed with a perforated absorber without any glazing surface. Commonly used absorber materials in experimental flat plate solar air heating collectors are black painted copper, aluminium and galvanized steel with a thickness of 1 mm. Absorber thicknesses vary between 0.4 mm and 1 mm.

The geometry of a perforated absorber for a CTAH is similar to that of UTC collectors. Experimental analysis of previous research suggested that the porosity of perforated absorbers need to be less than 5% to avoid the effect of the conductivity of the absorber material. The perforation of the absorber basically enhances the heat transfer which reduces the obligation of the absorber to be with high conductive material as flat plate collector. So a non metallic perforated absorber with inherent perforation can reduce manufacturing cost. The use of a fabric absorber (carbon fibre) with inherent perforation leads to a reduction in the overall life-cycle cost. The low weight of the absorber surface may also allow the designer to reduce the overall weight of the system.

A glazed solar collector traps heat using a glazing surface on top of the absorber. Glazing of solar collectors is a critical issue considering the weather (wind speed, rain, and dust) of the location which may have an effect on the performance of the collector, deterioration of the concentration surface and dust deposition causing regular maintenance. The glazing material used in previous experimental prototypes varied in material type, number of glazing and thickness.

The material of the glazing in experiments varied within glass, polycarbonate, polyethylene etc. Glass was the most commonly used glazing material in experiments which varies in quality and thickness. Glass was used from 3 mm to 10 mm and its quality varied from low iron glass to general window glass. The number of glazing used was either one or two. Polyethylene was the thinnest with 150μm. Two glass of 5 mm was the thickest glazing. A glazing cover transmits shorter wavelength solar radiation but blocks the longer wavelength solar radiation from re-radiating from the absorber plate. Glass for this application fulfils the requirements of transmission and toughness and is almost totally opaque to thermal radiation (5 – 50 µm)

The insulation materials used in previous experimental solar air collectors were: styrofoam, polystyrene, wood, foam, glass wool and hardboard. The highest thickness was 5 cm of polystyrene and the thinnest was 2 cm of Styrofoam and hardboard.

There has been no previous relevant research reported on transpired inverted solar absorber integrated with CPC concentrator to heat air. The CTAH was designed in this research with low concentration ratio ACPC to collect most of diffuse insolation. Considering high latitude locations, an integrated ACPC can increase the density of solar radiation that reaches the absorber surface. A highly reflective concentrator can allow solar radiation to be reflected onto the inverted absorber. Concentrating solar energy with transpired absorber fundamentally improves the utility of such systems, by providing higher outlet air temperatures at higher air flow rate. The reduced surface area of the absorber decreases radiation loss and the inverted transpired absorber reduces convection loss from the absorber to glazing.

CHAPTER 3

OPTICAL DESIGN OF CONCENTRATING TRANSPIRED AIR HEATING SYSTEM

The aim of this chapter is to develop an optically optimised Concentrating Transpired Air Heating (CTAH) system which is an integration of Inverted Transpired Absorber (ITA) and Asymmetric Compound Parabolic Collector (ACPC). The objectives of this chapter are:

- To develop an optimised geometric design of an optical concentrator.
- To develop a two-dimensional (2D) ray-trace model of the Concentrating Transpired Air Heating (CTAH) system using Matlab software to calculate the optical efficiency of the concentrator.
- To validate using laser test.
- To optically analyse and optimise the optical CTAH model considering effects of reflector, and tertiary height.

3.1 Introduction

The CTAH system shown in Figure 3.1 is used to concentrate incident solar radiation onto an inverted perforated absorber. Optical concentration was applied to increase the intensity of solar radiation incident on the perforated absorber that is used to heat air. Air was used as the working fluid and output product of the CTAH system. As the CTAH is a stationary system, the optical efficiency of the system varies for different incident angles over the sunshine hours. A cross-section diagram of the CTAH with an inverted downward facing horizontal absorber was developed in this work and shown in Figure 3.1.

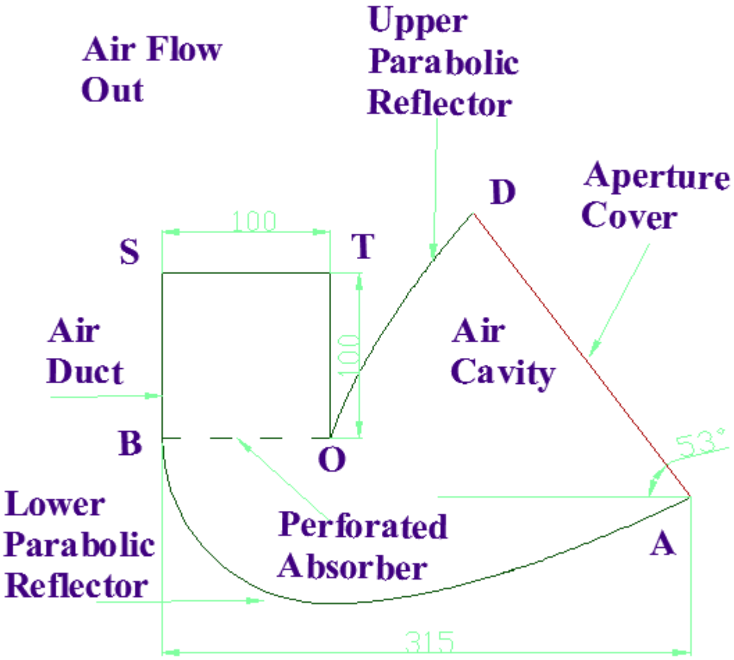

Figure 3.1: Cross-sectional diagram of the CTAH

The incident solar radiation on the aperture of the CTAH undergoes reflection losses and absorption losses at the aperture surface due to the properties of the glazing material as it passes through the aperture. The transmitted ray experiences a further loss at the reflector material of the concentrator before it reaches the inverted absorber surface of the CTAH. The calculated absorbed radiation was considered as the input radiation in the heat transfer model which is discussed in chapter 6.

The ACPC was constructed using a Compound Parabolic Concentrators (CPC) of a 20^{o} half acceptance angle. The geometry of the CTAH was used to develop the boundary equations. The methodology employed and analyses of the results are described in this chapter. The optically optimised geometric dimensions were used to construct prototypes for outdoor experimental analysis which is discussed in chapter 5.

3.2 Geometric Design of CTAH

ACPC works as a primary concentrator in CTAH which is a combination of upper and lower parabolic reflectors with different geometric shapes. In CTAH the lower reflector can be explained as a combination of a primary parabolic reflector and a secondary circular reflector. An absorber unit consisting of a perforated absorber, back plate and plenum is placed at the end of the secondary circular reflectors. Air flows through the right end of the primary reflector of the concentrator system to the secondary reflector and a fan is placed at the end of the air duct to extract air through the perforated absorber.

The outlet of the concentrator system is placed at the top right end of the air duct. The construction of a basic CPC has been detailed in section 2.5. The design of CPC was developed from a 20^{o} half acceptance angle and 100 mm absorber, using the x-y coordinate system of the equation (2.1) for parabola. In the process of design the symmetric CPC was truncated and connected to a circular reflector of 100 mm radius. The connection point of the lower parabolic reflector and the circular reflector has an identical tangent which ensures the uniformity of the lower reflector surface. The axis CPC was rotated to connect the parabolic surface to the circular surface. The design process has been detailed using Figure 3.2, Figure 3.3 and Figure 3.4.

Two parabola of identical geometry were created as ABC and DEF showed in Figure 3.2. B is the focus point of the parabola DEF and similarly, E is the focus point of the parabola ABC. BE is the absorber width of 100 mm. DEBA becomes a symmetric CPC with an acceptance angle of 40^{o} and TS is the centre axis of the CPC.

Any radiation on the aperture PQ, within the acceptance angle will be received by the absorber BE. Aperture is determined when the tangent of DE and BC is parallel to the CPC centre axis ST. Figure 3.3 illustrates the asymmetric CPC as ABXP'. XY is the absorber.

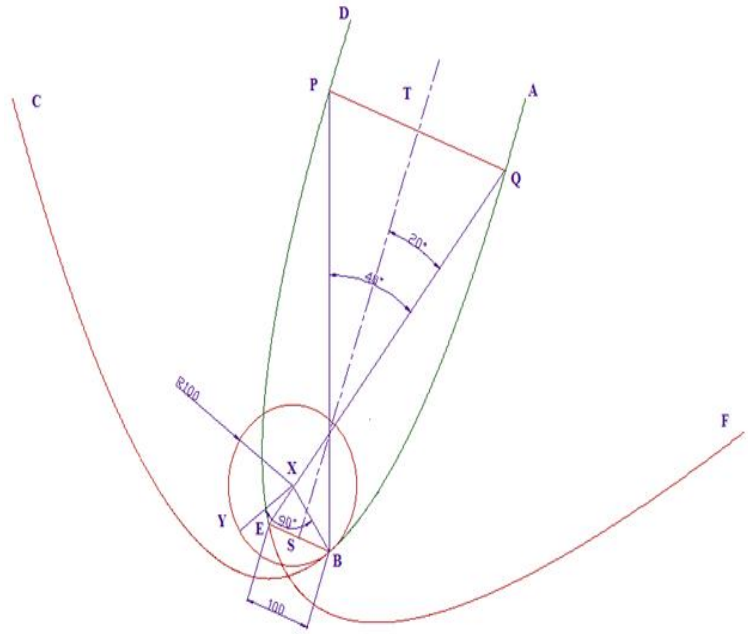

Figure 3.2: Development of CTAH concentrator combining two CPC and a circle

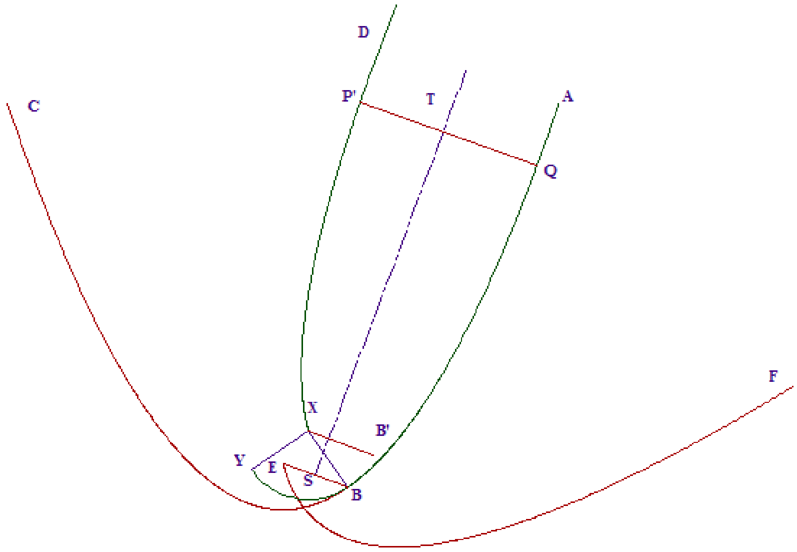

Figure 3.3: A developed shape of untrancated CTAH with upper and lower parabolic primary and circular secondary reflector

A basic shape of CTAH was generated, as in Figure 3.4, where AQBY is the lower reflector, DP´X is the upper reflector, P´Q is aperture and XY is the absorber surface. P´XBQ is the asymmetric CPC which is the primary reflector section of CTAH. BY is a circular reflector section which is the secondary reflector. The circular section will always reflect all incoming irradiation with in acceptance angle onto the inverted absorber. Schematic diagram of the CTAH is a truncated shape of the basic design.

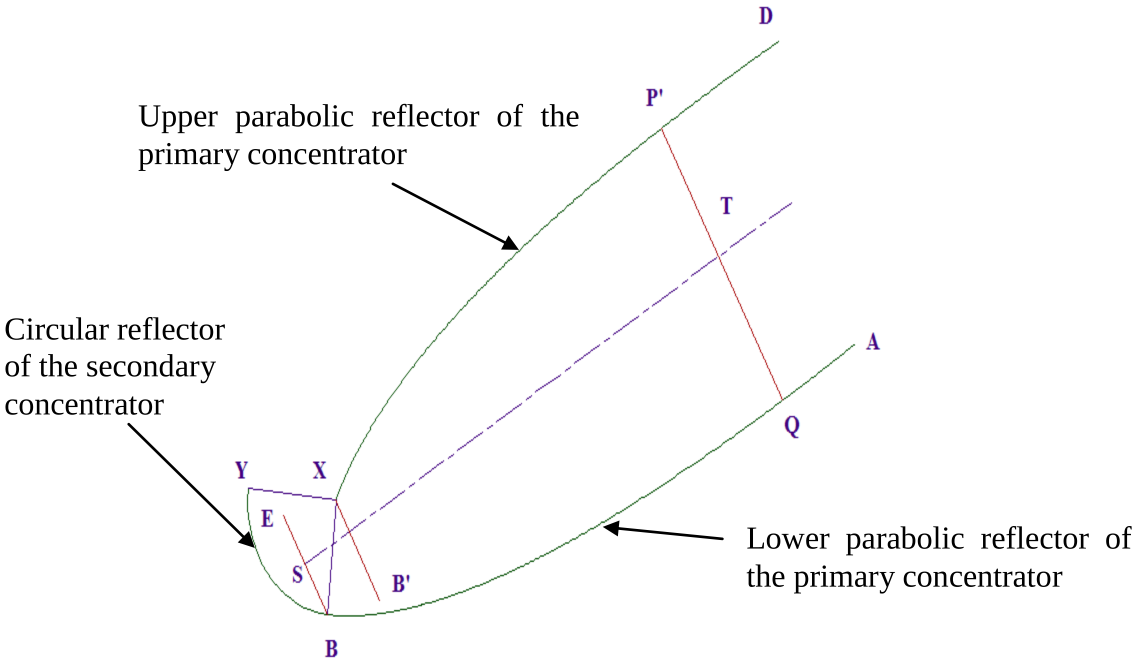

Figure 3.4: Basic shape of the CTAH without truncation at the primary concentrator

3.3 Ray trace simulation model of CTAH

Ray tracing techniques were used commonly to determine the optical performance of concentrating solar energy systems in numerous research works (Eames et al., 1996; Mallick, 2003; Rabl, 1976a, 1976b; Rabl, 1985; Welford & Winston, 1978; Welford & Winston, 1989). The front upper and lower surface of the optical CTAH geometry is highly asymmetric. However, the shape is symmetric in the longitudinal direction. A 2D ray tracing model was necessary to conduct optical analysis. A cross section of the geometrical CTAH was used as the boundary surface of the optical model where incident radiation intersects.

3.3.1 Ray tracing modelling assumptions

The following modelling assumptions were made when developing the 2D ray trace model:

- all reflectors were considered to be specular, i.e. the angle of incidence equals the angle of reflection. The incident ray, the reflected ray and the normal at the point of intersection are considered to be in the same plane;
- the incident direct solar flux at the aperture was assumed to be a number of parallel rays each carrying equal amounts of energy;
- the reflectivity of all reflectors was 95%;
- the absorber was a perfect blackbody for the purpose of absorption;
- positive real values of x and y coordinates used to model the concentrator surfaces and rays;
- the CTAH aperture was tilted at an angle equal to the latitude of the location;
- the transmittance of the glazing was assumed to be 88%.

3.3.2 Boundary Equation Generation

The boundary constraints of the optical model of CTAH system are a combination of circular, parabolic and straight surfaces as illustrated in Figure 3.5. The incident radiation intersects with these surfaces and the intersection points are necessary to identify for each incident radiation. The radiation was represented by equation of ray and parabolic equations were generated for parabolic reflector surface.

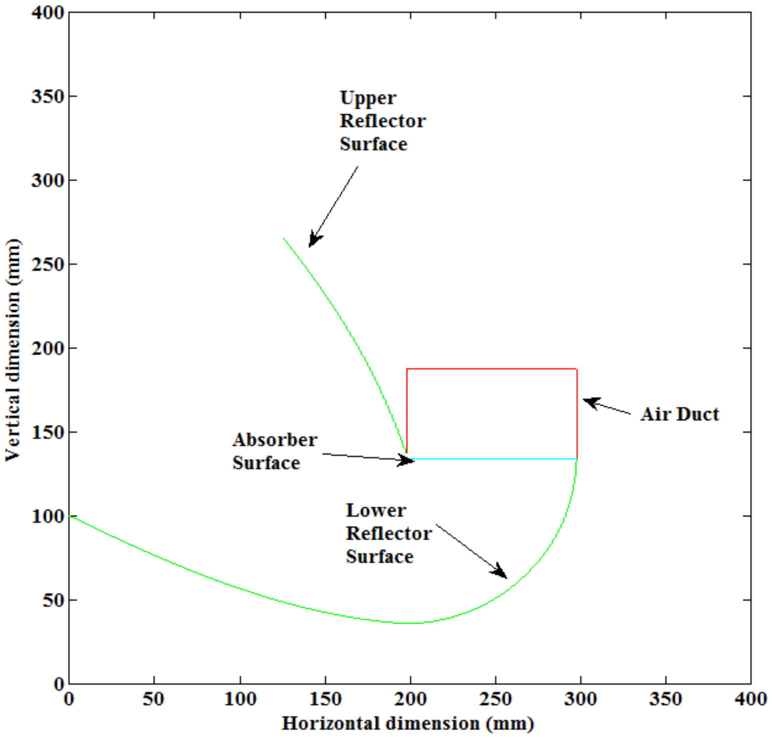

Figure 3.5: Boundary surfaces of the CTAH system

The equations of the surfaces were generated by using basic data plot fitting tools in Matlab. The geometric data which was described in section 3.2 were transferred from AutoCad to Matlab. Equations 3.1 and 3.2 were used for the lower and upper parabolic reflectors respectively. The values of corresponding coefficients are as follows:

1) **Solution for the lower reflector:**

$p_1 = 2.3565e^{-006}$, $p_2 = 0.00041055$, $p_3 = -0.4986$, $p_4 = 99.983$

$$y_{lower} = p_1 \times x^3 + p_2 \times x^2 + p_3 \times x + p_4 \qquad 3.1$$

2) **Solution for the upper reflector:**

$p_1 = 5.4096e^{-022}$, $p_2 = -6.699e^{-007}$, $p_3 = 0.00032549$, $p_4 = -0.061316$, $p_5 = 3.9925$,

$p_6 = 253.14$

$$y_{upper} = p_1 \times x^5 + p_2 \times x^4 + p_3 \times x^3 + p_4 \times x^2 + p_5 \times x + p_5 \qquad 3.2$$

Initial boundary conditions (incident angle, increment and the initial ray coordinate) were defined as model inputs. Solutions were carried out for incident radiation on different concentrator surfaces (lower parabolic, circular and upper reflector) considering different modules. Figure 3.6 illustrates the general flow chart of the simulation process.

Rays from the aperture experience a series of reflections for different incident angles before they reach the inverted absorber. The rays lose energy at each reflection on the concentrator surface. The determination of the number of reflections for each ray was necessary to predict the optical performance of the CTAH. The methodology used in the simulation process can be adapted in design optimisation of solar concentrators for different locations and weather conditions.

3.3.3 Solution of individual ray intersect concentrator surface

3.3.3.1 Calculation for the lower parabolic reflector

Solar radiation passes through the aperture and is incident on the reflector surfaces of the CTAH. The co-ordinates of source points and the incident angles are known inputs of the simulation. For a particular angle of incidence, rays intersect the reflector surface. In the simulation model the value of the coordinates of the intersection points are always greater than zero, because all the calculations are on the positive axis.

To calculate the average number of reflections, all reflection paths of the incident rays were traced. Radiation passes through the aperture surface inclined at 53.3^o. The incident radiation equation is a function of the incident angle and point on the glazing cover. As a result, the law of reflection on an intersection point on the parabola is applicable only considering each point exists in a different plane. The change in plane has to be considered in the calculation.

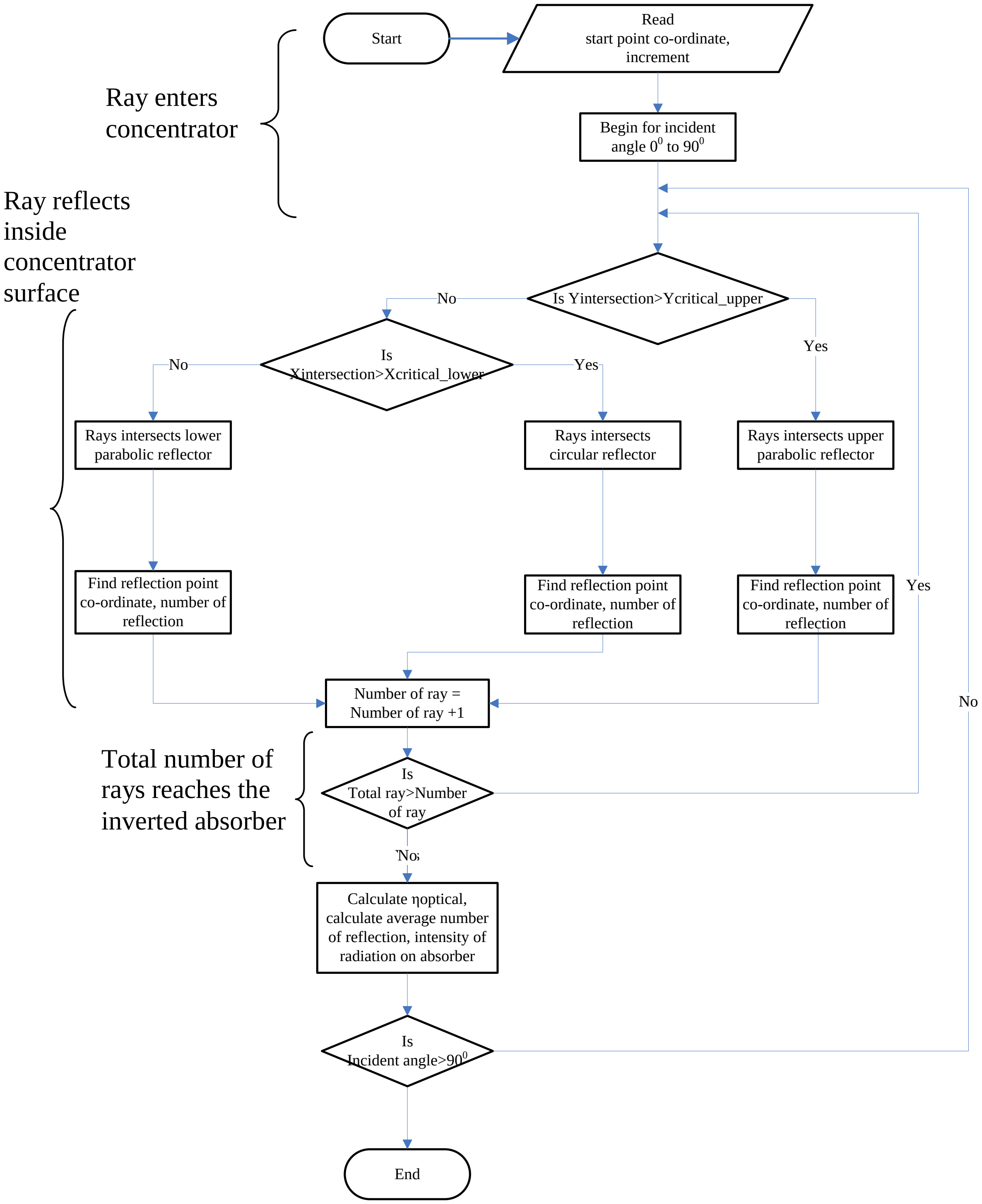

Figure 3.6: Ray trace program flow chart

Figure 3.7 illustrates the calculation process of a single ray incident on the lower parabolic reflector from the aperture. As it can be seen, the ray intersects the lower parabola and reflects towards the circular reflector. It then reaches the absorber after another reflection on the circular reflector. The calculation process was repeated for 120,000 numbers of rays during the optical calculation of the concentrator. However for representation 120 rays are shown in upper section of the Figure 3.7.

Figure 3.8 presents the corresponding calculation of incident angles, reflection angles and intersection point. For a radiation source point A, the ray AB intersects the lower parabola at intersection point B. The values of angles at the intersection point B on the lower parabolic surface become: Slope of angle of the polynomial corresponding to the positive x-axis = CBC'.

Assuming specular reflection, the rays follow the law of reflection on a highly reflective surface of the reflector. So, the incident angle ABB' = Reflection angle B'BE. The incident ray AB reflects on the lower reflector B at an angle CBE from the positive x axis and intersects the circular surface at point E. The centre of the circular reflector is at O. The ray BE reflects on the circular reflector surface at an angle BED and intersects the absorber as DE. The angle can be calculated from the positive x axis of point B as shown in the Figure 3.8.

The necessary angles were calculated in Matlab at each point of intersection for all incident rays. However, the calculations are complicated for all rays incident on the lower parabola using Matlab for particular angles of incidence. Because the angle CBE changes direction from positive to negative as the y co-ordinate of the reflection rays at the incident point of lower parabola becomes negative. Similar phenomenon occurs on the circular reflector surface in case of multiple reflections inside the circular reflector surface. These changes are considered in this simulation model.

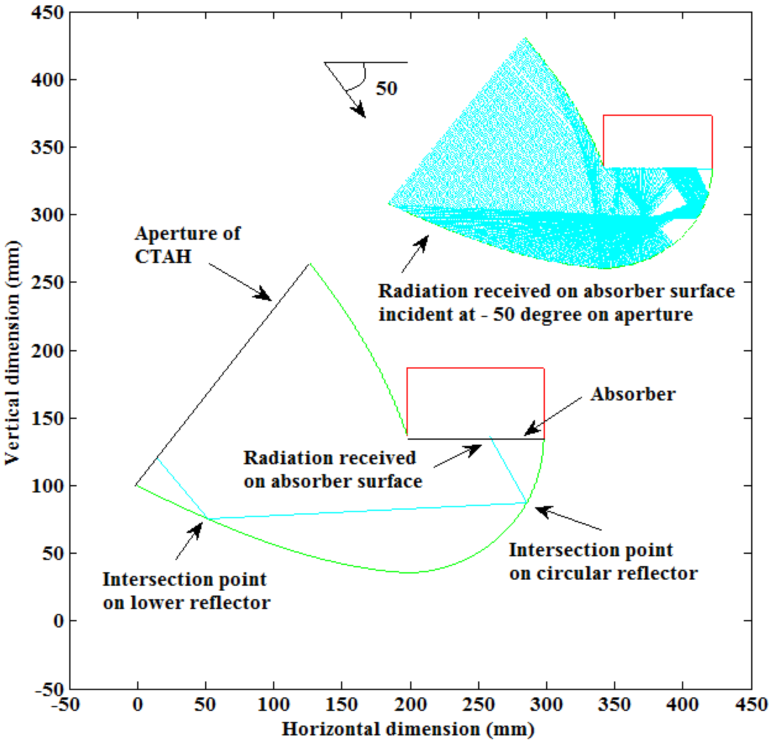

Figure 3.7: Ray incident at -50^o incident angle on lower parabolic reflector

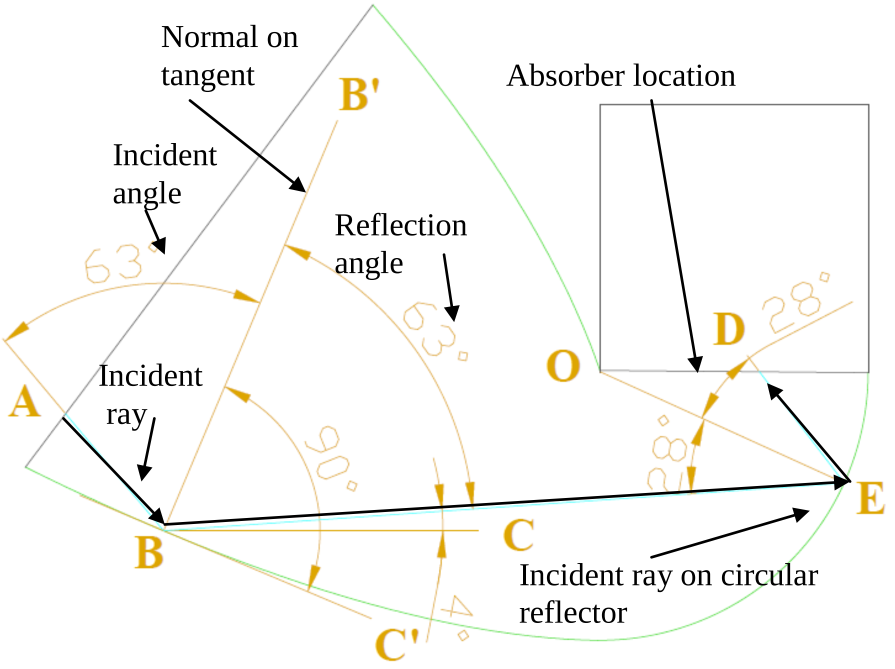

Figure 3.8: Important angles to find the absorbed radiation for rays incident at -50^o incident angle on the lower parabolic reflector

3.3.3.2 Calculation for the upper parabolic reflector

To calculate the average number of reflections, all reflection paths of the incident rays were traced after reflection from the upper reflector. The rays may intersect on the lower parabola or the circular reflector or may miss the lower reflector.

Figure 3.9 illustrates the calculation process of a single ray incident on the upper parabolic reflector from the aperture. The ray intersects the upper parabola and reflects towards the circular reflector. Then it reaches the absorber after experiencing another reflection at the circular reflector. The upper reflector is more active for rays entering aperture at low incident angles with the vertical during summer days at solar noon.

Figure 3.10 shows details of the corresponding calculation of incident angles, reflection angles and intersection points. The calculation process for the upper reflector is more complicated. The calculation process was repeated for 120,000 rays during the optical calculation of the concentrator. For a radiation source point A, the ray AB intersects the upper parabola at intersection point B. In a similar way as detailed above, it can be shown that Incident angle ABC = Reflection angle CBD. The incident ray AB reflects on the upper reflector B at an angle negative B’BD from the positive x axis and intersects the lower reflector surface at point D and intersects the absorber at DE. The angle can be calculated from the positive x axis of point B as shown in Figure 3.10 for the upper reflector and point D of the lower reflector.

The formulas were used in Matlab to calculate the necessary angles on each point of intersection for all incident rays. However, the calculation of all rays incident on the lower reflector surface from the upper parabola is complicated using Matlab. Because for particular angles of incidence, the reflection angle B’BD can be less than 90^0 or greater than 90^0. In both cases the result is completely different. Again when the reflection rays from the upper parabola intersect the lower reflector, it may intersect the parabolic part or the circular part. The exact intersection points have to be calculated independently in the simulation.

3.3.3.3 Calculation for the circular reflector

Figure 3.11 illustrates the calculation process for a ray incident directly on the circular reflector from the aperture. The rays reach the circular reflector directly only at higher incident angle from the vertical. The surface also concentrates rays after reflection from the upper and lower parabolic reflector. To calculate the average number of reflections, all reflection paths of incident rays were traced after reflection from the circular reflector.

The visualisation of an incident ray intersecting the circular reflector from the aperture has been shown in Figures 3.11 and 3.12. The incident radiation reaches the inverted absorber after one reflection on the circular reflector surface. For a radiation source at point A shown in Figure 3.12, the ray AB intersects the circular reflector at intersection point B. In a similar way as detailed above, it can be shown that Incident angle ABO = Reflection angle CBO.

The centre of the circular reflector section is O. The circular section basically concentrates all the incident radiation on the inverted absorber at a concentration ratio 1 until a ray intersects the centre before it reaches the circular reflector section. In that case, ray reflects back toward aperture.

The formulas are used in Matlab to calculate the necessary angles on each point of intersection for all incident rays on the circular reflector. However, if the reflection angle B'BC becomes less than 90^o from the positive x axis, the ray experiences multiple reflections inside the circle. A case of multiple reflections has been shown in Figure 3.13 in the laser test of the model.

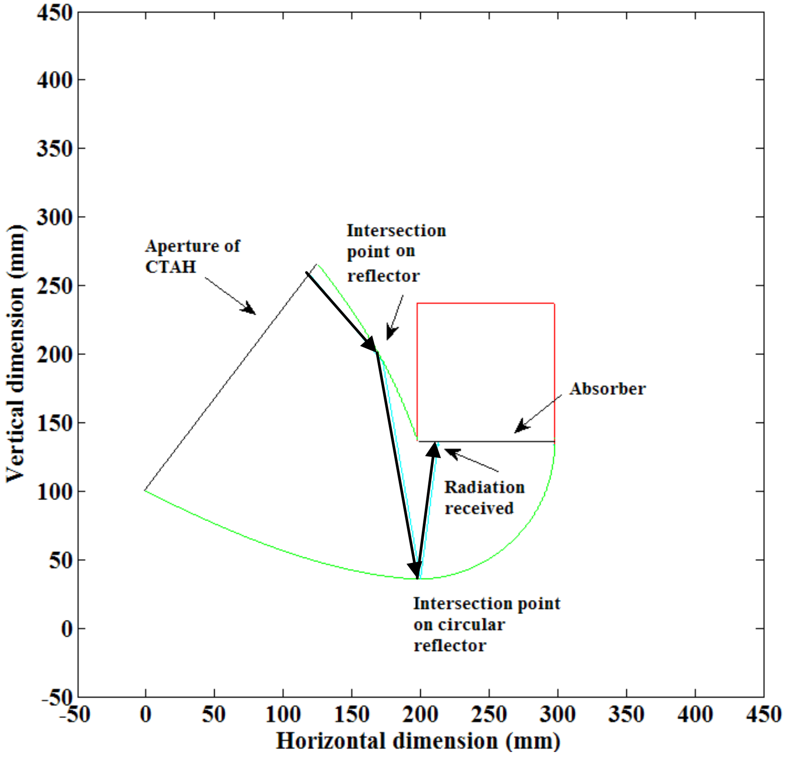

Figure 3.9: Ray incident at -50^{o} incident angle on the upper parabolic reflector

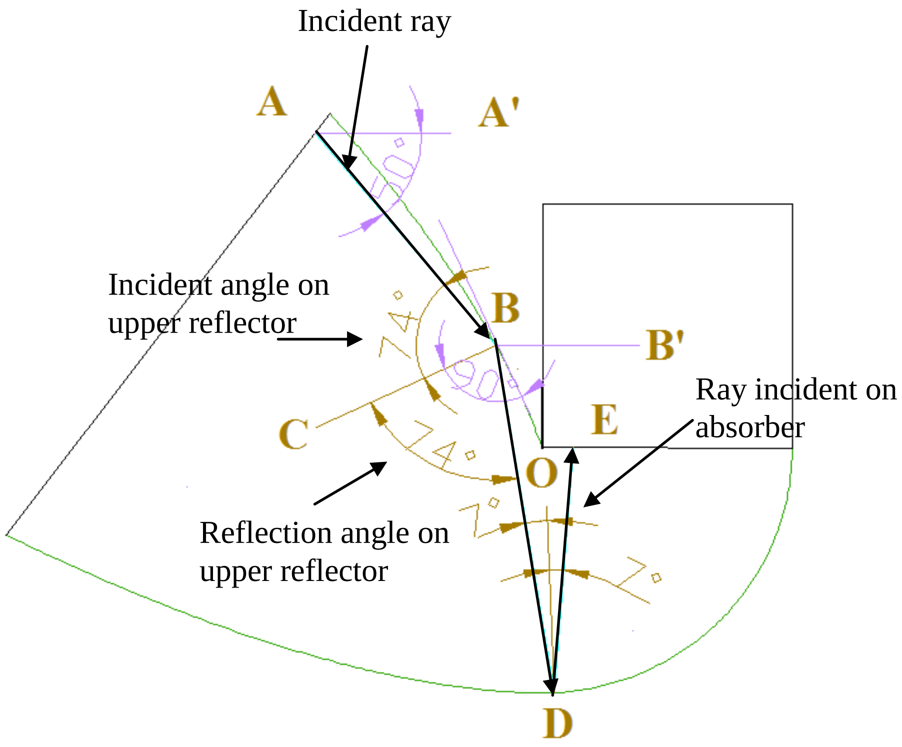

Figure 3.10: Incident and reflection angles for incident ray on the upper reflector surface

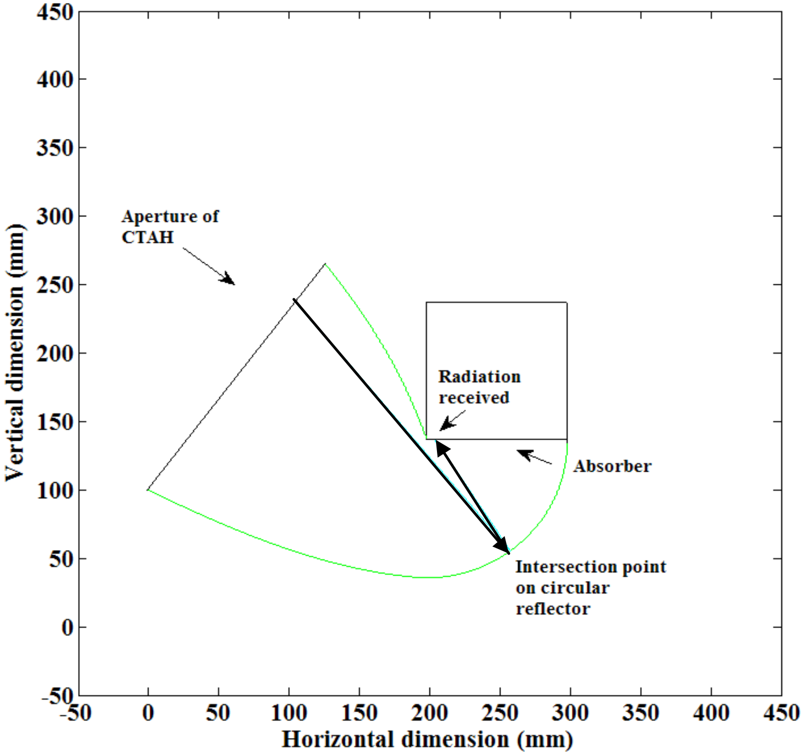

Figure 3.11: Ray incident at -50° incident angle on circular reflector

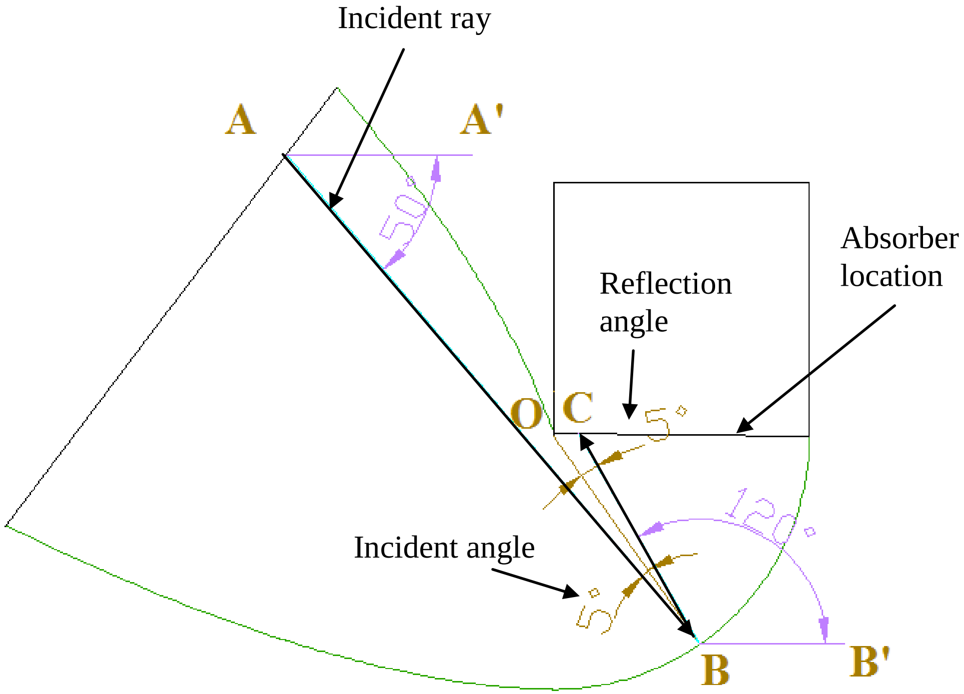

Figure 3.12: Incident and reflection angles for incident rays directly on the circular reflector

3.3.4 Ray tracing model validation

Laser visualisation tests were setup during the optical design process to provide a validation of both the Matlab model and its limits of operation as in Figure 3.13.

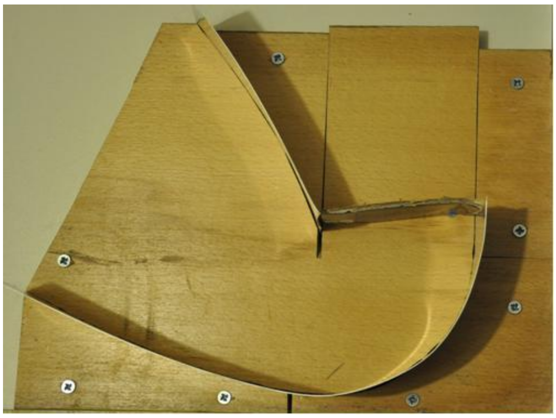

Figure 3.13: (a) Ray-trace analysis setup

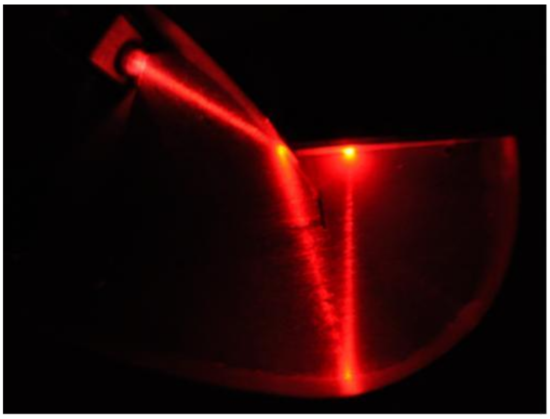

Figure 3.13: (b) Test-1 Laser ray on upper reflector of CTAH

Figure 3.13: (c) Test-2 Laser ray on circular reflector of CTAH

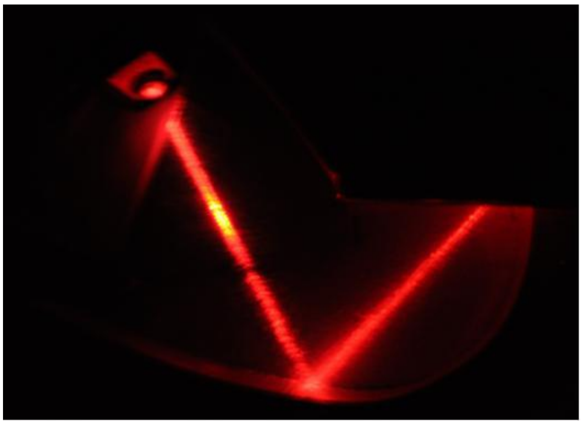

Figure 3.13: (d) Test-3, Laser on lower parabola of CTAH

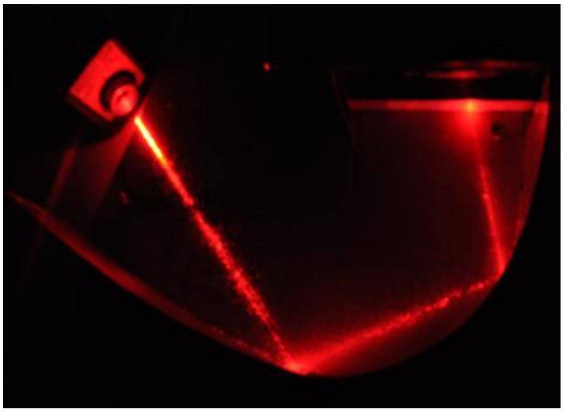

Figure 3.13: (e) Test-4, Laser (Two reflections) on lower parabolic reflector of CTAH

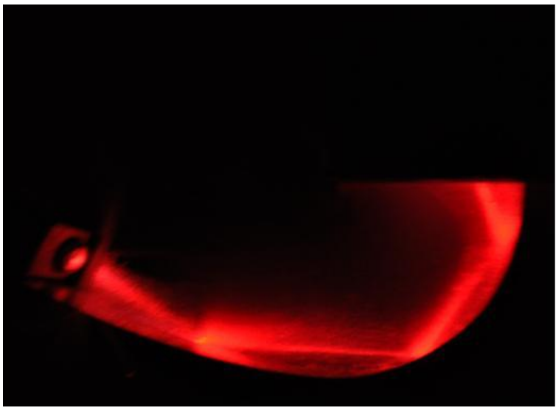

Figure 3.13: (f) Test-5, Laser (Three reflections) on lower parabola and circular reflector of CTAH

A physical model for the laser test is shown in the Figure 3.13 (a). This is basically a cross section of the prototype made with 95% reflective alanod reflector used in the prototype. The frame of the setup was made of wood. A laser source was used as the light source. Five tests were carried out to test the reflector surfaces.

Test 1 is shown in Figure 3.13 (b), a laser ray intersecting the upper parabolic reflector and the reflected ray intersects the circular reflector. The ray reaches the inverted absorber surface after reflection from the circular reflector. Test 2 is shown in Figure 3.13 (c). It explains how a laser ray intersects the circular surface directly from the aperture of the system. The ray reflects from the circular reflector and intersects the absorber surface. The circumstance is explained in Figures 3.11 to 3.12.

As the incident ray did not intersect the centre of the circular reflector O, it reaches the inverted absorber surface after concentration. Tests 3, 4 and 5 are illustrated in Figures 3.13 (d)-(f) respectively. Rays intersect the parabolic reflector at different points with different angle of incidence reaching the absorber after one or more than one reflections. Results of tests 1, 2, 3, 4 and 5 are presented in Figures 3.13 (b)-(f) demonstrate good affiliation to the ray-tracing results and these provided the confidence to build the prototype of the system.

3.4 Simulation results and analysis

The ray tracing model of the CTAH provides vital information about the system performance which includes:

a) average number of incident rays reflected before it reaches the absorber for each particular incidence angle;

b) instantaneous optical efficiency of the incident rays that reach the absorber;

c) visualisation of the incident rays, intersection points on the reflector boundary line and on the absorber surface; and

d) intensity of received ray distribution on the absorber surface for every individual incident angle.

The optical efficiency was calculated using the ray tracing model. The calculated optical efficiency was used as an input parameter in the heat transfer simulation model of the CTAH which was used to predict thermal performance of CTAH. The detailed thermal model with experimental validation will be discussed in chapter 6.

3.4.1 Optical performance of CTAH concentrator

Both diffuse and beam components of the incoming solar radiation are considered to calculate total available solar radiation on the aperture of the CTAH system. Rays incident on the CTAH from different directions are reflected by the reflector surface.

The imperfections in a real concentrator surface (Welford & Winston, 1982; Mallick, 2003) give optical errors that combine with a real radiation source to yield an effective radiation source (Welford & Winston, 1982). The effective source $S_{eff}(\theta)$ is the angular distribution that describes how much radiation is incident from the direction θ on the aperture of a perfect reflector. The radiation intercepted by the receiver is defined by the angular acceptance functions $f(\theta)$ as the function of a uniform beam of parallel rays incident on the aperture at an angle θ that would reach the receiver if the optics were perfect (Rabl, 1985; Welford & Winston, 1978).

Therefore, the intensity of radiation on the aperture from the direction θ reaching the absorber becomes $S_{eff}(\theta)f(\theta)$. The optical efficiency of the CTAH is defined as the fraction of solar radiation incident on the aperture which reaches and is absorbed by the absorber (Duffie & Beckman, 2006).

$$\eta_{optical} = \frac{S}{I_{global}} \qquad 3.3$$

S = total energy absorbed (diffuse and direct)

I_{global} = total energy incident on the aperture (diffuse and direct)

The angular acceptance was determined as shown in Figure 3.14. All the incident rays on the concentrator surface from the aperture have more than one reflection before intersecting the inverted absorber. The reflectors are not identical asymmetric structures. It can be seen from the Figure 3.14 that the angular acceptance functions are not symmetric for all acceptance angles. The angular acceptance and the optical efficiency for the CTAH have been shown without the tertiary section and with 95% reflector reflectance.

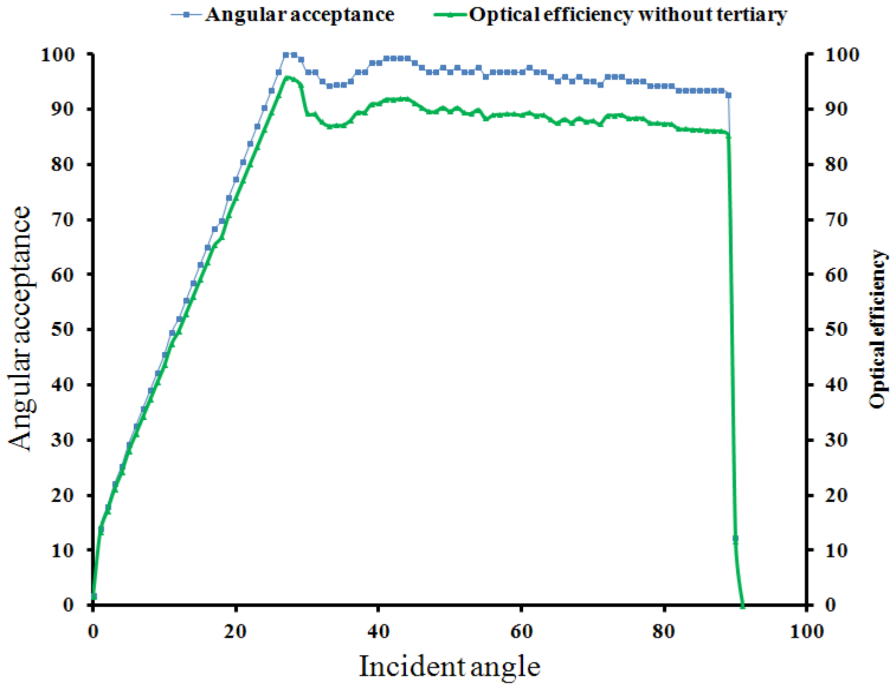

Figure 3.14: The angular acceptance and optical efficiency for the CTAH without tertiary section

3.4.2 Effect of number of rays on optical performance

Individual rays undergo different numbers of reflections inside the concentrator surface before it reaches the absorber surface. Each number of reflections on the concentrator surface indicates a portion of optical loss from the available solar radiation. However, the optical loss inside the cavity increases the thermal energy of air in the cavity. The geometrical construction of the CTAH is a complex shape of different surfaces.

A deterministic approach to ray tracing was adopted that considered specular incident rays where every intersection point and reflection angles inside the concentrator cavity was calculated. The error reduces as the number of rays used increased.

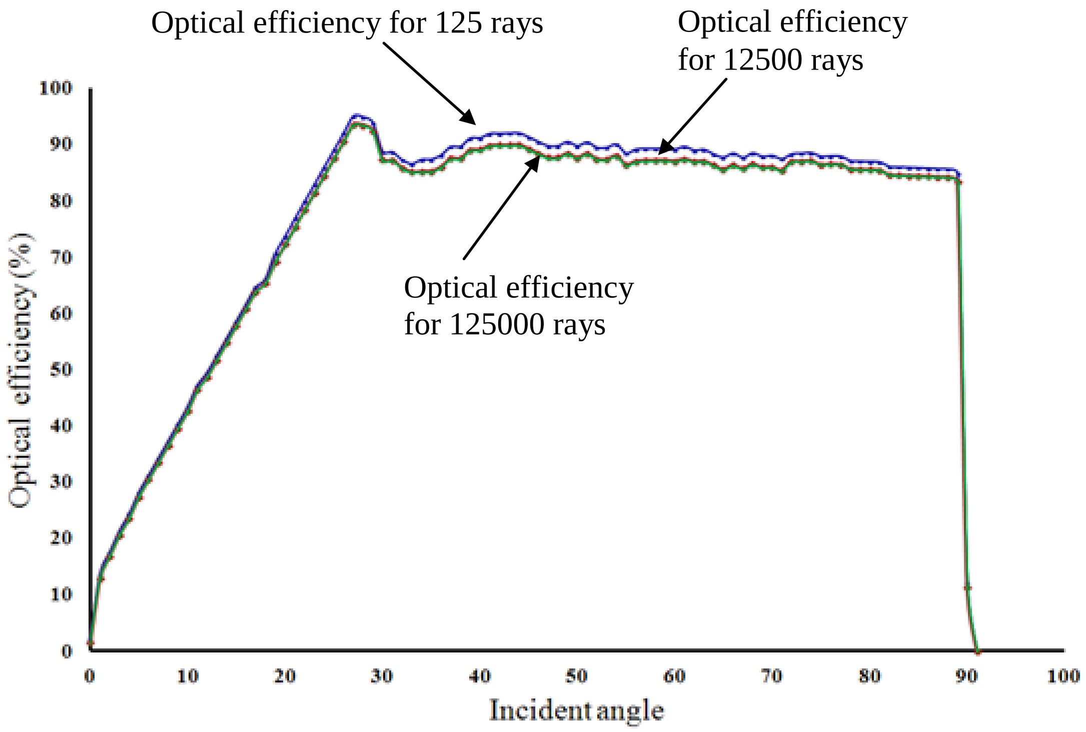

Figure 3.15: Optical efficiency of the CTAH without the tertiary section for different number of rays (125 rays, 12,500 rays and 125,000 rays)

However, an enlarged number of rays increased the simulation time significantly. An analysis was carried out to find an optimum number of rays to reduce calculation errors. An increase in the number of rays from 125 to 12,500 reduced the percentage error to approximately 1.1%. The error reduced to 0.19% when the number of rays increased from 12,500 to 125,000 as can be seen from the coincidence of the curves for 12,500 rays and 125,000 rays in figure 3.15. The results presented in this chapter are calculated for 125,000 rays to minimise the percentage error.

3.4.3 Effect of tertiary section and reflector reflectivity on optical performance

Figure 3.16 illustrates the intensity (rays/mm) of concentrated rays on the inverted absorber without the tertiary height.

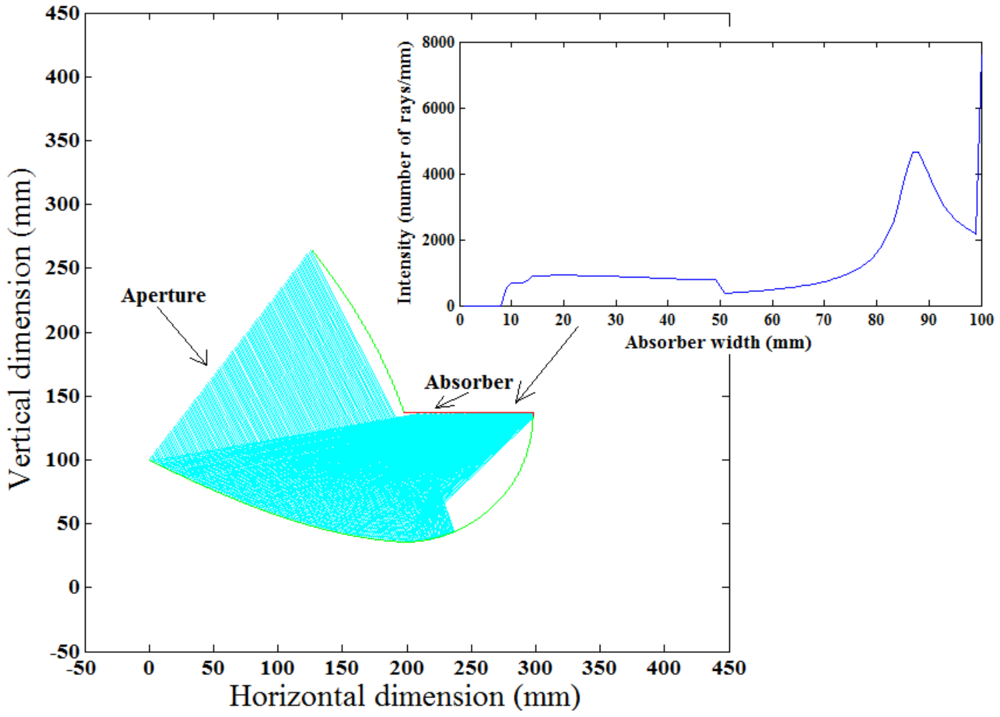

Figure 3.16: Concentration of incident rays at 27° incident angle and 0 mm tertiary height

As can be seen in Figure 3.16, peaks occur near the outer end of the absorber. It can also be seen that the concentrated insolation incidence is non-uniform over the absorber surface. The tertiary section and the reflectivity of the reflector are two factors which affect the optical efficiency of the CTAH over different incident angles. Another factor is the distribution of concentrated radiation over the absorber surface.

The incident rays from the aperture were equally spaced parallel to each other. Figure 3.17 presents the intensity (rays/mm) of concentrated rays on the CTAH absorber with 50mm tertiary height. As can be seen in Figure 3.17, peaks shift towards the middle of the absorber's width. Again, it can be seen that the concentrated insolation incidence is non-uniform over the absorber width.

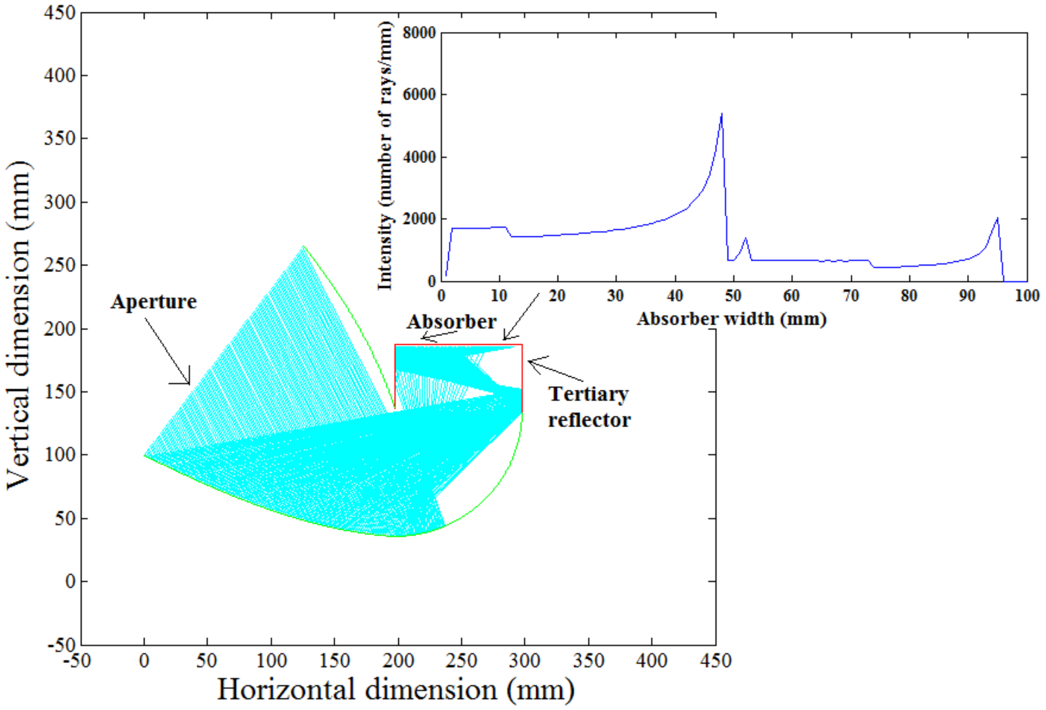

Figure 3.17: Concentration of incident rays at 27^{o} incident angle and 50 mm tertiary height

The increase in tertiary height allows the radiation to increase uniformly over the absorber width which is desirable for improved system performance. The tertiary reflector is supposed to be highly reflective to avoid increasing reflection loss due to higher number of reflections within the tertiary section. However, optical losses within the cavity and tertiary section increase the thermal energy of air in the cavity. Figure 3.18 details the intensity (rays/mm) of concentrated rays with 100mm tertiary height. As can be seen in Figure 3.18, peaks are more distributed over the absorber width. However, the concentrated insolation is non-uniform.

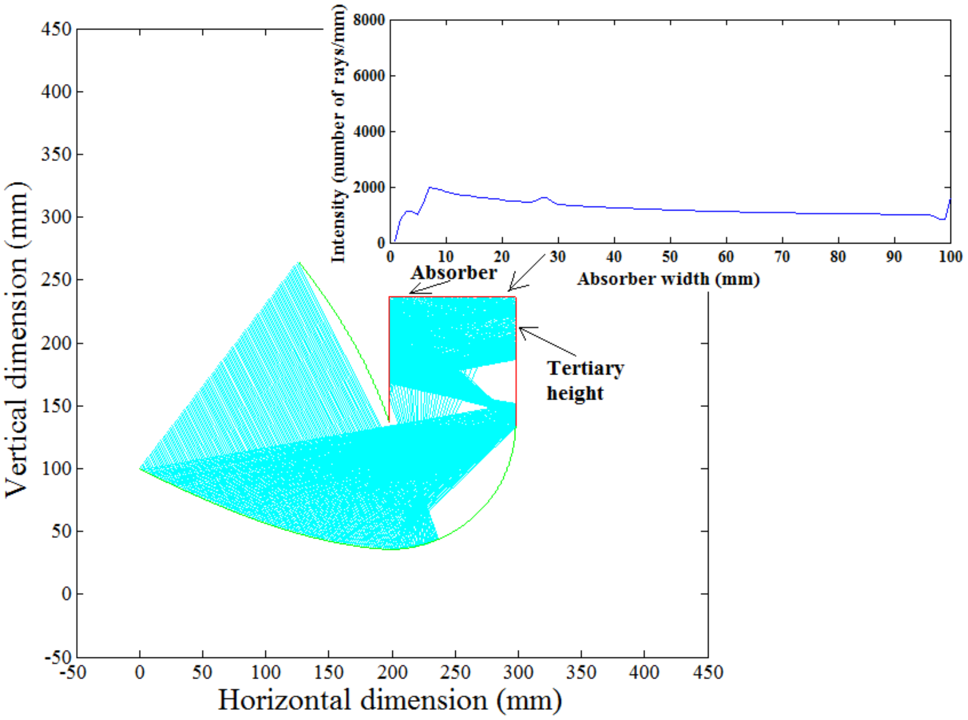

Figure 3.18: Concentration of incident rays at 27^{o} incident angle and 100 mm tertiary height for 125,000 rays

Figure 3.19 shows the effect of tertiary height from 0 mm to 100 mm and reflector reflectivity from 90% to 95% on optical efficiency of the concentrator. The concentrator efficiency is the maximum at zero tertiary height. The highest level of the optical efficiency was found for the reflector with 95% reflectivity. The lowest level of the optical efficiency was found for the reflector reflectivity of 90% and the tertiary height of 100 mm. It can be seen the optical efficiency increases with decreasing tertiary height and increasing reflector reflectivity. However, it is a complex factor to define the higher significant factor between reflector reflectivity and tertiary height for optical efficiency of the CTAH. These analyses were carried out assuming the transmittance of the aperture is 100% to avoid the influence of transmittance on the results.

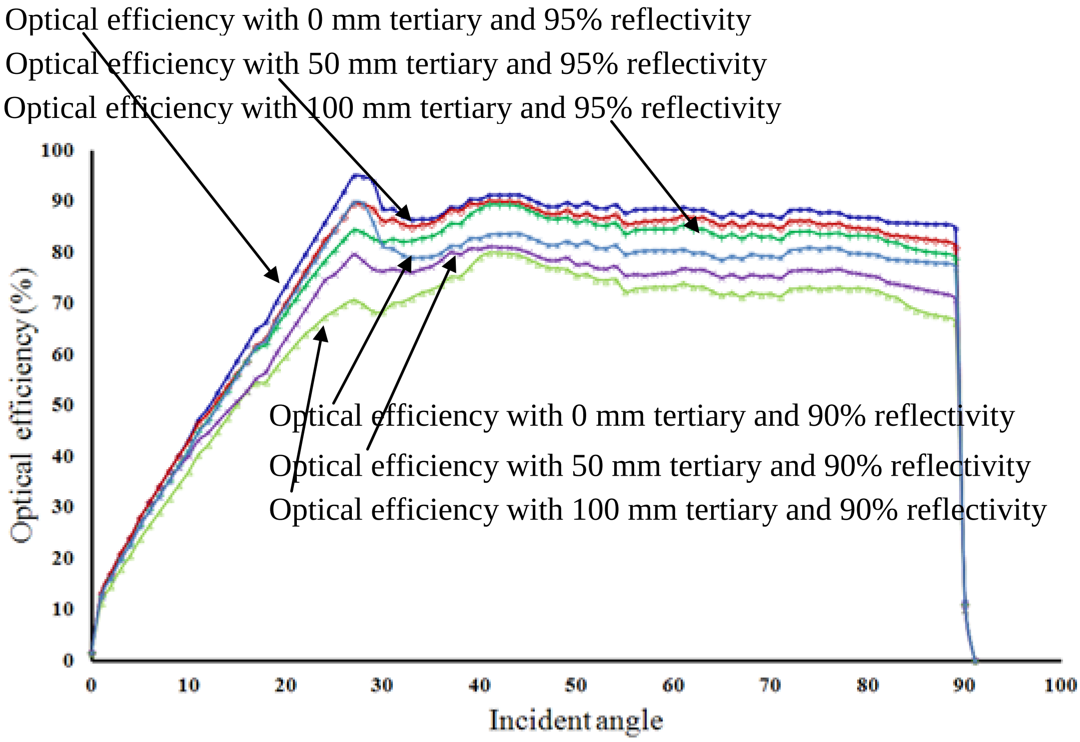

Figure 3.19: Effect of tertiary height from 0 mm to 100 mm and reflector reflectivity from 90% to 95% on optical efficiency

A tertiary height is necessary to develop thermally stratified layer below absorber surface. Though the lowest tertiary height provides the highest optical efficiency, a straight tertiary height is necessary.

Again improved reflector reflectivity (95%) enhanced optical efficiency. Considering 90% reflectivity of the concentrator surface, the 50 mm tertiary height reduced average optical efficiency by 5.4% and 100 mm tertiary reduced it by 10.2%. In case of a more reflective (95%) surface, the optical efficiency reduced by 2.7% for 50mm tertiary height and only 5.2% for 100 mm tertiary reflector cavity. This indicates that the effect of tertiary height is comparatively much lower for higher reflective surfaces.

To keep the optical efficiency loss due to combine effect of reflectivity and tertiary height at its minimum permissible range of 2.7% to 5.2%, the tertiary height needs to be maximum 50 mm and reflector reflectivity within 90-95%.

3.4.4 Effect of individual concentrator surfaces and average reflection on optical efficiency

Figure 3.20 shows the proportion of incident radiation on different reflector surfaces as it enters the CTAH aperture at different incident angles.

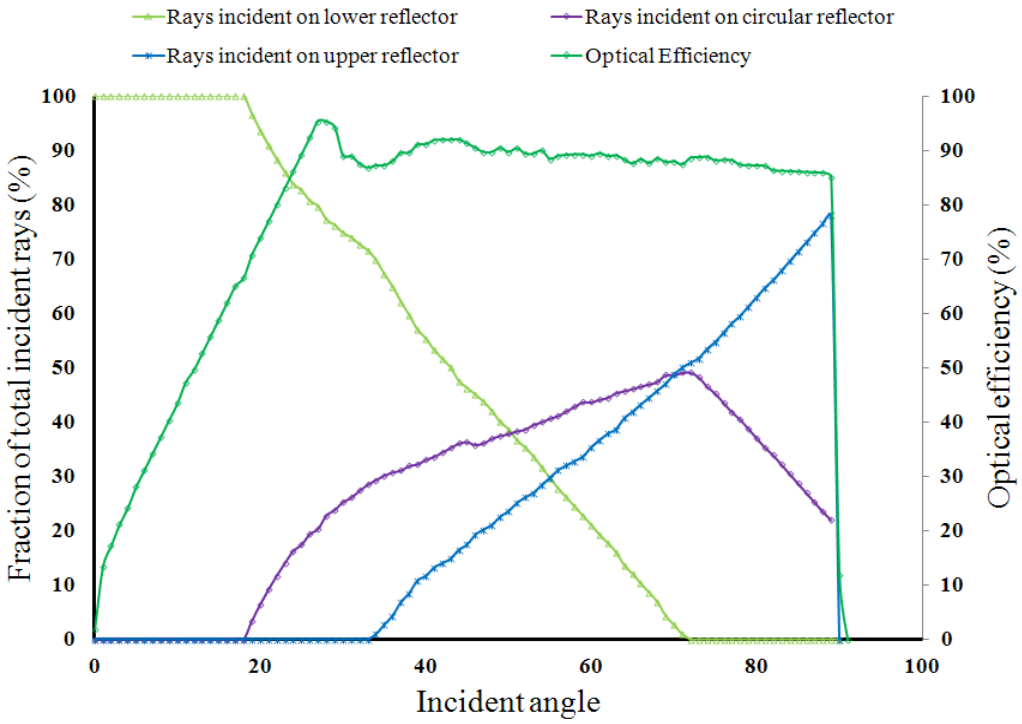

Figure 3.20: Fraction of total incident rays on different reflector surface within angular acceptance angle

The concentrator of the CTAH is an ACPC which is a combination of different surface shapes. The proportion of incident radiation on each reflector surface at a particular incident angle is different. Again, the incident rays on surfaces of the concentrator undergo different number of reflections before they reach the absorber surface. This phenomenon creates complexity on the prediction of surface contribution to the performance of the CTAH. Figure 3.21 illustrates the number of reflections for different incident angles.

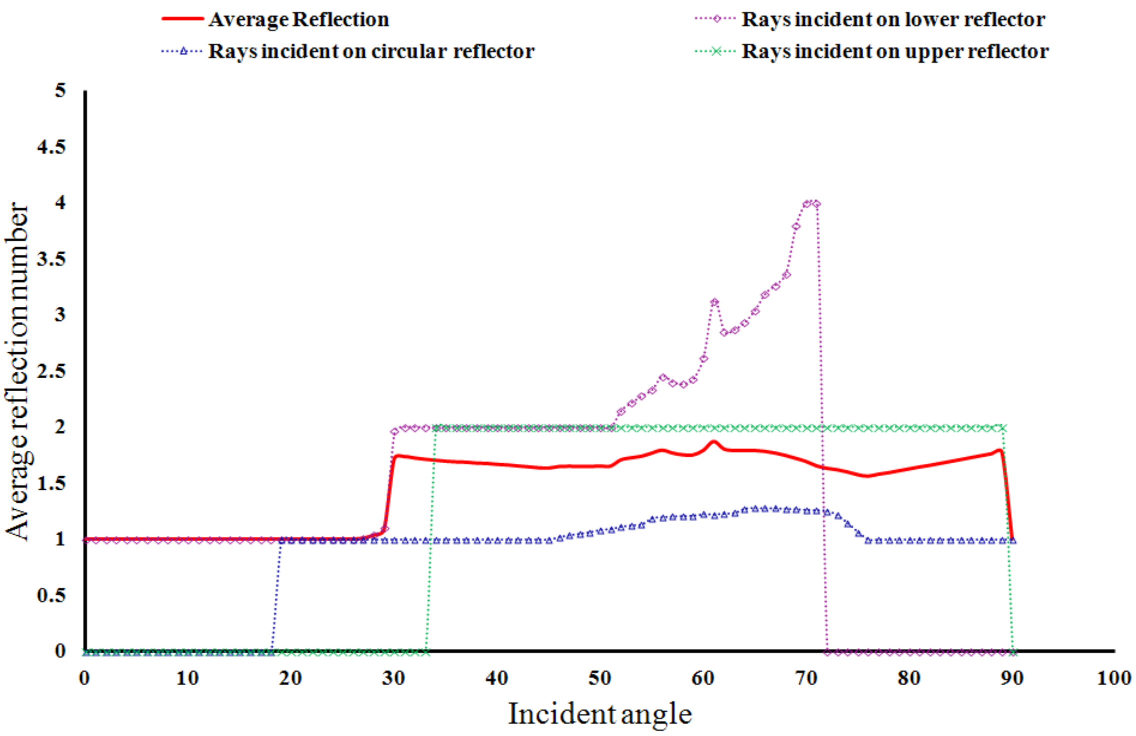

Figure 3.21: Average reflection for different incident angle

It can be seen that most of the incident radiation at lower incident angle first intersects the lower reflector surface. As the incident angle increases, the contribution of the circular reflector increases. The upper reflector becomes active at around 37 degree incident angle and the contribution increases afterward for higher degrees. The trend indicates that during the summer season at lower incident angles, the lower parabolic reflector contributes the most. During the winter season, as the incident angle increases, the contribution of the other two surfaces increases with the lower reflector.

The average reflection is lower at lower incident angles and as the incident angle increases the number of reflection increases. Between 27^o and 70^o incident rays from the aperture intersects the entire three reflector surfaces as shown in the Figure 3.21. The higher reflection occurs when rays incident on the lower reflector at higher incident angle cause declination in optical performance of the concentrator at higher incident angles.

3.4.5 Absorbed radiation distribution at the absorber surface

Figure 3.22 illustrates the energy distribution at the absorber of the CTAH for different tertiary heights at incident angle 27°, to the vertical.

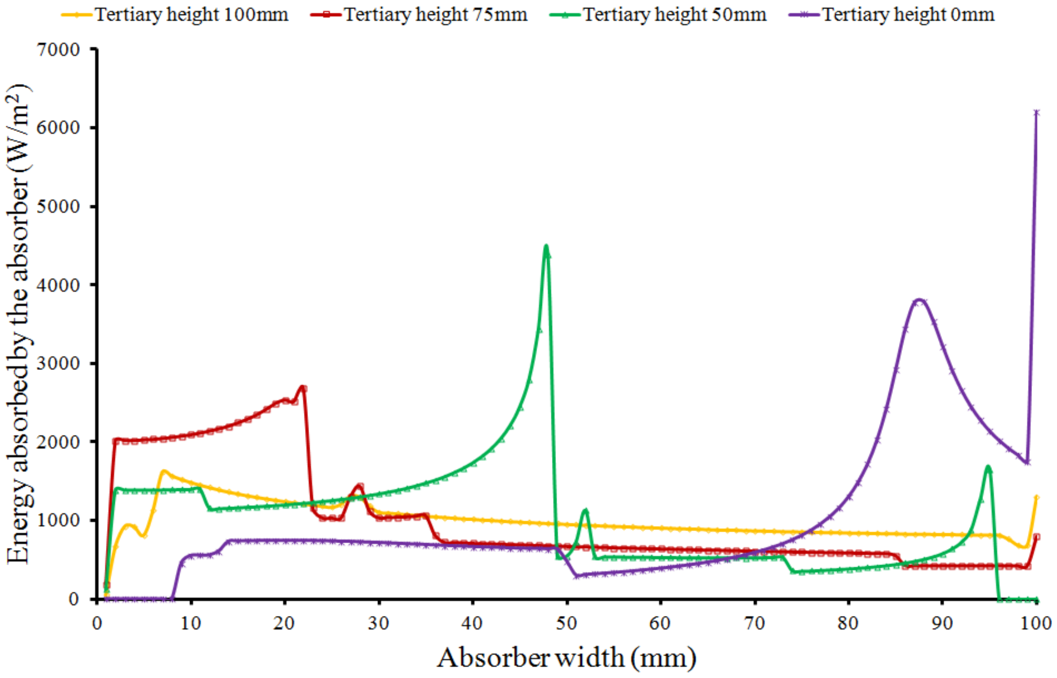

Figure.3.22: Energy distribution at 27° incident angle for different tertiary heights

For all predictions the incident solar radiation intensity was assumed to be 1000 W/m^2. As it can be seen in Figure 3.22, higher peaks occur near the corners of the CTAH without a tertiary section. It can also be seen that as the tertiary height increases, the height of the peak reduces. This trend can be identified clearly for tertiary heights from 0mm to 100mm. Figure 3.23 illustrates the energy distribution at the absorber of the CTAH for different incident angles for 50 mm tertiary height.

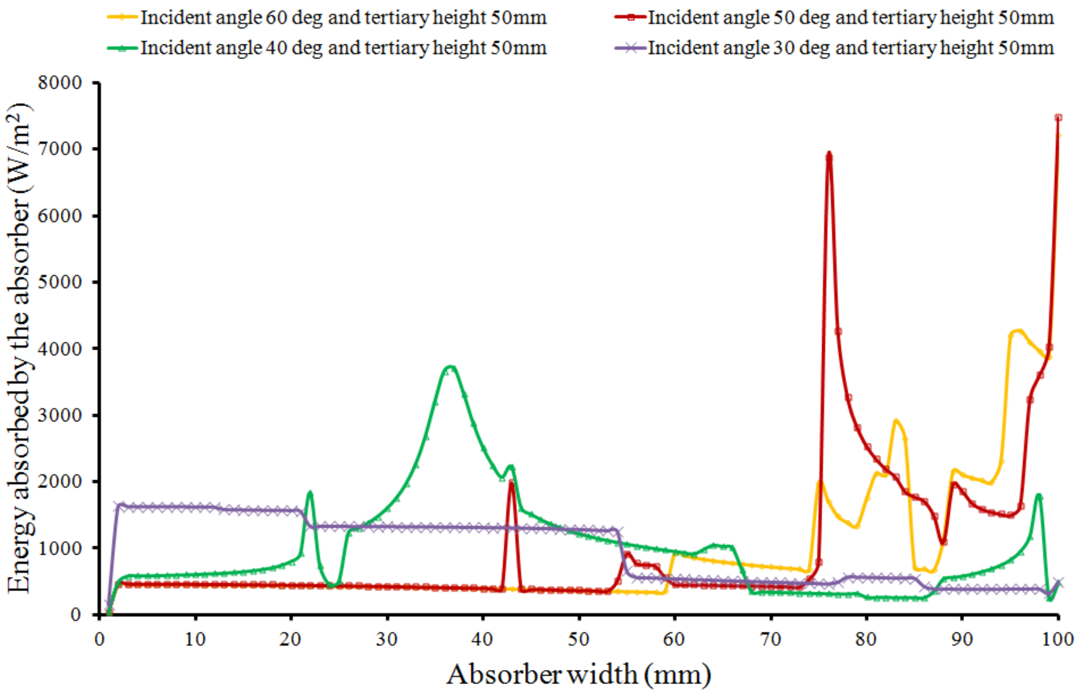

Figure.3.23: Energy distribution at different incident angle for a 50mm tertiary height

For all predictions, the incident solar radiation intensity was assumed to be 1000 W/m^2. As it can be seen in Figure 3.23, higher peaks occur near the corners of the CTAH for higher incident angles. It can also be seen that as the incident angle reduces, the energy becomes more distributed over absorber width.

3.4.6 Optical loss on reflector surfaces

The optical losses at different reflector surfaces and tertiary surfaces due to reflection on the concentrator surfaces are illustrated in Figure 3.24. Optical loss on individual reflector surfaces fluctuates to a great extent. Higher losses are observed on the lower parabolic and tertiary reflector during lower incident angles. Losses over these two sections decreased after 20 degrees incident angle. By contrast, losses over the circular reflector rose dramatically after 20 degrees followed by a steep drop at higher incident angles.

Losses at the upper reflector rose steadily during higher incident angles. The overall reflector loss showed a steady rise up to incidence angle 30 degree. The loss dropped slightly before making a steady recovery. The loss trends indicate that losses over the lower parabola dominate during lower incident angles. At medium and higher incident angles, losses occur over the lower parabolic, circular and upper reflectors. The number of reflections in the tertiary section increased with increased tertiary height. The circular section is highly active for incident angles between 30^o to 70^o. This section has a concentration radio is 1; it does not amplify the concentration but solely redirects all the incoming rays to the inverted face of the absorber. So the reflectivity of this section needs to be very high to avoid large reflection loss.

Figure 3.25 illustrates the overall optical loss over reflector surfaces for different tertiary heights. Considering 1000 W/m^2 incident radiation, the average reflector optical loss for all acceptance angles is 67.6 W/m^2 for 0 mm tertiary height, 91.5 W/m^2 for 50 mm tertiary height and 109.7 W/m^2 for 100 mm tertiary height. Optical loss due to reflection on the reflector surface increases by 26% with increase of the tertiary height from 0 mm to 50 mm. A further increase in tertiary height of 50 mm resulted in increase of 19.9% of optical loss. It was also found that the concentration of radiation is more distributed due to integration of the tertiary. However, the optical loss due to reflection on the reflector surfaces increases as the tertiary height of CTAH increases. So the reflectivity of the reflector needs to be very high to avoid reflection losses in case of an incorporated tertiary reflector section.

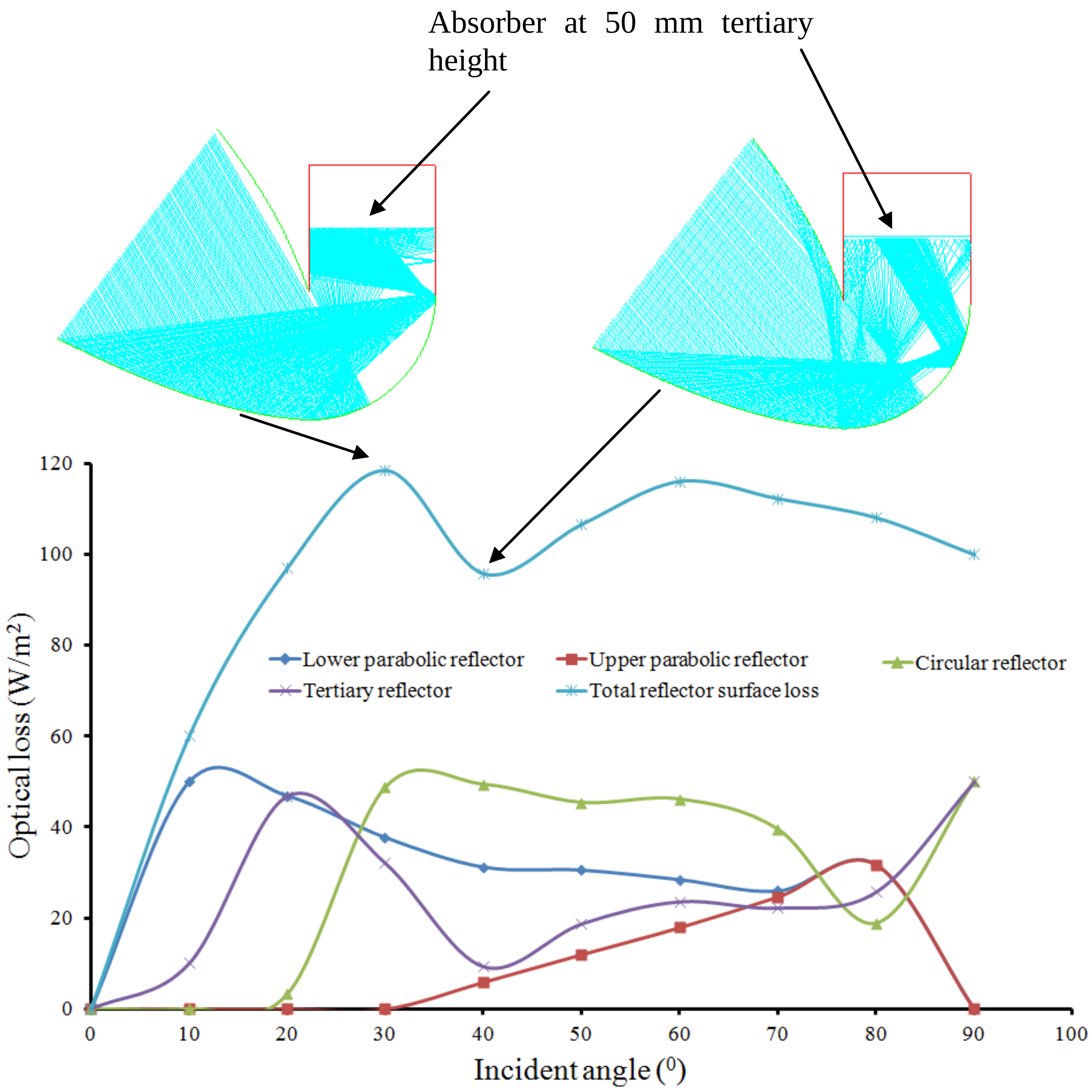

Figure 3.24: Optical loss on reflector surfaces for different incident angles for 50 mm tertiary height

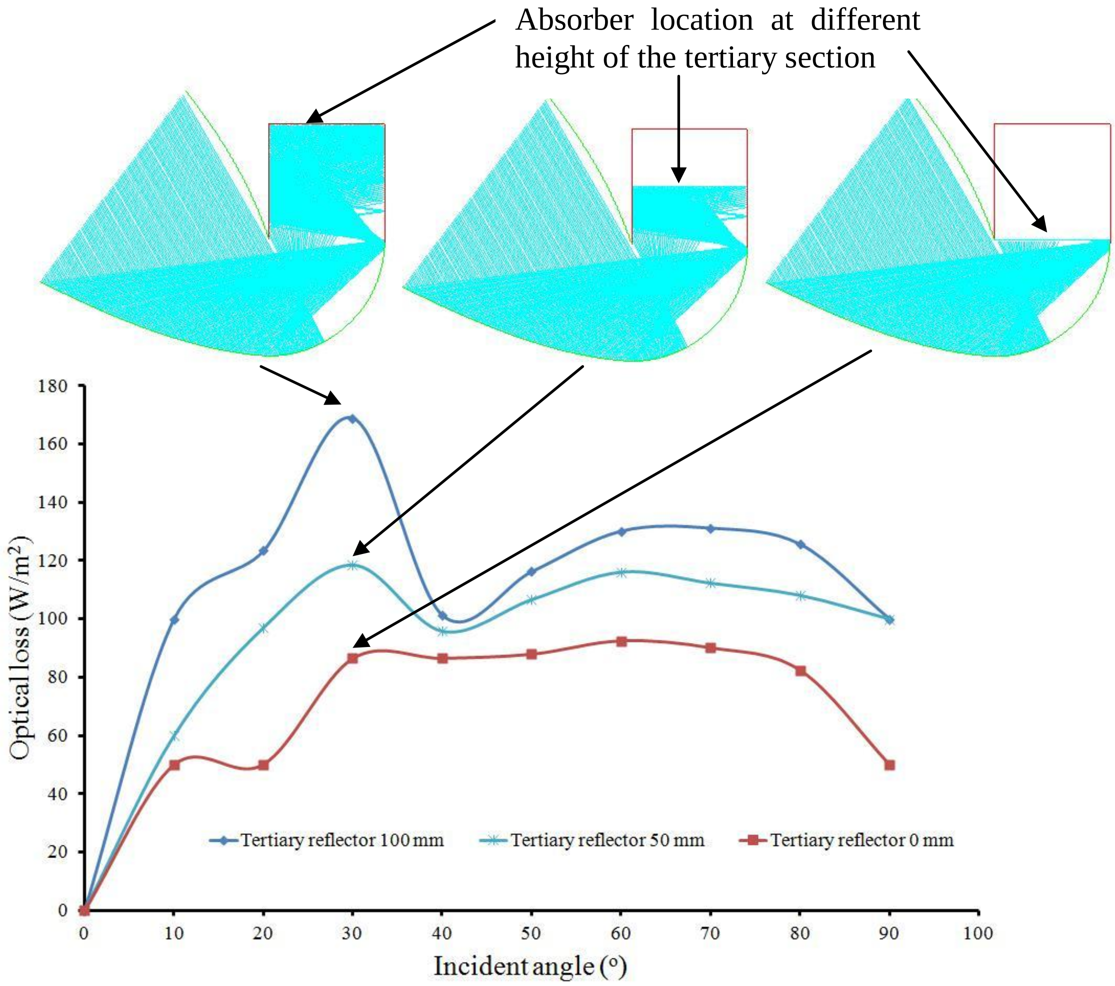

Absorber location at different height of the tertiary section

Figure 3.25: Overall optical loss over the reflector surfaces for different tertiary heights

3.4.7 Statistical analysis on simulation results

Higher reflectivity and lower tertiary height is desirable from an optical point of view. Statistical analysis was carried out to find the confidence of the combined effects of tertiary height and reflector reflectivity. A two way analysis of variance (ANOVA) was carried out on the optical efficiency of the CTAH for different tertiary height (0 mm and 100 mm) and reflector reflectivity (90% and 95%). However, the result shows highly significant effect on optical performance for all cases. It was difficult to separate the effect for each parameter.

The analysis suggested carrying out a t-test and one way ANOVA test to compare the relative performance to find out the significance of the parameters on optical performance. Appendix 2.1 shows the comparative table of one way ANOVA analysis. An unpaired t-test was carried out between 0 mm and 100 mm tertiary section for 90% reflective reflector which confirms a significant influence. However, in the second case a comparison between 0 mm and 100 mm tertiary section for 95% reflective reflector does not confirm a significant influence.

A t-test compares the mean difference between two data. A variance comparison was needed to confirm the effect of the parameters. A one way ANOVA was carried out to compare the variance of two groups. As expected, applying the null hypothesis between 100 mm tertiary with 90% reflectivity and 0 mm tertiary with 95% reflectivity shows very high significance effect.

3.4.8 Diffuse radiation modelling results

The incident solar radiation concentration was modelled by two angular skywards diffuse distributions (Prapas et al., 1987; Mallick, 2003) given in Equation 3.4 and 3.5. The distributions are shown in Figure 3.26. The isotropic diffuse model is conservative and thus tends to underestimate as it does not take account of the circumsolar diffuse (Duffie & Beckman, 2006).

Isotropic: $I_{D,\phi} = 1$ 3.4

Cosine: $I_{D,\phi} = \frac{\pi}{2}\cos\phi$ 3.5

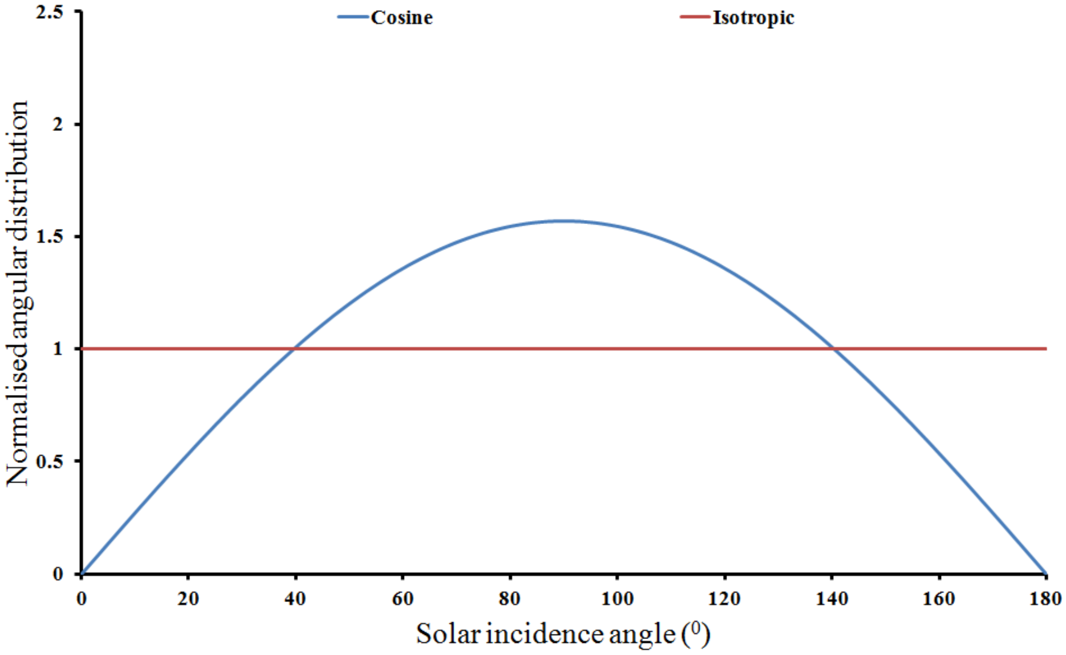

Figure 3.26: Alternative skyward angular distributions of diffuse solar radiation (Prapas et al., 1987)

The equation was incorporated into the ray tracing analysis program to determine the effects of diffuse solar radiation incident on the aperture. Figure 3.27 shows the optical efficiency of CTAH for cosine diffuse distribution. The efficiency increases linearly from 0 to 59.1% with the incident angle from 0 to 27^o. The maximum efficiency is 65% at 43^o. Between 27^o and 89^o efficiency varies within 65% to 48.2%.

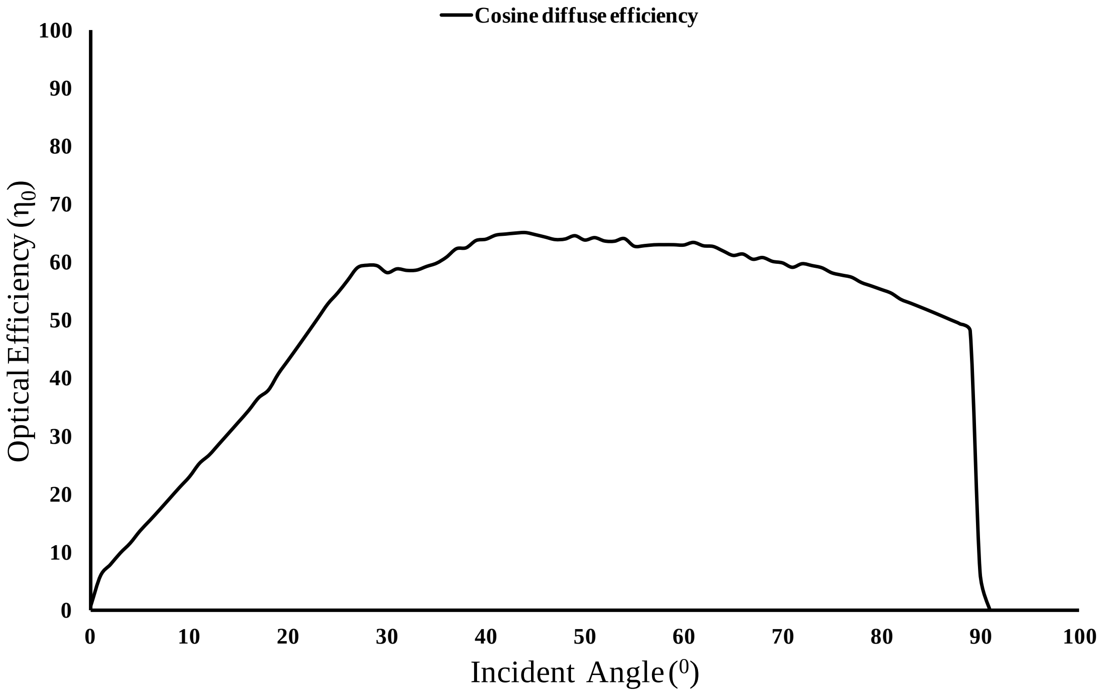

Figure 3.27: Diffuse optical efficiency considering 88% glazing transmittance and cosine diffuse distribution

3.4.9 Optical efficiency of optimised optical concentrator

Figure 3.27 shows the beam and diffuse efficiency of CTAH over its acceptance angle. The optical concentrator was optimised considering tertiary height (50 mm) and reflector reflectivity (95%). The optical efficiency is non uniform over the range of incident angles for beam and diffuse radiation. The incident angle varies with the solar time. The efficiency increases linearly for the incident angle from 0 to 27^o. The beam and diffuse efficiency at 27^o incident angle are 79.6% and 59.1%. Between 27^o and 89^o incident angle, beam efficiency varies within 79.6% and 72% and diffuse efficiency varies within 65% to 48.2%.

The maximum beam and diffuse efficiency are 79.6% and 65%. The maximum beam and diffuse optical efficiency of the CTAH were 79.5% and 65% respectively for 50 mm tertiary height, 88% transmittance of the glazing and 95% reflectance of the concentrator reflector. The acceptance angle of the CTAH varied between 100% at 27^{o} incident angle and 92.7% at incident angle 89^{o} which provide effective annual concentration for 7-8 hours. The beam efficiency within 27^{o} to 89^{o} incident angle varies between 79.5% and 72% and diffuse efficiency varies between 65% and 48.2%.

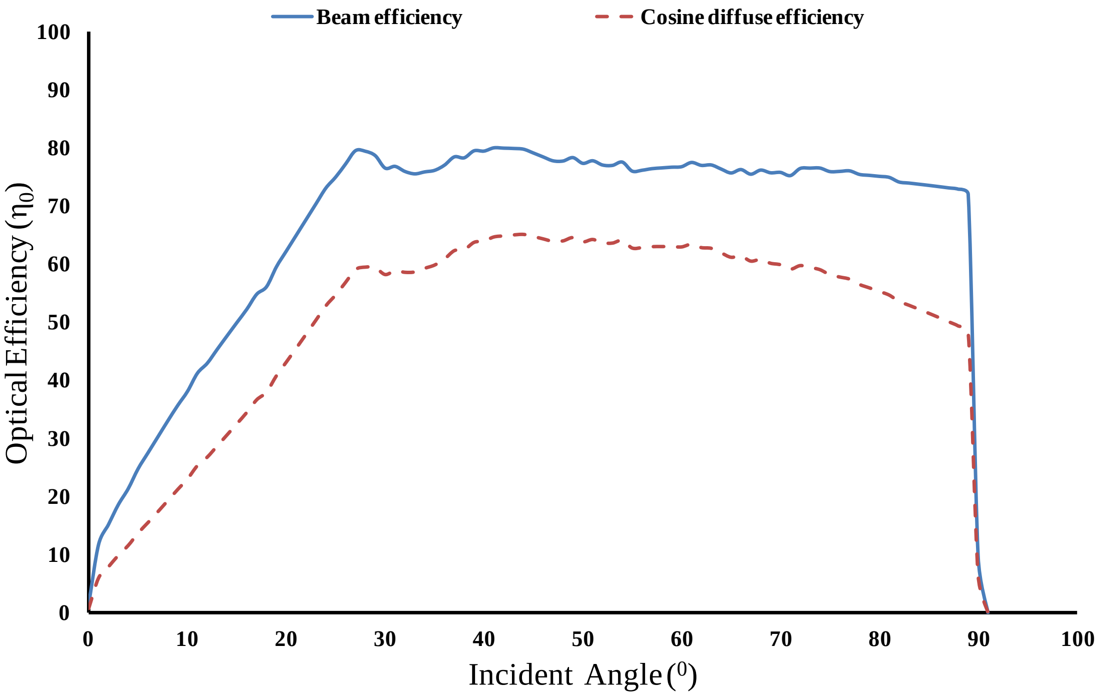

Figure 3.28: Beam and diffuse optical efficiency considering 88% glazing transmittance and optimised 50 mm tertiary height

3.5 Summary

The maximum beam and diffuse optical efficiency of the CTAH were 79.5% and 65% respectively for 50 mm tertiary height, 88% transmittance of the glazing and 95% reflectance of the concentrator reflector. The acceptance angle of the CTAH varied between 100% at 27^{o} incident angle and 92.7% at incident angle 89^{o} which provides effective annual concentration for 7-8 hours. The beam efficiency within 27^{o} to 89^{o}

incident angle varies between 79.5% and 72% and diffuse efficiency varies between 65% and 48.2%.

The development of the ray tracing model using Matlab was described comprehensively. Boundary equations generation, calculation of intersection points and angles, ray tracing programming were detailed in developing the 2D ray tracing model of the CTAH. The validation process of the optical concentration was carried out using a laser test.

The intensity of radiation on the absorber width was calculated using the model over different incident angles which were found to be non-uniform over the absorber width. The effect of tertiary height, reflector reflectivity and glazing cover on optical performance were analysed. Optical loss due to reflector surface was analysed for different incident angles and tertiary heights. The optical efficiency of the CTAH is used as an input of the heat transfer model. The heat transfer model of the CTAH is detailed in Chapter 6. The optical design was used to construct prototypes of the CTAH system (detailed in chapter 4) to conduct outdoor experimental performance analysis (detailed in chapter 5).

CHAPTER 4

CTAH CONCEPT DESIGN, CHARACTERISATION AND FABRICATION

The aim of this chapter is to carry out concept design and fabrication of outdoor experimental prototypes of a Concentrating Transpired Air Heating (CTAH) system using geometric design of CTAH which was optimised optically in chapter 3 to conduct outdoor experimental analysis (as described in chapter 5). This chapter focuses on the following objectives:

- Concept design of Concentrating Transpired Air Heating (CTAH) system;
- Material selection and characterisation of different component of the system;
- Fabrication of the experimental prototypes.

4.1 Introduction to concept design of CTAH

The concentrating reflector, transpired absorber and the glazing cover are the main components of the CTAH system. In choosing the optimum component materials for the CTAH the aims were to overcome inherent short comings of the conventional solar air heating systems such as high thermal losses due to high thermal conductivity of the absorber material and low thermal conductivity of air.

As discussed in chapter 2, the main components of the conventional flat plate collectors are high transmittance glazing cover and high conductive metal absorber. However, unlike conventional air heating system, as the air flows through the perforations of the absorber in both CTAH and the Unglazed Transpired Collectors (UTC), the challenges in heat transfer mechanisms are partially similar. The main component of UTC is the perforated metallic transpired absorber.

Figure 4.1 illustrates the heat transfer mechanism in the UTC. Where, $Q_{rad.col-sur}$ is radiation loss from the collector surface to the surrounding, $Q_{conv.col-air}$ is convection between collector and inward air. Radiation and convection between backplate and surrounding air are $Q_{rad.-bp-sur}$ and $Q_{conv.bp-sur}$. As shown in the figure, the UTC system's inherent radiation loss ($Q_{rad.col-sur}$) is from the large exposed absorber surface area. Though researchers (Kutscher et al., 1993) estimated insignificant convection loss from absorber to ambient, in the case of reverse flow effects, some captured heat ($Q_{conv.col-air}$) may also be lost from the perforation.

Figure 4.2 illustrates the midsection analysis of CTAH, a combination of perforated absorber with concentrator. Concentrating solar energy with transpired absorber fundamentally improves the utility of such systems, by providing higher outlet air temperatures. The absorber surface in the CTAH was oriented horizontally facing downward as shown in the Figure 4.2. The radiation loss from absorber surface to the glazing ($Q_{rad.abs-glazing}$) can be trapped using a glazing surface at the aperture.

Furthermore, the stratified thermal layer in the cavity and tertiary section reduces the radiation and convection loss from absorber to glazing. A portion of incident solar energy may be captured by the concentrator material due to multiple reflections inside cavity. However, a good insulation for the concentrator material and a cross ward air flow can recapture the loss as thermal energy input. In a glazing air collector a portion of incident radiation loss occurs due to reflection and absorption on the glazing surface.

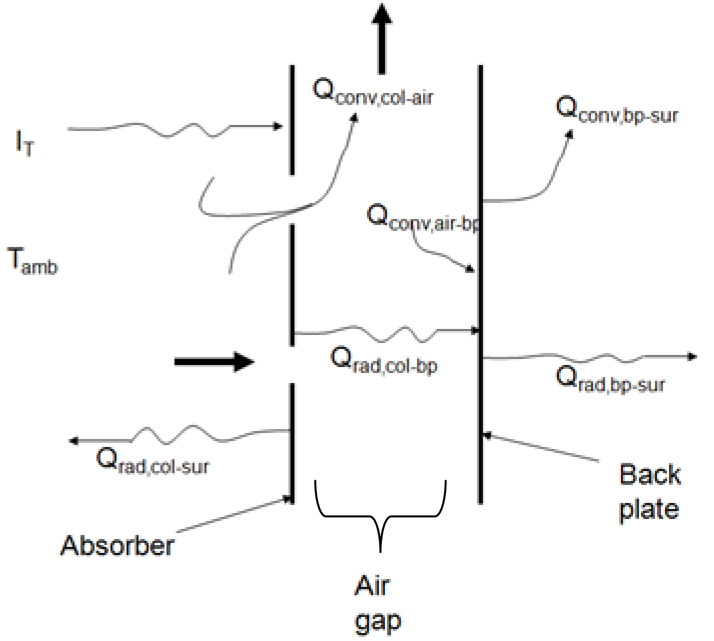

Figure 4.1 (a): Unglazed transpired collector

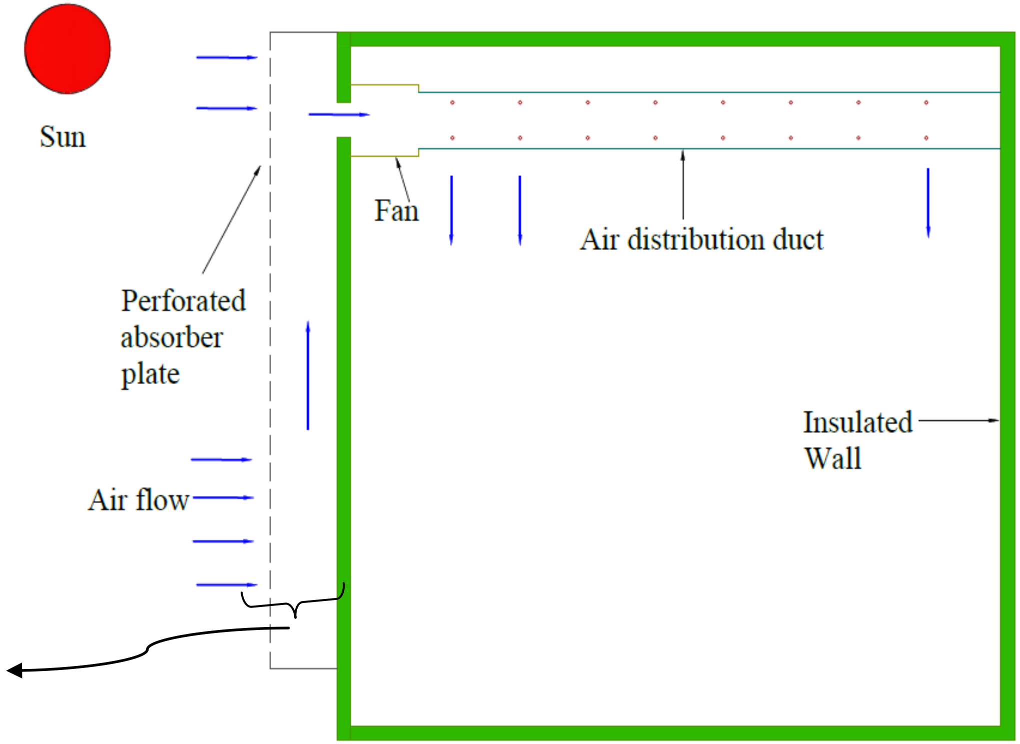

Figure 4.1 (b): Heat transfer mechanism in UTC system with vertical absorber plate

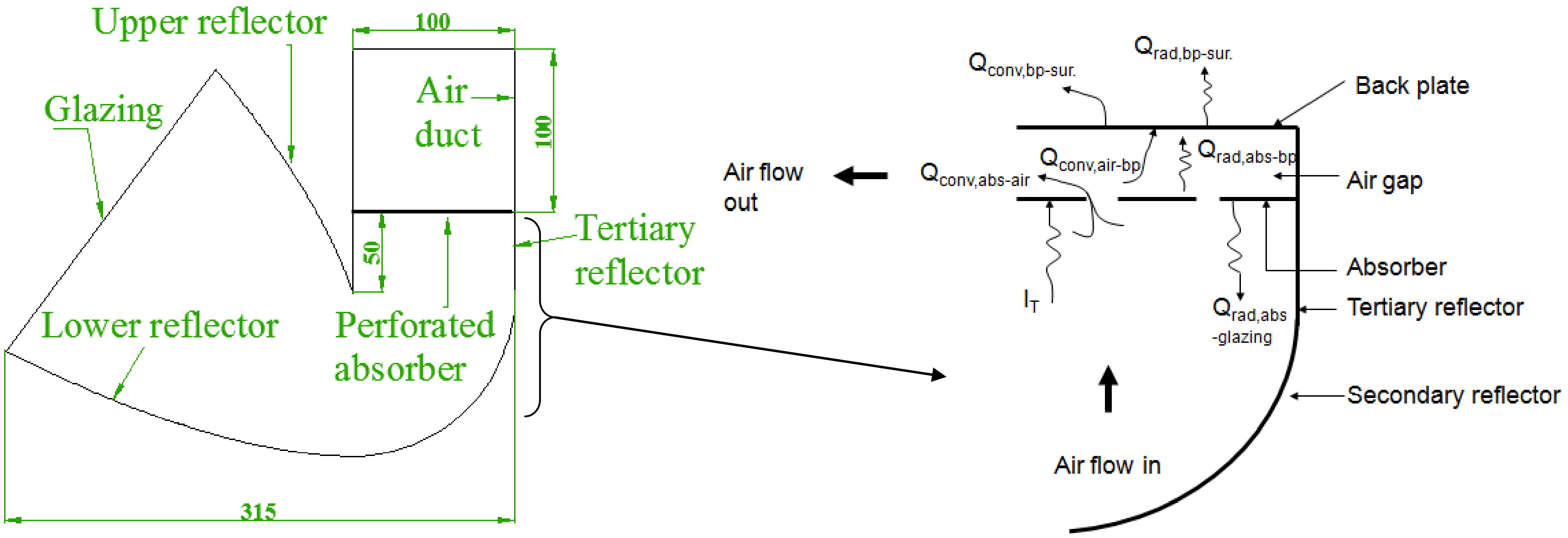

Figure 4.2 (a): Schematic Diagram of CTAH

Figure 4.2 (b): Midsection analysis of CTAH absorber

The glazing cover of CTAH is a critical issue when considering the weather conditions of the location which may have an effect on the performance of the collector due to deterioration of the concentration surface from dust deposition.

The novel concept of CTAH is to concentrate the solar radiation onto a low perforated absorber which is placed at inverted orientation and significantly far from the aperture of the collector compared to flat plate collectors. The integrated absorber material was inherently perforated with low conductance.

$$D_{abs} >> W_{abs} \qquad 4.1$$

Where,

D_{abs} = Distance between the absorber and the aperture

W_{abs} = Absorber width

One of the critical issues of UTC was to overcome the reverse flow effect which causes heat loss requiring high pressure drop. Also, many improvements of conventional air heating systems have caused increased pressure drop through the collector. This increased pressure drop due to collector configuration causes higher operating costs. The configuration of the inverted perforated absorber of CTAH causes low pressure drop during system operation by eliminating complicated absorber design inside the concentrator cavity.

4.2 Absorber selection and characterisation of CTAH

The purpose of the absorber plate is to convert incident solar radiation into heat energy by minimising the re-emitted energy. A carbon fibre fabric was used as the solar absorber material in CTAH system. This is an unconventional absorber material for solar air heating systems.

4.2.1 Selection criteria of carbon fibre as the perforated absorber

The black colour carbon fibre with inherent lower pitch and perforation diameter combination (porosity < 5%) was adopted in the CTAH design. Porosities in transpired collector installations are suggested as low as 5%, so the effect of porosity on conductivity becomes small (Christensen et al., 1997). The higher weight and cost of the conventional absorber was avoided by selecting carbon fibre as the absorber material of CTAH. For a fixed percentage perforation, pitch decreases with perforation diameter.

The decreasing pitch and perforation diameter of metal perforated absorber increases the manufacturing difficulties and therefore cost. Another issue is the selective coating of the absorber which further increases the cost of the perforated absorber in conventional solar collectors. The necessary equations to optimise perforation of porous metal absorber has been added in Appendix 3. However, the porosity of the carbon fibre was very low with non uniform square perforation. It was necessary to measure the carbon fibre porosity using high precision Scanning Electorn Microscope (SEM) which will be discussed in next section.

The prime selection criteria of perforated absorber materials are perforation geometry (pitch length and porous diameter), thickness and material property of the absorber.

The perforation in the perforated absorber can be defined by porosity which is the ratio of the perforated area within pitch area. The geometrical parameters of absorber perforation are directly related with the pressure drop across the absorber plate.

The effects of perforation diameter, pitch and the perforation have been discussed in chapter 2. The above mentioned parameters play a vital role in the amount of air flow through the perforation and heat transfer mechanism.

Porosity of the perforated absorber depends on the type of the pitch and the diameter of the perforation. Several authors studied square and triangular pitch with different perforation diameter (Dymond & Kutscher, 1997; Gawlik et al., 2005; Gawlik & Kutscher, 2002; Kutscher, 1994; Leon & Kumar, 2007; Decker et al., 2001). For optimised transpired absorber design, it is necessary to determine the absorber porosity. The effect of absorber material and thickness on system performance has been discussed in chapter 2.

Earlier researchers used highly porous absorber plates much higher than used for transpired solar collectors as reported by (Kutscher et al., 1993). This is probably intended to enhance the heat transfer between air and absorber perforation. However most recently researchers became interested with low porous absorber plate to enhance heat transfer mechanism. Kutscher (1994), Van Decker et al. (2001), Badache et al., (2010) conducted experiments on UTC for low porosity absorbe with a wide range of perforation and pitch combination as presented in chapter 2.

4.2.2 Characterisation of CTAH absorber

4.2.2.1 Instrumentation for characterization of absorber material

The porosity of the carbon fibre absorber was calculated from imaged data of morphology which was taken by a scanning electron microscope Hitachi SU6600 FE-SEM. Five samples were prepared using epoxy hardener and epoxy laminating resin as the corner boundary of the samples to protect from separation of fibres. The microscope images the sample surface by scanning with a high-energy beam of electrons in a raster scan pattern. The electrons interact with the shells in atoms that make up the sample producing signals that contain information about the sample's surface topography.

4.2.2.2 Property of carbon fibre

Carbon fibre plain weave (200 gm) was used as absorber material (Carbonmods, 2010). Incorporation of carbon fibre as an absorber material reduces absorber weight which increases the acceptance possibility of the CTAH in building integration. For example: an aluminium absorber of UTC with identical thickness (0.26 mm) and perforation (4.1%) is 251% heavier than carbon fibre absorber of CTAH.

Carbon fibre fabric is an industrial raw material with widespread industrial use as flat and tubular components, for support and as reinforcements where light weight and high strength are needed, optical equipment, wind turbines, aircraft and spacecraft parts, racing car bodies, golf club shafts, bicycle frames, fishing rods and automobile springs (Zoltek, 2010; ECGA, 2011).

Figure 4.3 shows the diameter of a loose carbon fibre as 6.55 μm. The image was taken using Hitachi SU6600 FE-SEM at 500x magnification. A carbon fibre is a long, thin strand of material about 7μm mm. These carbon atoms are bonded together in microscopic crystals that are more or less aligned parallel to the long axis of the carbon fibre.

Filament is equal to a single strand of carbon fibre. Thousands of filaments make up a Fibre/Yarn. Fibre is made up of thousands of filaments that are grouped together. Tow is the amount of continuous filaments per fibre bundle. Tow is measured in K (1,000).

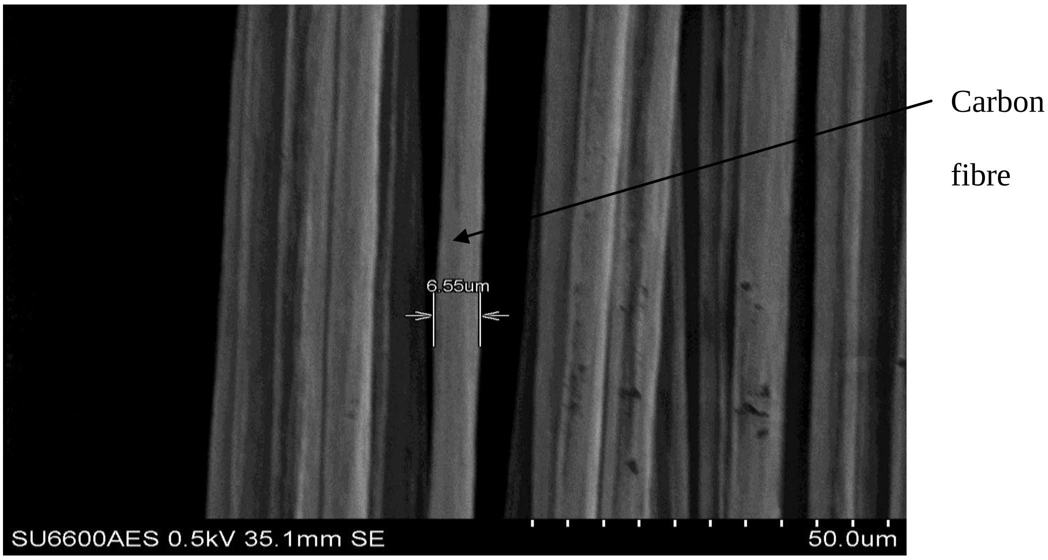

Figure 4.3: Taken top down at a magnification of 500x to measure strand thickness

Table 4.1 shows the properties of carbon fibre weave fabrics. The crystal alignment makes the fibre incredibly strong for its size. In 3k carbon fibre 3000 filaments are twisted together to form a yarn, which is used and woven into a fabric.

Table 4.1: Properties of carbon fibre weave fabrics

Properties of carbon fibre weave	Measurements
Thickness	0.26 mm (measured)
Colour	Carbon black
Conductivity	7 W/mK[a]
Filament diameter	7 μm[a]
Number of filament	3000[a]
Strength	640 MPa[a]
Weight	200 g/sqm[c]

[a](Grafil, 2010), [b](Matweb, 2010), [c](Easycomposite, 2010)

A 3K means there are 3,000 carbon filaments per fibre. Warp indicates the fibre running the length of a woven fabric. Fill means the fibres running the width of a woven fabric. A 12x12 fabric means there are 12 fibres in the warp direction per inch and 12 fibres in the fill direction per inch (Fibreglast, 2010).

The ultrahigh modulus carbon fibres have a tensile modulus of 500 million-1.0 billion kPa. As a comparison, steel has a tensile modulus of about 200 million kPa. The strongest carbon fibres are ten times stronger than steel and eight times that of aluminum, and much lighter than both materials. Additionally, their fatigue properties are superior to all known metallic structures, and they are one of the most corrosion-resistant materials available (Zoltek, 2010).

Previous research showed that the conductivity of absorber has very low effect on perforated air heating collector performance (Christensen et al., 1997). However, in case of concentrating solar collector, the absorber material needs to have properties to work at high temperature. Carbon fibre is a perforated material which provides a reduced cost perforated absorber. However, it is very difficult to design the integration of the carbon fibre with CTAH system without a proper frame and resin. Epoxy laminating resin with carbon fibre kit epoxy hardener (Easycomposite, 2010) combination was used in this research as carbon fibre resin at the corners of the absorber to avoid any splitting in carbon weave fabrics. These corners were attached with thin wooden frame of specific absorber dimension (100mm X 1250 mm).

Figure 4.4 shows the isothermal oxidation of carbon fibre in air at 923^o to 1123^0K. Assuming perfect concentrator with 1.9 CR, at stagnation condition the maximum instantaneous absorber surface temperature of CTAH, at 1000 W/m^2 incident radiation can be calculated as approximately 155^oC. Oxidation factor is important to investigate for longtime performance of carbon fibre as the absorber material. The oxidation temperature (923 to 1123K) is much higher than the range of CTAH operating temperature which ensures the safety of the fabric absorber material. However, if a solar concentrating air heating system needs higher concentration, the carbon fibre may not be an appropriate absorber material.

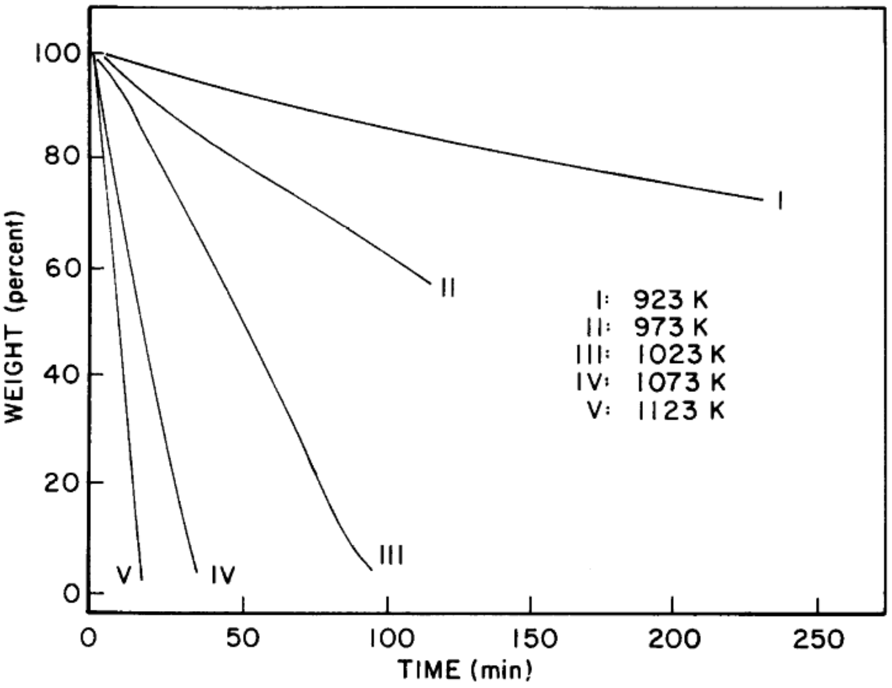

Figure 4.4: Isothermal oxidation of carbon fibre in air at 923 to 1123K

(Ismail, 1991)

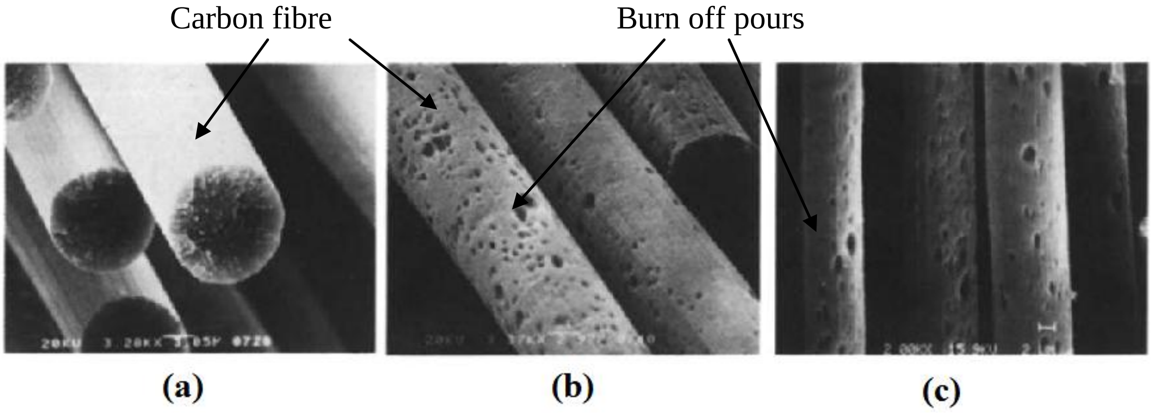

(a) (b) (c)

Figure 4.5: Scanning electron micrographs of carbon fibre (a) Burn off (4.1%) in air at 773 K, (b) Burn off (4.5%) in air at 873 K, (c) Burn off (7.6%) in air at 973 K (Ismail, 1991)

Figure 4.5 shows the scanning electron micrographs of carbon fibre (a) Burn off (4.1%) in air at 773 K, (b) Burn off (4.5%) in air at 873 K, (c) Burn off (7.6%) in air at 973 K. The experimental data shows that carbon fibre can be used for long life span with negligible burn off.

4.2.2.3 Measurement of porosity of the carbon fibre absorber

The porosity of the carbon fibre absorber was calculated from data of morphology image using the Equation 4.2 which will be used in chapter 6 as an input of the heat transfer model. The average perforation area was 0.147 mm^2. The average porosity was measured as 4.19% which is a low value as expected.

$$Porosity = \frac{N\sum A_{pore}}{A_m} \tag{4.2}$$

Where,

A_m = Area of the measured sample;

N = Number of pores; and

A_{pore} = Area of the individual pore.

Figure 4.6 shows the top down image at a magnification of 15x with each of the 12 pores measured for breadth (as visible on the image)

All images were taken using a Hitachi SU6600 FE-SEM at an accelerating voltage of 0.5kV and utilising the SE (Secondary Electron) detector. Samples were measured to obtain overall averages based on 12 pores from each.

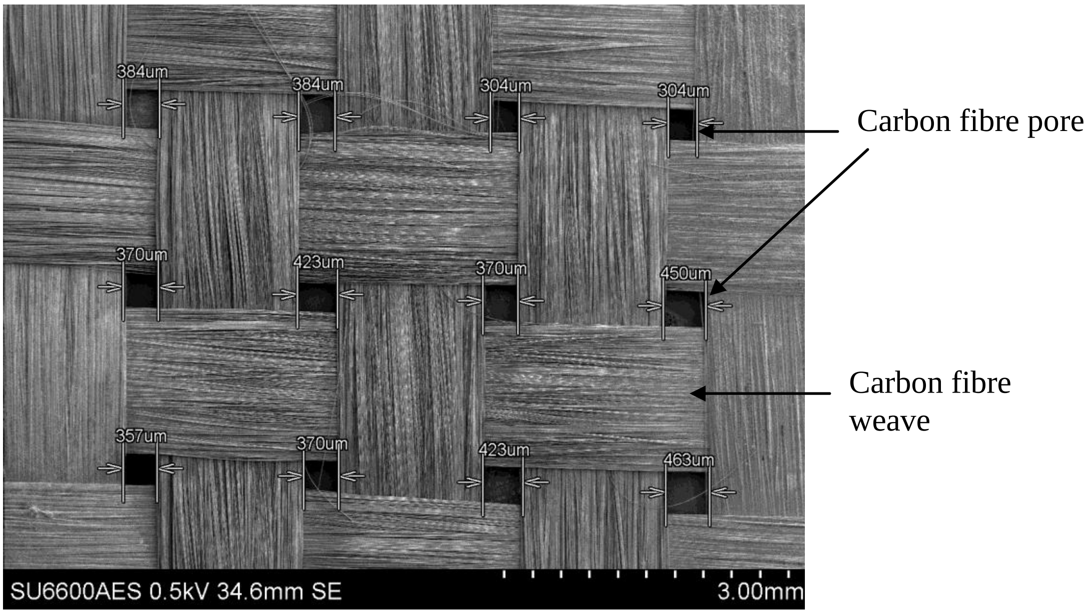

Figure 4.6: Image taken top down at a magnification of 15x with each of the 12 pores measured for breadth (as visible on the image)

This was done because of the size of the sample relative to the magnification required to get clear and coherent good quality images. The scale bar for these samples is misleading. The numerical value in the scale bar is the distance from the first white line to the last white line, not for each incremental line. This is due to the Hitachi software coding.

4.3 Selection and characterization of glazing component

4.3.1 Selection of CTAH glazing cover

The glazing material of the CTAH system is one 6 mm thick low iron glass cover. The glazing surface protects the reflecting and absorbing surfaces and reduces thermal losses from the carbon fibre fabrics absorber. However, the beam and diffuse radiation effectively entering the CTAH are reduced by the transmittance of the glazing cover. The effect of glazing on optical performance has been discussed in chapter 2. The transmittance of a transparent glazing of CTAH system is a function of the reflection losses at the boundary surfaces of the glazing and the absorption losses in the glazing material itself. The reflection losses of the glazing surface depend on the refractive index of the cover material and structural orientation of the glazing. The lowest reflection losses can be achieved if an antireflective coating with a refractive index between the air and the cover material is used.

The most common type of glazed solar air heaters are designed with one glass cover. In order to minimize the upward heat loss from the collector, more than one transparent glazing may be used. However, with the increase in the number of cover plates, transmittance is decreased. Glass is the most common glazing material. Glass can break easily. However, this disadvantage can be minimized by using tempered glass. Transparent plastics, such as polycarbonates and acrylics are also used as glazing. Their main advantage is resistance to breakage.

The main disadvantage of plastics is that their transmittance in the longer wavelength is also high; therefore, they are not as good a trap as glass (Cheremisinoff & Regino, 1978). Other disadvantages include deterioration over a period of time due to ultraviolet solar radiation (Goswami et al., 2000; Kalogirou, 2009). The modification factors of glazing materials were discussed comprehensively in chapter 2. A list of commercially available glazing materials with enhanced optical properties has been added in Appendix 1.2.

4.3.2 Characterization of CTAH glazing cover

The transmittance of the glazing material and reflectivity of the reflector material has been characterized. The results of the material characterisation are presented in this chapter which are also used as input parameters of the optical and heat transfer model. CTAH addressed the appropriate material selection and consideration in design process. The prototype of the system was built with a modular approach and the critical issues of each unit component construction and fabrication are discussed in this chapter.

4.3.2.1 Instrumentation for characterization of glazing material

The transmittance of glazing surface was recorded in Perkin Elmer Lambda 900 UV/Vis/NIR spectrometer. Figures 4.7 and 4.8 illustrate the principle of the UV/Vis/NIR spectrometer. The light beam was divided into two equal components after diffraction grating and both of the light was measured using detector after they pass through reference surface and the sample. The Perkin Elmer Lambda 900 is a double beam, double monochromator ratio recording spectrometer which uses tungsten halogen and deuterium lamps as light source. The broadband light source is first passed through a grating monochromator, producing narrow band radiation that is divided by a beam-splitter.

The positions of the main components are shown in Figure 4.7 and 4.8 as:

1. Light source
2. Diffraction grating with mirrors
3. Reference and sample
4. Detector

Perkin Elmer Lambda 900 UV/VIS/NIR spectrometer has been shown in Figure 4.7.

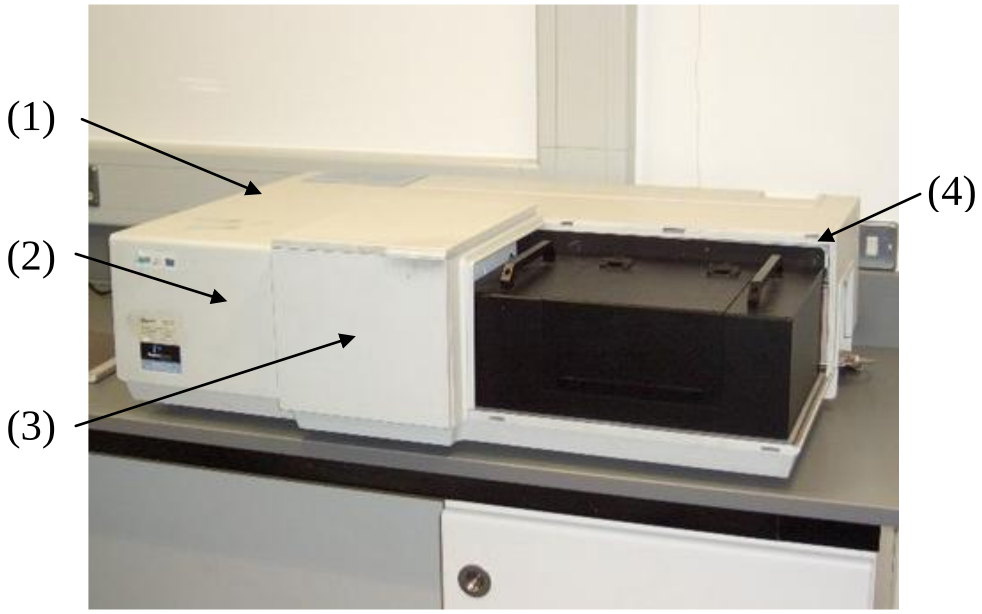

Figure 4.7: Perkin Elmer Lambda 900 UV/VIS/NIR spectrometer
(DEL, 2009)

Figure 4.8 shows the principle of Perkin Elmer Lambda 900 UV/Vis/NIR spectrometer.

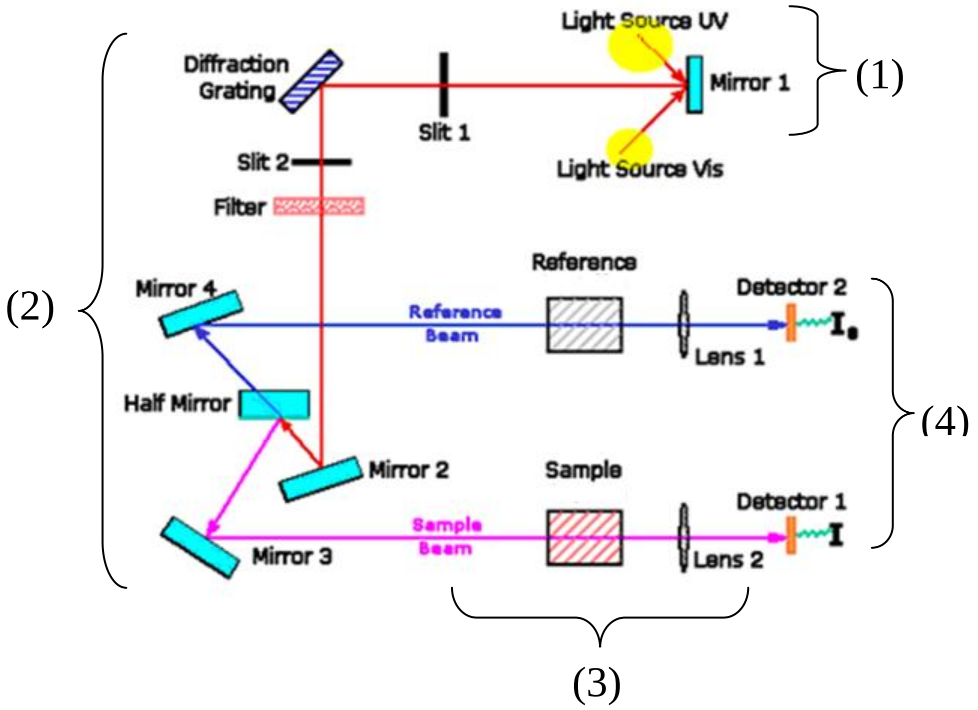

Figure 4.8: Principle of Perkin Elmer Lambda 900 UV/Vis/NIR spectrometer
(DEL, 2009)

The component 1 indicates the light source deuterium lamp which produces the light and the light pass through the component 2 (Diffraction grating with mirrors). Then two components of split light pass through component 3 (the sample and as reference beam) which are detected by component 4.

4.3.2.2 Measurement of CTAH glazing cover transmittance

Figure 4.9 shows the measured transmittance of the glass material. Solar simulator was used as the source of light.

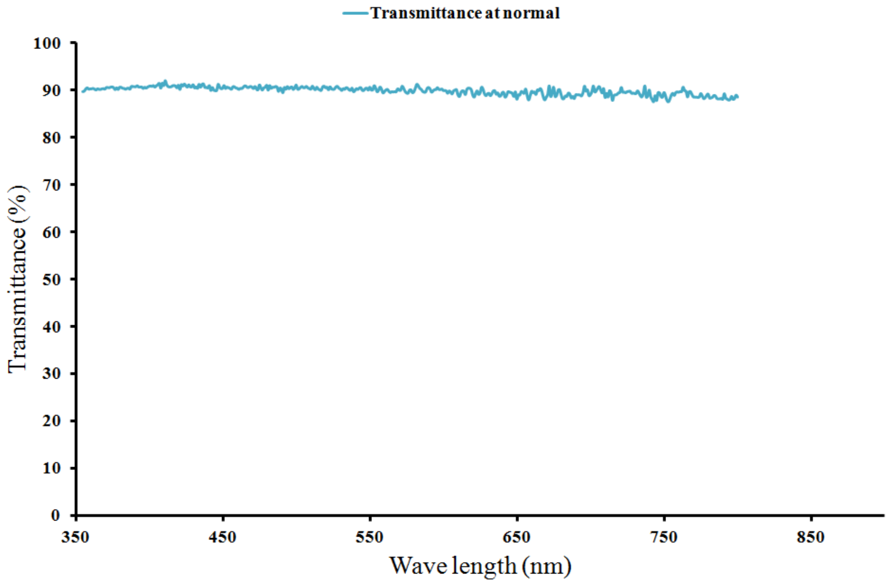

Figure 4.9: Measurement of the opti-white low iron glazing transmittance

The light flows through the optical fibre and reaches the integrating surface. The spectralon reflective surface is used as a reference surface with 98% reflectivity. Spectrometer measures the amount of light received after passing through the integrating surface. The transmittance was approximately 0.9 for the wave length of 400 nm to 750 nm. The glazing inclination of the CTAH was designed at an angle of the latitude of the location of experiment which reduces the effect of the reflection loss during experimental hours. A 0.88 tranasmittance was used in simulation considering 2% loss due to angular variation within acceptance angle.

4.4 Reflector of CTAH

Highly reflective reflector material was used (95% total light reflection) from the company ‘Alanod’. This is a German company that manufactures a variety of aluminum grades. It markets one product specifically for solar applications. That is ‘Miro-Sun’. Figure 4.10 illustrates layer system of the reflector. Mirosun is manufactured using continuous PVD process was applied for a super reflective layer to coil anodized material and afterwards the reflective surface was protected by a nano-composite in a coil-coating process. The mirosun reflector material (dimension 1250mm x 1000mm x 0.5mm) was ordered from the manufacturer ‘Alanod’ in Germany for prototype construction.

Reflector of the CTAH was constructed with two sections. Upper reflector surface and lower reflector surface. However, theoretically, the reflector cavity is separated into three sections. These are upper reflector, lower reflector and tertiary reflector section. Upper reflector is parabolic. Lower reflector is a combination of parabolic and circular reflector.

The CTAH has the highest optical efficiency if the cavity has no tertiary reflector section because the average number of reflection increases with the height of the tertiary section. However, a small section of tertiary section is crucial from thermal performance and construction point of view. A 50 mm tertiary section was combined with CTAH. Another popular high reflective (95%) film was VM 2000 which was used by Mallick (2003). However, VM 2000 was discontinued by 3M in 2008.

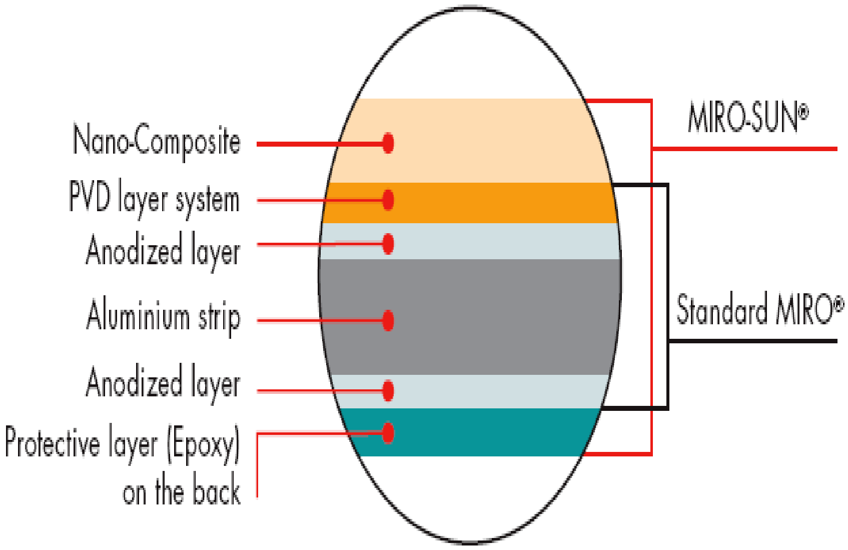

Figure 4.10: Layer system of Miro-Sun
(Alanod, 2009)

Table 4.2 shows the mechanical, optical and physical property of the reflector material.

Table 4.2: Properties of Mirosun reflector material

Properties	Parameters	Values
Mechanical	Tensile strength (Mpa)	160-200
	Yield strength (Mpa)	140-180
	Elongation a 50%	≥ 2
	Bending radius	≤1.5 fold of thickness
Optical	Total solar reflectance %	95%
	Front side	PVD-improved
	Reverse side	Anodised
Physical	Density (g/cm2)	2.7
	Heat resistance (1000h)	1500C
Dimension	Max. Width (mm)	1250
	Thickness (mm)	0.5
Warranty	10 years	

3M has other slightly reflective products with lower than 90% reflectivity which include VM 2002, 3M SA-85 solar film, Aluminised Mylar film, Anocoil aluminium sheet and Astro-foil etc. However, these films need separate metal substrate. As alanod is coated by PVD process and it is more suited to long-time performance. The cost of VM 2002 film (without aluminium substrate) is €45/m^2 where as the cost of alanod reflector (PVD glazing on aluminium substrate) is €55/m^2.

4.5 Insulation of CTAH

'Thermawrap' insulation of 4mm thickness was used in the CTAH as an insulation material as shown in Figure 4.11.

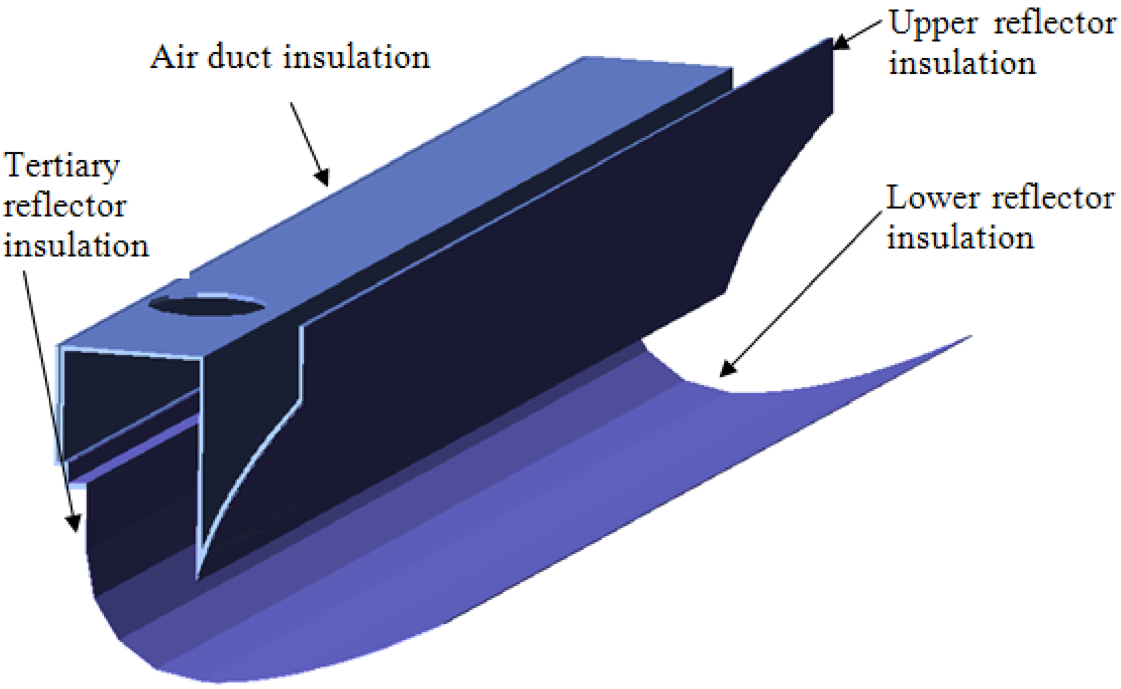

Figure 4.11: Location of insulation inside CTAH

Researchers have used different materials to insulate solar air heaters. Kurtbas & Durmus, (2004) used glass wool with conductive coefficient 0.038 W/mK. Kayuncu, (2006) used a 20 mm thickness hardboard with conductivity of 0.15 W/mK. Karsli (2007) used 5 cm and 2 cm glass wool insulation. Moummi et al., (2004) and Romdhane, (2007) used 5 cm thick polystyrene insulation. El-Sebaii, et al., (2011)[a] and

El-Sebaii et al., (2011)^b used 4 cm thick foam as insulation. El-Khawajah et al., (2011) used 2 cm thick Styrofoam of as external insulation.

Thermawrap is a durable thick bubble with high reflective foil facing to each side with a thermal resistance of 1.455 m^2K/W (equivalent to 65mm of Polystyrene). The insulation material was placed in between the reflector material and the wooden frame of CTAH. The inner surfaces of the air duct were also wrapped with the same insulation. The insulation material works as a jacket surrounding the reflector and air duct of CTAH. The wooden frame of the CTAH also served as an insulation material. The CTAH system was covered outside with two layers of water proof polyethylene.

4.6 CTAH construction and fabrication

4.6.1 CTAH frame design

The unit frames of the lower reflector as shown in Figure 4.12 were arranged in parallel positions as shown in Figure 4.13. The CTAH frame was made of wood. The upper and lower reflectors were supported with lower reflector frames and upper reflector frames. Lower reflector frame is a combination of four identical 18 mm individual wooden frame.

Each individual lower reflector frame is an addition of lower parabolic reflector and circular reflector support. Author constructed the prototype in Dublin Institute of Technology laboratory. The basic design was done using Matlab software.

The data was transferred to AutoCad to get the final shape of the reflector frame with specific dimensions which are included in Appendix 3. AutoCad drawing was printed with scale ratio of 1:1 which provide dimensions of the curves and each side.

A tracing paper was used to draw the design on the wood. During cutting the wooden frame, it is difficult task to get accurate dimension for the unique shape of the curves. An automatic jig saw cutter with very thin blade was used to cut the wood to the unique shapes. It is necessary to take extra care about the clamping during the whole process for accuracy and safety. The same procedure was followed to prepare four lower reflector frames. Then those wooden frames were carefully clamped in a vice for polishing.

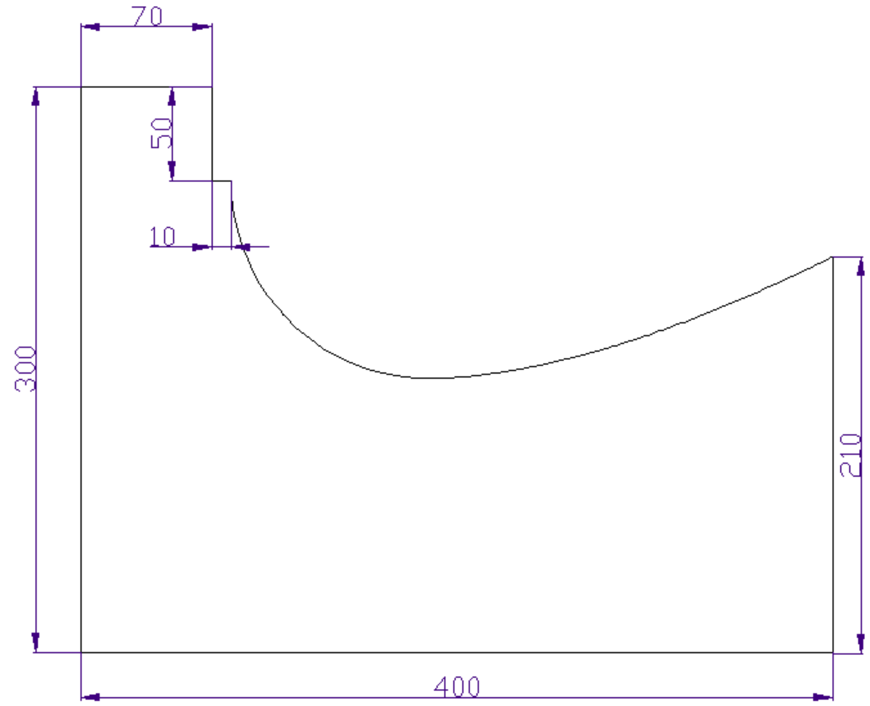

Figure 4.12: Dimension of lower reflector

Figure 4.13 shows the array of lower reflector wooden frame. At the top end of the lower reflector support frame there is a slot (50mm x 10mm). Figure 4.14 shows different parts of the lower reflector frame.

The thermawrap insulation was placed on the curves of the lower reflector units. The insulation also works as substrate of the reflector. The alanod reflector was placed on top of the insulation wrap. This is needed to combine a flat wooden support to the reflector substrate to avoid sagging as shown in Figure 4.14. This part also works as tertiary reflector support.

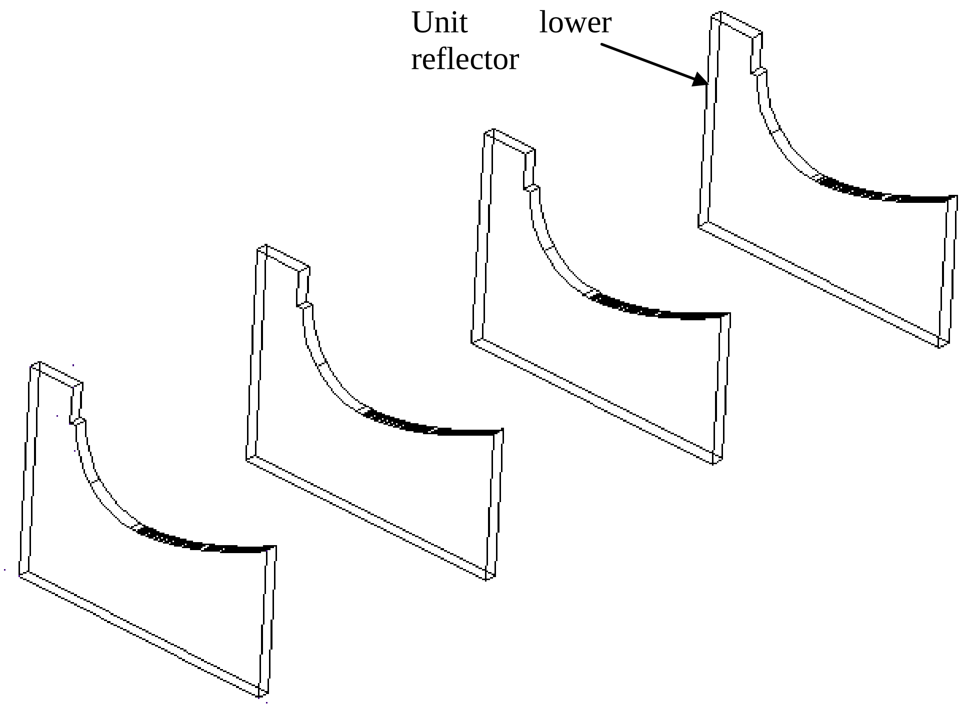

Figure 4.13: Array of lower reflector wooden frame

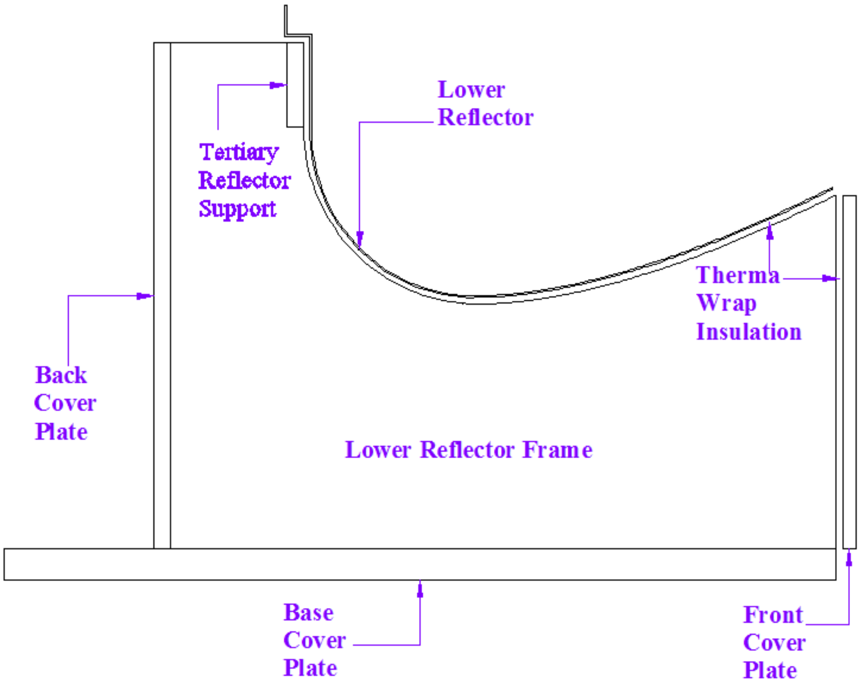

Figure 4.14: Different parts of lower reflector frame

A 3D view of the lower reflector with frame is shown in Figure 4.15 The construction of CTAH system is carried out as modular basis.

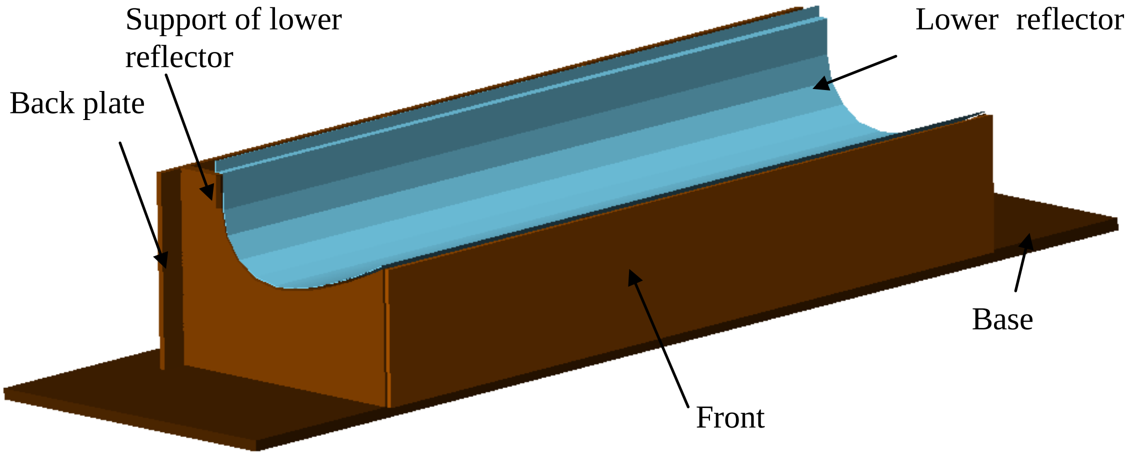

Figure 4.15: 3D view of lower support and the lower reflector

The unit frame of the upper reflector is shown in Figure 4.16. The lower reflector frame (shown in Figure 4.16) can be separated easily from the upper reflector frame (shown in Figure 4.17).

The combination of two is shown in Figure 4.18. The modular design would allow to do further experiment on different component of CTAH system. The dimensions of unit upper reflector support have been shown in Figure 4.16. The unit frames (18 mm thick) are placed parallel to each other as shown in Figure 4.18.

The frames were attached on the base wood (18 mm thick) of CTAH collector. A piece of wood (10 mm thick) was attached across the back of the upper reflector frames. The lower end part of upper reflector frame unit is thin and there is strong possibility to damage this part during fabrication process. A thin slot (12 mm thick) has been provided at the back of unit upper reflector frame. The top support in Figure 4.17 should be strong enough to hold the upper reflector frame unit and reflector.

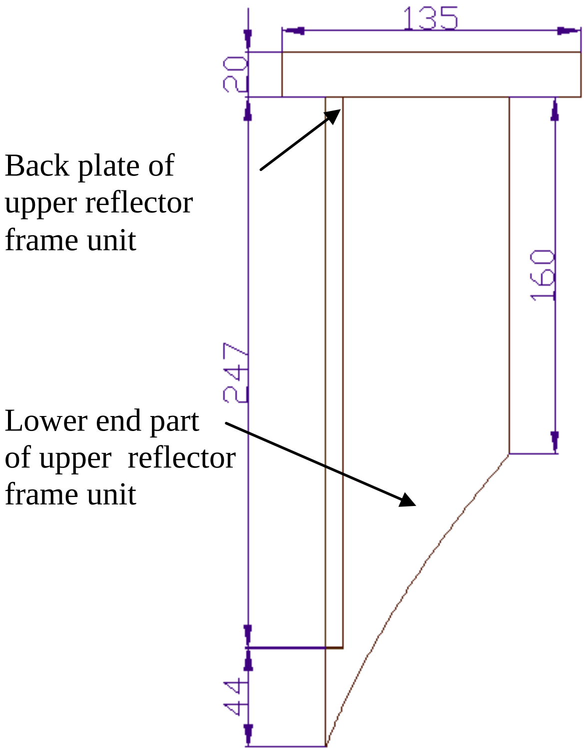

Figure 4.16: Unit upper reflector support

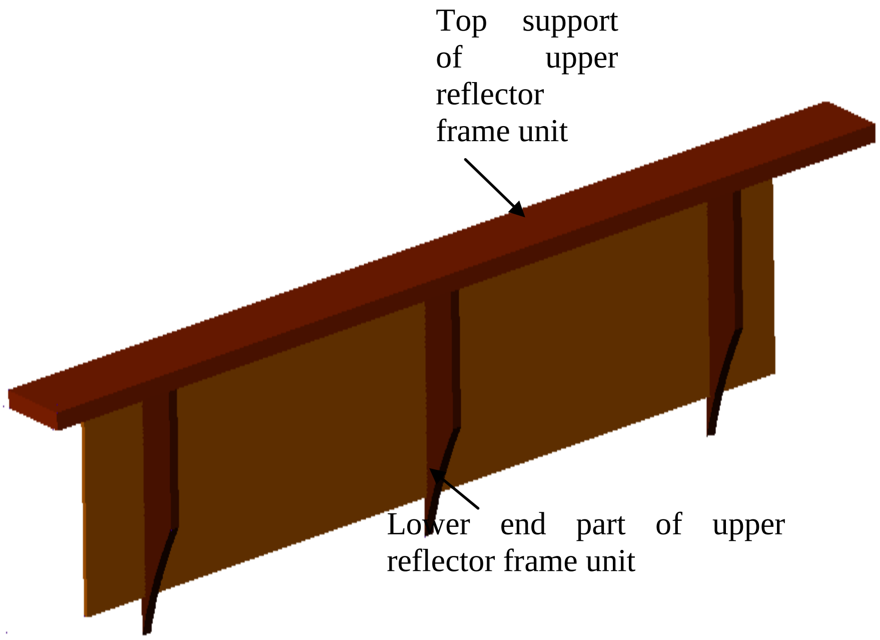

Figure 4.17: 3D view of upper reflector frame

A stronger wood of 20 mm was used in CTAH. The combination of upper Reflector frame, lower reflector frame, air duct and absorber frame has been shown in Figure 4.18. This is basically the skeleton of the CTAH.

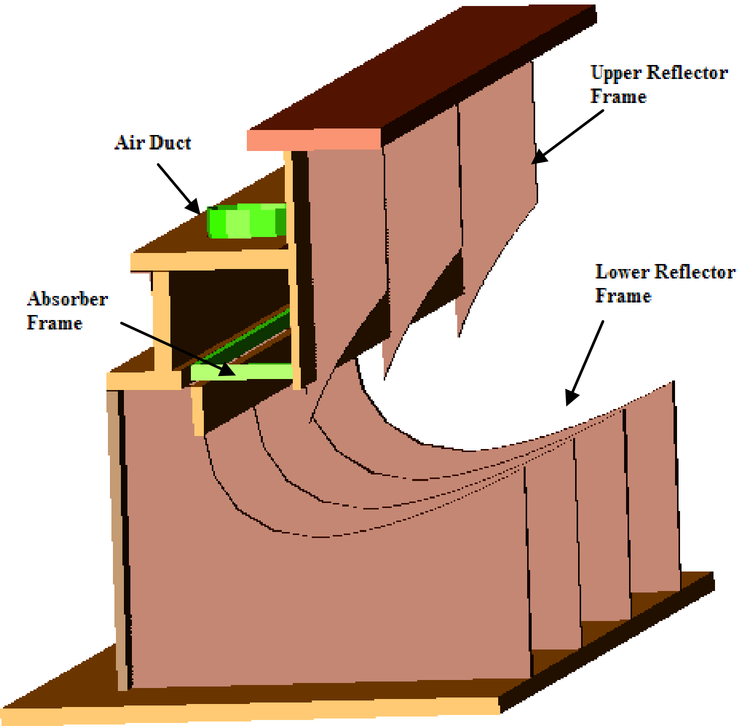

Figure 4.18: Combination of upper reflector frame, lower reflector frame, air duct and absorber frame

The end gap of different parts were filled with silicon sealer to make it air tight. The top cover of the air duct was attached with help of two angle bar and it can be removed to work inside air duct or absorber frame. The insulation material was sited over the skeleton wooden frame of the lower and upper reflector frames. The insulation material works as substrate of the reflector material. The diameter of the inlet and outlet duct is identical (100 mm). The hot glue and silicon sealer were used as necessary to ensure the ducts to be leak prove. The outlet surfaces of the ducts were insulated with thermal wrap.

The cavity geometry of CTAH is complex and it is difficult to calculate pressure difference and change of flow rate at the end of each geometric shape change from primary concentrator, secondary reflector and tertiary reflector. So the pressure measurements were carried out between inlet and outlet of the collector. A 3D view of the CTAH system is shown in Figure 4.19.

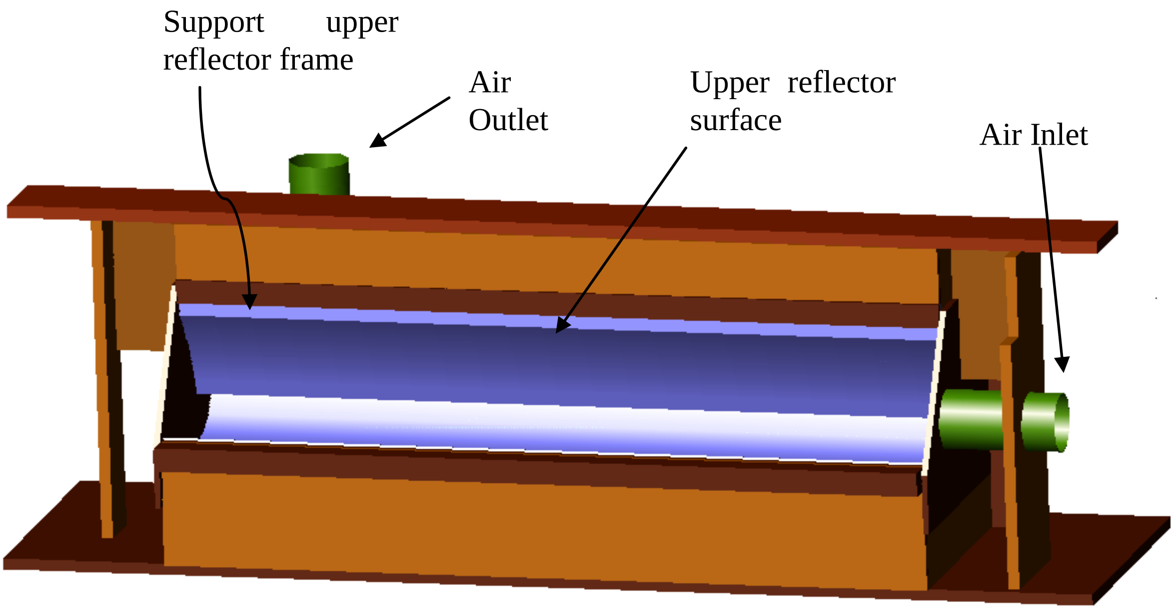

Figure 4.19: 3D view of the CTAH system

The inlet and outlet of the system are equal and constant air flow rate was maintained for the day of experiment. Two wooden supports of 18 mm are used to support upper reflector. It is important to confirm that the support do not create any shade on CTAH aperture.

4.6.2 CTAH fabrication

Two prototypes of CTAH were constructed. The first prototype of CTAH was constructed with a vertical aperture. The aperture of the second prototype was inclined at 53^{o} (same as the latitude of Dublin). The dimensions of separate parts of CTAH are provided in Apendix 3. The experiments of the CTAH were carried out for closed loop CTAH and open loop CTAH with or without glazing surface. The fabrication of the CTAH was carried out in the DIT laboratory.

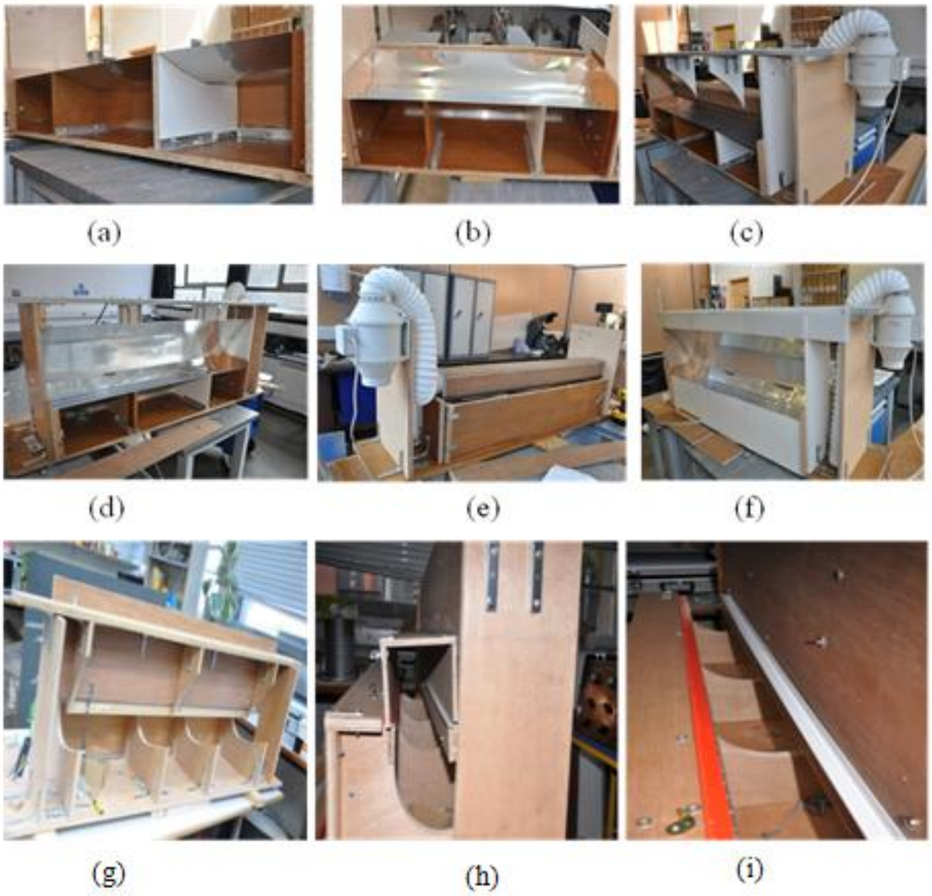

Figure 4.20: Fabrication of second prototype

The Figure 4.20 shows, different stage of CTAH construction. Figures 4.20 (a) to 4.20 (f) show the construction of the first prototype. Figures 4.20 (g) to 4.20 (i) show the second CTAH prototype. The each individual frames were manufactured separately using the designs detailed in section 4.6.1 and were assembled on a base wooden surface. A protective cover was used at the outer surface of the CTAH to protect the system during outdoor experiments.

4.7 Summary

The concept design and fabrication of outdoor experimental prototypes of Concentrating Transpired Air Heating (CTAH) system has been detailed in this chapter. Different parts of the CTAH system have been designed as subsystems and a physical system prototype has been constructed as integration of subsystems. This chapter outlined the selection criteria of component materials, design process and the fabrication process of the system. The basic system components of CTAH are perforated absorber, concentrator and glazing cover.

Carbon fibre weave was the optimum absorber material for the collector considering its properties of the material and the inherent perforation. High reflectance (95% reflectivity) mirosun reflector from a company ‘Alanod’ was selected as the reflector material. Low iron opti-white glass of 6 mm with 88% transmittance was selected as the glazing cover. ‘Thermawrap’ insulation of 4mm thickness was used in the CTAH as an insulation material. This is a durable thick bubble with high reflective foil facing to each side. Thermal resistance is 1.455 m^2K/W (equivalent to 65mm of Polystyrene according to company ‘Thermawrap’). The prototypes were made with wooded frame. A plastic cover was used as the projector cover during outdoor experiment.

CHAPTER 5

THERMAL PERFORMANCE ANALYSIS AND EXPERIMENTAL CHARACTERISATION OF CTAH

The objective of this chapter is to undertake a thermal performance analysis and characterise the outdoor experimental performance of the Concentrating Transpired Air Heating (CTAH) system. The outdoor experiments were carried out in two stages using two prototypes. The prototypes of the experimental setup were constructed and tested in Dublin Institute of Technology, Ireland. Specific objective of the chapter include to:

- Present the methodology used
- Describe the data collection procedure and equipment used
- Evaluate the performance of the CTAH in open and closed loop configuration
- Characterise the thermal performance of CTAH collector
- Comparison of thermal performance with glazed and unglazed air heating collector

5.1 Introduction

This chapter presents results of the thermal performance of glazed and unglazed CTAH operating under different air flow rates. The CTAH was developed as an integration of non-imaging Asymmetric Compound Parabolic Concentrator (ACPC) and a transpired absorber which provides a higher optical concentration of incident radiation on the inverted transpired absorber to deliver heated air at higher temperature than conventional transpired collectors.

The question to be answered was how the CTAH system would perform under typical Irish weather conditions characterised by intermittent sunshine, fluctuations of wind speed and dust deposition. It was expected that the absence of a glazing cover would increase the optical efficiency due to reduced reflection and absorption losses on the glazing cover. However, the efficiency of the CTAH was reduced by cross winds which caused reverse flow and an unstable thermal layer in the concentrator cavity without any tertiary section. An improved design of the CTAH was developed that included glazing cover at the aperture and optically optimised tertiary height as described in chapter 3.

5.2 Methodology

Initially, experiments were carried out for an open loop system design without any tertiary reflector section for both glazed and unglazed conditions. In the second stage, experiments were carried out for glazed closed loop system design with an optimised tertiary reflector section. In first prototype, the system aperture was designed at normal from the ground with geometric concentration ratio 3. The absorber was 50% perforated aluminium mesh.

The second prototype was build with a glazing cover and an optically optimised (as presented in chapter 3) integrated tertiary section to create heat pocket just below the transpired absorber which was investigated at different flow rate and weather conditions. The black carbon fibre absorber was used with inherent perforation. The design and characterisation of individual materials of different system elements of CTAH was presented in chapter 4. After experiments on the first prototype, it was found in the experiments that the glazing need to be covered to avoid regular maintenance to clean dust deposition and water particles. A tertiary section was also necessary to stabilize the thermal layers below absorber surface. The corrections in design were incorporated in the second prototype design. The experimental results of second prototype was carried out for experimental characterisation of CTAH and performance comparison were carried out with other solar air heating collectors.

The guideline for required ventilation rate for domestic dwelling was suggested by Environ building standard (Environ, 2009) which was discussed in section 7.3. This flow rate can be calculated considering number of occupants (5 l/s per person) or floor area (0.3 l/s per m^2 internal floor area). The minimum flow rate was calculated as 0.03 $kg/s/m^2$ considering 5 occupants and the highest flow rate was calculated as 0.09 $kg/s/m^2$ considering 250 m^2 floor area of a dwelling.

5.3 Thermal performance analysis of the CTAH

The thermal performance of the CTAH was analysed by evaluating the energy collected, energy delivered and collector efficiency.

5.3.1 Energy delivered

The useful energy delivered by the solar collector was calculated using Equation 5.1 (Duffie & Beckman, 2006; Kalogirou, 2009). The ambient air temperature was considered as the inlet air temperature in the open loop collector.

$$Q_u = \dot{m}_{air} C_{pair} \left(T_{out} - T_{in} \right) \tag{5.1}$$

$$q_u = \frac{Q_u}{A_{apt}} \tag{5.2}$$

Where,

Q_u = rate of useful energy delivered (W)

q_u = rate of useful energy per aperture area (W/m^2)

$\dot{m}_{air}$ = mass flow rate of air (kg/s)

C_{pair} = specific heat capacity (kJ/kgK)

T_{out} = air temperature at collector outlet (^{o}C)

T_{in} = air temperature at collector inlet (^{o}C)

A_{apt} = aperture aperture (m^2)

5.3.2 Collector Efficiency

The instantaneous efficiency η of a solar thermal collector can be defined as the ratio of the useful heat $\dot{Q}_u$ delivered per aperture area and the insulation I_{global} which is incident on the aperture.

$$\eta = \frac{\dot{Q}_u}{A_{apt} I_{global}} = \frac{\dot{q}_u}{I_{global}} \qquad 5.3$$

The useful heat is related to flow rate ($\dot{m}_{air}$), specific heat (C_{pair}) and inlet (T_{in}) and outlet (T_{out}) temperatures. The efficiency of the collector was calculated using Equation 5.4 (Duffie & Beckman, 2006):

$$\eta_{collector} = \frac{\dot{m}_{air} C_{pair} \left(T_{out} - T_{in}\right)}{A_{apt} I_{global}} \qquad 5.4$$

$\eta_{collector}$ = collector efficiency (dimensionless)

I_{global} = global solar irradiance (W/m^2)

5.3.3 *Collector Effectiveness*

The effectiveness of a solar thermal collector can be defined as the ratio of the absorber temperature increase to outlet air temperature increase (Duffie & Beckman, 2006; Kutscher et al., 1993).

$$\varepsilon_{collector} = \frac{\Delta T_{outlet}}{\Delta T_{absorber}} \qquad 5.5$$

Where,

ΔT_{outlet} = Outlet air temperature rise (^{o}C)

$\Delta T_{absorber}$ = Absorber temperature rise (^{o}C)

5.3.4 *Characteristic Equation*

Characterisation of solar thermal collectors entails determining the efficiency and heat losses under well-defined operating conditions. The efficiency of a solar thermal collector depends on many factors which include collector temperature, ambient air temperature, insulation, mass flow rate and incident angle of radiation. It decreases with increasing temperatures because of increasing losses. A general equation for the instantaneous solar collector efficiency is given by Duffie and Beckman (2006) as:

$$\eta_{collector} = F_R \left[\left(\tau\alpha\right)_{collector} - U_L \left(\frac{T_{out} - T_{amb}}{I_{global}} \right) \right] \qquad 5.6$$

$$F_R = \frac{\dot{m}_{air} C_p (T_{out} - T_i)}{A_{apt} \left[I_{global} \left(\tau\alpha\right)_{collector} - U_L (T_{out} - T_{amb}) \right]} \qquad 5.7$$

Where,

F_R = heat removal factor (dimensionless)

U_L = overall collector heat loss coefficient

$(\tau\alpha)_{collector}$ = collector transmission absorber absorption product (dimensionless)

5.4 Data collection and equipments used

The experimental setup used in field trial consisted of an outdoor test facility fully instrumented for air collector testing. Wind speed, ambient temperature, input air temperature, output air temperature, ambient temperature, absorber surface temperature, tertiary cavity air temperature, air flow rate, glazing surface temperature, solar radiation on the surface of the aperture and on horizontal surface were measured.

Solar radiation is strongly dependant on location and local weather so it is necessary to measure the available solar insolation for the test site. The incoming radiation was measured by a Kipp & Zonen CM6B pyranometer with a maximum spatial intensity distribution of ±2%**.** The inlet air, outlet air, tertiary section air and absorber plate temperatures, were measured using type T (Cu-CuNi) PTFE insulated twist fine wire thermocouple sensor with accuracy of ±0.5^{o}C.

All measurements were recorded at 1 minute intervals with a DL2e data logger. The data logger was connected directly to a computer where data was downloaded, read and extracted via a USB port. A small wind transmitter anemometer with accuracy of ±5% was used to measure wind speed. Inlet air flow rate was measured using an extech thermo anemometer with accuracy of ±5%. All thermocouples were labelled, inserted in a plug and connected to the data logger.

5.5 Performance of unglazed open loop collector without tertiary section

5.5.1 System description

The open loop experiment was carried out using prototype 1. The technical specifications of prototype 1 are shown in Table 5.1.

Table 5.1: Technical specifications of prototype 1

Absorber material	Absorber porosity (%)	System type	Tertiary height (mm)	Air flow ($kg/s/m^2$)	
				high	low
Aluminium	50	Open loop	0	0.06	0.03

A schematic diagram of the open loop experimental setup has been shown in Figure 5.1. The ambient air was extracted through the perforated absorber using a pump. A control valve was used to control the flow of the outlet air. Air was drawn using a fan through the open aperture of the CTAH and perforated absorber to the outlet of the collector.

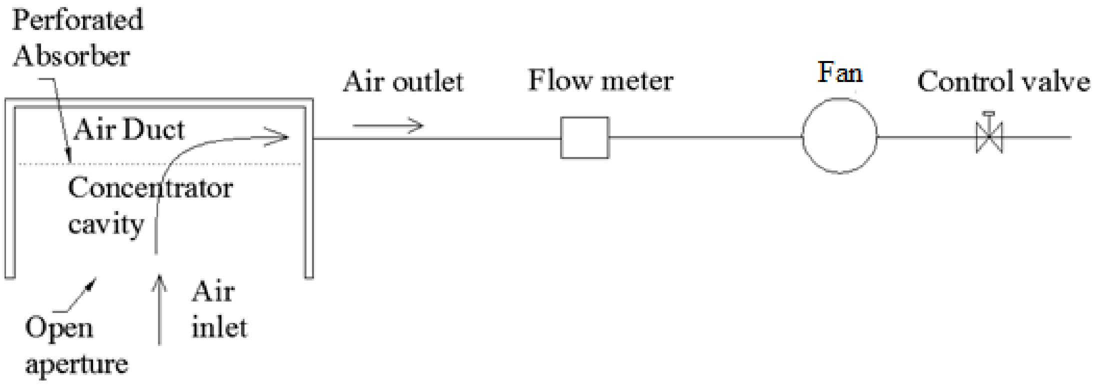

Figure 5.1: Open loop experimental setup

5.5.2 *Experimental results for open loop unglazed collector*

The thermal performance of the open loop unglazed CTAH is presented in Table 5.2. The field trials were conducted for the unglazed system without a tertiary collector between 22-29th August in 2010 at air flow rate 0.06 $kg/s/m^2$. Average efficiency and effectiveness were calculated using equations 5.4 and 5.5.

Table 5.2: Summary of experimental results for the unglazed system without a tertiary collector for prototype 1

Experiment Date	Average radiation (W/m^2)	Average absorber temperature (°C)	Average outlet temperature (°C)	Average ambient temperature (°C)	Average efficiency (%)	Effectiveness (%)
22-Aug	524.8	31.1	24.3	21.0	16.2	32.7
23-Aug	429.1	24.2	19.6	16.1	21.4	43.2
24-Aug	465.0	28.3	22.8	19.3	15.8	38.9
27-Aug	438.0	30.5	23.6	20.7	13.4	29.6
29-Aug	642.4	31.7	24.8	19.7	17.0	42.5

The results showed that the average absorber temperature and outlet temperature increased with increased radiation. The average daily solar radiation varied between 429.1 W/m^2 and 642.4 W/m^2 on the 23rd August and 29th August respectively. The average daily efficiency varied between 13.4% and 21.4% between 23 -27th August, 2010. The average absorber temperature varied between 24.2°C-31.7°C on the 23rd August and 29th August respectively. The average ambient temperature varied between 16.1°C-21°C, between 22nd and 23rd August. The average outlet air temperature varied between 19.6°C and 24.8°C on the 23rd August and 29th August respectively. The effectiveness varied between 29.6% and 43.2% on 27th August and 23rd August.

The experiments were carried out at an air flow rate of 0.06 kg/s/m^2 from 10 am to 5 pm between 22-29th August, 2010. The overall thermal efficiency of the system was 25.8%. A typical Irish day is a combination of sun, cloud and wind.

The performance of the collector without glazing and tertiary section on 25th August, 2010 is shown in Figure 5.2. The results were affected by various uncontrollable factors, such as: absence of glazing surface at the aperture, high perforation (50%) of the absorber and absence of tertiary height.

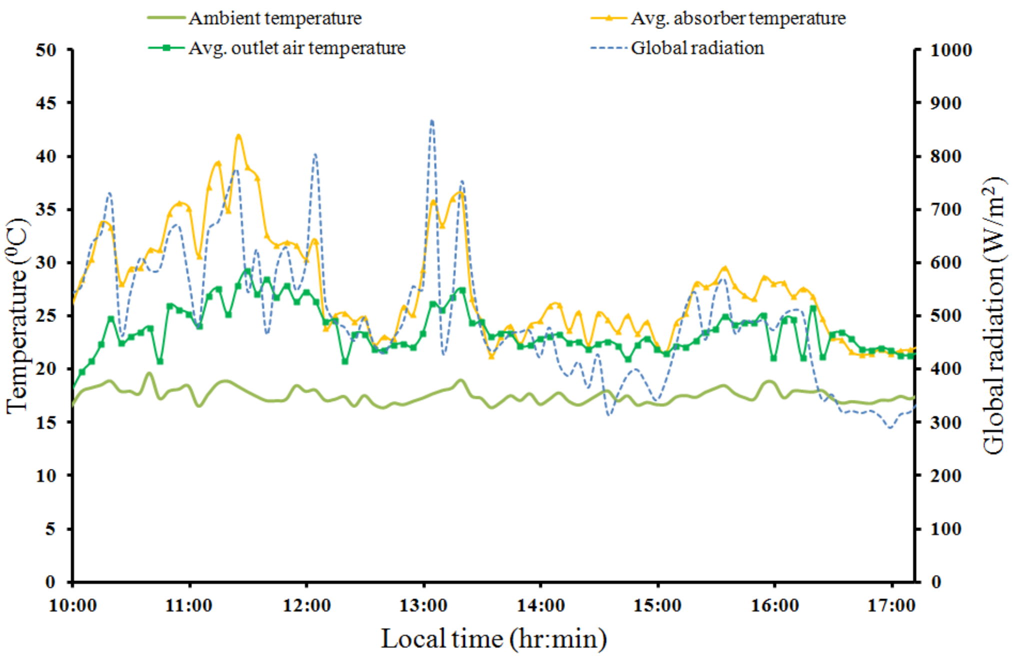

Figure 5.2: Performance of open loop collector for prototype 1 without glazing and tertiary section at air flow rate 0.06 kg/s/m^2

The day of 25th August represents one of the characteristic intermittent cloud cover day. The measured absorber temperature, outlet air temperature, and duct surface temperature followed a similar trend to that of measured radiation. The solar radiation on the aperture from 10am to 11.26am rose and fell over the period, but the trend was upwards from 557 W/m^2 to 771 W/m^2. After two sharp fluctuations, the radiation fell steeply and maintained an erratic behaviour between 300 W/m^2 to 500 W/m^2 until 5 pm. The average radiation was 504 W/m^2 between 10am and 5 pm. The ambient temperature fluctuated slightly over the period between 17.1° C and 18.1° C with an average 17.6° C.

The highest temperature of the absorber was 41.9° C at 11.26 am with an average 27.9° C between 10 am and 5pm. The average air temperature rise was 6.1° C with an average thermal efficiency 25.8% at air flow rate 0.06 kg/s/m^2. It was seen that on the 25th August, 2010, the maximum outlet air, absorber temperature and global radiation were 29.3°C, 41.9°C and 869.8 W/m^2 respectively with an average ambient temperature 17.6^o C. The temperature rise in CTAH experimental results on the 25th of August showed approximately 11.7^{o}C temperature rise at 869.8 W/m^2 and a flow rate of 0.06 kg/s/m^2.

*5.5.3 **Experimental results for open loop glazed collector** at high air flow rate*

The best option to avoid disturbance in the concentration cavity was to apply a glazing cover at the aperture. However, a 20 mm gap at the bottom of the glazing ensured air flow through the perforated absorber. The system was open looped with a glazing cover to reduce interference of uncertain wind speed, wind direction and rain. However, the effects could not be avoided totally due to the open loop system operation. Initially the system was operated at high air flow rate (0.06 kg/s/m^2) as in the previous experiment.

The absorber and outlet air temperatures increased due to the presence of the glazing cover. This led to an increase in the system's thermal efficiency. Table 5.3 shows a summary of the daily average performance of open loop glazed system without tertiary section at high air flow rate (0.06 kg/s/m^2). Average efficiency and effectiveness were calculated using equations 5.4 and 5.5.

Table 5.3: Summary of experimental results at high air flow rate for open loop glazed system for prototype 1 without tertiary section

Experiment Date	Average radiation (W/m^2)	Average absorber temperature (^{o}C)	Average outlet temperature (^{o}C)	Average ambient temperature (^{o}C)	Average efficiency (%)	Effectiveness (%)
30-Aug	624.1	37.3	29.5	18.7	36.2	58.1
31-Aug	543.4	34.5	29.0	19.5	36.6	63.3
01-Sep	463.0	29.6	26.3	19.6	30.2	67.0
02-Sep	580.1	37.3	31.2	21.7	33.2	60.9
03-Sep	564.7	34.4	28.3	21.5	24.7	52.7

The field trials were conducted from 30th August to 3rd September in 2010. The results show that the average absorber temperature and outlet air temperature increased with solar radiation. The average solar radiation varied between 463 W/m^2 and 624.1 W/m^2. The average efficiency varied between 24.7% and 36.6%. The average absorber temperature varied between 29.6^{o}C and 37.3^{o}C. The average ambient temperature varied between 18.7^{o}C and 21.7^{o}C. The average outlet air temperature varied between 26.3^{o}C and 31.2^{o}C. The effectiveness of the collector varied between 52.7% and 67.0%.

The maximum daily effectiveness increased due to glazing cover. The maximum effectiveness for open loop collector without glazing was 43.2% on 23rd August. The maximum effectiveness of open loop collector with glazing cover increased to 67% on 1st September with the same air flow rate (0.06 kg/s/m^2). The performance of the collector with glazing but without tertiary section at 0.06 kg/s/m^2 air flow rate on 31st August, 2010 has been shown in Figure 5.3.

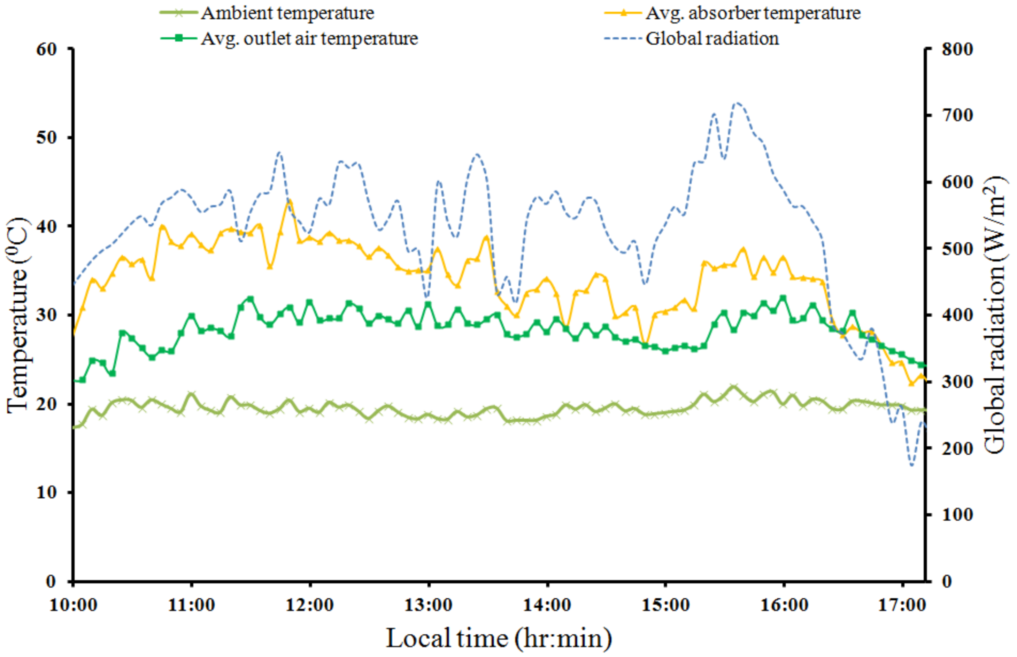

Figure 5.3: Performance open loop collector for prototype 1 with glazing and without tertiary section at flow rate 0.06 kg/s/m^2

The average thermal efficiency was 36.6% for an average radiation 543.4 W/m^2 and average ambient temperature 19.5°C. The average absorber temperature and outlet air temperature was 34.5°C and 29°C respectively.

5.5.4 ***Experimental results for open loop glazed collector** at low air flow rate*

The air flow rate (0.03 kg/s/m^2) was reduced to investigate the effect on system performance. Table 5.4 shows a summary of the daily average performance of open loop glazed CTAH system without the tertiary section at low air flow rate (0.03 kg/s/m^2). Average efficiency and effectiveness were calculated using equations 5.4 and 5.5.

Table 5.4: Summary of experimental results for open loop glazed system for prototype 1 without tertiary section at low air flow rate 0.03 kg/s/m^2

Experiment Date	Average radiation (W/m^2)	Average absorber temperature (°C)	Average outlet temperature (°C)	Average ambient temperature (°C)	Average thermal efficiency (η)	Effectiveness (%)
11-Sep	456.5	45.2	27.4	18.1	27.7	34.3
12-Sep	398.7	40.4	25.4	18.2	19.3	32.4
24-Sep	322.7	33.2	22.3	15.6	21.6	38.1
26-Sep	416.1	45.5	28.7	15.7	33.5	43.6
29-Sep	358.5	40.8	24.8	16.8	24.5	33.3

The absorber temperature and outlet air temperature increased significantly compared to the previous experimental cases. However, the thermal efficiency reduced due to lower air flow rate. The field trials were conducted from 11th September to 29th September in 2010. The results show that the average absorber temperature and outlet air temperature increased with solar radiation. Throughout the field trial period, the average solar radiation varied between 322.7 W/m^2 and 456 W/m^2.

The average ambient temperature varied between 15.6°C and 18.2°C. The system had average efficiency between 19.3% and 33.5%, absorber temperature between 33.2°C and 45.5°C and thus effectiveness varied between 32.4% and 43.6%.

It was found that the maximum effectiveness of the collector was higher (67%) with flow rate 0.06 kg/s/m^2 compare to the maximum effectiveness (43.6%) with air flow rate 0.03 kg/s/m^2.

However the maximum daily average absorber temperature was higher (45.5°C) at lower air flow rate compare to maximum daily average temperature (37.3°C) at higher air flow rate. This means the effectiveness and air flow rate are proportional between air flow rate 0.03 kg/s/m^2 to 0.06 kg/s/m^2. Figure 5.4 shows the performance of glazed open loop CTAH at low air flow rate (0.03 kg/s/m^2) on 26th Sept., 2010 at lower wind speed (average 1.6 m/s).

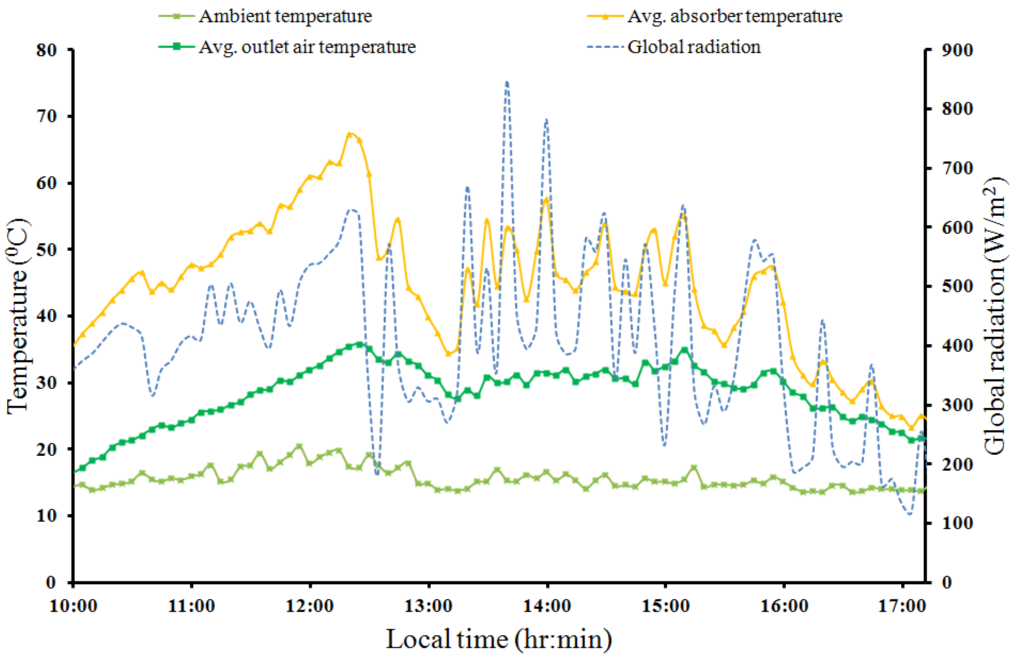

Figure 5.4: Open loop collector performances for prototype 1 at low air flow rate (0.03 kg/s/m^2)

The average thermal efficiency was 33.5% for an average radiation 416.1 W/m^2 and average ambient temperature 15.7^{o}C. The average absorber temperature and outlet air temperature was 45.5^{o}C and 28.7^{o}C respectively.

5.6 Performance of Glazed Closed loop collector with tertiary section

An optically optimised tertiary height (discussed in chapter 3) was integrated in the design in second prototype. Gunnewiek et al. (2002) analysed the effect of wind speed on UTC and recommended that the suction air flow should be increased during windy conditions to avoid reverse flow. If suction air flow cannot be increased, just have to accept the fact that there will be some reverse flow under high wind conditions. The air flow pattern was designed as cross flow in the closed loop CTAH collector. The effect of air flow on the air heating collector was discussed in chapter 2. The primary cavity was truncated and the tilt angle was 53^o which are equal to the latitude of the experimental location.

5.6.1 System description

The experiments were carried out for the close loop CTAH system. The technical specifications of prototype 1 are shown in Table 5.5.

Table 5.5: Technical specifications of prototype 2

Absorber material	Absorber porosity (%)	System type	Tertiary height (mm)	Air flow (kg/s/m^2)		
				low	medium	High
Carbon fibre	4.2	Closed loop	50	0.03	0.05	0.09

A schematic diagram of the closed loop experimental system CTAH has been shown in Figure 5.5. The inlet of the CTAH collector was connected with the air duct. The outlet of the CTAH collector was connected with a fan unit. The fan unit extracted air from the collector and supplied it to the air chamber. The air chamber and CTAH collector were connected with the air duct. Air flowed through the air duct to the collector. The integrated flow meter in the air duct measured the air flow rate.

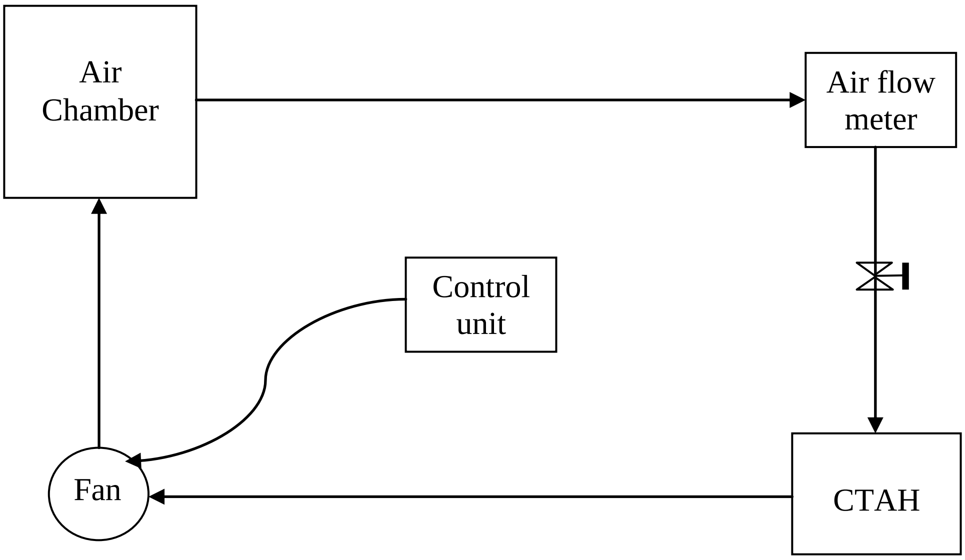

Figure 5.5: Closed loop outdoor experimental setup of CTAH

Figure 5.6 shows the CTAH with air inlet duct. Figure 5.7 shows the outdoor experimental setup with air chamber and the air fan unit. A waterproof plastic cover was used to protect the CTAH collector. The air flow meter was integrated with the air inlet duct. The input of the inlet duct and air chamber was connected with a flexible air duct.

The air chamber was protected and insulated with thermawrap insulation from the inside and outside walls as described in section 4.6.1. The fan was enclosed and protected from the environment during outdoor experiments.

Figure 5.6: Outdoor experimental setup with CTAH and long inlet duct

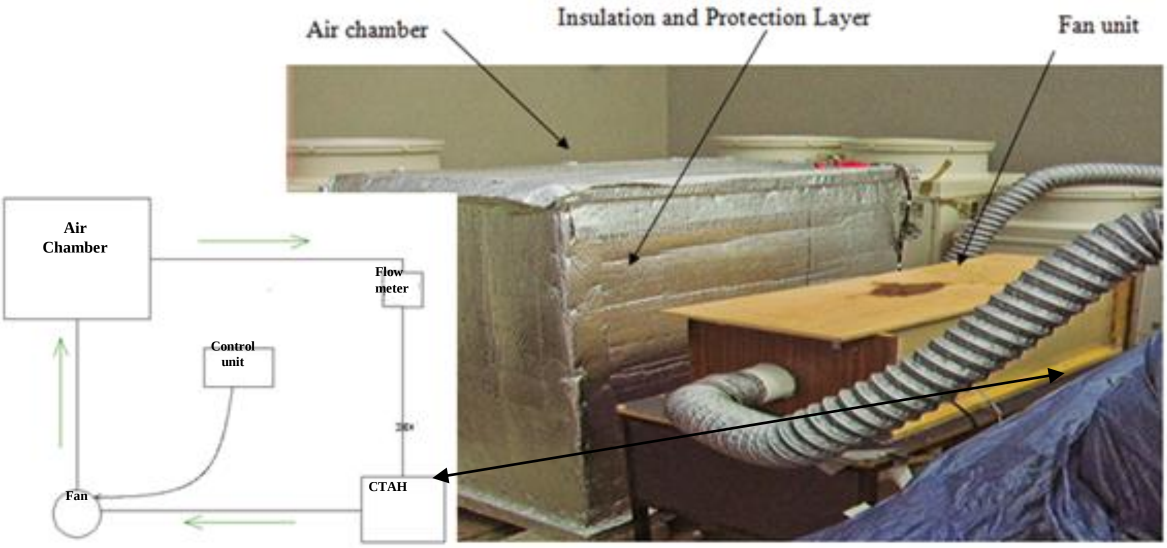

Figure 5.7: Outdoor experimental setup with the air chamber and fan unit

*5.6.2 **Experimental results** at zero air flow*

The instantaneous stagnation absorber temperature reached 135.9°C on 17th of August as shown in Figure 5.8. The absorber temperature and ambient temperature for CTAH are shown in Figure 5.8 for zero air flow rate (stagnation condition) on 17th August, 2011.

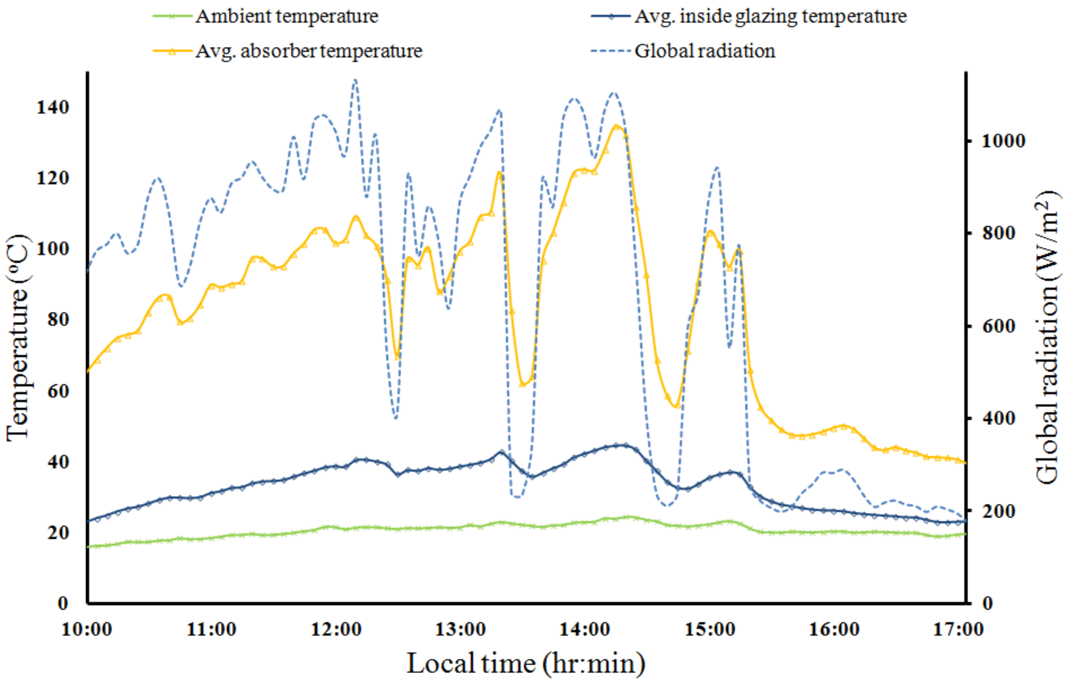

Figure 5.8: Absorber and ambient air temperatures of the CTAH for prototype 2 at zero flow rate

The entrance and exit of the CTAH were closed to conduct the stagnation experiment. The temperature of the glazing, air near glazing, air in tertiary cavity and the absorber surface were measured. The temperatures were measured over the day to investigate the effect of solar radiation variation over time.

The experimental results also indicated the maximum absorber temperature without air flow. The maximum glazing surface temperature was 45.3°C. The difference in temperature between the absorber and ambient air was 115°C. Most of the local sunny days were with intermittent cloud cover. Figure 5.9 shows the hourly stagnation performance of the CTAH on 17th August.

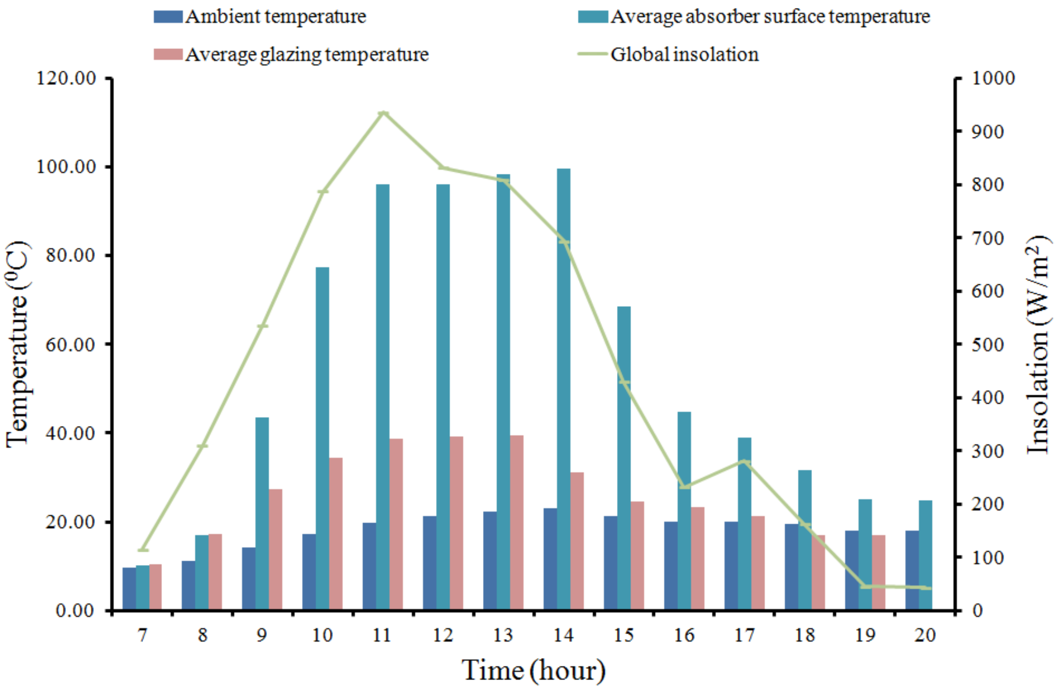

Figure 5.9: Hourly solar radiation, stagnation temperature of the absorber surface, glazing surface temperature for prototype 2 and ambient temperature

The day was sunny between 10 am and 2 pm. The maximum hourly absorber temperature reached 100°C with maximum hourly solar radiation of 900 W/m^2. As there was no air flow the heat loss through the glazing was highest and the absorber and glazing temperature reached the highest temperature. The air flow from inlet to outlet helps to keep the stratified thermal layer from absorber surface to glazing. This thermal layer reduces heat loss through glazing surface due to convection and radiation. Glazing temperature reduces as the air flow rate increases. The effect of flow on glazing temperature has been discussed in section 5.7.3 of this chapter.

*5.6.3 **Experimental results** at low air flow*

Table 5.6 shows a summary of the daily average performance of the closed loop glazed CTAH system with tertiary section at low air flow rate (0.03 kg/s/m^2). The field trials at low air flow rate (0.03 kg/s/m^2) for closed loop glazed CTAH system with tertiary section were conducted between 25-27th July in 2011. Average efficiency and effectiveness were calculated using equations 5.4 and 5.5.

Table 5.6: Summary of daily performance at low air flow rate for closed loop glazed system for prototype 2 with tertiary section

Expt. Date	Avg. radiation (W/m^2)	Avg. absorber temp. (^{o}C)	Avg. outlet temp. (^{o}C)	Avg. inlet temp. (^{o}C)	Avg. ambient temp. (^{o}C)	Avg. efficiency (η)	Effectiveness (%)
25-Jul	364.7	32.7	30.2	22.5	18.8	36.5	82.0
26-Jul	571.8	52.8	45.4	26.8	21.5	54.9	76.4
27-Jul	891.9	77.3	60.3	30.1	25.5	57.1	67.2

The results show that the average absorber temperature, outlet temperature and inlet temperature increased with solar radiation. The average solar radiation and ambient temperature varied between 364.7 W/m^2 and 891.9 W/m^2 and 18.8^{o}C and 25.5^{o}C on 25th July and 27th July respectively. The average thermal efficiency varied between 36.5% - 57.1% and effectiveness of the collector varied between 67.2% and 82%. It was found that the effectiveness was higher (82%) during low radiation level available (364.7 W/m^2) to the collector aperture.

However, effectiveness decreases to 67.2% with a higher radiation level (891.9 W/m^2). This reduction occurs due to higher thermal loss to the surrounding. The effectiveness of the closed CTAH was found to be higher compared to the open loop collector at low air flow (0.03 kg/s/m^2). The system performance is shown in Figure

5.10 at low air flow rate (0.03 kg/s/m^2) on the 27th July, 2011. The day was relatively sunny. The highest absorber temperature reached approximately 110°C at midday when the sky was clear from morning to mid day at average flow rate of 0.03 kg/s/m^2.

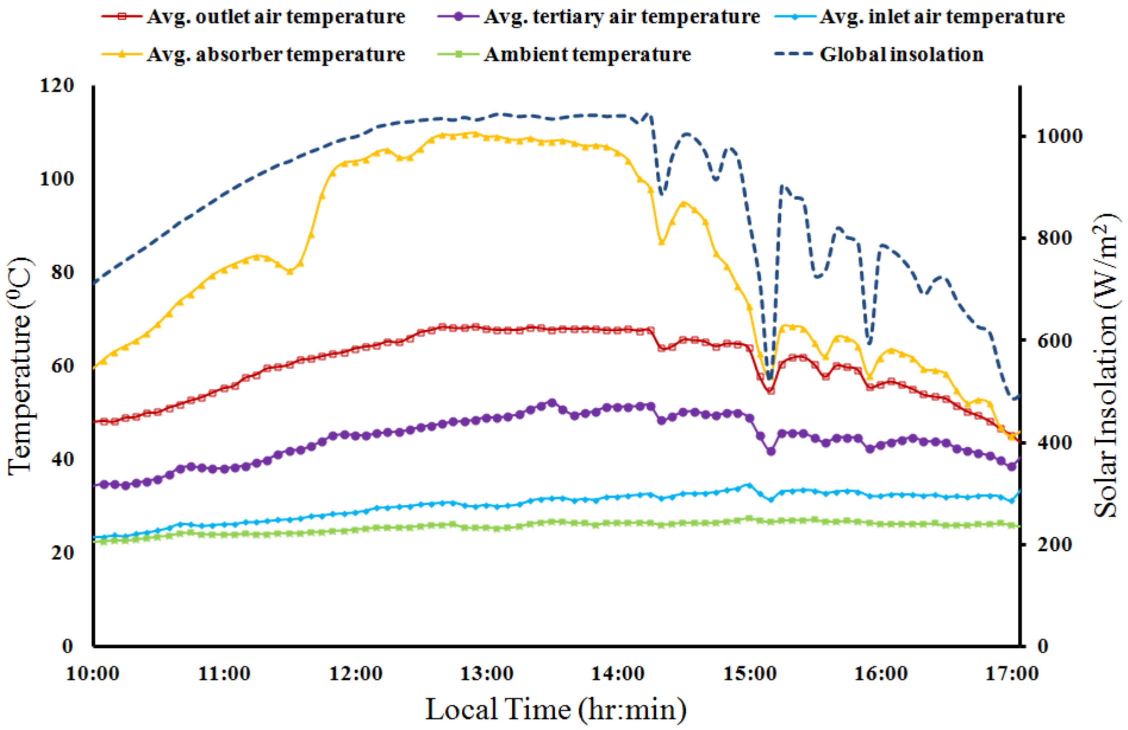

Figure 5.10: Solar radiation, absorber surface temperature, outlet air temperature, inlet air temperature and ambient temperature at air flow rate 0.03 kg/s/m^2 for prototype 2

The highest outlet air temperature at the same flow rate in CTAH was 67.92°C at an inlet temperature 31.09°C and ambient temperature 26.08°C. The outlet air temperature rise was 36.83°C from inlet air temperature and the temperature rise was 41.84°C from ambient air temperature.

The hourly performance is shown in Figure 5.11. The average hourly insolation available on a relatively clear sky day from 10am to 5pm was 3.21 MJ/m^2. The average hourly useful energy from the collector was 1.82 MJ/m^2 (see equation 5.1). The total available insolation for seven utilization hours was 22.47 MJ/m^2 and useful energy out of the collector was 12.9MJ/m^2 (see equation 5.1) and average thermal efficiency was 57%.

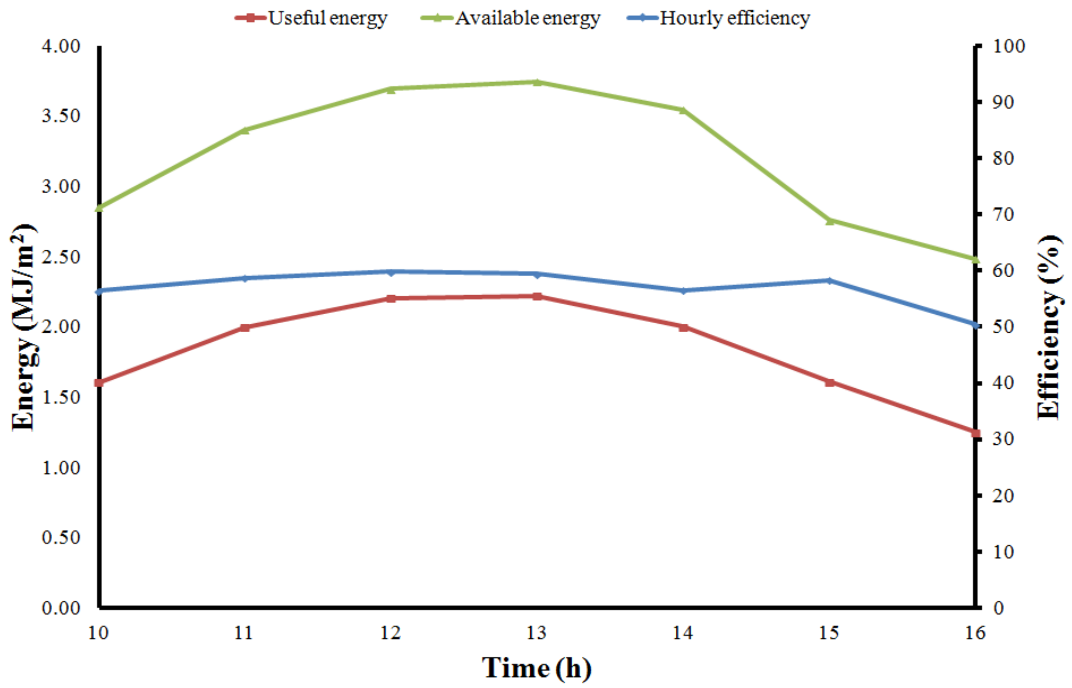

Figure 5.11: Available hourly insolation, useful energy and thermal efficiency at air flow rate 0.03 kg/s/m^2 for prototype 2

*5.6.4 **Experimental results** at medium air flow*

Table 5.7 shows a summary of the daily average performance of the closed loop glazed CTAH system with tertiary section at medium air flow rate (0.05 kg/s/m^2). The field trials at medium air flow rate (0.05 kg/s/m^2) for closed loop glazed CTAH system with tertiary section were conducted between 10-20th July in 2011. The results show that the average absorber temperature, outlet temperature and inlet temperature increased with solar radiation. Average efficiency and effectiveness were calculated using equations 5.4 and 5.5.

The average solar radiation varied between 348.3 W/m^2 and 905 W/m^2 on 10th July and 13th July respectively. The average ambient temperature varied between 18.7°C and 22.9°C on 14th July and 13th July respectively. The average inlet temperature varied between 22.8°C and 28.9°C on 14th July and 13th July respectively. The average thermal efficiency varied between 53.1% and 64.5%. The effectiveness of the collector varied between 75.2% and 85.5%.

Figure 5.12 illustrates solar radiation, absorber surface temperature, outlet air temperature, inlet air temperature and ambient temperature at medium air flow rate (0.05 kg/s/m^2) on 12th July, 2011.

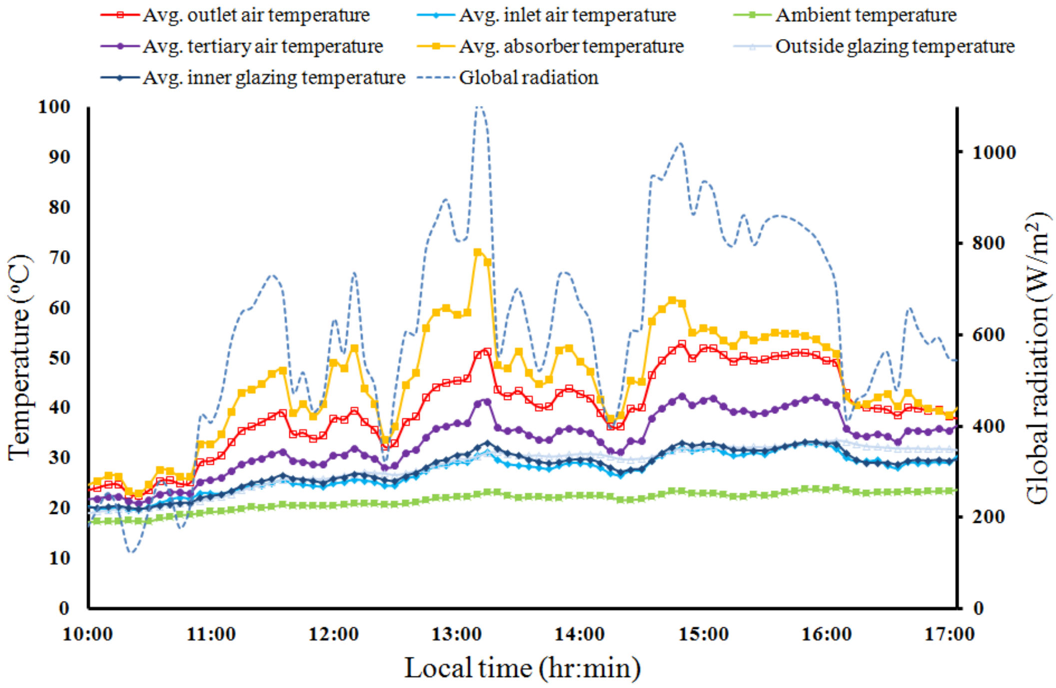

Figure 5.12: Solar radiation, absorber surface temperature, outlet air temperature, inlet air temperature and ambient temperature at medium air flow rate (0.05 kg/s/m^2) for prototype 2

The hourly performance of CTAH on 12th July has been shown in Figure 5.13. The average hourly insolation available on a day with intermittent cloud cover from 10am to 5pm was 2.2 MJ/m^2. The average hourly useful energy from the collector was 1.2 MJ/m^2.

Table 5.7: Summary of daily average performance for closed loop glazed system with tertiary section at medium air flow rate (0.05 kg/s/m^2) for prototype 2

Experiment Date	Average radiation (W/m^2)	Average absorber temperature (°C)	Average outlet temperature (°C)	Average inlet temperature (°C)	Average ambient temperature (°C)	Average efficiency (η)	Effectiveness (%)
10-Jul	348.3	32.0	30.2	23.4	19.6	53.1	85.5
11-Jul	556.5	41.3	37.7	26.2	21.2	56.1	82.1
12-Jul	612.9	43.5	39.7	27.2	22.4	54.6	82.0
13-Jul	905.0	60.4	51.1	28.9	22.9	64.5	75.2
14-Jul	451.4	34.5	32.0	22.8	18.7	55.2	84.2

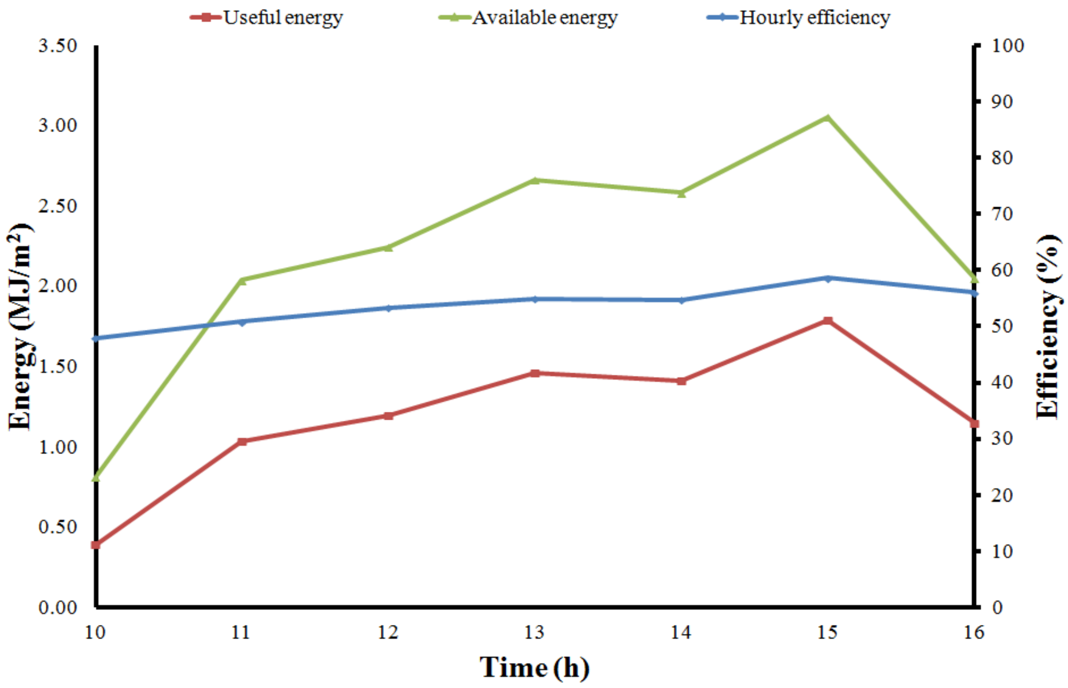

Figure 5.13: Available hourly insulation, useful energy and thermal efficiency at medium air flow rate (0.05 kg/s/m^2) for prototype 2

The total available insolation for seven utilization hours was 15.44 MJ/m^2 and useful energy out for the same period was 8.4 MJ/m^2 (see equation 5.1) with average thermal efficiency of 54.6%.

*5.6.5 **Experimental results** at high air flow*

Table 5.8 shows a summary of the daily average performance of the closed loop glazed CTAH system with tertiary section at high air flow rate (0.09 kg/s/m^2). The field trials at high flow rate (0.09 kg/s/m^2) for closed loop glazed CTAH system with tertiary section were conducted between 1-7th July in 2011. Average efficiency and effectiveness were calculated using equations 5.4 and 5.5.

The results show that the average absorber temperature, outlet temperature and inlet temperature increased with solar radiation. The average solar radiation varied between 413.8 W/m^2 and 743.8 W/m^2. The average ambient temperature varied between

19.7°C and 22.4°C. The average inlet temperature varied between 24.3°C and 26.6°C. The average outlet temperature varied between 29.4°C and 36.6°C. The average thermal efficiency varied between 53.7% and 65.3%. The effectiveness of the collector varied between 69.7% and 77.0%.

The system performance is shown in Figure 5.14 at high air flow rate (0.09 kg/s/m^2) on 5th July, 2011. The day was relatively sunny with intermittent cloud cover.

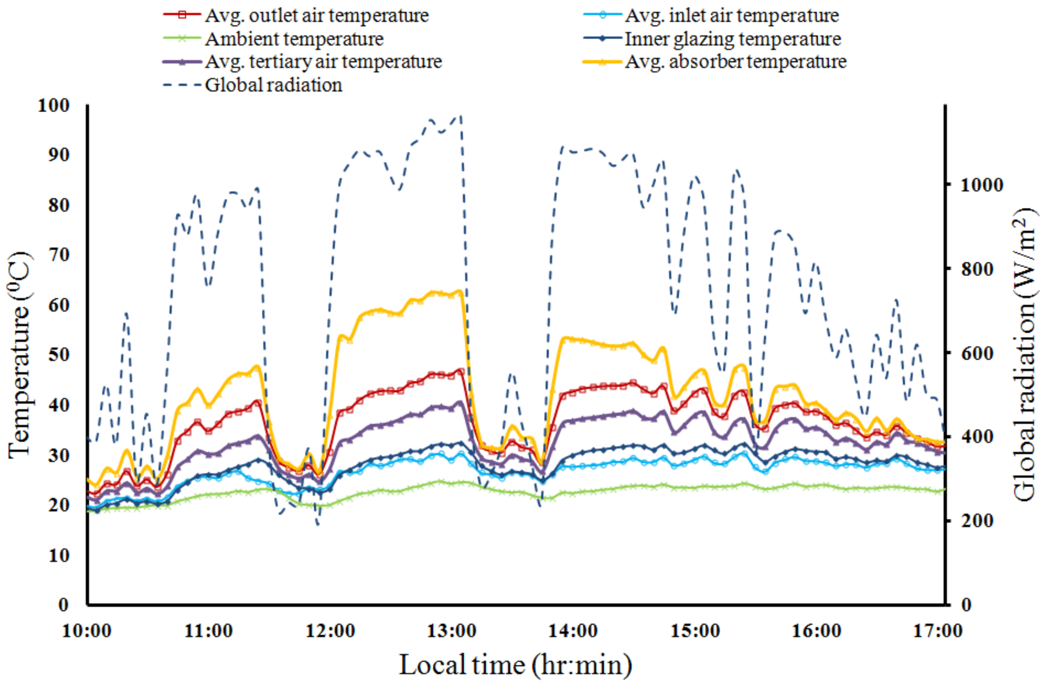

Figure 5.14: Solar radiation, absorber surface temperature, outlet air temperature, inlet air temperature and ambient temperature at high flow rate (0.09 kg/s/m^2) for prototype 2

The hourly performance of CTAH for which has been shown in Figure 5.15. The average hourly insolation available on a relatively clear sky day on 5th July, 2011 from 10am to 5pm was 2.67 MJ/m^2. The average hourly useful energy from the collector was 1.75 MJ/m^2. The total available insolation for seven utilization hours was 18.75 MJ/m^2 and useful energy out for the same period was 12.2 MJ/m^2 with average thermal efficiency 65.3%.

Table 5.8: Summary of daily average performance for closed loop glazed system with tertiary section at high air flow rate (0.09 kg/s/m^2) for prototype 2

Experiment Date	Average radiation (W/m^2)	Average absorber temperature (^{o}C)	Average outlet temperature (^{o}C)	Average inlet temperature (^{o}C)	Average ambient temperature (^{o}C)	Average efficiency (η)	Effectiveness (%)
01-Jul	541.1	34.5	30.9	25.2	19.7	53.7	75.7
02-Jul	413.8	32.2	29.4	24.3	20.0	59.8	77.0
05-Jul	743.8	42.5	36.4	26.6	22.4	65.3	69.7
06-Jul	581.6	37.3	32.9	25.5	21.3	63.4	72.5
07-Jul	681.0	40.3	35.4	26.5	22.1	64.6	73.1

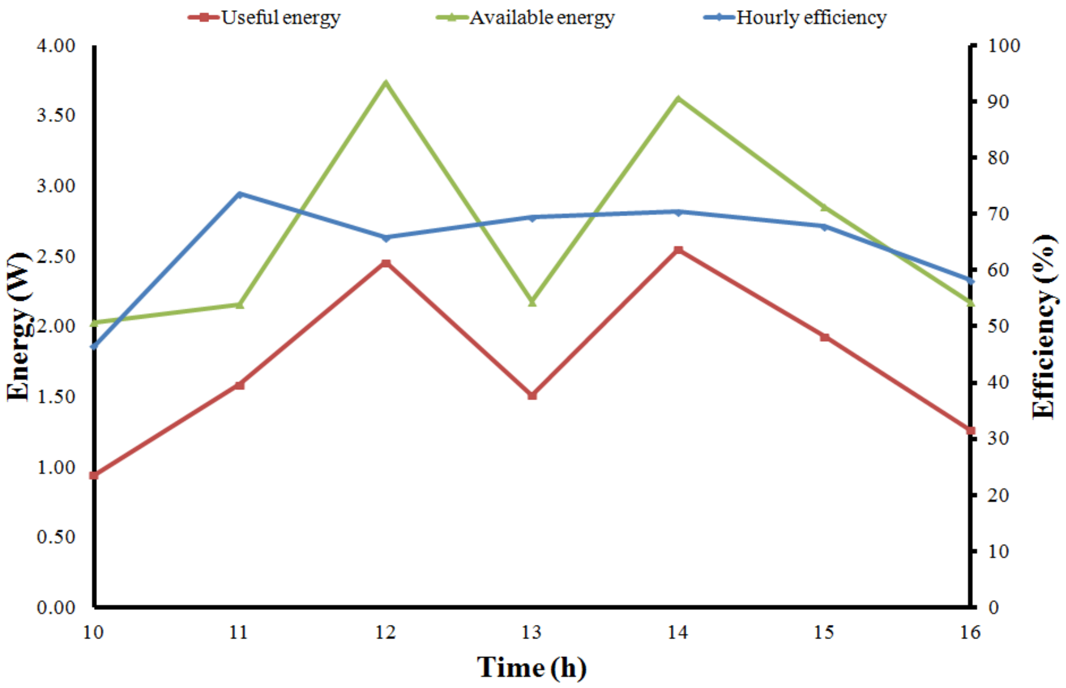

Figure 5.15: Average hourly insolation, useful energy and thermal efficiency at high flow rate (0.09 kg/s/m^2) for prototype 2

5.7 Effect of air flow rate

Air mass flow rate was identified as a parameter that had an effect on the performance of the CTAH system. Its effect on the cavity temperature, collector pressure difference and glazing temperature was investigated.

5.7.1 Effect on cavity temperature stratification

Stratification of the air temperature was consistent for different air flow rates inside the CTAH as shown in Figures 5.10 and 5.12. The outlet air temperature was always higher than the tertiary air section and the tertiary air temperature was always higher than the glazing temperature and inlet air temperature. The experimental system was closed loop so the inlet temperature was constantly higher than the corresponding ambient air temperature. The stratified thermal air layer reduced heat loss from the absorber to ambient through the glazing surface. A portion of optical heat loss through the reflector surface was recaptured as the air was flowing from the inlet to outlet.

5.7.2 Effect of flow rate on collector pressure difference

The CTAH system contains a thin perforated absorber with horizontal orientation which causes very low pressure difference between inlet and outlet. The unglazed transpired collector without concentrator requires a large surface area to be effective in heating outside air on a once through basis for ventilation or drying application. The critical issues of the UTC systems were the suction velocity which had to be very low, the plenum which should be wide and the plate's hydraulic resistance which should be relatively low to operate the heating system efficiently.

However, the conditions were fairly close to those corresponding to reverse flow (Gunnewiek et al., 1996). The pressure drop across the absorber plate has to be at least 25 Pa to ensure a uniform flow and temperature distribution over the UTC collector (Kutscher, 1997). If the temperature distribution is not uniform, hot spots could develop on the collector surface, which would increase the radiation loss to the surroundings (Kokko & Marshal, 1992) as referred by Leon and Kumar (2007).

Figure 5.16 shows the pressure drop measurement between the inlet and outlet of CTAH system at different air mass flow rates. The regression curve shows that the pressure drop as expected varies with the square of the air flow rate.

The pressure drop was relatively small (approximately 10 Pa) for a flow rate of 0.1 kg/s/m^2. Assuming that the combined efficiency of the electric motor and fan was only 20%, the resulting electric power consumption would be around 5.2 Watt for 1 m^2 of absorber area.

Again for an air flow rate of 0.2 kg/s/m^2, the electric power consumption for 1 m^2 absorber area is 8.3 W. The required power consumption for driving the flow through the CTAH collector is very small compared to the recovery energy. This information is very useful for design purposes.

In chapter 2 the performance of different solar air heating collectors were discussed. Double pass flow air heating collector showed higher efficiency compare to single pass air heating collector. Again introducing obstacles on the air flow passage further increased heat transfer between air and absorber surface resulting in an increase in thermal efficiency.

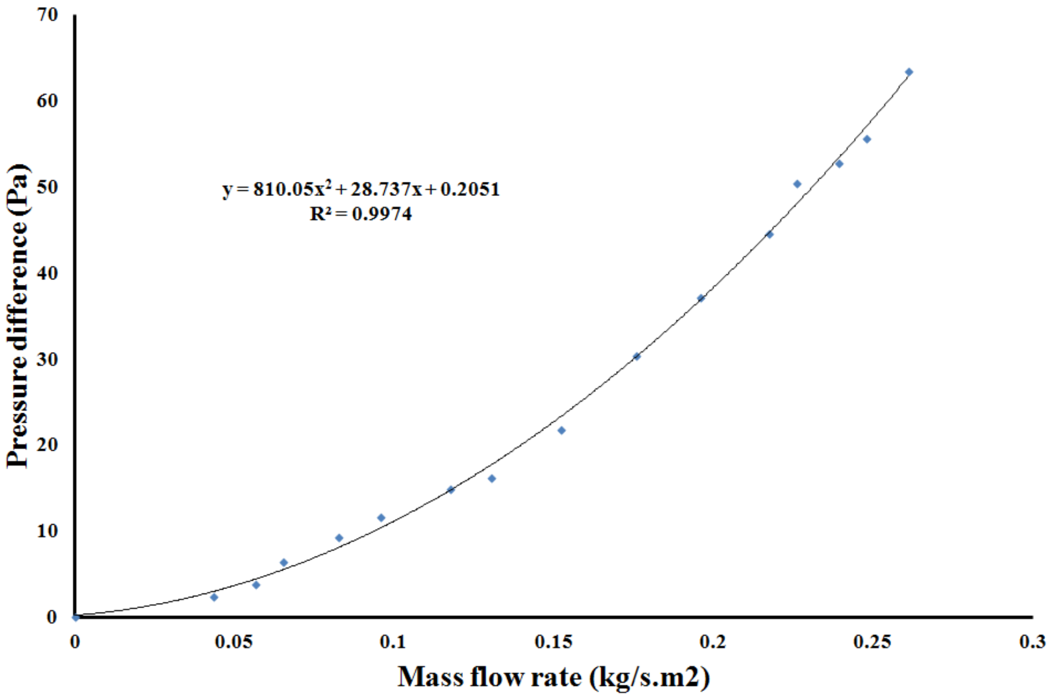

Figure 5.16: Measured pressure difference between inlet and outlet of CTAH for prototype 2

However, the pressure difference increased due to these system modifications which also increased operating cost of the air heating collector. Integrating fins with absorber surface is one of the ways to introduce the obstacle on the absorber surface.

The effect of using transverse fins on a double pass flow solar air heater with wire mesh as an absorber was reported by El-Khawajah et al. (2011).

The average daily efficiency increased with the number of fins with 2 and 4 fins having efficiencies of 68.9% and 75.3% respectively at an air flow rate of 0.04 kg/s/m^2. However, the maximum pressure differences for 2 and 4 fins were 76 Pa and 82 Pa. The pressure difference was approximately 7 to 8 times higher than that of the CTAH system with similar air mass flow rate.

5.7.3 Effect of air flow rate on glazing temperature

A conventional SAH consists of an absorber plate and a transparent cover. Major heat losses from flat plate SAH are found to be through the glazing cover (El-Khawajah et al., 2011). The CTAH system:

(i) is an integration of a concentrator and a perforated absorber,

(ii) has the absorber and the glazing surface separated by the concentrator which reduces losses through the aperture,

(iii) has the inverted horizontal perforated absorber and air flows through the absorber perforation which reduces convection loss between the absorber and glazing and

(iv) has a defined stratified thermal layer in the vertical tertiary section and cavity air minimises heat loss from the absorber to glazing.

For a natural convection mode, the inner glazing surface temperature was maximum approximately 70^{o}C with maximum absorber temperature of approximately 100^{o}C at an average ambient temperature of 34.8^{o}C. The average values of absorber, inner surface and ambient air temperatures from 10am to 5pm were 90.8^{o}C, 60.5^{o}C and 36.1^{o}C respectively. The glazing temperature rise was 24.5^{o}C when the absorber temperature rise was 54.8°C. The inner glazing surface temperature rise was 44.7% compared to absorber temperature rise which was much higher than CTAH.

The absorber temperature, inner surface glazing temperature and ambient temperature for the CTAH system are shown in Figure 5.17 for zero air flow rate (stagnation condition). Radiation loss from the absorber to the glazing should be highest when the absorber reaches its highest temperature. The highest absorber and glazing temperatures were 135.9 °C and 45.3 °C respectively.

Average values of absorber, glazing and ambient air temperatures were 83.1°C, 33.5°C and 20.7°C respectively. The glazing temperature rise from ambient was only 20.6% compared to the absorber temperature rise which was 44.7% in the case of a flat plate collector with natural air flow.

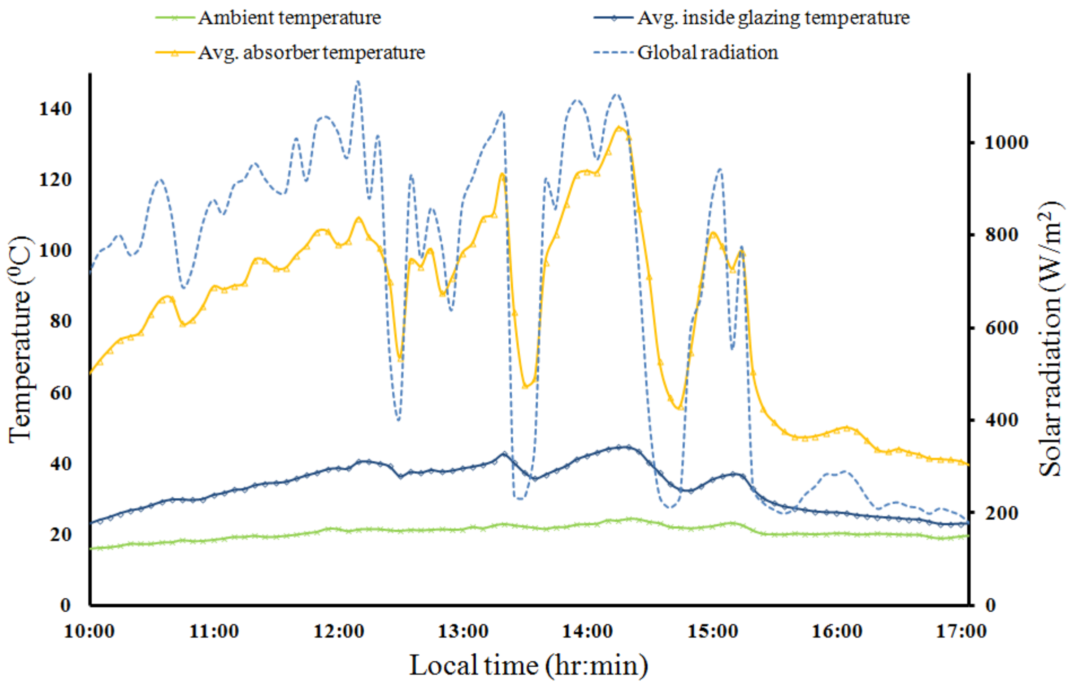

Figure 5.17: Glazing, absorber and ambient air temperatures of the CTAH at zero flow on 17th August, 2011 for prototype 2

The absorber temperature, inner surface glazing temperature and ambient air temperature for the CTAH system are shown in Figure 5.18 for a high flow rate (0.09 kg/s/m^2). The highest absorber, glazing and ambient temperatures were 62.5^{o}C, 32.4^{o}C and 24.7^{o}C respectively. The average absorber, glazing and ambient air temperatures were 42.1^{o}C, 27.9^{o}C and 22.5^{o}C respectively between 10 am and 5 am. The average temperature rise of the inner glazing surface compared to ambient air temperature was only 5.4 ^{o}C when the average absorber temperature rise was 19.6^{o}C. Compared to the inlet air temperature, the average temperature rise was only 8%. The inlet air flows over the glazing surface as it enters the concentrator cavity. As a result, the glazing temperature cools down more closely to the inlet air temperature.

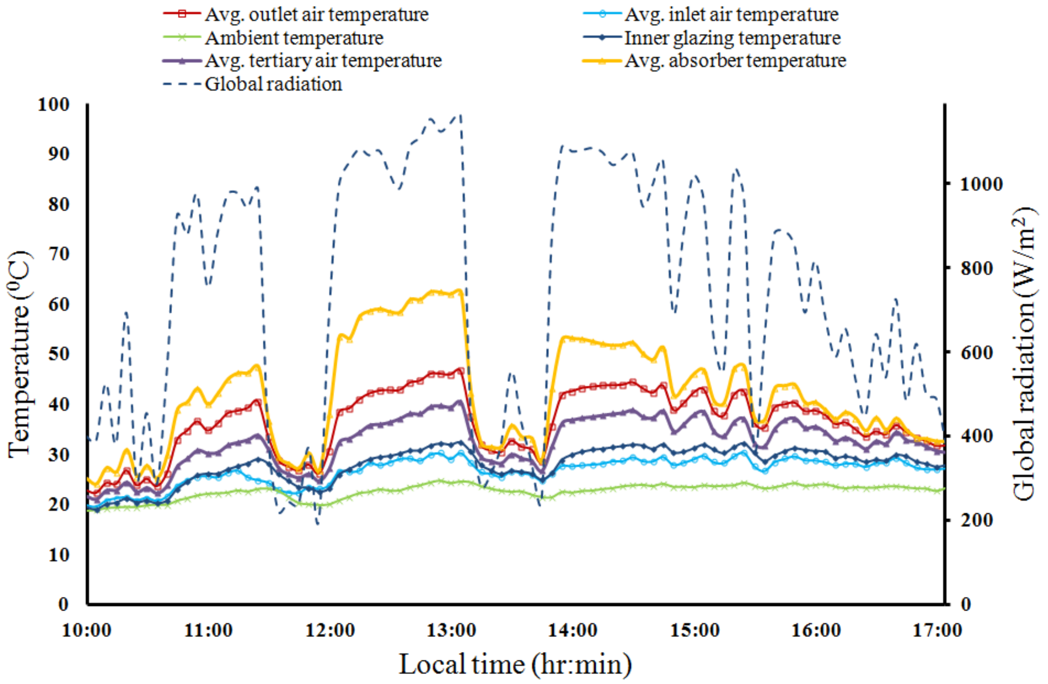

Figure 5.18: Glazing, absorber and ambient air temperatures of the CTAH at high flow (0.09 kg/s/m^2) on 5th July, 2011 for prototype 2

The absorber temperature, inner surface glazing temperature and ambient air temperature for the CTAH are shown in Figure 5.19 for a low flow rate (0.03 kg/s/m^2).

The day was mostly clear and sunny. The highest absorber, glazing and ambient air temperatures were 77.3°C, 38.3°C and 27°C respectively. The average temperature rise of the inner glazing surface compared to ambient air was only 9.2°C when the average absorber temperature rise was 51.8°C. Compared to the inlet air temperature, the average temperature rise was only 9.7%.

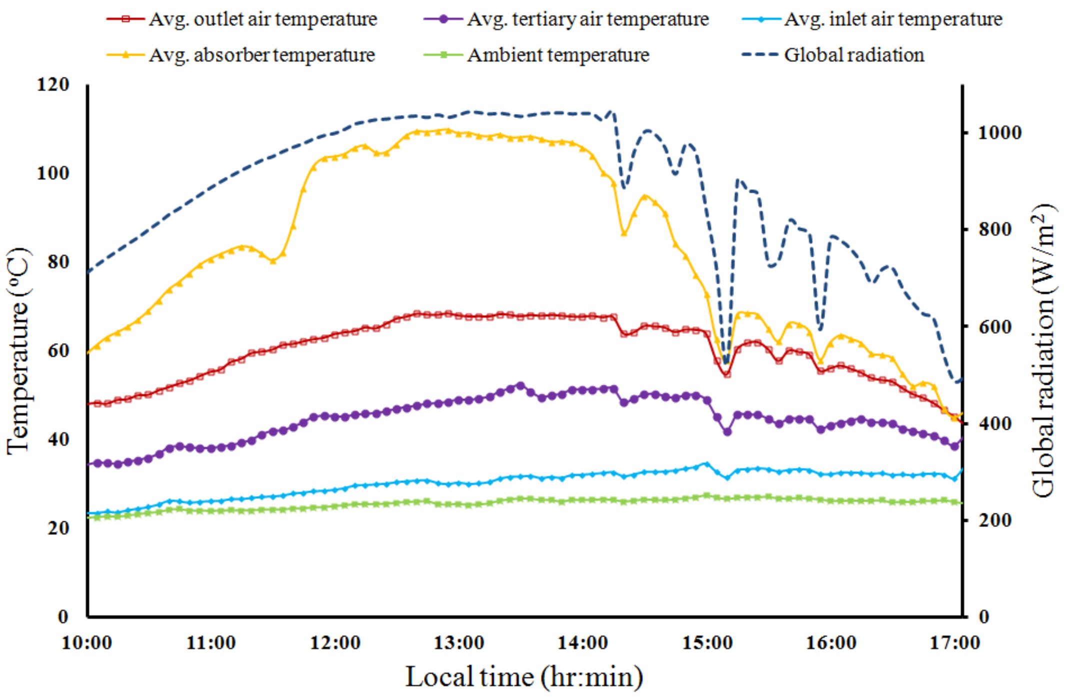

Figure 5.19: Glazing, absorber and ambient air temperature of the CTAH at low flow (0.03 kg/s/m^2) on 27th July, 2011 for prototype 2

5.8 Characterisation of the CTAH system

Equation 5.5 is based on the collector outlet temperature rather than the arithmetic mean temperature as is applicable to liquid collector. This is because in air heating collectors, the outlet air temperature rise can be up to 30°C to 40°C depending on the air mass flow resulting in a small amount of heat being transmitted from the absorber to the air. This results in a non-linear increase in the air temperature along the absorber plate resulting in the arithmetic mean collector temperature not being representative of the heat loss. The physical mean temperature of the collector is therefore often much closer to the outlet air temperature than the arithmetic mean temperature (Hastings & Morck, 2000; Struckmann, 2008).

If it is assumed that F_R, τ, α, U_L in Equation 5.6 are constants for a given collector then the efficiency is a linear function of the three parameters defining the operating condition: solar irradiance (I_{global}), fluid outlet temperature (T_{out}) and ambient air temperature (T_{amb}) (Struckmann, 2008). The performance of the CTAH collector can therefore be approximated by measuring these three parameters in experiments. The collector efficiency η is plotted against $(T_{out}-T_{amb})/I_{global}$. The slope of this line ($-F_RU_L$) represents the rate of heat loss from the collector.

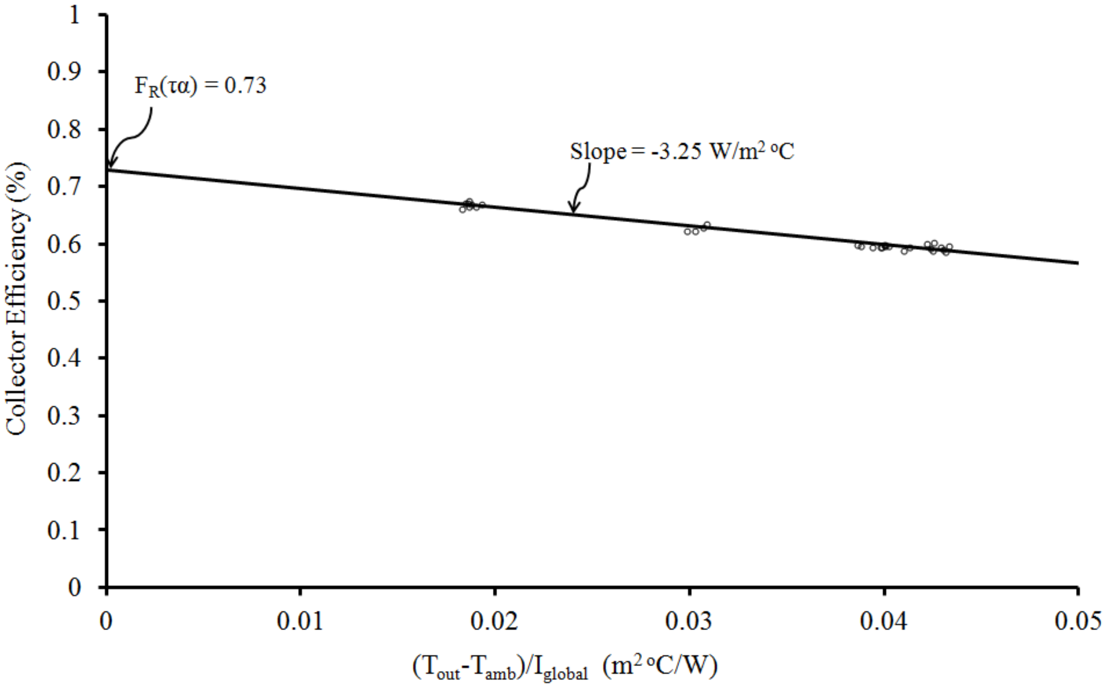

Figure 5.20: Collector efficiency characteristic of the CTAH for prototype 2

In order to characterise the CTAH system presented in this thesis, the instantaneous efficiency was calculated for periods when the solar radiation varied between 937.6 W/m^2 and 1,085.4 W/m^2. The corresponding values for $(T_{out}-T_{amb})/I_{global}$ were calculated and then plotted with a regression coefficient (R^2) of 0.974 for the line of best fit as shown in Figure 5.20. This resulted in an optical efficiency (η_o) of 0.73 and heat loss of -3.25 W/m^2 ^{o}C.

Rabl (1985) reported that in order to characterise a solar thermal collector, the conditions under which the efficiency is measured or calculated must be carefully specified to define the efficiency unambiguously and measure it reproducibly. This he said can be accomplished most easily if one bases the efficiency on clear sky conditions. He explained that even though clear skies are not identical, they are sufficiently reproducible to provide a useful reference for collector testing.

5.8 Comparative Performance Assessment

5.8.1 Thermal performance comparison of the CTAH with commercial glazed collector

Figure 5.21 shows the efficiency curves related to the outlet temperature for the CTAH and four commercially available solar air heating collectors. It is seen that there are different characteristics between these collectors. The selection of one or another of these collectors would depend on the operating conditions, that is, on the range of values of $(\Delta T)/I_G$ that are expected in an application, and on costs. Glazed collectors mentioned below from A to D varied for absorber properties (Hastings & Morck, 2000).

- Glazed collector A has an aluminium absorber with U-profiles with selective coating and underflow (Hastings & Morck, 2000)
- Glazed collector B has a plain black painted absorber with underflow (Hastings & Morck, 2000)

- Glazed collector C is a plain black painted absorber used as a façade element with air flow on both sides (Hastings & Morck, 2000)
- Glazed collector D is a plain black painted absorber used as a façade element with underflow (Hastings & Morck, 2000)
- transpired absorber with slatted glazing air heating collector developed by Zomorodian and Zamanian (2012)

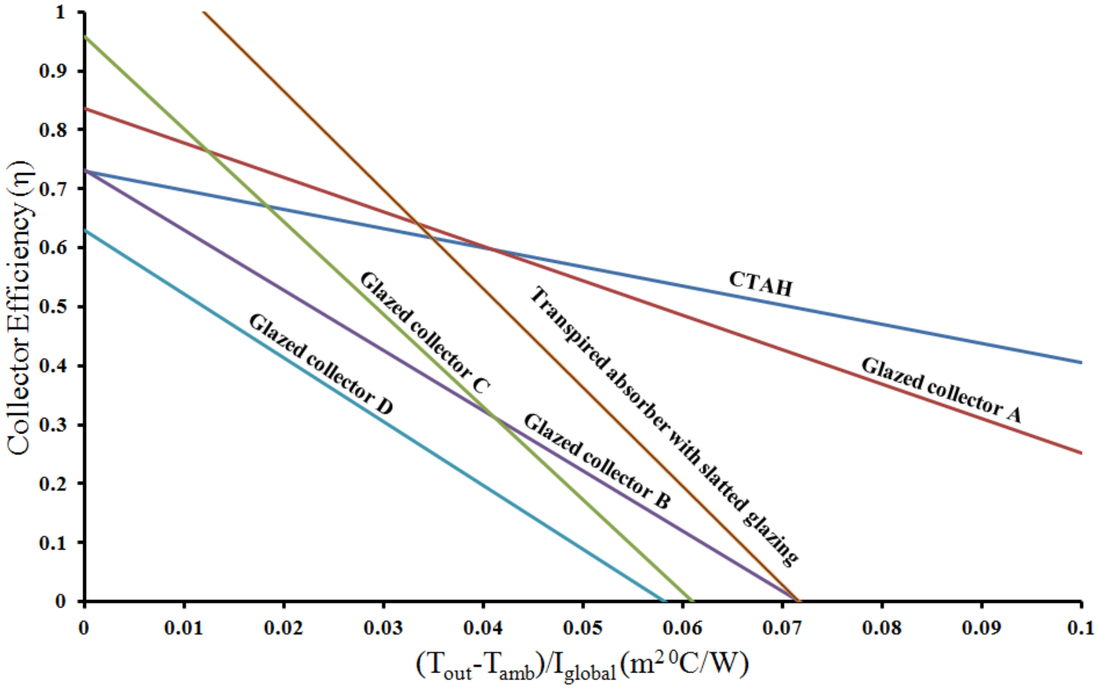

Figure 5.21: Comparison of CTAH thermal efficiency with glazed flat plate and transpired solar air heating collectors

Table 5.9: Optical efficiency and heat loss for different air heating collectors

Collector Type	$F_R(\tau\alpha)_{collector}$	F_RU_L (W/m^2 °C)
CTAH	0.73	-3.25
Glazed collector A	0.84	-5.85
Glazed collector B	0.73	-10.20
Glazed collector C	0.96	-15.70
Glazed collector D	0.63	-10.82

Table 5.9 shows the optical efficiency and heat loss for the CTAH and other commercially available air heating collectors. The highest and lowest $F_R(\tau\alpha)_{collector}$ were 0.96 and 0.63 for glazed collectors C and D respectively. The highest and lowest F_RU_L were -15.70 and -3.25 for glazed collector C and the CTAH. The C type collector showed superior performance for low temperature application. The efficiency however drops drastically with increasing temperature difference.

5.8.2 *Thermal performance comparison of CTAH with unglazed solar collector*

The temperature rise of solar heated air at various air flow rates and solar radiation levels for the UTC are presented in Figure 5.22. Conventional unglazed solar air heating collectors perform poor at air flow rate higher than 0.04 kg/s/m^2.

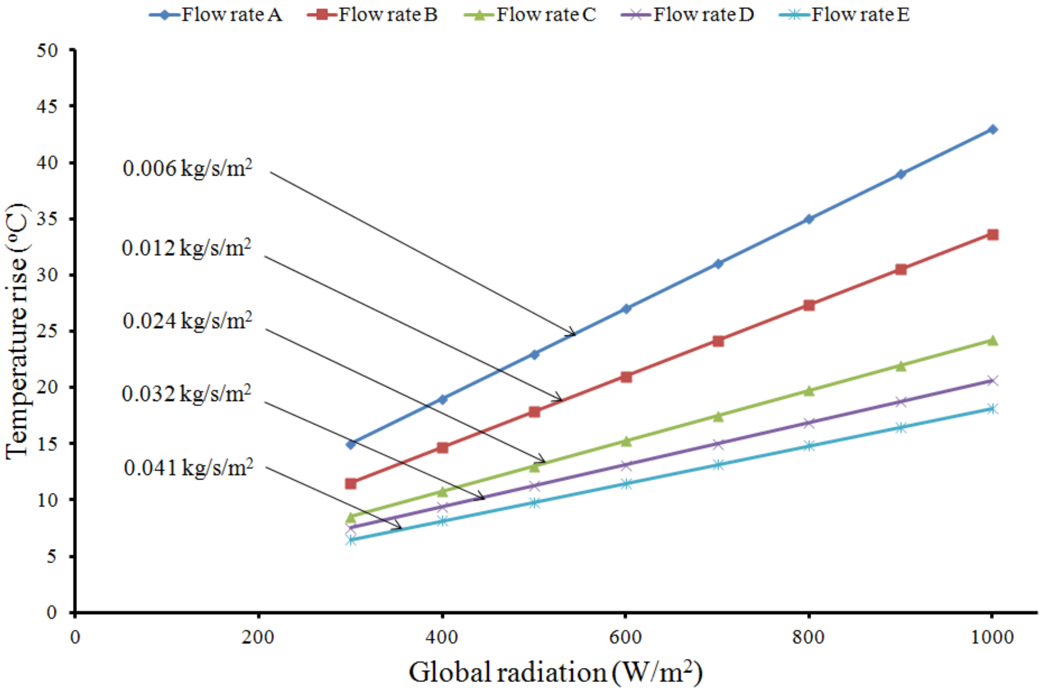

Figure 5.22: Temperature rise of UTC at different air flow rates and solar radiation levels (after Hollick, 1994)

The purpose of integrating a concentrator with perforated absorber is to concentrate solar radiation on a reduced absorber area which can provide effective temperature rise of flowing air at higher air flow rates. At 1000 W/m^2 solar radiation level the highest flow rate applicable in UTC was 0.04 kg/s/m^2 and the expected maximum temperature rise in the UTC was 18.2^{o}C. The performance of the CTAH system can be compared with Unglazed Transpired Collector (UTC) at different air flow rate. The values of the different flow rates for UTC operation are presented in Table 5.10 (Hollick, 1994). A to E indicate UTC operated at different air flow. A is the lowest operating flow rate of 0.006 kg/s/m^2 while E is the highest flow rate of 0.04 kg/s/m^2.

Table 5.10: Flow rates of different types of UTC operation (Hollick, 1994)

	A	B	C	D	E
Volume flow rate (m^3/s/m^2)	0.005	0.010	0.020	0.027	0.035
Mass flow rate (kg/s/m^2)	0.006	0.012	0.024	0.032	0.041

Figure 5.23 shows the air temperature rise of CTAH at different air flow rate (0.03 kg/s/m^2 to 0.09 kg/s/m^2). The lowest experimental operating flow rate (0.03 kg/s/m^2) resulted in the highest temperature rise of 38^{o}C at a radiation of 1000 W/m^2. The highest experimental operating flow rate (0.09 kg/s/m^2) on the other hand resulted in a temperature rise of 19.6^{o}C at a radiation of 1000 W/m^2.

Figure 5.24 shows a comparison of the air temperature rise by the CTAH compared to that by the UTC at an air flow rate of 0.03 kg/s/m^2. The air temperature rise was 20.6^{o}C by the UTC compared to 38^{o}C for the CTAH when the solar radiation was 1000 W/m^2. The air temperature rise was only 11.5^{o}C by the UTC compared to 19^{o}C for the CTAH when the solar radiation was 500 W/m^2. This resulted in a temperature rise of 86.9% by CTAH compared to UTC at a solar radiation level of 1000 W/m^2 which reduced to 65.2% at radiation level 500 W/m^2.

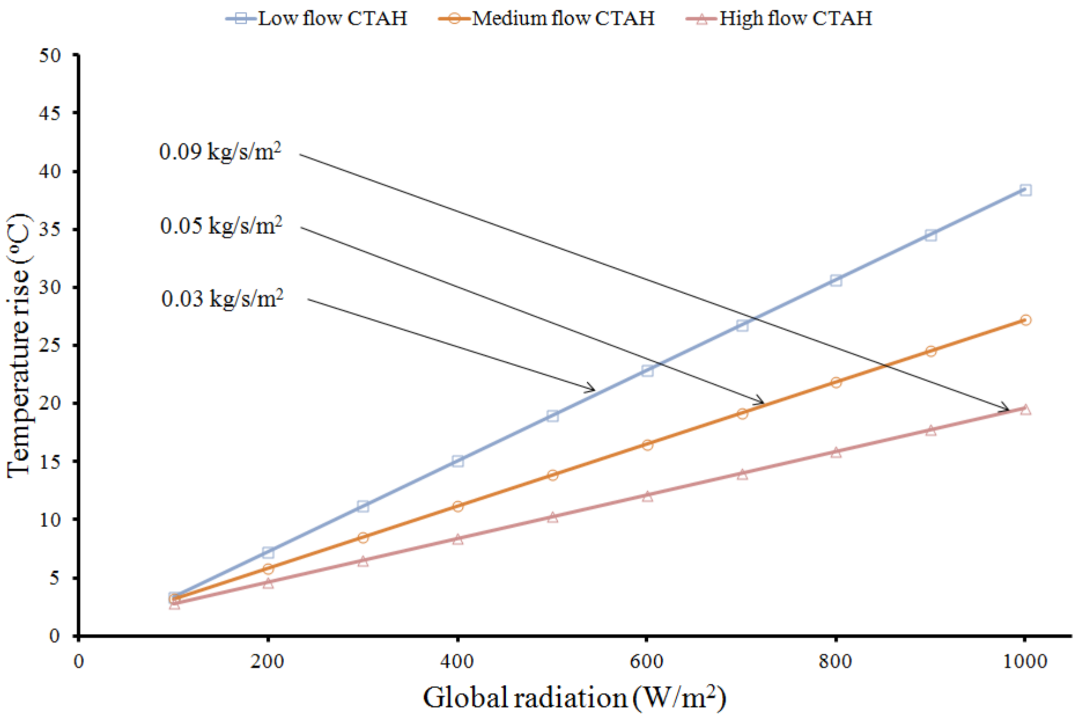

Figure 5.23: Temperature rise of CTAH at various air flow rates and solar radiation levels for prototype 2

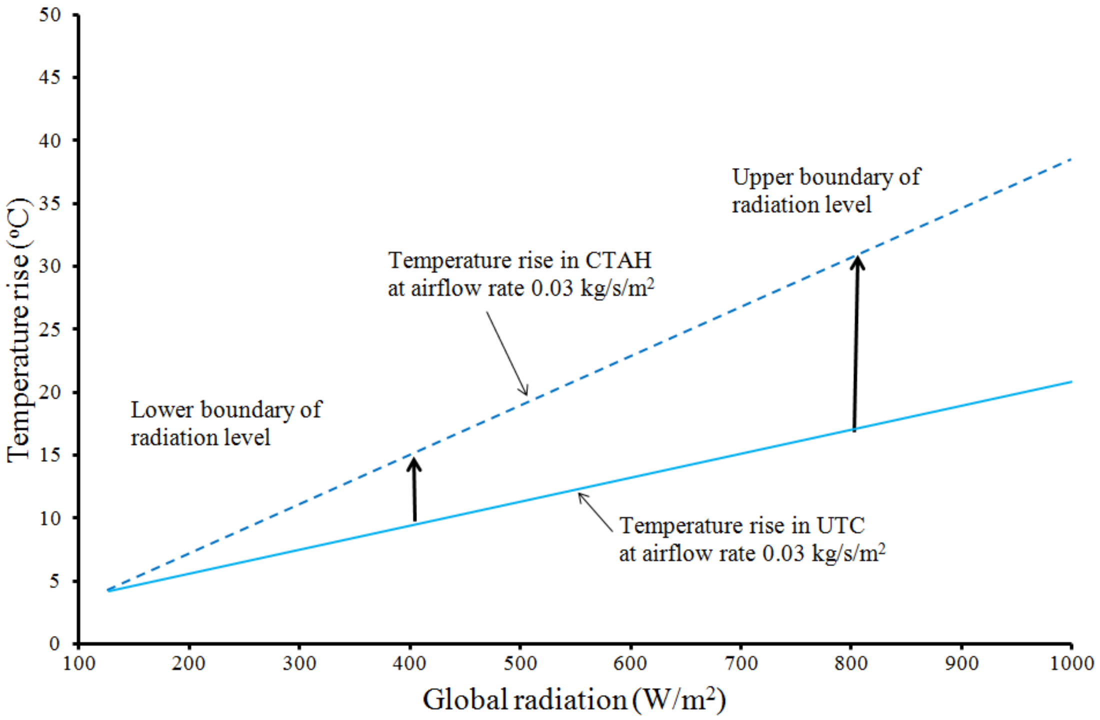

Figure 5.24: Comparison of the air temperature rise by the CTAH compared to UTC at an air flow rate of 0.03 kg/s/m^2 for prototype 2

Figure 5.25 shows the comparison of the air temperature rise by the CTAH at different air flow rate. The temperature rise was higher at all levels of radiation for an air flow rate 0.03 kg/s/m^2 compare to flow rate 0.09 kg/s/m^2. For low and high air flow rates, the air temperature rise was 38^{o}C and 19.6^{o}C respectively at a solar radiation level of 1000 W/m^2. The air temperature rise for low and high flow rates was 19^{o}C and 10.3^{o}C at a solar radiation level of 500 W/m^2.

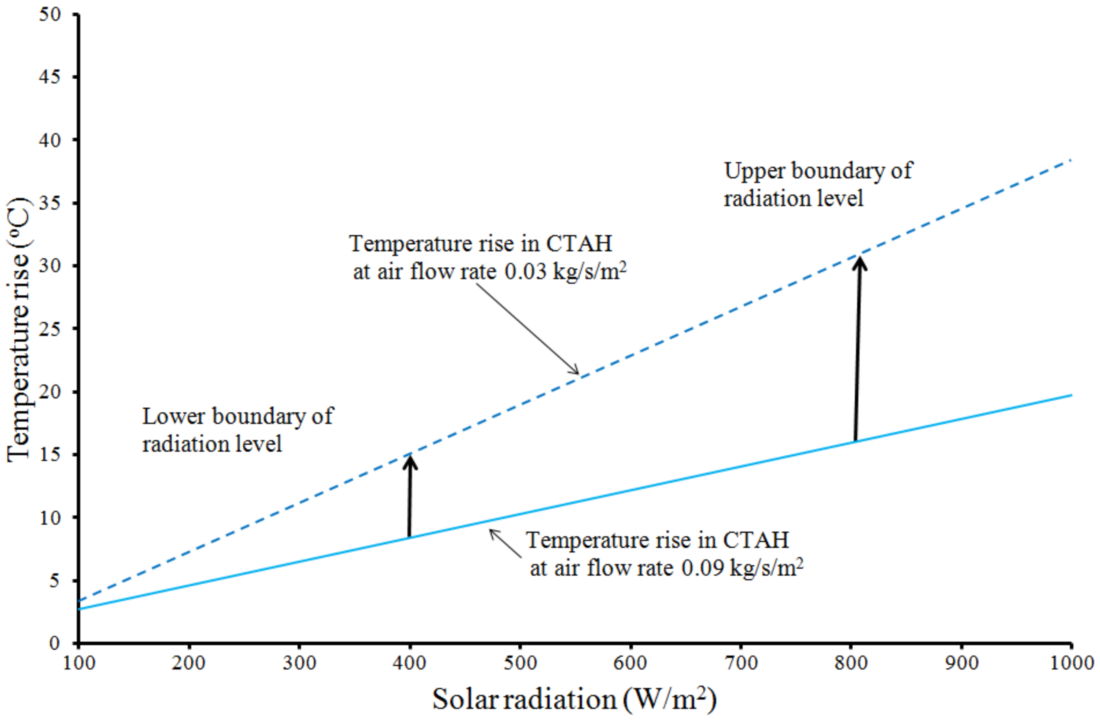

Figure 5.25: Comparison of the air temperature rise by the CTAH at air flow rates 0.03 kg/s/m^2 and 0.09 kg/s/m^2 for prototype 2

The air temperature rise increases at higher radiation level and decreases at high air flow rate. However, the effect of radiation on temperature rise is more significant at higher level of solar radiation for both high and low air flow rates.

5.9 Summary

The outdoor experimental performance of the Concentrating Transpired Air Heating (CTAH) system designed in chapter 3 was carried out in two stages using two prototypes constructed and tested in Dublin, Ireland. The experiments were carried out for open and closed loop configurations for first and second prototype of CTAH. The first prototype was constructed with a perforated metal absorber and the absorber was placed at the end of the secondary cavity at tertiary height zero.

Experimental analysis on the unglazed open loop orientation clearly suggested that it was necessary to develop a glazed collector to avoid interference from weather conditions. Reverse flow effects and conduction loss due to metal absorber with metal framing reduced collector performance for the open loop experimental configuration. During first prototype construction it was assumed that the corner effect would be negligible due to perforation geometry of the absorber. However, in case of metal absorber concentrated absorber size and non uniform solar radiation intensity caused degradation of system performance.

An optically optimised 50 mm tertiary height (discussed in chapter 3) was integrated in the design of the second prototype. Experimental results were analysed for different air flow rate ranging between 0.03 and 0.09 kg/s/m^2 for the closed loop configuration. At a low air flow rate of 0.03 kg/s/m^2 the absorber, outlet air, inlet air and ambient air temperatures were 109^{o}C, 67.9^{o}C, 30.3^{o}C and 25.4^{o}C respectively. At clear sky condition at 13:00 the instantaneous radiation was 1037.3 W/m^2. The outlet air temperature rise against inlet air was 37.6^{o}C and the temperature rise was 42.5^{o}C from ambient air temperature.

At a medium air flow rate of 0.05 kg/s/m^2 the absorber, outlet air, inlet air and ambient temperatures were 72.8^{o}C, 57.3^{o}C, 30.9^{o}C and 23.8^{o}C respectively. At 13:00 hours under clear sky condition the instantaneous solar radiation was 1,048.3 W/m^2. The outlet air temperature rise was 26.4^{o}C from inlet air while the temperature rise was 33.5^{o}C from ambient air.

At the highest air flow rate of 0.09 kg/s/m^2 the absorber temperature, outlet air temperature; inlet air temperature and ambient temperature were 57.7^{o}C, 46.6^{o}C, 31.9^{o}C and 22.5^{o}C. At 13:00 hours the instantaneous solar radiation under clear sky condition was 1,061.3 W/m^2. The outlet air temperature rise was 14.7^{o}C from inlet air temperature and the temperature rise was 24.1^{o}C from ambient air temperature. The thermal efficiency remained high at higher air flow rate. The average thermal efficiency was found to be approximately 55-65% with average radiation above 400 W/m^2. Solar radiation was the parameter with the greatest effect on thermal efficiency in the closed loop configuration.

Due to thermal stratification in the tertiary section and concentrator cavity of glazed CTAH, the effect of wind speed and ambient air temperature was low. Stratification of the air temperature was consistent for different air flow rates inside the CTAH. The outlet air temperature was always higher than the tertiary section air temperature which was also always higher than the glazing temperature and inlet air temperature. The experimental system was closed loop so the inlet temperature was constantly higher than the corresponding ambient air temperature.

The stratified air thermal layer reduced heat loss from the absorber to ambient through the glazing surface. A portion of optical heat loss through the reflector surface was recaptured as the air flowed from inlet to outlet. Pressure drop in the CTAH was found 10 Pa for a flow rate of 0.1 kg/s/m^2. The required power consumption for driving the flow through the CTAH collector was very small in comparison to the recovered energy which increased the attractiveness of the collector. The measured experimental performance data collected was used to validate the energy output model validation in chapter 6.

CHAPTER 6

CTAH ENERGY OUTPUT MODELLING

The aim of this chapter is to develop and validate a heat transfer model to predict the energy output from the CTAH system. Specific objectives are to:

- determine the quantity of incident solar radiation absorbed;
- determine the thermal and optical losses;
- evaluate the outlet air temperature;
- develop and validate the energy model for the CTAH system;
- evaluate the annual energy collected by the CTAH system;

6.1 Introduction

Accurate determination of the energy output from the CTAH system under different weather conditions is essential in order to assess its long-term performance. Year round field testing would provide such data but several constraints such as cost, time, and equipment failure make it impractical for such extensive tests to be successfully undertaken. A pragmatic mathematical representation or model of the CTAH system was developed and validated with measured field trial data.

In this chapter, a model was developed to predict the energy output from the CTAH system. It was validated against field trial data presented in Chapter 5 using statistical methods. The validated model was used to simulate the total energy generated by the CTAH system for different months over an entire year using weather data for

Dublin, Ireland. The model was also used to investigate the effect of different air mass flow rates on the maximum outlet air temperature from the CTAH system.

6.2 CTAH Energy Output

In order to determine the useful energy output from the CTAH system it is important to evaluate energy exchanges that occur between its components. The energy absorbed by the absorber, heat losses and outlet air temperature from the CTAH system have to be evaluated. A thermal network of the CTAH system was developed in order to illustrate the sources of energy exchange. The useful energy output from the CTAH system is given as:

$$q_{useful,i+1} = \dot{m}_{air} Cp_{air} \left(T_{out,i} - T_{inlet,i} \right) \qquad 6.1$$

Where,

q_{useful}	useful energy output (J)
$\dot{m}_{air}$	air mass flow rate (kg/s)
Cp_{air}	specific heat capacity of air (J/kgK)
$T_{out,i}$	outlet air temperature (^{o}C)
$T_{inlet,i}$	inlet air temperature (^{o}C)

Accurate determination of the outlet air temperature at any given instant is important to calculate the useful energy output from the CTAH system. At any given instant, i, the air mass flow rate and the inlet air temperature are known while the specific heat capacity of air is determined using the mean inlet and outlet air temperature.

6.2.1 Thermal Network of CTAH

The assumptions used to develop the thermal network for the CTAH system are:

1. Conduction losses from the absorber through the frame are neglected (however the conduction loss through envelop will be estimated in later section).
2. Temperature variation along the length of the absorber is also neglected.
3. The absorber and glazing cover are regarded as nodes in the thermal network.

Heat losses from the absorber of the CTAH system are primarily convective and radiation. Convection or radiation heat loss is considered as a series thermal resistance when acting alone but when acting together they are considered as being in parallel. The thermal network of the CTAH system is shown in Figures 6.1 a-c.

Glazing cover, absorber surface and back plate were considered as the node of the equivalent thermal network. Figure 6.1 (b) shows the equivalent thermal network of the CTAH. An exact calculation requires iterations to determine the temperature of each node as the equations for convective and radiative heat transfer are non-linear. The equivalent network has been expressed in terms of $U_{abs\_glazing}$ and $U_{glazing\_ambient}$. Rabl (1985) proposed linearization of the thermal network by approximating all resistances by temperature independent constants.

It is seen in Figure 6.1c that energy output from the CTAH system contained in air flowing through the perforated inverted absorber depends on the ambient temperature, inlet air temperature, energy absorbed by the absorber and overall heat loss coefficient of the CTAH system.

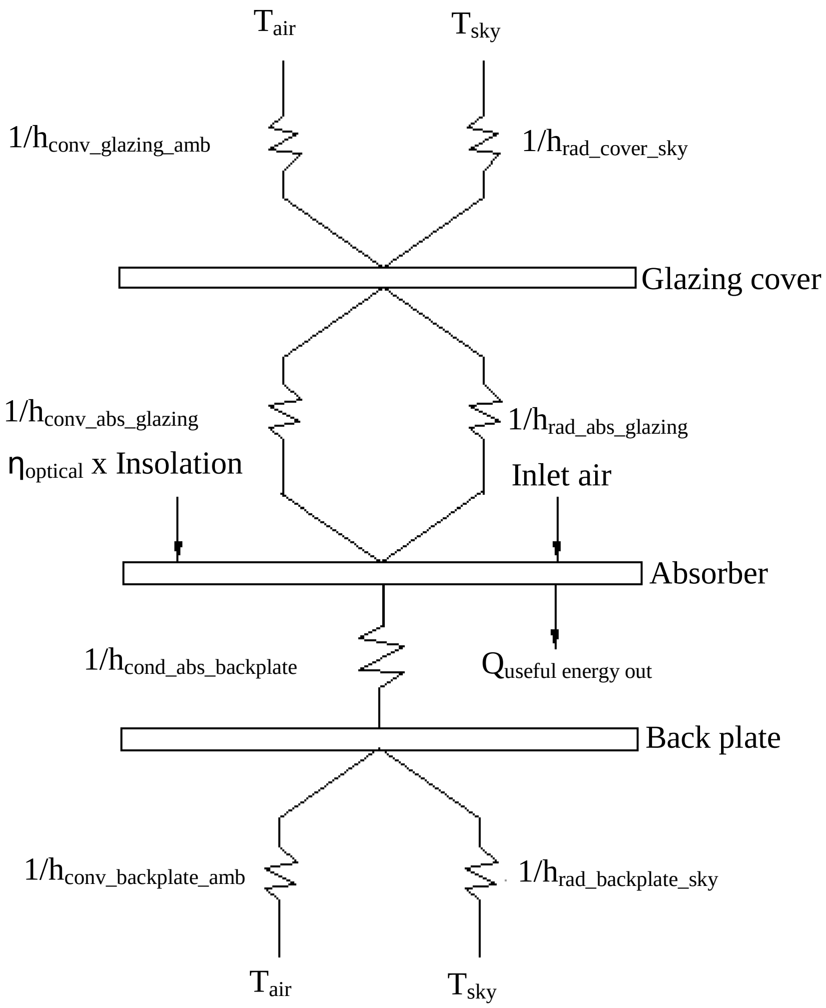
T_{air}
T_{sky}
$1/h_{conv\_glazing\_amb}$
$1/h_{rad\_cover\_sky}$
Glazing cover
$1/h_{conv\_abs\_glazing}$
$1/h_{rad\_abs\_glazing}$
$\eta_{optical}$ x Insolation
Inlet air
Absorber
$1/h_{cond\_abs\_backplate}$
$Q_{useful\ energy\ out}$
Back plate
$1/h_{conv\_backplate\_amb}$
$1/h_{rad\_backplate\_sky}$
T_{air}
T_{sky}

(a)

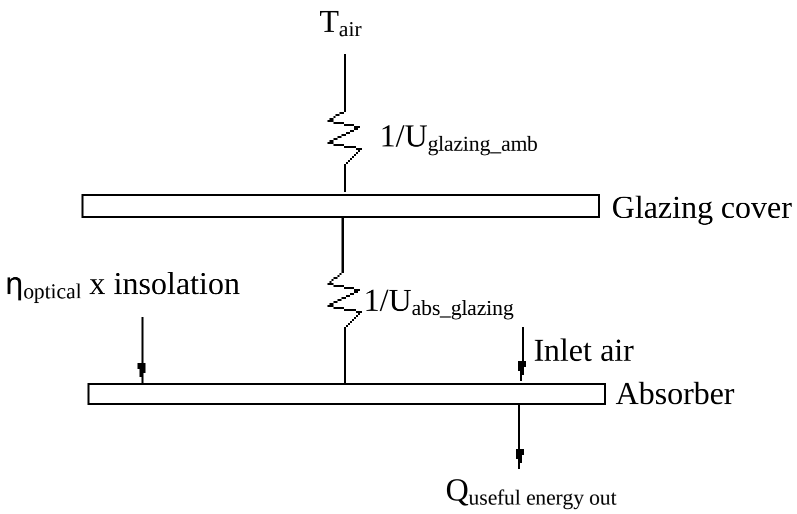
T_{air}
$1/U_{glazing\_amb}$
Glazing cover
$\eta_{optical}$ x insolation
$1/U_{abs\_glazing}$
Inlet air
Absorber
$Q_{useful\ energy\ out}$

(b)

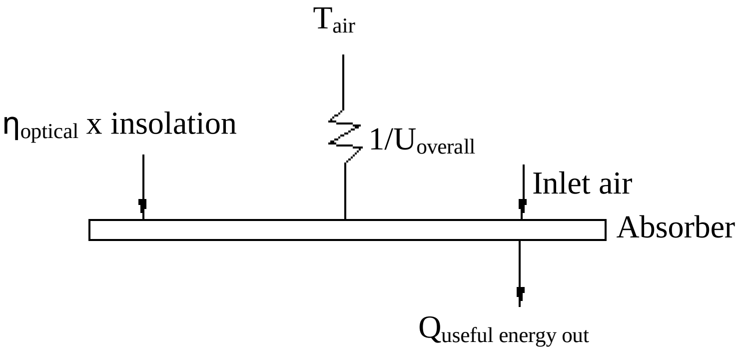

(c)

Figure 6.1: Thermal network of the CTAH

Where,

$h_{conv\_glazing\_amb}$ = Convection coefficient between glazing and ambient

$h_{rad\_cover\_sky}$ = Radiation coefficient between glazing and sky

$h_{con\_abs\_glazing}$ = Convection coefficient between absorber and glazing

$h_{rad\_abs\_glazing}$ = Radiation coefficient between absorber and glazing

$h_{con\_abs\_backplate}$ = Convection coefficient between absorber and back plate

$h_{con\_backplate\_amb}$ = Convection coefficient between back plate and ambient

$h_{rad\_backplate\_sky}$ = Radiation coefficient between back plate and sky

$U_{glazing\_amb}$ = Equivalent heat loss between glazing and ambient

$U_{abs\_glazing}$ = Equivalent heat loss between absorber and glazing

$Q_{useful\ energy}$ = Useful outlet energy from the collector

T_{air} = Temperature of the outside air

T_{sky} = Temperature of the sky

6.2.2 Energy Absorbed by CTAH

Solar radiation incident on the aperture of the CTAH undergoes optical losses on aperture glazing and concentrator surface before it reaches the inverted absorber. The optical loss on the glazing surface depends on the incident angle which varies over time of day and the absorption property of the glazing material. The optical efficiency varies based on the proportion of the beam and diffuse radiation for a particular time of the day. Equation 6.2 gives the optical loss on the glazing surface of the CTAH expressed as a function of reflector material and incidence angle of solar radiation.

$$\text{Optical Loss} = f\left(\theta_{\text{incident}}, \rho_{reflector}, m, \alpha_{abs}, I_b/I_d\right) \qquad 6.2$$

Where,

θ_{incident} = Incident angle

$\rho_{reflector}$ = Reflector reflectance

m = Average number of reflection

α_{abs} = Absorbtance of the absorber

I_b = Beam radiation

I_d = Diffuse radiation

Measured solar radiation incident on the aperture of the CTAH was the available energy to the system. However, it was not possible to measure the portion of that the incident radiation that reached the inverted absorber surface. Determination of the portion of the energy absorbed by the absorber surface at any given instant was paramount to determine the energy performance of the CTAH system.

Global radiation (I_{global}) incident on the tilted aperture of the CTAH was considered to be composed of the sum of beam (I_b), diffuse (I_d) and ground albedo reflected (I_r) components as shown in Equation 6.3.

$$I_{global} = I_b + I_d + I_r \qquad 6.3$$

Each of the components of the incident radiation needs to be treated individually to achieve an optimum approximation of the available energy. The total solar radiation absorbed by the absorber of the CTAH system is expressed as (Duffie & Beckman, 2006):

$$S = I_{b,CPC}\tau_{b,glazing}\tau_{CPC,b}\alpha_{abs} + I_{d,CPC}\tau_{d,glazing}\tau_{CPC,d}\alpha_{abs} + I_{g,CPC}\tau_{g,glazing}\tau_{CPC,g}\alpha_{abs} \qquad 6.4$$

where,

$I_{b,CPC} = C_f I_b \cos\theta$ and $I_{d,CPC} = \frac{I_d}{C}$.

S = Total radiation absorbed on the inverted absorber surface of CTAH (W/m^2)

I_b= The beam radiation on the aperture of the CTAH within the acceptance angle (W/m^2)

I_d= The diffuse radiation on the aperture of the CTAH within the acceptance angle (W/m^2)

I_g= The ground reflected diffuse radiation on the aperture of the CTAH within the acceptance angle (W/m^2)

$\tau_{b,glazing}$ = Transmittance for beam radiation of any glazing cover within the acceptance angle

$\tau_{d,glazing}$ = Transmittance for diffuse radiation of any glazing cover within the acceptance angle

$\tau_{g,glazing}$ = Transmittance for ground reflected radiation of any glazing cover within the acceptance angle

$\tau_{CPC,b}$ = Transmittance of the CPC for beam radiation which accounts the reflection losses and is a function of average number of reflection

$\tau_{CPC,d}$ = Transmittance of the CPC for diffuse radiation which accounts the reflection losses and is a function of average number of reflection

$\tau_{CPC,g}$ = Transmittance of the CPC for ground reflected radiation which accounts the reflection losses and is a function of average number of reflection

α_{abs} = Absorptance of the carbon fibre fabrics absorber for diffuse radiation

C_f = Control function. The value is 1 when beam radiation is incident on the aperture within acceptance angle otherwise the value is zero.

$\tau_{CPC,b}$ and $\tau_{CPC,d}$ are transmittances of the CPC that account for specular reflectance of the concentrator, the average number of reflections (n_i) and reflectance (ρ) of the reflector surface. $\tau_{CPC,b}$ and $\tau_{CPC,d}$ can be calculated as $\tau_{CPC} = \rho_{reflector}^{n_i}$. The average number of reflections (n_i) for different incident angles was calculated using the 2D Matlab Ray-tracing model for the CTAH. The reflector material had a reflectance ($\rho_{reflector}$) of 95% as cited by the supplier company (Alanod, 2009).

Considering that there is only a very small portion of ground reflected radiation that reaches the inverted absorber via the circular reflector, the third component in Equation 6.4 can be neglected i.e. $I_{g,CPC} = 0$. Equation 6.4 therefore reduces to:

$$S = I_{b,CPC}\tau_{b,glazing}\tau_{CPC,b}\alpha_{abs} + I_{d,CPC}\tau_{d,glazing}\tau_{CPC,d}\alpha_{abs} \qquad 6.5$$

6.2.3 Overall Heat Loss of CTAH

6.2.3.1 Back Loss

Back losses from the CTAH system are due to conduction and convection from the outer surface of the back plate and from reflector surfaces through the back of the collector. It is assumed that the flow of heat is one dimensional. In most cases the insulation thickness provided is such that the thermal resistance associated with conduction dominates. Thus, neglecting the convective resistance at the bottom surface of the collector casing, the heat loss through the back of the CTAH (q_{back}) is expressed in Equation 6.6 as:

$$q_{back} = A_{back} k_{insulation} \left(\frac{\Delta T}{\delta_{insulation}} \right) \tag{6.6}$$

The absorber material in CTAH has a low conductivity compared to conventional solar collector metal absorbers. Due to light weight of the material, the framing of the absorber can be made by a low cost insulation material. It is convenient to lump all conductive losses through the back, side and frame into a single effective conductance U_{back}. The CTAH was insulated with a material that had a thermal resistance of 1.455 m^2K/W which is close to a building's thermal resistance 1.462 m^2K/W (SEAI, 2011). Rabl (1976b) suggested that U_{back} for CPC to be 0.3 W/m^2K. Conduction loss through the concentrator surface was calculated as 0.9 % and through the air duct as 1.2 % of incident solar insolation. U_{back} can be calculated using Equation 6.7 given as:

$$U_{back} = \frac{k_{insulation}}{\delta_{insulation}} \tag{6.7}$$

Where,

$k_{insulation}$ = thermal conductivity of the insulation.

$\delta_{insulation}$ = Thickness of insulation

6.2.3.2 Top Loss

Energy loss from the top of the glazing at the CTAH system's aperture was a combination of convection and radiation loss. The heat transferred by convection and radiation between the absorber plate, glass cover and surroundings can be written from the glass cover to the surroundings. The top heat loss is the sum of heat loss due to convection between the glazing and ambient air and radiation between the glazing and sky. Q_{top_loss} can be estimated for known values of $T_{glazing}$,T_{amb}, ε , $\varepsilon_{glazing}$ and T_{abs}. It is also necessary to have some co-relation for calculating the convection heat transfer co-efficient $h_{conv.glazing\sim amb}$ and sky temperature T_{sky}. This is expressed mathematically as:

$$Q_{top\_loss} = A_{top}\left\{h_{conv.glazing-amb}\left(T_{glazing} - T_{amb}\right) + \sigma\varepsilon_{glazing}\left(T_{glazing}{}^{4} - T_{sky}{}^{4}\right)\right\} \qquad 6.8$$

The convective heat loss coefficient for convection from the exterior glazing surface was estimated using different correlations to compare their effects on the results. These are the correlations by McAdams (1954) and Watmuff et al. (1977) as mentioned by several authors (Duffie & Beckman, 2006; Mallick, 2003; Tchinda, 2008) as a function of wind speed in m/s:

$$h_{Cov.\_glazing} = 5.7 + 3.8.V_{wind} \qquad 6.9$$

$$h_{Cov.\_glazing} = 2.8 + 3.0V_{wind} \qquad 6.10$$

Heat transfer is due to free convection in the absence of forced convection across the aperture cover. For free convection the heat transfer coefficient would be between 2.8 and 5.7 W/m^{2}K. For average wind speed of 2 m/s to 3 m/s, the forced convection coefficient value range would be from 8.8 to 17.1 W/m^{2}K. A heat transfer loss coefficient of 12.95 W/m^{2}K was chosen as a reasonable estimate. However, a portion of heat captured by the glazing cover was recovered due to inward air flow.

Sukhatme (1996) and Tchinda (2008) presented a simple empirical relationship to calculate the effective sky temperature in a case of CPC integrated solar air heating collector given as:

$$T_{sky} = T_{amb} - 6 \qquad 6.11$$

The temperatures are expressed in Kelvin. Assuming a solar radiation of 10^3 W/m^2, emissivity of glazing cover 0.94 and 14^o temperature difference between the glazing and the sky, 8.7% was estimated as the radiation loss from the aperture glazing. 12.9% convection loss was calculated without considering heat recovery due to inward air flow. Absorption due to the glazing surface was estimated as 2% and the average reflection loss was considered as 10%. The overall heat loss was calculated as 25.7%.

6.2.4 *Effective Convection Coefficient*

As air flows through the porous absorber of the CTAH system it gains heat through convection. This flow can either be laminar or turbulent depending on the resulting Reynolds number. The air flow at the entrance of the CTAH is laminar as air enters from the duct to concentrator cavity. However, after passing through the perforated absorber, turbulence increases as air approaches the collector outlet. In this work, it was assumed that air flow through the porous absorber would be mixed between laminar and turbulent. The Nusselt number used to calculate the effective convective heat transfer coefficient was obtained as an average of the Nusselt numbers for laminar and turbulent flow. The effective convection heat transfer coefficient was calculated using Equation 6.12 given as:

$$h_{conv\_eff} = \frac{N_u K_{air}}{D_h} \qquad 6.12$$

h_{conv_eff}	effective convection heat transfer coefficient (W/m^{2}K)
Nu	Nusselt number (dimensionless)
K_{air}	thermal conductivity of air (W/mK)
D_{h_l}	hydraulic diameter (m)

The hydraulic diameter (D_{h_l}) is expressed as:

$$D_{h\_l} = \varphi_p \frac{2L_{length}L_{width}}{L_{length} + L_{width}} \qquad 6.13$$

Where,

L_{length}	absorber length (m)
L_{width}	absorber width (m)
φ_p	absorber porosity (dimensionless)

For a laminar flow regime where *Re < 2300*, the Nusselt number is given as:

$$N_{u\_l} = N_{u\_\alpha} + \frac{a\left[\operatorname{Re}\Pr\left(\frac{D_h}{L}\right)\right]^m}{1 + b\left[\operatorname{Re}\Pr\left(\frac{D_h}{L}\right)\right]^n} \qquad 6.14$$

Where,

N_{u_α}	Nusselt number (dimensionless)
Pr	Prandtl number (dimensionless)

a, b, m and n are constants whose values are 0.0019, 00563, 1.71 and 1.17 respectively when *Pr* is 0.7. *Re* and *Pr* were calculated using the mean air temperature given as:

$$T_{mean} = \frac{T_{outlet} + T_{inlet}}{2} \qquad 6.15$$

For transient flow regime where 2,300 < Re < 6,000, the Nusselt number is given as:

$$N_{u\_t} = 0.116\left(\operatorname{Re}_t^{2/3} - 125\right)\Pr_t^{1/3}\left[1 + \left(\frac{D_{h\_t}}{L}\right)^{2/3}\right]\left(\frac{\mu}{\mu_{abs}}\right) \qquad 6.16$$

The Reynolds number was calculated using Equation 6.17 given as:

$$\mathrm{Re} = \frac{\rho_{air} V_{air} D_h}{\mu} \tag{6.17}$$

For mixed flow the Nusselt number, N_u is obtained using Equation 6.18 given as:

$$N_u = \left(N_{u\_l} + N_{u\_t}\right) / 2 \tag{6.18}$$

The resulted Nusselt number is an average value of the intermittent and laminar flow. The laminar flow occurs inside cavity. Due to glazing there is no interference of the outside wind on the cavity air. Only air entering into the cavity is through the inlet of the collector. It was assumed that there is no flow reversal as the inlet and outlet dimension of the collector were identical. The higher Nu was calculated near the outlet of the collector after transpired absorber.

6.2.5 *Energy Balance Equations*

Figure 6.1 showed the thermal network of the CTAH. Solar radiation is the energy input and air with higher temperature at the exit is the energy output of the collector. The relation between different nodes of the collector is described as follows:

Glazing cover was considered as the first node of the thermal network which has interaction with the outside air convection and sky. The sky temperature was calculated by using Equation 6.11. Glazing cover gains heat energy by absorbing part of the incident radiation and emitted radiation from the concentrator and absorber surface. Absorber of the CTAH absorbs the concentrated incident radiation and raise air temperature by convection.

$$\begin{aligned} & I_{global} \mathrm{A}_{\mathrm{aperture}} \alpha_{absorp.} + U_{overall\_abs\_glazing} \mathrm{A}_{\mathrm{abs}} \left(T_{abs} - T_{glazing}\right) - h_{conv.glazing\_amb} \mathrm{A}_{\mathrm{glazing}} \left(T_{glazing} - T_{amb}\right) \\ & - h_{rad.glazing\_sky} \mathrm{A}_{\mathrm{glazing}} \left(T_{glazing} - T_{sky}\right) = M_{glazing} C_{p\_glazing} \frac{dT}{\Delta t} \end{aligned} \tag{6.19}$$

The absorbed energy by absorber was calculated by Equation 6.5. The absorber faces downward and it is separated by a glazing surface from the outside air. As a result heat loss occurs from absorber to glazing and back surface.

$$S(i) - A_{abs} U_{abs\_glazing}\left(T_{abs,i} - T_{glazing,i}\right) - A_{abs} h_{conv.abs\sim mair}\left(T_{abs,i} - T_{inlet,i}\right) = M_{abs} C_{p\_abs}\frac{dT}{\Delta t} \qquad 6.20$$

$$\begin{aligned} & S(i) - A_{abs} U_{abs\_glazing} T_{abs,i} + A_{abs} U_{abs\_glazing} T_{glazing,i} - A_{abs} h_{conv.abs\sim mair} T_{abs,i} \\ & + A_{abs} h_{conv.abs\sim mair} T_{inlet,i} = M_{abs} C_{p\_abs}\frac{dT}{\Delta t} \end{aligned} \qquad 6.21$$

$$\begin{aligned} & S(i) + A_{abs} U_{abs\_glazing} T_{glazing,i} - \left(A_{abs} U_{abs\_glazing} + A_{abs} h_{conv.abs\sim mair}\right) T_{abs,i} \\ & + A_{abs} h_{conv.abs\sim mair} T_{inlet,i} = M_{abs} C_{p\_abs}\frac{\Delta t}{dT} \end{aligned} \qquad 6.22$$

As air flows through the porous absorber, it exchanges heat through convection. The useful energy gained by the air is manifested by an increase in the inlet air temperature. An energy balance for air flowing through the porous absorber is expressed as:

$$A_{abs} h_{conv\_eff,i}\left(T_{abs,i} - T_{inlet,i}\right) = \dot{m}_{air,i} Cp_{air,i}\left(T_{out,i} - T_{inlet,i}\right) \qquad 6.23$$

The effective convection coefficient (h_{conv_eff}) between the absorber and air flow is obtained from Section 6.2.4.

Outlet air temperature:

$$T_{outlet,i+1} = T_{inlet,i} + \frac{A_{cv} q_{useful,i}}{\dot{m}_{air} C_{p\_air,i}} \qquad 6.24$$

6.3 Useful energy simulation model

6.3.1 Simulation inputs

A thermal simulation model was developed to calculate the useful energy output from the CTAH system and validated using field trial data presented in Chapter 5.

Input data to the model used to calculate the useful energy output from the CTAH system consists of measured solar radiation on tilted aperture, measured inlet air temperature and measured ambient temperature.

6.3.2 Useful energy simulation Model Development

Figure 6.2 shows a flow chart of the energy output model.

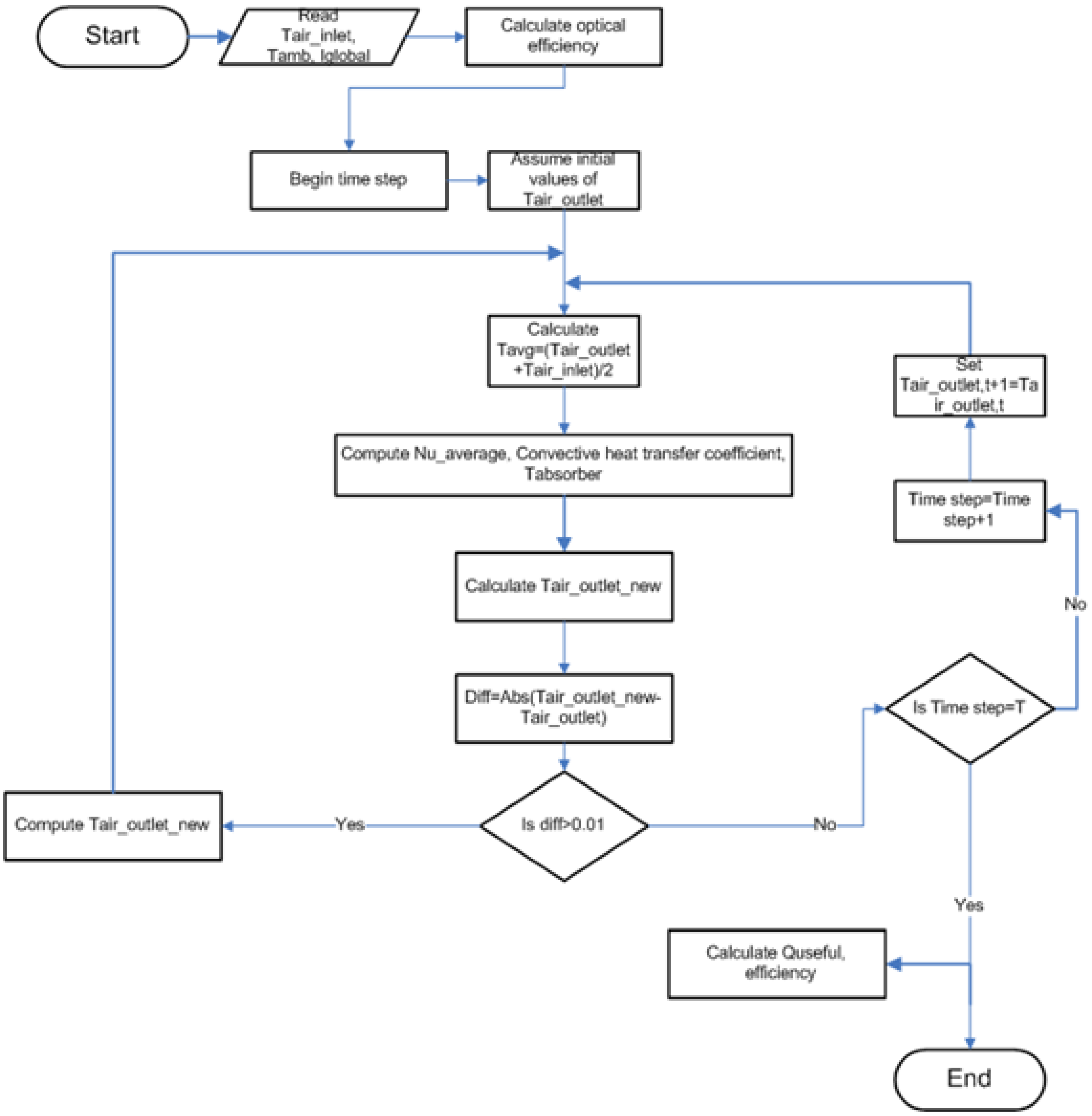

Figure 6.2: Flow chart for calculating the useful energy from the CTAH system

The model receives measured input data consisting of ambient air temperature, inlet air temperature and global in-plane solar radiation. The model then proceeds to calculate the optical efficiency and the radiation flux concentration on the surface of the inverted absorber. The simulation time is divided into hourly intervals between 10 am and 5 pm daily as shown in Figure 6.3-6.5.

A numerical model for the CTAH was developed. The model required solutions at previous time steps. Matlab software was used to numerically solve the model. The transient and steady state models were applied with input parameters such as solar radiation, glazing temperature, wind speed and air flow rate corresponding to the day of the experiment.

The optical model was used to calculate the radiation flux concentration on the surface of the inverted absorber. For each time interval an initial value of the outlet air temperature is assumed. The average air temperature is then calculated as a mean of the outlet and inlet air temperature. The properties of air are determined for this mean temperature and used to compute the convective heat transfer coefficient, Nusselt number and absorber temperature.

The new outlet air temperature is calculated and compared to the previously assumed value. Their difference is compared to a defined convergence criteria and the program advances to the next time step if the difference is lower than the convergence criteria.

Alternatively, the computed outlet air temperature is set as the new assumed value for outlet air temperature. This process continues until all the time steps have elapsed. The useful energy output from the CTAH system and its efficiency are then calculated for each time interval.

6.3.3 Model Validation with experimental results

6.3.3.1 Validation parameters

Variations between predicted and measured values were quantified using three statistical parameters (Singh and Ahmed, 2011; Gharamaleki et al., 2010; Seo et al., 1990) which include: percentage mean error (PME) and cumulative error (CE). The statistical parameters used to validate the modelled against measured values are expressed mathematically as:

1) Percentage Mean Error (PME)

$$PME = \frac{100}{N}\sum_{i=1}^{N}\frac{m_i - M_i}{M_i} \qquad 6.25$$

Where,

m_i = modelled values;

N = total number of observations;

M_i = measured values.

Negative modelled PME value underestimates and positive modelled PME value overestimates,

2) Cumulative Error (CE)

$$CE = 100 \times \frac{\sum_{i=1}^{N} m_i - \sum_{i=1}^{N} M_i}{\sum_{i=1}^{N} M_i} \qquad 6.26$$

PME evaluates the percentage mean of sum of errors of individual observations. It is the calculated average value of percentage errors by which estimated forecasts differ from the experimental values. A negative value of PME indicates a net underestimation while a positive value indicates net over estimation of the modelled values. CE evaluates the percentage mean errors of cumulative observations. A negative value of CE indicates a cumulative underestimation while a positive value indicates cumulative over estimation of the modelled values (Singh and Ahmed, 2011; Gharamaleki et al., 2010; Seo et al., 1990).

6.3.3.2 Validation results with experimental data

The total energy incident on the aperture was measured during the experiment. Equation 6.5 was used to calculate the total radiation that was absorbed by the inverted absorber after concentration. Figure 6.3 shows in-plane global solar irradiation, modelled and measured outlet air temperature as well as the measured and modelled energy output from the CTAH system on the 13th of July, 2011.

It is seen that the on a day with clear sky (13th July, 2011) the modelled output air temperature and energy output from 10 am to 4 pm were close to the measured values with PME and CE of 1.4% and 0.5% respectively. Detailed measured and modelled values of in-plane solar radiation, energy output and efficiency on the 13th of July 2011 are shown in Appendix 4.1. The validation results show that the modelling errors are within acceptance range for a representative day of experiment with high flow rate.

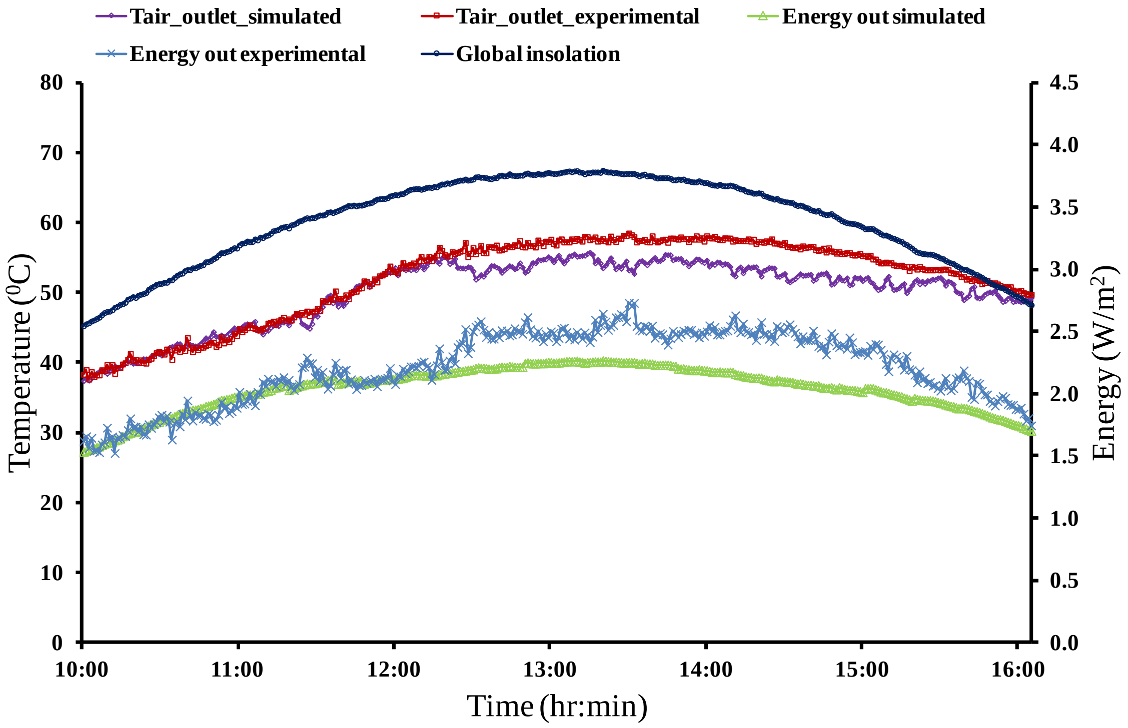

Figure 6.3: In-plane global solar irradiation, outlet air temperature and energy output from CTAH system for prototype 2 on the 13th of July, 2011

Figure 6.4 shows in-plane global solar radiation, modelled and measured outlet air temperature as well as the measured and modelled energy output from the CTAH system on the 15th of July, 2011. Detailed measured and modelled values of in-plane solar radiation, energy output and efficiency on the 15th of July 2011 are shown in Appendix 4.2.

It has been seen that the on a heavily overcast day (15th July, 2011) the modelled output air temperature and energy output from 10 am to 4 pm followed the trend of the measured values with PME and CE of 3.4% and 3.8% respectively. The validation results show that the modelling errors are within acceptance range for a representative day of experiment with medium flow rate.

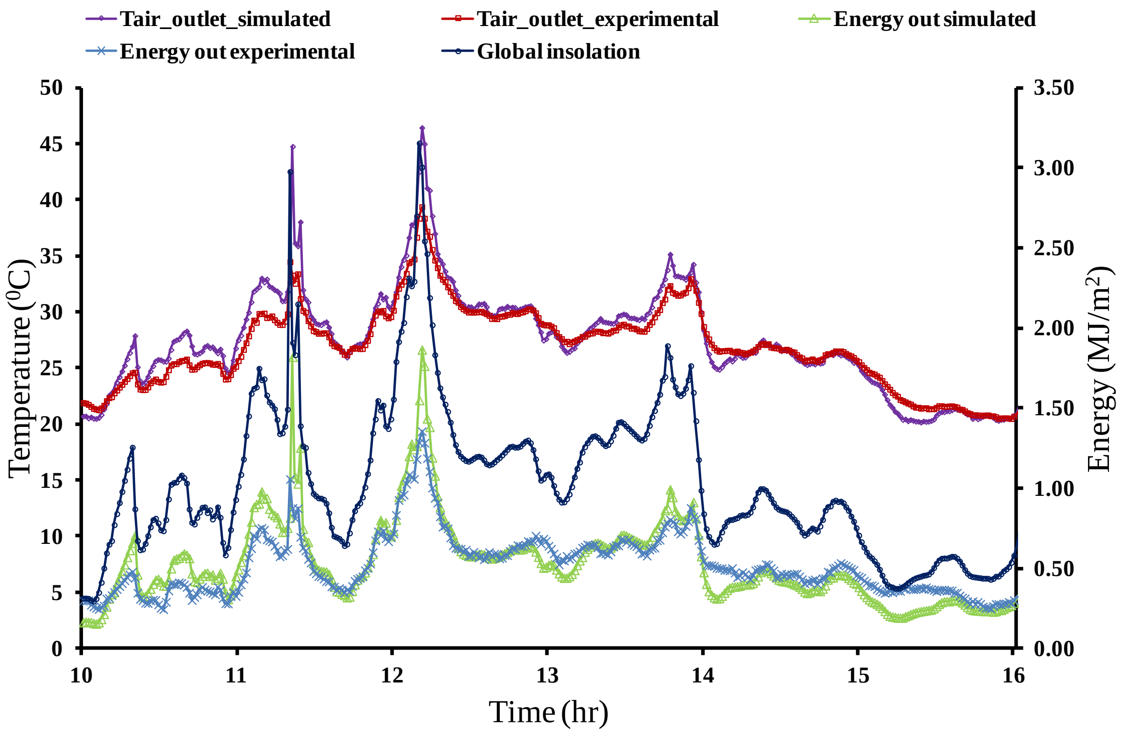

Figure 6.4: In-plane global solar irradiation, outlet air temperature and energy output from CTAH system for prototype 2 on the 15th of July, 2011.

Figure 6.5 shows in-plane global solar radiation, modelled and measured outlet air temperature as well as the measured and modelled energy output from the CTAH system on the 27th of July, 2011. It is seen that the on a day with intermittent cloud cover (27th July, 2011) the modelled output air temperature and energy output from 10 am to 4 pm followed the trend of the measured values with PME and CE of 6.3% and 5.2% respectively. Detailed measured and modelled values of in-plane solar radiation, energy output and efficiency on the 27th of July 2011 are shown in Appendix 4.3. The validation results show that the modelling errors are close to acceptance range for a representative day of experiment with low flow rate.

The experiments results for air flow rate range 0.032-0.094 kg/s/m^2 were validated with simulation model and the errors were within acceptance range. The maximum PME and CE were 6.3% and 5.2% for low limit of the air flow rate and the minimum PME and CE were 1.4% and 0.5% for the high limit of the air flow rate.

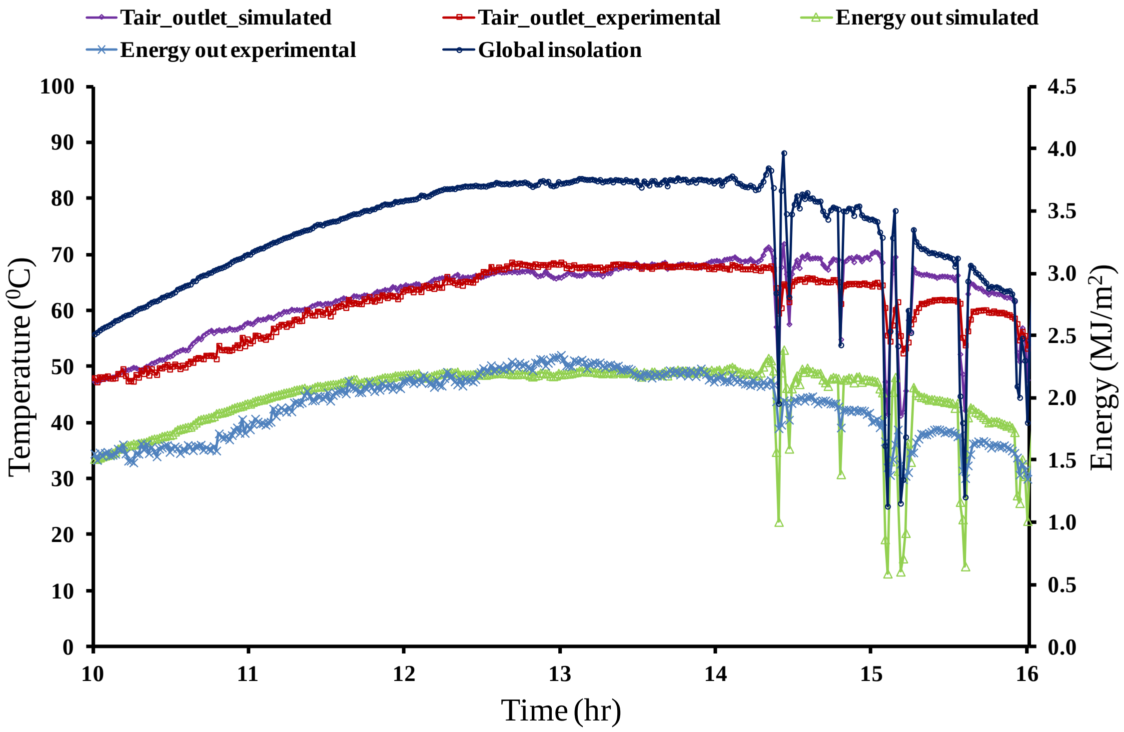

Figure 6.5. Insolation, measured and modeled outlet air temperature and energy output for prototype 2 on the 27th July, 2011

6.4 Annual performance simulation

6.4.1 Inputs

The simulation model for energy output from the CTAH system uses hourly input data consisting of ambient air temperature, inlet air temperature and global in-plane solar insolation. The model then proceeds to calculate the optical efficiency and the radiation flux concentration on the surface of the inverted absorber. The simulation time is divided into hourly intervals between 10 am and 5 pm daily. The inlet air temperature was considered to be a function of ambient temperature and was assumed to be 5 degrees above the ambient temperature.

6.4.1.1 Solar radiation

Measured monthly average daily solar irradiation data for Dublin obtained from the Irish Meteorological service over a 20 year period was used in the simulation. Figure 6.6 shows monthly average daily insolation on a horizontal surface and an inclined surface at 53^o. Insolation on the inclined plane is higher than that on the horizontal plane except between May and July.

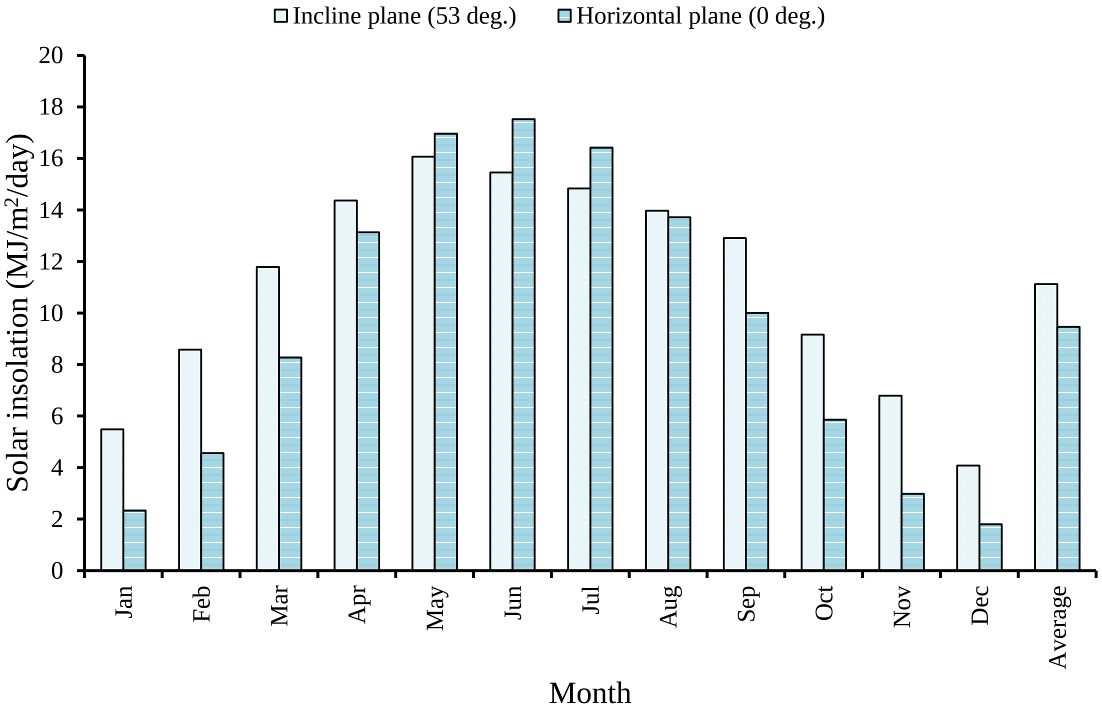

Figure 6.6: Monthly average daily solar insolation on a horizontal surface and inclined surface at 53^o

The monthly average daily solar insolation is varied between 4.1 MJ/m^2/day in December and 16.1 MJ/m^2/day in April with an annual average of 11.1 MJ/m^2/day. The insolation data was synthesised using Graham and Hollands algorithm (Graham &

Hollands, 1990) which results in a data sequence that has realistic day to day and hour to hour variability and autocorrelation.

6.4.1.2 Ambient and inlet air temperature

Figure 6.7 shows monthly average ambient and inlet air temperatures used in the simulation. The ambient air temperature for Dublin, Ireland varied between 5.0°C in January and February to 15.1°C in July. The inlet air temperature varies between 10°C in January and February to 20.1°C in July.

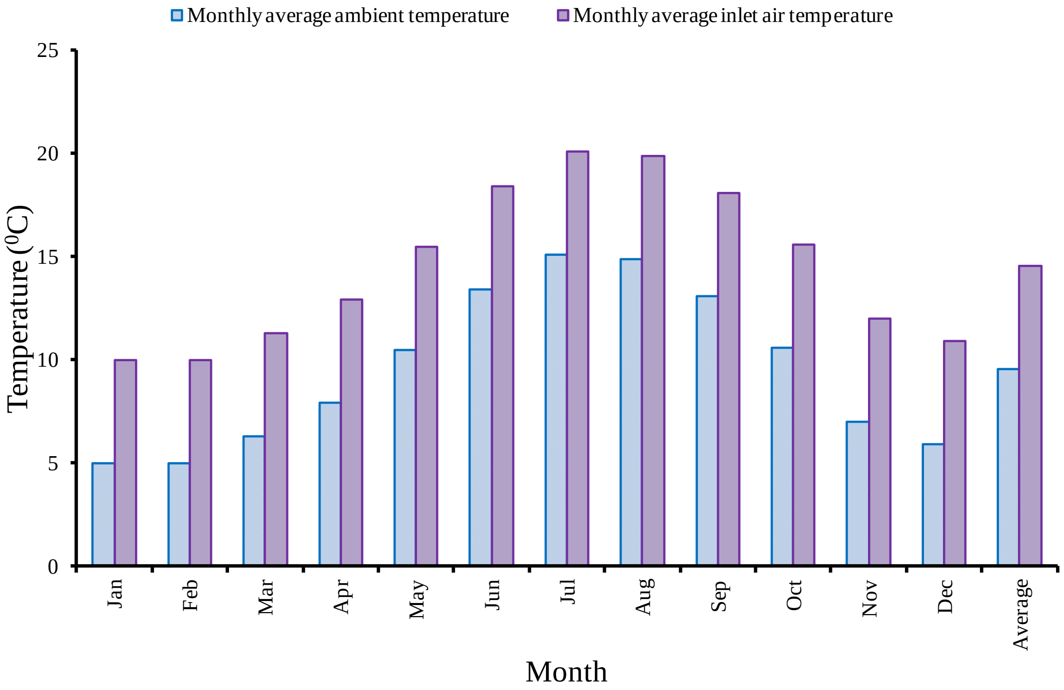

Figure 6.7: Monthly average daily ambient and inlet air temperature

The monthly ambient air temperature was obtained from ground measurements reported by the Irish Meteorological service while the inlet air temperature was considered to be 5° higher than the ambient air temperature throughout the year.

6.4.2 Annual performance simulation results

Output to the annual performance simulation model consists of outlet air temperature from CTAH for different flow rates and useful energy output for different flow rates. Figure 6.8 shows the average monthly insolation and energy out for collector aperture of 1 m^2. The data table has been added in Appendix 4.4.

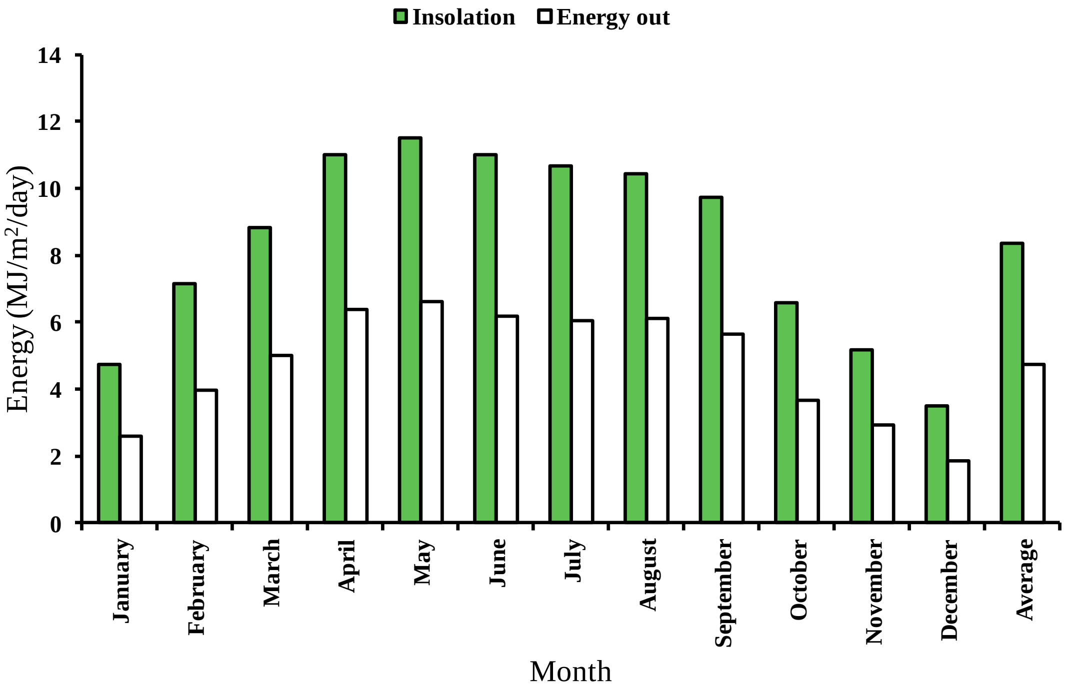

Figure 6.8: Monthly average daily insolation and energy output of CTAH for January to December

The maximum and minimum monthly average daily useful energy was calculated for May (11.5 MJ/m^2/day) and December (3.5 MJ/m^2/day). The maximum and minimum monthly average daily insolation was found for May (6.6 MJ/m^2/day) and December (1.9 MJ/m^2/day). The annual average daily insolation and useful energy out was 8.4 MJ/m^2/day and 4.8 MJ/m^2/day. Figures 6.9 and 6.10 shows the monthly average daily energy out from the CTAH system and monthly average daily solar insolation at 53^o from January to June.

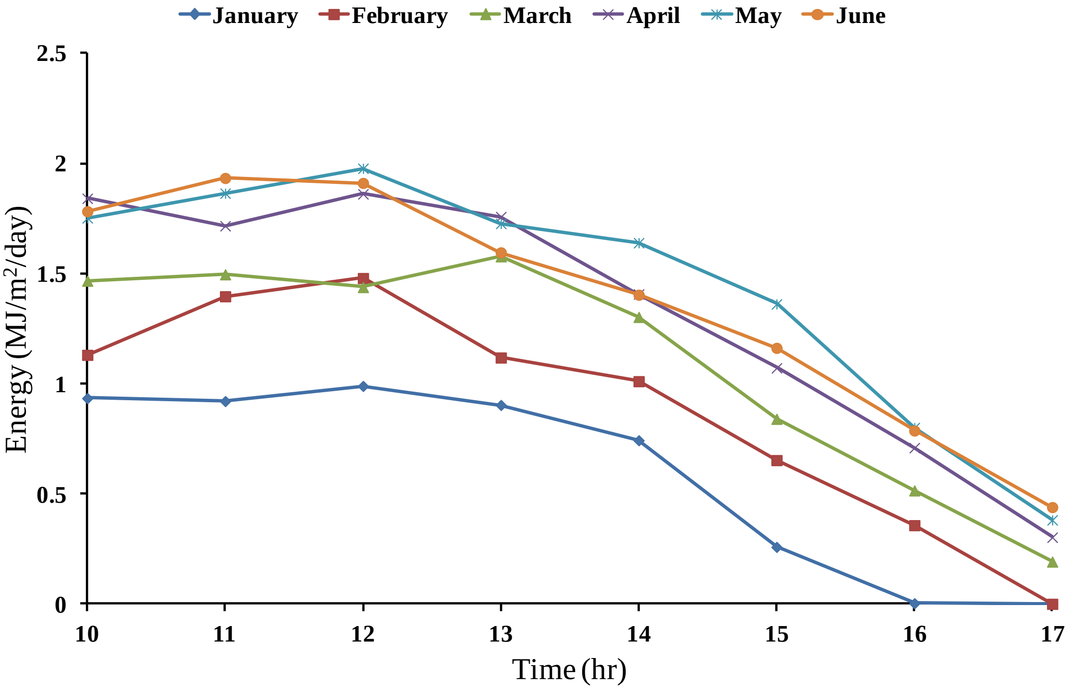

Figure 6.9: Monthly average daily insolation at 53^{o} for January to June

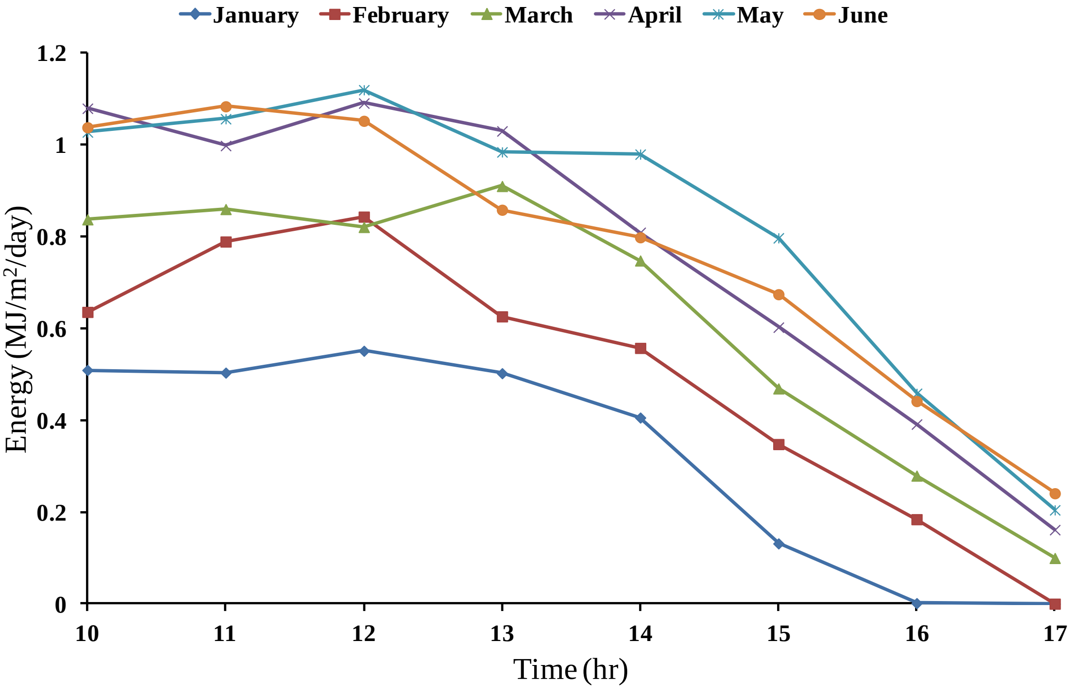

Figure 6.10: Monthly average daily energy output of CTAH for January to June

The data used to plot the figures are presented in Appendix 4.5. The months of April, May and June show higher levels of solar insolation and energy compared to January, February and March. January has the lowest level of energy out with insolation while May has the highest level of energy out with insulation.

The monthly average daily energy out and solar insolation are 0.55 MJ/m^2/day and 0.99 MJ/m^2/day respectively in January with maximum values occuring at 12 noon local time. The monthly average daily energy out and solar insolation are 1.12 MJ/m^2/day and 1.98 MJ/m^2/day in May with maximum values occuring at 12 noon local time.

Figures 6.11 and 6.12 shows the monthly average daily energy out from the CTAH system and monthly average daily solar insolation at 53^o from July to December. The data used to plot the figures are presented in Appendix 4.6.

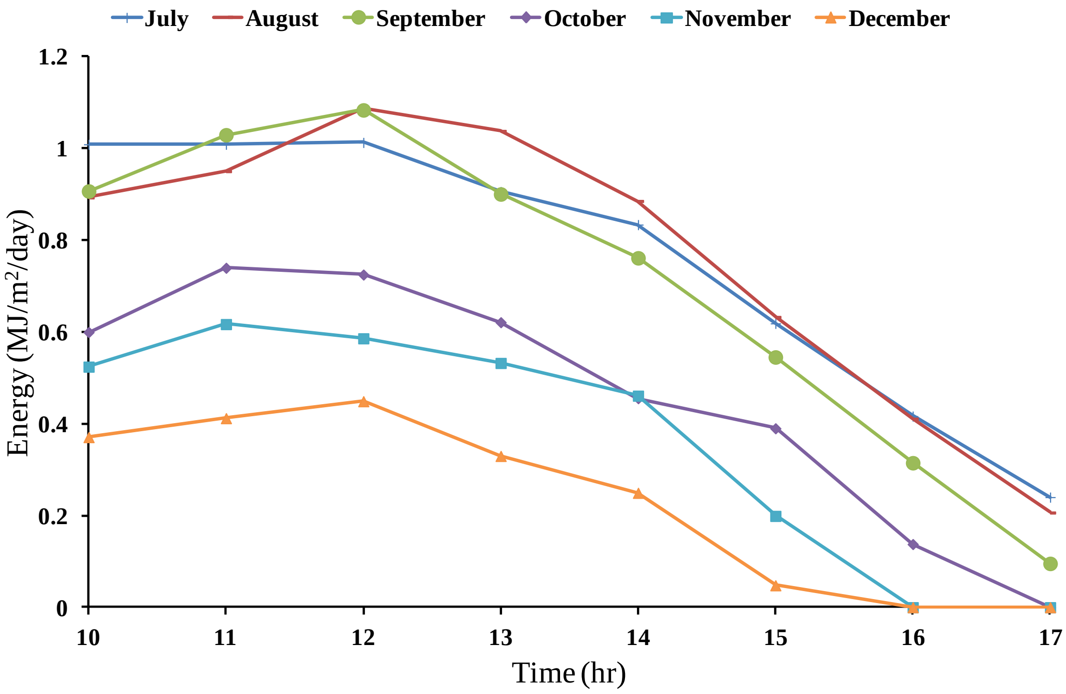

Figure 6.11: Monthly average daily energy output from July to December

The months of July, August and September have higher levels of insolation and energy out compared to October, November and December. December shows the lowest level of energy out with insolation while August has the highest level of energy out with insolation. The monthly average daily energy out and solar insolation are 1.09 MJ/m^2/day and 1.85 MJ/m^2/day respectively in January. The monthly average daily energy out and solar insolation are 0.43 MJ/m^2/day and 0.85 MJ/m^2/day respectively in May.

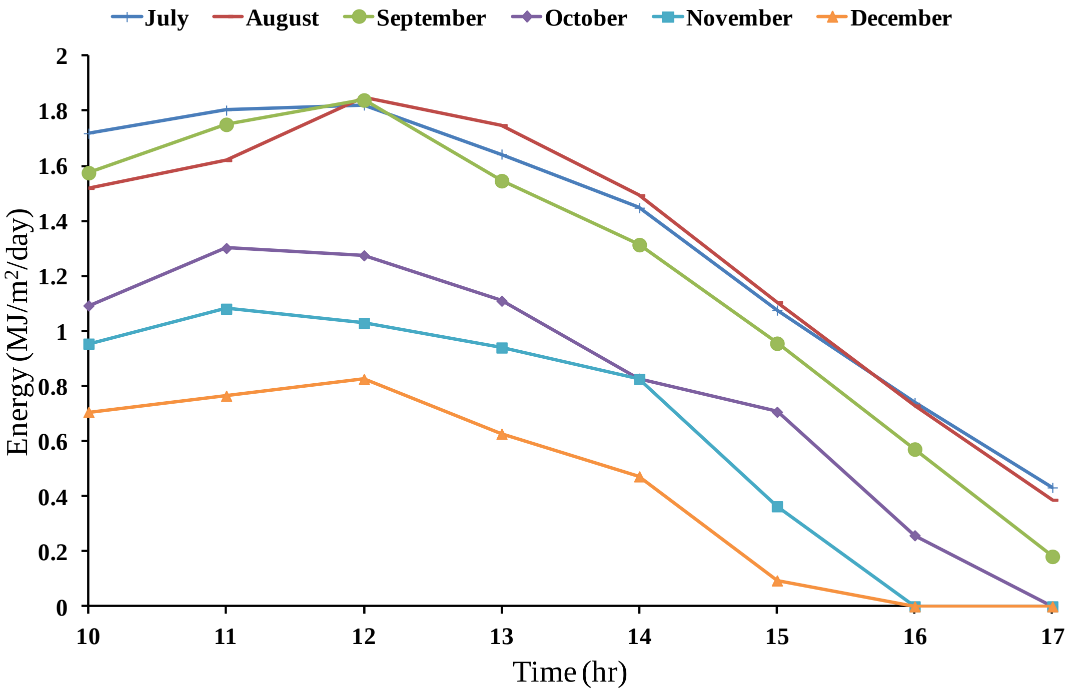

Figure 6.12: Monthly average daily insolation at 53^o from July to December

6.5 Summary

A model to determine the energy output from the CTAH system was developed and implemented using Matlab. The model was validated using field trial data for three days with clear, heavily overcast and intermittent cloud covered sky which are typical of

Irish weather conditions. On the day with clear sky, the PME and CE were 1.4% and 0.5%. On the day with heavily overcast sky, the PME and CE were 3.4% and 3.8% while on the day with intermittent cloud cover the PME and CE were 6.3% and 5.2%.

The estimated annual average daily insolation and useful energy out were 8.4 MJ/m^2/day and 4.8 MJ/m^2/day respectively. The total annual insolation and energy out were found to be 3,053.1 MJ/m^2 and 1743.6 MJ/m^2 respectively. This is the amount of useful energy that can be generated from the available solar energy using CTAH to raise the air temperature at the outlet of the collector. The economic analysis will be carried out in the following chapter to evaluate the feasibility of CTAH in domestic dwelling application.

CHAPTER 7

TECHNO-ECONOMIC AND ENVIRONMENTAL PERFORMANCE ANALYSIS

The aim of this chapter is to conduct a technological, economic and environmental analysis of the CTAH system for thermal heating applications in domestic dwellings. Objectives of this chapter include:

- To access the technical aspects of the CTAH system in solar thermal heating applications;
- To access the economical performance using various investment appraisal techniques;
- To evaluate the environmental aspects by Greenhouse Gas (GHG) emission analysis.

7.1 Introduction

Technological, economic and environmental aspects of the CTAH system are discussed in this chapter for different heat demand scenarios. The aperture size, heat demand scenarios and discount rate are vital factors in determining the viability of solar thermal collectors. In previous research under Irish weather conditions building integrated solar thermal collectors with low aperture area ($\leq 4m^2$) were found to be uneconomical. The building integrated flat plate Solar Water Heater's (SWH) had simple payback periods ranging between 10.2 and 48.2 years under Irish weather condition depending on different type of auxiliary heaters used (Ayompe, 2011).

In another study carried out by Sreekumar (2010), the payback period for a roof integrated solar air heating system with an aperture of 46 m^2 used to dry fruits and vegetables in India was calculated to be 0.58 year. Fudholi et al. (2001) reported a payback period of 2.33 years for a double pass solar collector with an aperture of 11.72 m^2 designed for seaweed drying in Malaysia. The payback period for the above two cases were economical due to their constant heat demand and high levels of insolation in the locations where the studies were undertaken.

The heating system designed in this chapter is a closed loop solar collector which can be used in domestic dwelling with limited energy demand and lower aperture area for solar thermal applications. The CTAH system's annual thermal performance was compared with that of conventional solar thermal collectors (FPC/ETC) in a domestic dwelling with space and water heating demand. The amount of displaced CO_2 emissions resulting from the use of different fuel types was used as a measure of the environmental performance.

7.2 Assumptions

1) The domestic dwelling considered in this study had roof space that could accommodate a CTAH system with aperture area ≤ 8 m^2.
2) The heat demand was for a 215 m^2 house in Galway, Ireland and the water heating load was for 200 litre/day.
3) The domestic dwelling is considered to have 4-6 occupants.
4) The CTAH system is integrated with the boiler.

5) In domestic dwelling energy generated by the CTAH system can be used directly for space heating if there is any space heating demand available and surplus energy can be used to heat water via a heat exchanger.

7.3 Technical, economic and environmental aspects

7.3.1 Technical aspects of thermal heating operation using CTAH

The CTAH system installed in a domestic dwelling delivers the amount of fresh air at the required temperature using an air mixer and control valves operated by a controller. Two operating scenarios considered for the air heating system in this study are: winter and summer operation depending on space heating and water heating requirements.

According to Environ building standard (Environ, 2009): *"The minimum capacity of mechanical ventilation with heat recovery system should be based on the calculated general ventilation rate, adjusted to allow for air infiltration due to permeability of the building fabric."*

The calculated general ventilation rate can be based on the number of occupants or floor area as suggested by Environ building standard (Environ, 2009a)

a) 5 l/s plus 4 l/s per person. This means for five people living in domestic dwelling the required ventilation rate is 25 l/s. This is based on two occupants in the main bedroom and a single occupant in all other bedrooms. This should be used as the default value. If a greater level of occupancy is expected, then 4 l/s per occupant has to be added.

b) 0.3 l/s per m^2 internal floor area which means 64.5 l/s for 215 m^2 in domestic dwelling.

Another way of calculating the required fresh air is in terms of volume of the space. The adjustment to the calculated general ventilation rate to allow for air infiltration is 0.04V l/s, where V is the gross internal volume of the dwelling in m^3. However, selecting a flow rate depending on floor area is convenient for estimation.

Incorporation of CTAH into domestic dwelling for space heating can be carried out by adapting any of six types of system modification suggested by ‘Task 19’ (Hastings & Morck, 2000) detailed in section 2.2.4. The type-f which is collector heated air transferred to water via an air/water heat exchanger has been adapted in this analysis to model water heating using heated air.

The annual operation of CTAH was divided into two scenarios: summer operation of CTAH for water heating and winter operation for space heating. Because the demand of space heating during summer time is nearly zero. Figure 7.1 shows a schematic diagram of the summer operation of the CTAH system incorporated into a building.

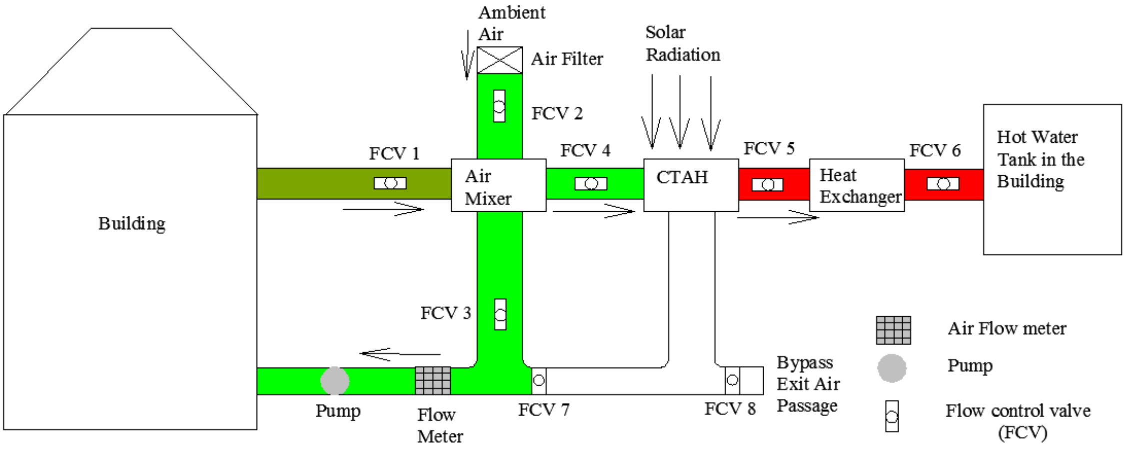

Figure 7.1: Summer operation of the air heating system

During summer, the space heating requirement is at minimum level which will be discussed later in this chapter. Flow control valve 1 (FCV1) remains open which allows air from the building to flow through an air mixer. Flow control valve 2 (FCV2) and flow control valve 4 (FCV4) allow the mixed air to flow through the CTAH system's collector where solar radiation is captured to heat air. The high temperature air flows through flow control valve 5 (FCV5) and flow control valve (FCV6) to heat water. Flow control valve 7 (FCV7) remains closed to restrict air from flowing towards the building.

Flow control valve 8 (FCV8) is used as a bypass valve to prevent the building from overheating. Ambient air flows through FCV2 and FCV3 to allow fresh air into the building in order to satisfy building standard (Environ, 2009) requirements. The flow meter measures the amount of air flowing to the building.

Figure 7.2 shows a schematic diagram of the winter operation of the CTAH system incorporated into a building. In winter, hot air from the CTAH system is used for space and water heating.

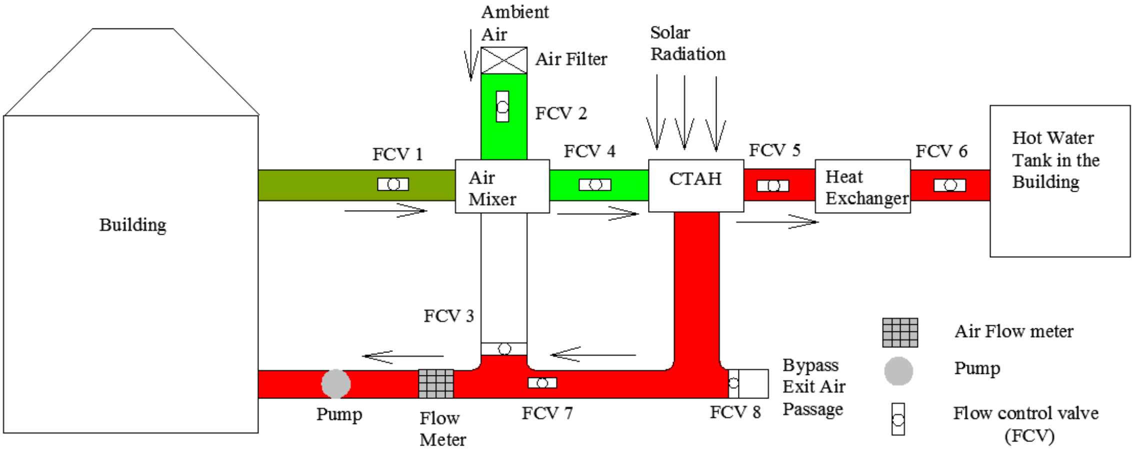

Figure 7.2: Winter operation of the air heating system

FCV1 remains open which allows air from the room to flow through an air mixer. FCV2 and FCV4 allow the mixed air to flow through the CTAH collector where solar radiation is captured to heat air. The heated air flows through FCV5 and FCV6 to heat water. The heated air also flows through FCV7 to the building in order to satisfy building standard (Environ, 2009) requirements. The flow meter measures the amount of air flowing into the building. FCV3 remains closed to restrict air from flowing towards the air mixer. FCV8 is used as a bypass valve to prevent the building from overheating. An auxiliary heating system (boiler) is used to heat air to the required temperature when solar radiation is low or not available.

7.3.2 Economic aspects of thermal heating operation using CTAH

Economic appraisal techniques used to assess the financial performance of the CATH system consist of: Simple Payback Period (SPP); Net Present Value (NPV); Benefit/Cost Ratio (BCR).

7.3.2.1 Simple payback period

Simple Payback Period (SPP) or Payback Period (PBP) is one of the most commonly used cost analysis methodologies. The SPP determines the number of years required to recover an initial investment through project returns (Capehart et al., 2008). The formula of payback period is the ratio of the initial investment, ΔC to the annual cost savings, S is given as (Masters, 2004).

$$\text{SPP} = \frac{\text{Initial investment}}{\text{Annual cost savings}} \qquad 7.1$$

$$\text{SPP} = \frac{\Delta C}{S} \qquad 7.2$$

Annual revenues are the energy cost avoided annually, which consists of the annual energy savings multiplied by the cost per energy unit. In case of the CTAH system annual cost saving was calculated by multiplying the unit cost of electricity with the total amount of energy produced. When deciding between two or more competing projects, the usual decision is to accept the one with the shorter payback period.

The advantage of the SPP is its simplicity, and it is easily understood by workers and management. It does provide a rough measure of the worth of a project. The primary drawbacks of this method are that the timing of cash flows is ignored and cash flows beyond the payback period are not accounted (Kaplan, 1983). No specific lifetime estimate of the project is required, but it is assumed that the lifetime is longer than the SPP. These limitations mean the SPP tends to favour shorter lived projects, a bias that is often economically unjustified. However, using the SPP in conjunction with one of the discounted cash flow methodologies can provide better understanding of an investment's worth (Capehart et al., 2008).

7.3.2.2 Net Present Value

The net present value (NPV) method considers the time value of money with cash savings (cash inflows) in earlier years being of higher value than the same amount in a later year. It achieves this by evaluating the present value of any future cash flow using an assumed interest rate which is usually referred to as a discount rate. Discounting is the opposite process to compounding which is used to determine the future value of present cash flows (Beggs, 2002). NPV is expressed mathematically as (Power et al., 2009):

$$\mathrm{NPV} = \mathrm{CIF} - \mathrm{COF} \tag{7.3}$$

where,

NPV net present value (€)

CIF present value of cash inflows (€)

COF present value of cash outflows (€)

The present value of a future cash flow is given as (Beggs, 2002):

$$PV = \frac{FV}{(1+d)^n} \qquad 7.4$$

where,

PV Present value of a cash flow (€)

FV Future value of a cash flow (€)

d Discount rate (%)

n Period of investment (years)

The discount rate is the cost of capital or interest rate which has to be paid on acquiring the capital to invest in the project.

7.3.2.3 Benefit/Cost ratio

A benefit/cost ratio (BCR) also known as a savings/investment ratio (SIR), calculates the present worth of all benefits then calculates the present worth of all costs and takes the ratio of the two sums. The BCR or SIR is another alternative economic decision making criterion (Thuesen & Fabrycky, 2000). The Equation of BCR can be defined as:

$$BCR = \frac{B_{equivalent}}{C_{equivalent}} \qquad 7.5$$

Where,

BCR = Benefit/Cost Ratio

$B_{equivalent}$ = Equivalent benefits (€)

$C_{equivalent}$ = Equivalent costs (€)

7.3.3 Environmental aspects of thermal heating operation using CTAH

The CTAH system uses solar radiation as its primary source of energy which has no associated GHG emissions. In order to access the environmental impact of the CTAH system, the quantities of avoided CO_2 emissions were calculated and compared with those from four different types of heating systems powered by electricity, natural gas, oil and wood pellets.

7.3.3.1 Policy context of CO_2 emission

The world's economies need to get on a sustainable energy path to tackle climate change and ensure economic and social growth based on secure, diverse and affordable energy supply. Ireland, as part of the international community will have to continue to playing a proactive role in the work of the International Energy Agency (IEA) and other international fora, including the United Nations Sustainable Development Commission (UNSDC), to overcome global energy challenges including those for developing countries.

Policies to encourage the most efficient supply and use of energy can, according to the IEA, contribute to almost 80% of avoided CO_2 emissions by 2030. In that context technological breakthrough is essential for a sustainable energy future. The IEA also offers a Beyond Alternative Policy Scenario which sees even more ambitious goals for 2030 and which would take radical technology breakthrough. Irish energy policy is set firmly in the global and EU context which has put energy security and climate change among the most urgent international challenges. The White Paper sets out the actions to be taken in response to the energy challenges facing Ireland. The objective is to deliver a sustainable energy future, starting now, with a time horizon of 2020 but also looking beyond that (SEAI, 2007).

The EU has committed to reduce its overall greenhouse gas (GHG) emissions to at least 20% below 1990 levels by 2020. With ambitious targets towards reduction of primary energy consumption, adoption of renewable and energy efficiency measures set for 2020 by the European Parliament, Europe is seen as taking the lead in efforts to address climate change by striving to transform itself into a low carbon economy while increasing its energy security (O'Leary et al., 2008).

The need to meet these obligations has resulted in countries, like Ireland, to seek alternative methods for energy production which are more efficient and effective. If these limits are not achieved, penalties in the form of fines will be imposed.

Renewable and sustainable energy technologies have the potential to reduce Ireland's dependence on fossil fuels, increase economic competitiveness and contribute towards GHG emissions reduction as set by European Union (EU) member states. The residential sector accounted for 26.5% of EU energy requirements in 2009 and was the second largest after transport with 33.2%. CO_2 emission from the sector was 431.9 $MtCO_2$ which accounted for 10.7% of the total CO_2 emissions within the EU (European Commission, 2012). This sector therefore has great potential to enable the EU to achieve its greenhouse gas emissions reduction targets.

Implementation of CTAH into domestic dwelling can reduce the emission significantly compare to conventional primary heating source electric heater, gas boiler and oil boiler. Basically it is a green technology which provides heat from captured solar energy and produce negligible amount of CO_2 compare to delivered energy.

7.3.3.2 Calculation of CO_2 emission

7.3.3.2.1 CTAH system CO_2 emission

In a building integrated with the CTAH system, the total quantity of emitted CO_2 is the sum of the quantity of CO_2 associated with electricity imported from the grid only. This is expressed as:

$$EC_{CTAH} = E_{imp} CI_{electricity} \qquad 7.6$$

where,

EC_{CTAH}	emitted carbon associated with electricity imported from the grid for CTAH ($kgCO_2$)
E_{imp}	electricity imported from the grid (kWh)
$CI_{electricity}$	carbon intensity of grid electricity ($kgCO_2$/kWh)

7.3.3.2.2 Boiler CO_2 emission

In a house fitted with a condensing gas boiler, the amount of CO_2 emitted is the sum of emissions due to electricity imported from the grid and heat generated by the boiler. This is expressed as:

$$EC_b = E_{imp} CI_{electricity} + \frac{Q_h CI_{electricity}}{\eta_{gas,b}} \qquad 7.7$$

Where

EC_b	emitted carbon associated with electricity imported from the grid for boiler ($kgCO_2$)
E_{imp}	imported electricity from grid (kWh)
$CI_{electricity}$	carbon intensity of grid electricity ($kgCO_2$/kWh)
Q_h	quantity of heat generated by CTAH (kWh)

CI_{ng}	carbon intensity of natural gas ($kgCO_2/kWh$)
$\eta_{gas,b}$	thermal efficiency of condensing gas boiler (%)

7.3.3.2.3 Electric heater CO_2 emission

In a house fitted with an electric heater, the amount of CO_2 emitted is the sum of emissions due to electricity imported from the grid due to generate heat by the electric heater and to distribute heat using a fan. This is expressed as:

$$EC_{elc,heater} = E_{imp\_fan} CI_{electricity} + \frac{Q_h CI_{electricity}}{\eta_{elc,heater}} \tag{7.8}$$

$$E_{imp,fan} = h_{operation} E_{consumed} \tag{7.9}$$

Where

$EC_{elc,heater}$	emitted carbon associated with electricity imported from the grid ($kgCO_2$)
$E_{imp,fan}$	Imported electricity from grid to operate fan (kWh)
$h_{operation}$	Total pump hours (hours)
$E_{consumed}$	Energy consumed by the fan (kWh)
CI_{ge}	Carbon intensity of grid electricity ($kgCO_2/kWh$)
Q_h	Quantity of heat generated by CTAH (kWh)
$\eta_{elc,heater}$	Thermal efficiency of electric heater (%)

7.4 Application of CTAH in domestic dwelling

Heat recovery from exhaust air is possible using a building integrated CTAH system. Vents in the house cause a lot of heat loss due to uncontrolled infiltration of ambient air which increases the heat requirement. But this ventilation is compulsory to meet building regulation (Environ, 2009). The current practice in Irish houses used to fulfil this requirement is through the provision of manually controlled vents in each habited room. However, the manual operation of vents is not efficient. The CTAH system can easily be retrofitted with existing domestic dwellings.

7.4.1 Optimisation of CTAH aperture considering thermal demand profile

7.4.1.1 Space heating demand in domestic dwelling

The space heating demand in domestic dwellings varies due to floor size, number of occupants and location etc. The space heating demand profile for the 215 m^2 house in Galway, Ireland was used in this analysis. The recorded space heating annual demand was 1,195 kWh (Colclough et al., 2011). Table 7.1 shows the monthly demand profile for space heating.

7.4.1.2 Water heating demand in domestic dwelling

The average daily hot water demand was assumed to be 200 litres (0.2 m^3) for domestic dwelling 4-6 persons. Assuming an average inlet water temperature of 10^{o}C and an outlet water temperature 60^{o}C, the daily water heating demand was calculated using Equations 7.10 and 7.11.

$$\text{Daily energy requirement} = MCp\Delta T \qquad 7.10$$

$$M=\rho_{water}V_{\mathrm{water}} \qquad 7.11$$

Where,

M = 200 kg, Cp = 4200 J/kgK

The daily energy requirement was calculated as 42 MJ (11.67 kWh). The annual hot water requirement was calculated as 4,259 kWh.

Table 7.1: Space heating demand for a house in Galway

Month	Jan	Feb	Mar	Apr	May	Jun	Jul	Aug	Sep	Oct	Nov	Dec
Heat required (kWh)	291.3	223.6	120.3	69.6	0	0	0	0	0	36.6	86.8	367

7.4.1.3 Total thermal energy demand for the domestic dwelling

Figure 7.3 shows the monthly space heating, water heating and total thermal energy demand in the domestic dwelling. The data table has been added in Appendix 5.1.

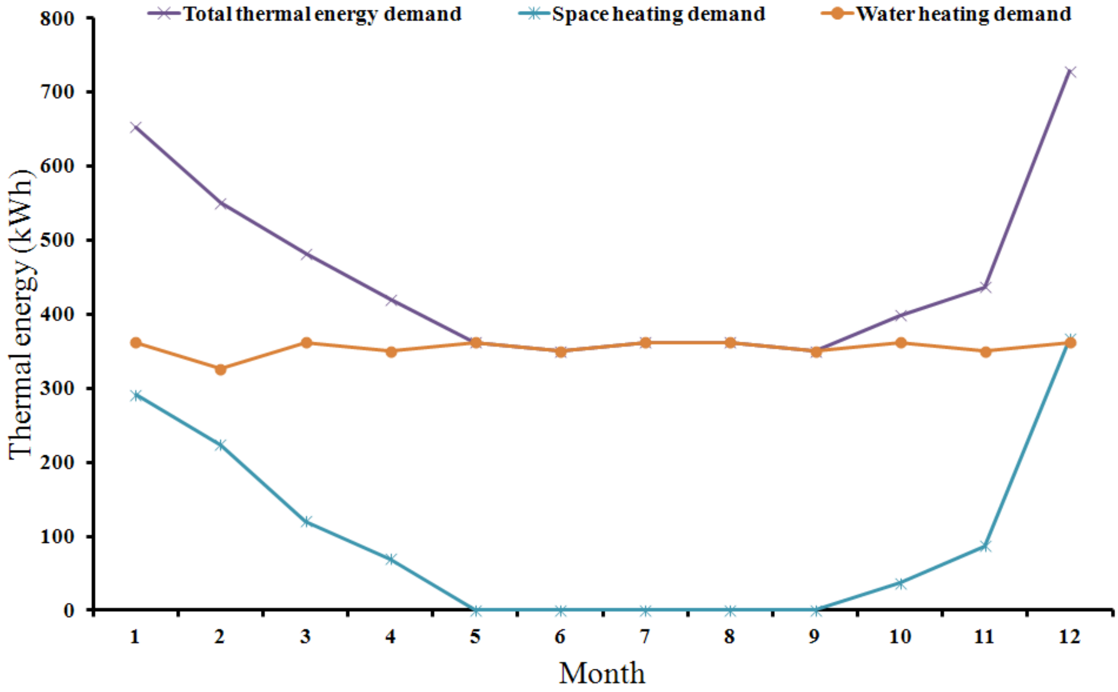

Figure 7.3: Total thermal energy, space and water heating demand for domestic the dwelling

The space heating demand was negligible from May to September and irregular during the remaining months. A solar energy collect designed to deliver the required heat during winter months would be ideal during summer months but results in an increase in the manufacturing cost. An optimised space heating system cannot be designed based on available solar energy to meet this unequal heating demand. The water heating demand was found to be constant throughout the year. The water heating demand was combined with space heating demand to obtain the annual heat demand profile. It was thus necessary to optimise the collector aperture based on cost and energy demand.

7.4.1.4 Sizing the CTAH aperture considering thermal demand for the domestic dwelling

Table 7.2 shows the monthly calculated solar fraction; thermal (water heating and space heating) deficit and surplus for aperture area of CTAH form 1 m^2 to 8 m^2. The sizing of CTAH aperture is crucial because during summer months from May to September there is no space heating demand. Again the space heating demand is very high in the months of November and December. The monthly solar fraction was calculated using individual monthly energy generated by CTAH and monthly solar water and space heating demand. The monthly deficit and surplus were also calculated by subtracting the demand from the generated energy.

Figures 7.4 to 7.6 shows the surplus/deficit energy for different aperture sizes of the CTAH system required for solar space and water heating. Figure 7.4 shows energy generated by the CTAH system, thermal heating energy demand for the domestic dwelling and surplus/deficit for 1 m^2 aperture size. The solar fraction for water and space heating varies for different aperture sizes of the CTAH system.

Table 7.2: Solar fraction for space heating and water heating for different aperture size of CTAH

	(1 m^2 aperture)			(4 m^2 aperture)			(8 m^2 aperture)			
Month	Space heating Fraction	Water heating Fraction	Space +Water heating deficit (%)	Space Heating Fraction	Water Heating Fraction	Space +Water heating deficit (%)	Space Heating Fraction	Water heating Fraction	Space +Water heating deficit (%)	Space +Water heating surplus (%)
Jan	0.08	0.00	0.97	0.31	0.00	86.27	0.62	0.00	72.53	0.00
Feb	0.14	0.00	0.94	0.55	0.00	77.48	1.00	0.07	54.97	0.00
Mar	0.36	0.00	0.91	1.00	0.15	64.11	1.00	0.62	28.21	0.00
Apr	0.76	0.00	0.87	1.00	0.41	49.42	1.00	1.00	0.00	1.16
May	Zero demand	0.16	0.84	Zero demand	0.63	36.89	Zero demand	1.00	0.00	26.21
Jun	Zero demand	0.15	0.85	Zero demand	0.59	41.09	Zero demand	1.00	0.00	17.82
Jul	Zero demand	0.14	0.86	Zero demand	0.58	42.45	Zero demand	1.00	0.00	15.10
Aug	Zero demand	0.15	0.85	Zero demand	0.58	41.90	Zero demand	1.00	0.00	16.19
Sep	Zero demand	0.13	0.87	Zero demand	0.54	46.33	Zero demand	1.00	0.00	7.34
Oct	0.86	0.00	0.92	1.00	0.25	68.29	1.00	0.60	36.57	0.00
Nov	0.28	0.00	0.94	1.00	0.03	77.73	1.00	0.31	55.46	0.00
Dec	0.04	0.00	0.98	0.17	0.00	91.22	0.35	0.00	82.44	0.00
Annual	0.36	0.06	0.90	0.72	0.31	60.27	0.85	0.63	27.52	6.98

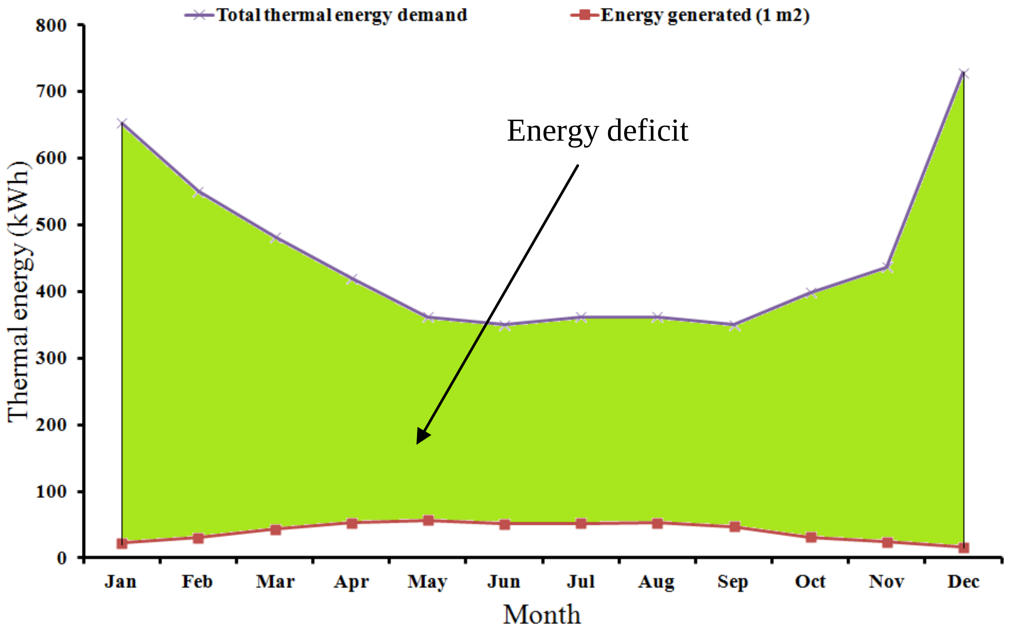

Figure 7.4: Energy generated, thermal heating energy demand for 1 m^2 CTAH aperture

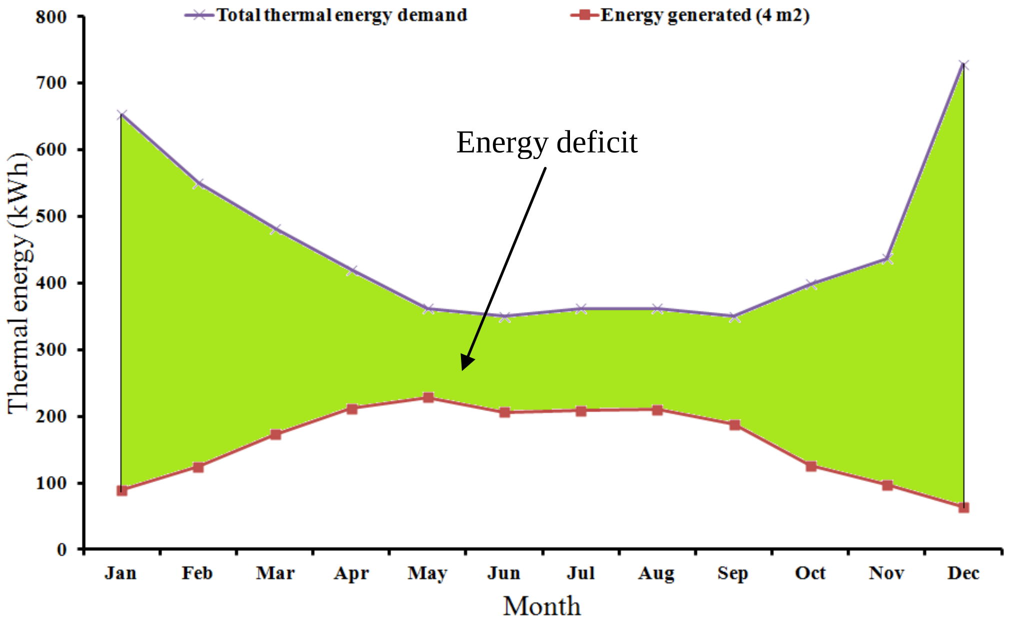

Figure 7.5: Energy generated, thermal heating energy demand for 4 m^2 CTAH aperture

The annual solar fraction for space and water heating for the 1 m^2 CTAH system was 36% and 6% respectively. Figure 7.5 shows energy generated by CTAH, thermal heating energy demand for domestic dwelling and surplus/deficit for 4 m^2 aperture size. An increase of the aperture to 4 m^2 increases the solar fraction for water and space heating to 72% and 31% respectively. Figure 7.6 shows energy generated by the CTAH system, thermal heating energy demand for the domestic dwelling and surplus/deficit for 8 m^2 aperture size.

The Solar fraction for space and water heating can be increased to 85% and 63% respectively for 8 m^2 aperture of the CTAH system. However, an increase in the aperture size also increases the cost of the system and the available area for installation.

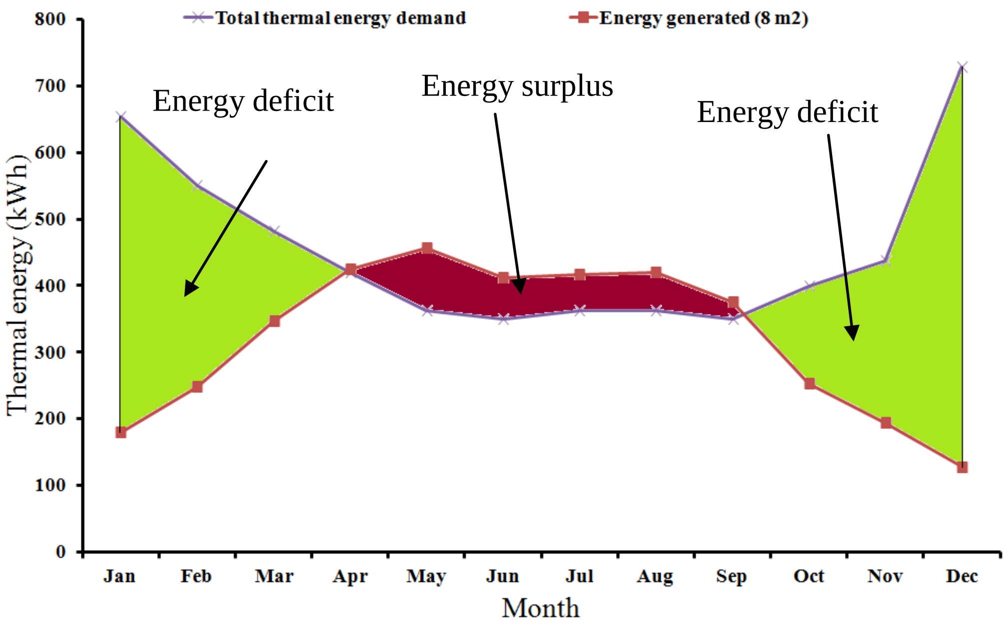

Figure 7.6: Energy generated, thermal heating energy demand for domestic dwelling and surplus/deficit for 8 m^2 aperture of the CTAH system

The solar fraction for space heating improves only 13% for doubling the aperture from 4 to 8 m^2 which increases the manufacturing cost of the system and installation space requirement. The optimised aperture area of the CTAH system was calculated as 4 m^2 with the solar fractions for water and space heating of 72% and 31% respectively.

The optimised aperture size of the solar heating collector reduces required initial investment. However, the heating system is unable to deliver 100% heating energy required for space heating and water heating.

7.4.2 Technical and Economic parameters

The energy generated by the CTAH system from solar energy can be used throughout the year in domestic dwellings. Table 7.3 shows a summary of the energy demand for space and water heating and solar fractions for different sizes of the CTAH system's aperture from 1 m^2 to 8 m^2 for the domestic dwelling.

Table 7.3: Energy demands and solar fractions

	Aperture Area (m^2)		
	1	4	8
Annual solar thermal energy generated by CTAH (kWh)	481.84	1927.36	3854.73
Annual space heating demand (kWh)	1195.20	1195.20	1195.20
Annual water heating demand (kWh)	4259.55	4259.55	4259.55
Solar fraction for space heating	0.36	0.72	0.85
Solar fraction for water heating	0.06	0.31	0.63

The calculated annual space and water heating demand were 1,195 kWh and 4,260 kWh respectively. The annual thermal energy generated by the CTAH system increased from 482 kWh to 3,855 kWh when the aperture area is increased from 1 m^2 to 8 m^2. The solar fraction for space heating increases from 36% to 85% and solar fraction increases from 6% to 63% when the aperture area is increased from 1 m^2 to 8 m^2. The economic parameters used in this analysis are presented in Table 7.4.

Table 7.4: Economic parameters

$^+$ Sustainable Energy Authority Ireland calculator (SEAI Calculator, 2012)

Description of parameters	Units	Value
Electricity cost	(€/kWh)	0.15$^+$
Fuel cost:		
Gas	(€/kWh)	0.0474$^+$
Pellet	(€/kWh)	0.0469$^+$
Oil	(€/kWh)	0.0831$^+$
System life	(Years)	20
Discount rate	(%)	8
Annual electricity escalation rate	(%)	3
Annual gas escalation rate	(%)	3

The electricity cost/unit was considered €0.15. Oil was the most expensive fuel compared to natural gas and wood pellets. The useful life for all cases was considered as 20 years. The discount rate and fuel annual escalation rate were considered as 8% and 3% respectively. The CTAH system life was considered 20 years.

7.4.3 Cost estimation of the CTAH system for the domestic dwelling

The natural gas or oil boiler was considered as the primary energy source to meet the thermal demand in the domestic dwelling. A comparison of the economic performance was carried out for different scenarios where the CTAH system and SWH (with FPC and ETC) was integrated in domestic dwellings with and without a boiler.

7.4.3.1 Primary cost of solar thermal collectors for domestic dwelling

Table 7.5 shows the installed cost of different solar thermal heating systems used in this analysis. It is seen that the costs of the CTAH system is comparable to that of the SWH with FPC but lower than the cost of the SWH with ETC. Table 7.6 shows a detailed breakdown of the installed cost of a 4 m^2 CTAH system. The prices of the system elements used in this analysis were adapted from the suppliers to develop the experimental prototype.

Fabrication and other miscellaneous expenses account for about 50% of the components cost. Installation cost accounts for about 20% of the components cost. Carbon fibre was used as absorber material. Compared to conventional solar thermal absorber materials carbon fibre is cheaper and with low weight. The primary cost for a 4 m^2 CTAH system was calculated as €1,800.

7.4.3.2 Annual operating cost estimation for the domestic dwelling

7.4.3.2.1 House with boiler and CTAH system

This is a combination of a boiler and the CTAH system integrated in a domestic dwelling. The available solar radiation is captured by the solar collector which can be used for water and space heating application. The annual thermal energy demand was calculated as a combination of space and water heating. The annual thermal energy demand of the domestic dwelling and energy generated by 4 m^2 aperture of the CTAH system was 5,454.8 kWh and 1,927.4 kWh respectively.

Table 7.7 shows the solar fraction and energy generated by the CTAH system and SWH with ETC and FPC. The ETC generated more heat for water heating (solar fraction (SF) of 53.6% for water heating) than the FPC (SF of 38.6%) and CTAH (SF of 31%). The CTAH system also generated 860.54 kWh of heat which accounted for 72% of the space heating requirement.

Table 7.5: Installed cost of different solar thermal heating systems

Description of parameters	Units	Value
FPC	(€)	4,400*
ETC	(€)	5,000*
CTAH	(€)	1,800

*(Ayompe, 2011)

Table 7.6: Primary cost of 4 m^2 CTAH

Name of Elements	Price (€)/m^2	Quantity (m^2)	Component Cost (€)	Total Cost (€)
Glazing (Opti white)	80.0	4.0	320	
Anti reflecting coating	45.0	4.0	180	
Reflector	55.0	4.0	220	
Absorber material	23.9	2.0	48	
Insulation material	4.2	4.0	17	
		Subtotal		785
Fabrication and other cost	50% of component cost			392
Fan				223
Integration of heat exchanger for water heating				400
		Total		1800

Table 7.7: Solar fraction and energy generated by the CTAH system and SWH

Type of collector	Solar Fraction (%)	Energy generated (kWh)
ETC (3 m^2)	40.2% *	1,712
FPC (4 m^2)	38.6%*	1,644
CTAH (for water heating) (4 m^2)	31%	1,320
CTAH (for air heating) (4 m^2)	72%	861

*(Ayompe, 2011)

The fraction of generated energy for space heating can be calculated as:

$$E_{f\_air} = E_{a\_CTAH} \times F_{air} \qquad 7.12$$

Where,

E_{f_air} Generated energy fraction for space heating

E_{a_CTAH} Total annual thermal energy generated by CTAH (kWh)

F_{air} Solar fraction for space heating

The generated energy fraction for water heating can be calculated as:

$$E_{f\_water} = E_{a\_CTAH} \times F_{water} \qquad 7.13$$

Where,

E_{f_water} Generated energy fraction for water heating (kWh)

E_{a_CTAH} Total annual energy generated by CTAH (kWh)

F_{water} Solar fraction for water heating

The annual thermal energy generation required in the case of the boiler and CTAH system integrated in the building can be calculated as:

$$E_{boiler\_CTAH} = \frac{\left(ED_a - E_{a\_CTAH}\right)}{\eta_{boiler}} \qquad 7.14$$

Where,

E_{boiler_CTAH} Annual thermal energy generation requirement by boiler (kWh)

ED_a Total annual thermal energy demand (kWh)

E_{a_CTAH} Total annual thermal energy generated by the CTAH system (kWh)

η_{boiler} Boiler efficiency

Total annual fuel cost for the boiler can be calculated as:

$$C_{boiler\_CTAH} = E_{boiler\_CTAH} \times F_{boiler\_Oil} \qquad 7.15$$

Where,

C_{boiler_CTAH} Total annual fuel cost by boiler (€)

F_{boiler} Unit oil cost for boiler (€/kWh)

The annual fuel cost for boiler and CTAH integrated building (€341 for oil and €194 for gas) was calculated using equations 7.14-15.

7.4.3.2.2 House with boiler only

In this case a boiler was used in the domestic dwelling to supply thermal energy to the building. A solar energy collector was not integrated with the heating system.

Total annual thermal energy demand = 5,454 kWh

Considering the boiler efficiency, energy generation required by the boiler can be calculated as:

$$E_{boiler} = \frac{(ED_a)}{\eta_{boiler}} \qquad 7.16$$

Where,

E_{boiler} Annual thermal energy requirement by boiler (kWh)

ED_a	Total annual thermal energy demand (kWh)
η_{boiler}	Boiler efficiency

Total annual fuel cost by boiler can be calculated as:

$$C_{boiler} = E_{boiler} \times F_{boiler} \tag{7.17}$$

Where,

C_{boiler} = Total annual fuel cost by boiler (€)

F_{boiler} = Unit fuel cost for boiler (€/kWh)

The annual fuel cost for only boiler integrated building (€527 for oil and €300 for gas) was calculated using equations 7.16-17.

7.4.3.2.3 House with boiler and SWH

This is a combination of boiler and solar water heating system integrated in the domestic dwelling to heat water of 200 litres tank.

Available solar radiation is captured by SWH which can be used for water heating.

Total annual thermal energy demand = 5,454 kWh

Total annual energy generated by ETC = 1,712 kWh

Total annual energy generated by FPC = 1,644 kWh

Considering boiler efficiency energy generation required by boiler with ETC can be calculated as:

$$E_{boiler\_ETC} = \frac{\left(ED_a - E_{a\_ETC}\right)}{\eta_{boiler}} \tag{7.18}$$

Where,

E_{boiler_ETC}	Annual thermal energy requirement by boiler (kWh)
ED_a	Total annual thermal energy demand (kWh)

E_{a_ETC} Total annual generated thermal energy by ETC (kWh)

η_{boiler} Boiler efficiency

Total annual fuel cost of the boiler can be calculated as:

$$C_{boiler\_ETC} = E_{boiler\_ETC} \times F_{boiler} \qquad 7.19$$

Where,

C_{boiler_ETC} Total annual fuel cost by boiler with ETC (kWh)

F_{boiler} Unit fuel cost for boiler (€/kWh)

The annual fuel cost for boiler and ETC integrated building (€362 for oil) was calculated using equations 7.18-19.

Considering the boiler efficiency, energy generation required by the boiler with FPC can be calculated as:

$$E_{boiler\_FPC} = \frac{\left(ED_a - E_{a\_FPC}\right)}{\eta_{boiler}} \qquad 7.20$$

Where,

E_{boiler_FPC} Annual thermal energy requirement by boiler with FPC (kWh)

ED_a Total annual thermal energy demand (kWh)

E_{a_FPC} Total annual generated thermal energy by FPC

η_{boiler} Boiler efficiency

Total annual fuel cost by the boiler can be calculated as:

$$C_{boiler\_FPC} = E_{boiler\_FPC} \times F_{boiler} \qquad 7.21$$

Where,

C_{boiler_FPC} Total annual fuel cost by boiler with FPC (€)

F_{boiler} Unit fuel cost for boiler (€/kWh)

The annual fuel cost for boiler and FPC integrated building (€368 for oil) was calculated using equations 7.20-21.

7.4.4 Economic analysis of the CTAH system's integration in the domestic dwelling

In case of the domestic dwelling, the CTAH system's application was compared with other conventional solar thermal collectors (FPC/ETC). Economic appraisal techniques used in this chapter consist of: SPP, NPV and BCR which were detailed in section 7.2.2.

7.4.4.1 Simple payback period

Simple Payback Period (SPP) or Payback Period (PBP) was calculated using Equation 7.2. The calculated SPP for the CTAH system in the domestic dwelling considered was 6.2 years. The calculated SPP for the FPC and ETC system for specified energy demand in section 7.4.1 using Equation 7.2 for the domestic dwelling in this study was 19.5 and 17.8 years.

7.4.4.2 Net Present Value

A cash flow diagram is a pictorial display of the costs and revenues associated with a project (Capehart, 2008). Figure 7.7 illustrates the Discounted Cash Flow (DCF) diagram for the CTAH system, ETC and FPC.

It is seen that all heating systems have negative cash flows during installation as a result of their capital cost. During successive years, positive cash flows arise as a result of heat generated. The CTAH system is seen to have higher annual revenues compared to both solar thermal systems. The annual revenue seems to be very close for all of three collectors. However, the initial cost of CTAH was significantly low compare to ETC and FPC solar collectors.

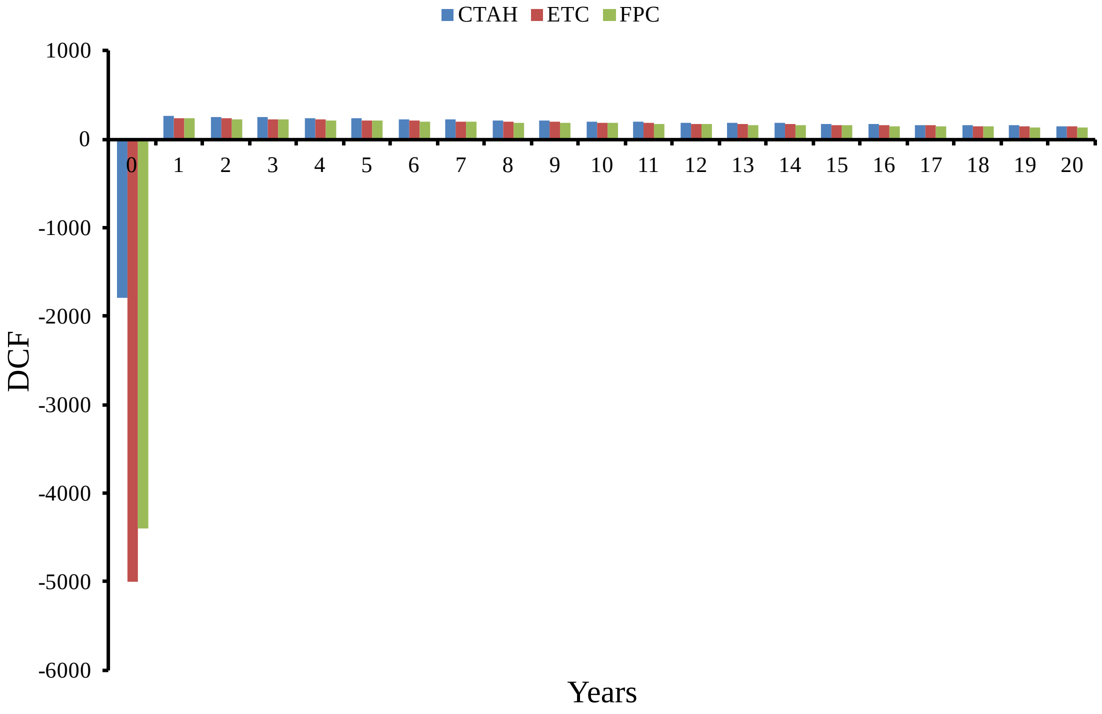

Figure 7.7: Comparative DCF diagram for the CTAH system, ETC and FPC.

The NPV value was calculated using Equation 7.3 for the CTAH system. The calculated NPV considering 8% discount rate for the CTAH system, ETC and FPC solar systems considering a 20 years lifespan and specified energy demand in section 7.4.1.3 (Total thermal energy demand for the domestic dwelling) were €1,609, -€1,853 and -€1,379 respectively.

7.4.4.3 Benefit/Cost ratio

Figure 7.8 shows the BCR of the CTAH system, SWH with FPC and ETC. The present worth of all benefits and costs are calculated and the critical life of the CTAH system was determined when the benefit/cost ratio equals 1.

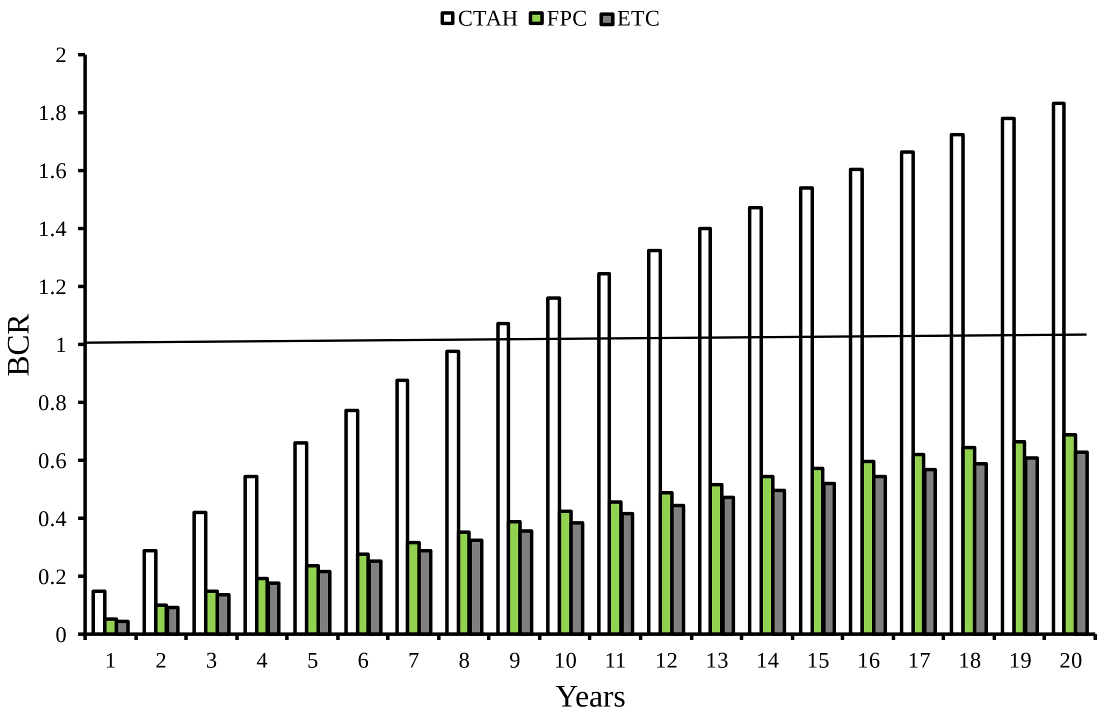

Figure 7.8: BCR of the CTAH system, SWH with FPC and ETC over a 20 year lifespan

It is seen that the service life of the CTAH system has to be at least 9 years to be considered as a profitable investment for an 8% discount rate. The FPC and ETC need a higher than 20 year operating life span to be profitable. This is the reason an additional grant was necessary to adapt FPC and ETC in to domestic dwelling in Ireland. GHG emission analysis considered later in this chapter further reinforces the acceptability of the CTAH system. Compared to SWH with ETC and FPC, the CTAH system is a better alternative since both solar thermal systems have BCR less than 1.

7.4.4.3 Effect of discount rate on economic viability of the CTAH system in the domestic dwelling

Sensitivity analysis was carried out in order to investigate the effect of discount rate on cumulative DCF of the CTAH system in the domestic dwelling. The effect of the discount rate was investigated by assuming a range of discount rates from 4 to 17% as shown in Figure 7.9-7.12.

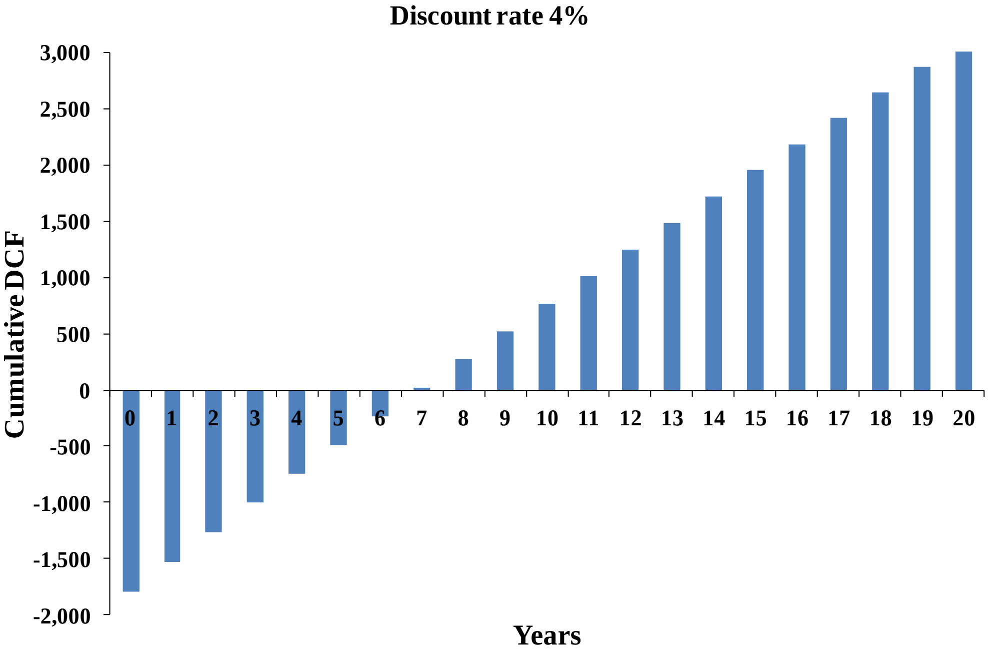

Figure 7.9: Cumulative discounted cash flow of CTAH for 4% discount rate

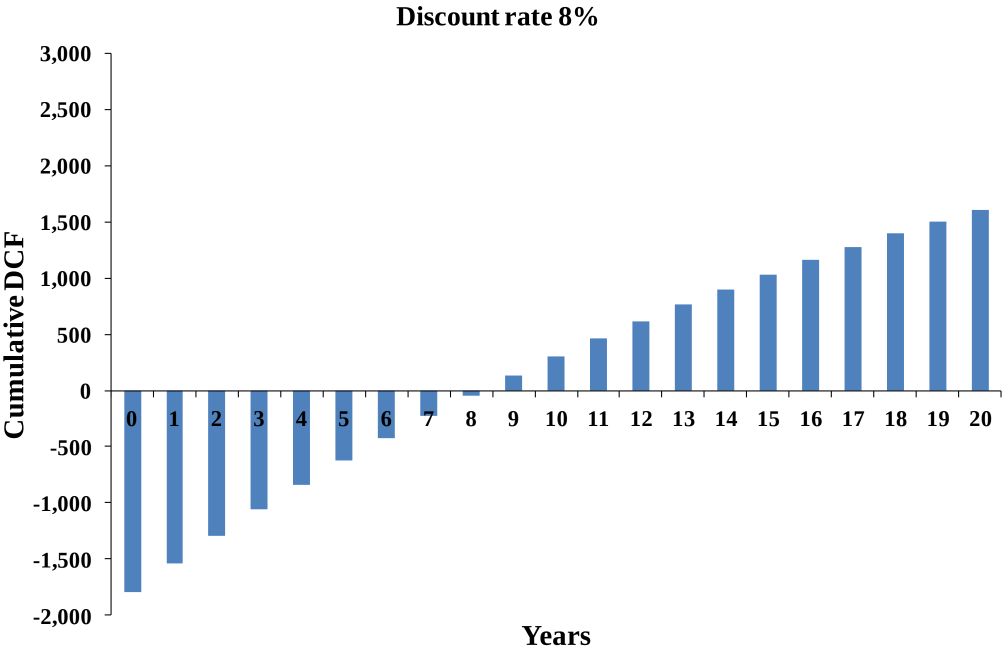

Figure 7.10: Cumulative discounted cash flow of CTAH for 8% discount rate

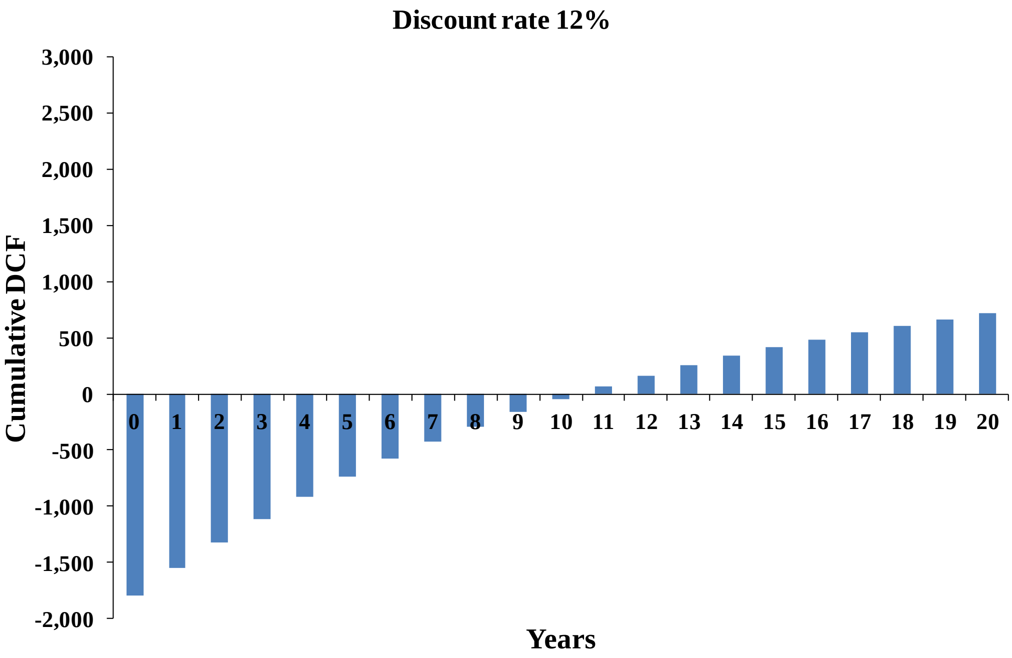

Figure 7.11: Cumulative discounted cash flow of CTAH for 12% discount rate

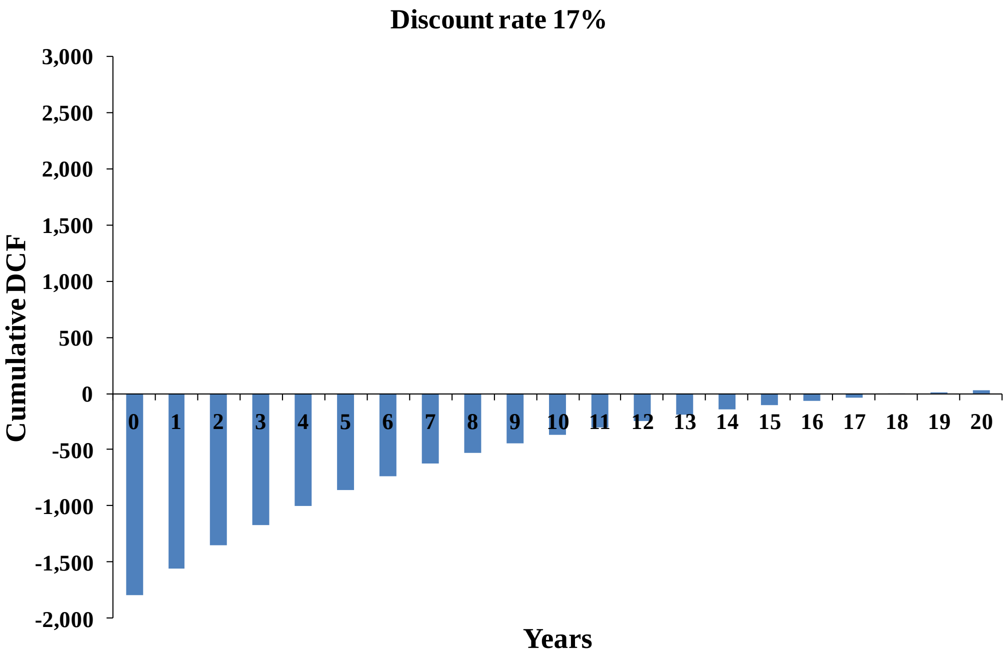

Figure 7.12: Cumulative discounted cash flow of CTAH for 17% discount rate

It is seen that the critical lifespan decreases with increase of discount rate. Reducing the discount rate from 17% to 4% would reduce the critical service life of the

CTAH system from 20 to 7 years. The critical service life would be 9 years at 8% discount rate.

7.5 GHG Emission analysis of CTAH

The GHG emission analysis undertaken in this work consists of evaluating the quantity of avoided CO_2 emissions by the CTAH system relative to a boiler and an electric heating system. The useful annual heat delivered by a unit area of the CTAH system was calculated in chapter 6. The recommended baseline boiler and electrical heating efficiency are 86% and 100% (SEAI, 2011).

This requires an evaluation of emissions associated to a house fitted with either a boiler or an electric heater. Emissions generated by a building fitted with a CTAH system may be due to imported grid electricity to operate a suction fan. Considering 4 m^2 aperture area of the CTAH system, the amount of annually produced CO_2 was calculated using the emission factor for different fuels according to SEAI emission calculator (SEAI, 2012). The emission factor and fuel price for different fuel types are listed in Table 7.8.

Table 7.8: Average fuel cost and emission factors (SEAI, 2012)

Fuel type	Average Cost €/kWh	Emission Factor kg CO_2/kWh
Electricity	0.1500	0.582
Oil	0.0831	0.263
Gas	0.0474	0.205

The quantity of CO_2 emitted was then calculated for different fuel types. Table 7.9 shows the annual kgCO_2 emitted by different heating systems. The CTAH system produced the minimum amount of CO_2 of 42 kg. The electric heater produces the highest amount of CO_2 of 1,164 kg.

Table 7.9: Annual quantity of CO_2 emitted by different heating systems

Alternatives	Annual emitted (kgCO_2)
CO_2 emitted by CTAH	42
CO_2 emitted by electric heater	1,164
CO_2 emitted by gas	492
CO_2 emitted by oil	631

7.6 Summary

In this chapter, an analysis of the technological aspects, financial performance and GHG emission reduction potential of the CTAH system was undertaken to investigate its suitability as a building integrated air and water heating system. The performance of the CTAH system was compared with other heating systems for domestic dwellings.

The CTAH system was found to be beneficial when integrated in domestic dwellings for heating ventilation air. Due to mandatory BER regulation on fresh air, vents are usually installed in domestic dwellings that cause a lot of heat loss due to uncontrolled infiltration of ambient air thereby increasing the heat requirement. The current practice in Irish houses used to fulfil BER requirement is through the provision of manually controlled vents in each habited room which are inefficient. The CTAH system can be retrofitted with existing domestic dwellings which can provide controlled fresh air. In domestic dwellings the CTAH system was found to be technologically superior to SWH with FPC and ETC because it can be used both for both space and water heating.

In a domestic dwelling with space heating demand and 200 litres daily hot water demand, the annual heating cost can be reduced by integrating a CTAH system with 4 m^2 collector aperture from €527 to €341. Comparatively, the heating cost can be reduced to €362 and €368 for SWH with ETC and FPC respectively.

SPP of CTAH was calculated as 6.2 years for the domestic dwelling in this study. NPV and BCR calculations were carried out to compare the CTAH system with different alternatives taking into consideration the time value of money. Considering an 8% discount rate, the BCR was found 1 on the year 9 of 20 year lifespan. A sensitivity analysis of discount rate on the critical life of the CTAH system showed the effect of varying the discount rate from 4% to 17% on cumulative DCF. For 4% discount rate, the BCR value 1 was calculated to be on 6 year. At a discount rate 17%, the BCR becomes 1 on year 20 within a lifespan of 20 years.

CO_2 emissions reduction was the primary environmental advantage of the CTAH system. The annual CO_2 emission reduced by the CTAH system was calculated as 280 $kgCO_2/m^2$ against electric heater, 112 $kgCO_2/m^2$ for a gas boiler and 147 $kgCO_2/m^2$ for an oil boiler. The emitted CO_2 by the CTAH system was calculated as 11 $kgCO_2/m^2$. This was found to be negligible compared to that of heating systems with electricity (291 $kgCO_2/m^2$), condensing gas boiler (123 $kgCO_2/m^2$) and oil boiler (158 $kgCO_2/m^2$) which make the CTAH system more attractive compared to other alternatives.

CHAPTER 8

CONCLUSIONS AND RECOMMENDATIONS

8.1 Conclusions

Despite high space heating demand in the Irish residential sector, solar air heating systems have not been adopted due to their high capital cost and non-uniform space heating demand during different months of the year. This research was undertaken to design, evaluate and carryout a techno-economic analysis of a novel air heating system to overcome practical constrains that have served as barriers to the adoption of solar air heating systems in Ireland.

Total estimated cost of the CTAH was €450/m^2 which can be used for air heating during winter months which is included air to water heat exchanger and manufacturing cost. The annual energy delivered by CTAH, ETC and FPC was 545kWh/m^2, 571kWh/m^2 and 411kWh/m^2 respectively.

The main system components of the CTAH system are a transpired fabric absorber, concentrator reflector and glazing. Selection of each system component was carried out to reduce cost and system weight. The cost of the perforated carbon fibre fabric was €23/m^2. Carbon fibre is 251% lighter than aluminium which is commonly used as an absorber material in conventional Unglazed Transpired Collectors (UTC). The preparation of a customised thin aluminium (0.5 mm thick) absorber with less than 5% perforation is highly expensive (€500/m^2) as it needs high precision equipment. Low iron glass with 88% transmittance that costs €60/m^2 was selected as the glazing material of the CTAH and an additional €20/m^2 was needed to temper the glazing material because of its low strength. An antireflection coating can increase the transmittance by 8% with an additional cost of €45/m^2. Anti reflecting coating was therefore not used in the CTAH to reduce system cost.

Polycarbonate with antireflection coating can reach such transmittance and is available at a cost of €70/m^2 which is much cheaper than glass. However, the polycarbonate glazing's maximum life span is 5-7 years and the yellowing problem may cause degradation of system performance. Polyethylene terephthalate (PET) that costs only €5/m^2 was used as glazing material in previous research as discussed in Chapter 2.

A thicker PET material of 500 μm is nearly opaque. The maximum thickness available in the market is 250 μm with 90% transmittance. Though this is a cheap material with high transmittance but the level of durability is low. Despite being more expensive, glass was chosen as the preferred glazing material for the CTAH because of its longer life span and sustainability. However, if weight is an critical issue, commercial brands of clear polycarbonate (e.g. Plexiglass) has very low density (1.19 g/cm^3) compared to low iron glass (2.5 g/cm^3).

Alanod reflector with 95% reflectivity coated by PVD process was selected as the reflector material of the CTAH since it is more suitable for long term performance. The cost of alanod reflector (PVD glazing on aluminium substrate) is €55/m^2. If an additional aluminium substrate is required it will add an additional cost of €25/m^2.

The optimum tertiary height of the CTAH was 50mm considering optical losses within the tertiary section. The maximum beam and diffuse optical efficiency of the CTAH were 79% and 65% respectively considering 50 mm tertiary height, 88% transmittance of the glazing and 95% reflectance of the concentrator reflector. The acceptance angle of the CTAH varied between 100% at 27^o incident angle and 93% at incident angle 89^o which provide effective annual concentration. The beam efficiency within 27^o to 89^o incident angle varies between 79% and 72% and diffuse efficiency varies between 65% and 48%.

Optical efficiency increases without applying glazing surface and tertiary height. However, it was found in this research that it is essential to incorporate a glazing surface during outdoor operation. Absence of a glazing surface causes unwanted dust deposition, dirt accumulation and water film after heavy rain. These factors reduce the optical performance of the concentrator. The reverse flow effect is another factor which affects the thermal performance of the solar collector by taking away heat out of the concentrator cavity. The glazing surface also protects the perforated absorber surface from unwanted dust deposition.

The closed loop experimental results showed that the thermal efficiency remained high at higher air flow rate. The average thermal efficiency was found to be approximately 55-65% with average radiation above 400 W/m^2 for flow rate range ($0.03kg/s/m^2$ to $0.09kg/s/m^2$). Solar radiation was the parameter with the greatest effect on thermal efficiency in the closed loop configuration. Due to thermal stratification in the tertiary section and concentrator cavity of glazed CTAH, the effect of wind speed and ambient air temperature was low. Stratification of the air temperature was consistent for different air flow rates inside the CTAH.

The outlet air temperature was always higher than the tertiary section air temperature which was also always higher than the glazing temperature and inlet air temperature. The experimental system was closed loop so the inlet temperature was constantly higher than the corresponding ambient air temperature. The stratified air thermal layer reduced heat loss from the absorber to ambient through the glazing surface. A portion of optical heat loss through the reflector surface was recaptured as the air flowed from inlet to outlet. Pressure drop in the CTAH was found 10 Pa for a flow rate of 0.1 kg/s/m^2. The required power consumption for driving the flow through the CTAH collector was very small in comparison to the recovered energy which increased the attractiveness of the collector.

The tertiary reflector section after the secondary circular reflector helps to maintain the stratified thermal layers which prevent convection loss from the absorber's surface. The inverted absorber reduces radiation loss as it does not face the glazing surface. In a parallel orientation radiation loss increases as in flat plat solar collectors. A smaller absorber surface area results in lower radiation loss. The inverted transpired absorber reduces convection loss from the absorber to the glazing due to the stratified thermal layer and upward direction of air flow. The experimental results support these facts because the heat loss for flat plat air heating collectors varies between -5.85 W/m^2 ^{o}C (absorber surface with selective coating) and -10.82 W/m^2 ^{o}C (ordinary absorber surface). On the other hand, heat loss from the CTAH is -3.25 W/m^2 ^{o}C. Basically the parallel orientation of a flat plate absorber with glazing increases heat loss which is minimised in the CTAH by integrating an ACPC concentrator.

At an air flow rate of 0.03 kg/s/m^2 and solar radiation intensity of 1,000 W/m^2 the air temperature rise by the UTC was 21^{o}C while it was 38^{o}C with the CTAH. The air temperature rise was 12^{o}C by the UTC and 19^{o}C with the CTAH at a solar radiation intensity of 500 W/m^2. The outlet temperature rise by the CTAH was 87% higher than that of the UTC at a solar radiation intensity of 1,000 W/m^2 while it reduced to 65% at solar radiation intensity of 500 W/m^2. The UTC can only work at flow rates less than 0.04 kg/s/m^2. Air temperature rise by the UTC was only 18^{o}C at a solar radiation intensity of 1000 W/m^2 at its highest applicable air flow rate (0.04 kg/s/m^2). On the other hand, experimental results on the CATH at air flow rates from 0.03 kg/s/m^2 to 0.09 kg/s/m^2 showed temperature rise of 38^{o}C and 20^{o}C respectively at a solar radiation intensity of 1,000 W/m^2. The low performance of the UTC is mainly due to radiation loss from the unglazed absorber surface although reverse flow effect was another contributing factor.

SPP, NPV and BCR calculations were carried out to compare the economic performance of the CTAH system with conventional solar thermal collector used domestic dwelling under Irish weather: Evacuated Tube Collector (ETC) and Flat Plate Collector (FPC). The primary cost of CTAH, ETC and FPC were €450/m^2, €1,667/m^2 and €1,100/m^2. The SPP of CTAH, ETC and FPC were calculated as 6 years, 19 years and 18 years for the domestic dwelling. Considering 8% discount rate the Benefit Cost Ratio (BCR) for CTAH was found 1 on the year 9 of the 20 year lifespan. The NPV of CTAH, ETC and FPC were €1,609, -€1,853 and -€1,379 respectively. The annual CO_2 emission reduced by the CTAH system was calculated as 280 kg/m^2 against an electric heater, 112 kg/m^2 compared to a gas boiler and 147 kg/m^2 against an oil boiler which makes the CTAH an attractive air heating system in the residential sector.

8.2 Research Contributions

The main contributions of the research presented in this thesis can be summarized as follows:

1. The design of an optically optimised air heating system which integrates a low weight perforated inverted absorber and an asymmetric compound parabolic concentrator.
2. Evaluation of the field performance, characterisation and simulation of the thermal performance of a prototype of the air heating system

3. Comparative assessment of the economic and environmental performance of the air heating system relative to other air heating systems in a domestic dwelling in Ireland.

8.3 Recommendations for Future Work

Further research is recommended in the following areas:

- The integration of CATH systems into buildings in order to optimise their optical and thermal efficiency
- Field trials should be undertaken for use of the CATH system in different applications such as crop drying, space and water heating in residential and commercial buildings.
- A building integrated CTAH-PV system can be designed using the proposed optical and heat transfer model in this work to meet both thermal and electrical requirements. Ambient air flowing at the back of the PV module can be used to cool it while the heated air can be mixed with air from the CTAH system.
- The integration of new CTAH models into energy simulation programs such as TRNSYS or COMSOL may be examined.

References

Ayompe, L. M. (2011). *Performance and policy evaluation of solar energy technologies for domestic application in Ireland.* (PhD), Dublin Institute of Technology, Dublin, Ireland.

Antisclad, Hot water temperature, scalding and legionnaires disease. Available: http://antiscald.com/prevention/legionnaires/hotwater.php (Accessed 3rd January, 2012)

Alanod. Mirosun, Available: http://alanod.com/opencms/opencms/en/ (Accessed 12 July, 2009)

Astro-foil. Available: http://www.astrofoil.net/ (Accessed 12th July, 2009)

Acrylite. Available: http://www.acrylite.net/product/acrylite/en/products/sheet/ff/pages/default.aspx (Accessed 5th March, 2011)

Adsten, M. (2002). *Solar Thermal Collectors at High Latitudes: Design and Performance of Non-Tracking Concentrators.* (PhD), Uppsala University, Sweden.

Alta, D., Bilgili, E., Ertekin, C., & Yaldiz, O. (2010). Experimental investigation of three different solar air heaters: Energy and exergy analyses. *Applied Energy, 87*(10), 2953-2973.

Athienitis, A. K., Bambara, J., O'Neill, B., & Faille, J. (2011). A prototype photovoltaic/thermal system integrated with transpired collector. *Solar Enrgy, 85(1),* 139-153.

Badache, M., Rousse, D. R., & Halle, S. (2010). *Experimental Characterization of an Unglazed Transpired Solar Collector*. Paper presented at the, International Conference on Solar Heating, Cooling and Buildings, Graz, Austria.

Beggs, C. (2002). *Energy management: supply and conservation*: Oxford: Butterworth-Heinemann.

Capehart, B. L., Turner, W. C., & Kennedy, W. J. (2008). *Guide to energy management*. US: The Fairmont Press, Inc.

Cansolar. Available:http://www.cansolair.com/(Accessed 5th March, 2011)

Carbonmods, Carbon fibre. Available: http://www.carbonmods.co.uk/ (Accessed 16th January, 2010)

Cheremisinoff, P. N., & Regino, T. C. (1978). *Principles & applications of solar energy*. Michigan, USA: Ann Arbor Science.

Christensen, C. B., Kutscher, C. F., & Gawlik, M. (1997). Unglazed transpired solar collector having low thermal conductance absorber. U. S. Patent No. 569249, Application No. 08/639,852, 8 pp.

Colclough, S. M., Griffiths, P. W., & Hewitt, N. J. (2011). *A year in the life of a passive house with solar energy store*. Paper presented at the IC SES Energy Storage Conference, Belfast.

Communities, An Energy Policy for Europe. Available: http://ec.europa.eu/energy/energy_policy/doc/01_energy_policy_for_europe_en.pdf (28th September, 2009)

CSA. (2012). Canadian Standards Association. Available: www.csa.ca/cm/ca/en/home (Accessed 12ed May, 2012)

DCENR. National Renewable Energy Action Plan, IRELAND. Available: http://www.dcenr.gov.ie/NR/rdonlyres/C71495BB-DB3C-4FE9-A725-0C094FE19BCA/0/2010NREAP.pdf (Accessed 19th January, 2012)

DEHLG, Statutory Instrument S.I.No. 259 of 2008. Building Regulations (Part L Amendment) Regulations. Available:

http://www.environ.ie/en/Legislation/DevelopmentandHousing/BuildingStandards/FileDownLoad,17840,en.pdf (Accessed 10th March, 2010)

Dennehy, E., Howley, M., Gallachóir, B. Ó., & Holland, M. (2012). Renewable Energy in Ireland 2011. (Accessed 15 July, 2012)

DEL. Hitachi Su-6600 FESEM. Available: http://www.dit.ie/focas/facilities/hitachisu-600fesemwithgatancryotransferstage/ (Accessed 18th August, 2009)

Duffie, J. A., & Beckman, W.A. (2006). *Solar Engineering of Thermal Process* (3rd ed.). NY: J. W. & Sons.

DupontTeijin. Available: http://www.dupontteijinfilms.com/(Accessed 12th July, 2009)

Dymond, C., & Kutscher, C. (1997). Development of a flow distribution and design model for transpired solar collectors. *Solar Energy, 60*(5), 291-300.

Eames, P. C. & Norton, B. (1993a). Validated, unified model for optics and heat transfer in line-axis concentrating solar energy collectors. *Solar Energy 50 (4)*, 339-355.

Eames, P. C. & Norton, B. (1993b). Detailed parametric analyses of heat transfer in CPC solar energy collectors. *Solar Energy 50 (4)*, 321-328.

Eames, P. C. & Norton, B. (1995). Thermal and optical consequences of the introduction of baffles into compound parabolic concentrating solar energy collector cavities. *Solar Energy 55 (2)*, 139-150.

Eames, P. C., Norton, B. & Kothdiwala, A. F. (1996). The state of the art in modelling line-axis concentrating solar energy collectors. *Renewable Energy*, 9, 562-567.

Eames, P. C., Smyth, M., & Norton, B. (2001). The experimental validation of a comprehensive unified model for optics and heat transfer in line-axis solar energy systems. *Solar Energy, 71*(2), 121-133.

Easycomposite. Carbon Fibre Products. Available: http://www.easycomposites.co.uk/ (Accessed 16th January, 2010)

ECGA. Carbon and graphite. Available: www.carbonandgraphite.org (Accessed 16th January, 2010)

El-Khawajah, M. F., Aldabbagh, L. B. Y., & Egelioglu, F. (2011). The effect of using transverse fins on a double pass flow solar air heater using wire mesh as an absorber. *Solar Energy, 85*(7), 1479-1487.

El-Khawajah, M. F., Aldabbagh, L. B. Y., & Egelioglu, F. (2011). The effect of using transverse fins on a double pass flow solar air heater using wire mesh as an absorber. *Solar Energy, 85*(7), 1479-1487.

El-Sebaii, A. A., & Al-Snani, H. (2010). Effect of selective coating on thermal performance of flat plate solar air heaters. *Energy, 35*(4), 1820-1828.

El-Sebaii, A. A., Aboul-Enein, S., Ramadan, M. R. I., Shalaby, S. M., & Moharram, B. M. (2011a). Investigation of thermal performance of-double pass-flat and v-corrugated plate solar air heaters. *Energy, 36*(2), 1076-1086.

El-Sebaii, A. A., Aboul-Enein, S., Ramadan, M. R. I., Shalaby, S. M., & Moharram, B. M. (2011b). Thermal performance investigation of double pass-finned plate solar air heater. *Applied Energy, 88*(5), 1727-1739.

Environ (a). Building Regulations (Part F) http://www.environ.ie/en/Publications/DevelopmentandHousing/BuildingStandards/FileDownLoad,1647,en.pdf (Accessed 8th June, 2009)

Environ (b), Department of the environment, heritage and local government. Available:

http://www.environ.ie/en/Publications/StatisticsandRegularPublications/HousingStatistics/ (Accessed 3rd January, 2012)

Esen, H. (2008). Experimental energy and exergy analysis of a double-flow solar air heater having different obstacles on absorber plates. *Building and Environment, 43*(6), 1046-1054.

ESTIF. Solar Thermal Markets in Europe. http://www.estif.org/fileadmin/estif/content/market_data/downloads/2009%20solar_thermal_markets.pdf (Accessed 16th May, 2011)

ESTTP. Solar Heating and Cooling for a Sustainable Energy Future in Europe. http://www.rhc-platform.org/fileadmin/user_upload/Structure/Solar_Thermal/Download/ESTTP_SRA_RevisedVersion.pdf (Accessed 4th January, 2012)

European Commission, Eurostat energy statistics. Available: http://epp.eurostat.ec.europa.eu/portal/page/portal/energy/data/main_tables (August, 2012)

Kothdiwala, F. A., Norton, B., & Eames, P. C. (1995). The effect of variation of angle of inclination on the performance of low-concentration-ratio compound parabolic concentrating solar collectors. *Solar Energy, 55*(4), 301-309.

Fibreglast. Carbon Fibre. Available: http://www.fibreglast.com/product/3K_Plain_Weave_Carbon_Fiber_Fabric_00530/155 (Accessed 16th January, 2010)

Fraidenraich, N. & Salcedo, I. H. (1993). Multimode analysis of compound parabolic concentrators with flat absorber. *Appl. Opt.,* 32, 2891-2900.

Fraidenraich, N., Tiba, C., Brandão, B. B. & Vilela, O. C. (2008). Analytic solutions for the geometric and optical properties of stationary compound parabolic concentrators with fully illuminated inverted V receiver. *Solar Energy*, 82, 132-143.

Fudholi, A., Othman, M. Y., Ruslan, M. H., Yahya, M., Zaharim, A., & Sopian, K. (2011). *Techno-economic analysis of solar drying system for seaweed in Malaysia.* Paper presented at the 7th IASME/WSEAS Int. Conf. on Energy, Environment, Ecosystems and Sustainable Development (EEESD, 11), France.

Gawlik, K. M. (1995). *A Numerical and Experiment Investigation of Heat Transfer Issues in the Practical Utilization of Unglazed, Transpired Solar Air Heaters.* (Ph.D.), University of Colorado at Boulder.

Gawlik, K. M., & Kutscher, C. F. (2002). *A numerical and experimental investigation of low-conductivity unglazed, transpired solar air heaters.* Paper presented at the Solar Engineering 2002, June 15, 2002 - June 20, 2002, Reno, NV, United states.

Gawlik, K., Christensen, C., & Kutscher, C. (2005). A numerical and experimental investigation of low-conductivity unglazed, transpired solar air heaters. *Journal of Solar Energy Engineering, Transactions of the ASME, 127*(1), 153-155.

Gharamaleki, A. J., Romero, S., Bustamante, P., & Clark, B. J. (2000). Multiple solubility maxima of oxolinic acid in mixed solvents and a new extension of Hildebrand solubility approach, Chem. Pharm. Bull, 48 (2), 175-178.

Goswami, D.Y., Kreith, F., & Kreider, J.F. (2000). *Principles of Solar Engineering*. NY: Taylor & Francis.

Graham, V. A., & Hollands, K. G. T. (1990). A method to generate synthetic hourly solar radiation globally. *Solar Energy, 44*(6), 333-341.

Grafil. (2010). Typical Thermal Properties. Available:

http://www.grafil.com/images/newpdf/thermal/Typical_Thermal_Properties_03_2010.pdf (Accessed 19th March, 2011)

Gunnewiek, L. H., Brundrett, E., & Hollands, K. G. T. (1996). Flow distribution in unglazed transpired plate solar air heaters of large area. *Solar Energy, 58*(4–6), 227-237.

Gunnewiek, L. H., Hollands, K. G. T., & Brundrett, E. (2002). Effect of wind on flow distribution in unglazed transpired-plate collectors. *Solar Energy, 72*(4), 317-325.

Hachemi, A. (1999). Experimental study of thermal performance of offset rectangular plate fin absorber-plates. *Renewable Energy, 17*(3), 371-384.

Hastings, S. R., & Morck, O. (2000). *Solar air system: a design handbook*. UK: James and James Science.

Ho, C. D., Yeh, C. W., & Hsieh, S. M. (2005). Improvement in device performance of multi-pass flat-plate solar air heaters with external recycle. *Renewable Energy, 30*(10), 1601-1621.

Ho, C. D., Yeh, H. M., Cheng, T. W., Chen, T. C., & Wang, R. C. (2009). The influences of recycle on performance of baffled double-pass flat-plate solar air heaters with internal fins attached. *Applied Energy, 86*(9), 1470-1478.

Hollick, J. C. (1994). Unglazed solar wall air heaters. *Renewable Energy, 5*(1–4), 415-421.

IEA. (1999). Low cost, high performance solar air heating systems using perforated absorbers. Final report of task 14 air systems working group. *IEA solar heating and cooling report no. SHC, T14, Air1*.

Ismail, M. K. (1991). On the reactivity, structure, and porosity of carbon fibers and fabrics. *Carbon, 29*(6), 777-792.

Iqbal, M. (1983). *An Introduction to Solar Radiation*. Toronto: Academic Press.

Kalogirou, S. A. (2009). *Solar energy engineering, processes and systems*. USA: Elsevier.

Karim, M. A., & Hawlader, M. N. A. (2006). Performance investigation of flat plate, v-corrugated and finned air collectors. *Energy, 31*(4), 452-470.

Karsli, S. (2007). Performance analysis of new-design solar air collectors for drying applications. *Renewable Energy, 32*(10), 1645-1660.

Kaplan, S. (1983). Energy Economics: Quantitative methods for energy and environmental decisions. New York: McGraw-Hill.

Kienzlen, V., Gordon, J. M., & Kreider, J. F. (1988). Reverse flat plate collector: A stationary, nonevacuated, low technology, medium solar collector. *Journal of Solar Energy Engineering, Transactions of the ASME, 110*(1), 23-30.

Kokko, J. P., & Marshal, S. (1992). *Performance of the next generation of Solarwalls.* Paper presented at the Annual Conference of the Solar Energy Society of Canada, Edmonton, Canada.

Kothdiwala, A. F., Norton, B., & Eames, P. C. (1995). The effect of variation of angle of inclination on the performance of low-concentration-ratio compound parabolic concentrating solar collectors. *Solar Energy, 55*(4), 301-309.

Kothdiwala, A. F., Eames, P. C., & Norton, B. (1996). Optical performance of an asymmetric inverted absorber compound parabolic concentrating solar collector. *Renewable Energy, 9*(1–4), 576-579.

Kothdiwala, A. F., Eames, P. C., & Norton, B. (1997). Experimental analysis and performance of an asymmetric inverted absorber compound parabolic concentrating solar collector at various absorber gap configurations. *Renewable Energy, 10*(2–3), 235-238.

Kothdiwala, A. F., Eames, P. C., Norton, B., & Zacharopolous, A. (1999). Technical note: Comparison between inverted absorber asymmetric and symmetric tubular-absorber compound parabolic concentrating solar collectors. *Renewable Energy, 18*(2), 277-281.

Koyuncu, T. (2006). Performance of various design of solar air heaters for crop drying applications. *Renewable Energy, 31*(7), 1073-1088.

Kreith, F., Löf, G. O. G., Rabl, A. & Winston, R. (1980). Solar collectors for low and intermediate temperature applications. *Progress in Energy and Combustion Science,* 6, 1-34.

Kurtbas, I., & Durmus, A. (2004). Efficiency and exergy analysis of a new solar air heater. *Renewable Energy, 29*(9), 1489-1501.

Kurtbas, İ., & Durmuş, A. (2004). Efficiency and exergy analysis of a new solar air heater. *Renewable Energy, 29*(9), 1489-1501.

Kutscher, C. F., Christensen, C. B., & Barker, G. M. (1991). Unglazed transpired solar collectors. Heat loss theory. *ASME-JSES-JSME International Solar Energy Conference*, 29-37.

Kutscher, C. F., Christensen, C. B., & Barker, G. M. (1993). Unglazed transpired solar collectors: heat loss theory. *Journal of Solar Energy Engineering, Transactions of the ASME, 115*(3), 182-188.

Kutscher, C. F. (1994). Heat exchange effectiveness and pressure drop for air flow through perforated plates with and without crosswind. *Journal of Heat Transfer, 116*(2), 391-399.

Kutscher, C. F. (1997). *Transpired solar collector systems: a major advance in solar heating. Energy Business Technology Sourcebook.* Paper presented at the Proceedings of the 19th World Energy Engineering Congress, Atlanta, Georgia.

Leon, M. A., & Kumar, S. (2007). Mathematical modeling and thermal performance analysis of unglazed transpired solar collectors. *Solar Energy, 81*(1), 62-75.

Leutz, R., & Suzuki, A. (2001). *Non-imaging Fresnel Lenses: Design and Performance of Solar Concentrators*. Germany: Springer.

Lin, W., Gao, W., & Liu, T. (2006). A parametric study on the thermal performance of cross-corrugated solar air collectors. *Applied Thermal Engineering, 26*(10), 1043-1053.

Mallick, T. K. (2003). *Optics and heat transfer for asymmetric compound parabolic photovoltaic concentrators for building integrated photovoltaics.* (Ph.D), University of Ulster, UK.

Mallick, T. K., Eames, P. C., & Norton, B. (2006). Non-concentrating and asymmetric compound parabolic concentrating building façade integrated photovoltaics: An experimental comparison *Solar Energy, 80*, 834-849.

Mallick, T. K., Eames, P. C., & Norton, B. (2007). Power losses in an asymmetric compound parabolic photovoltaic concentrator. *Solar Energy Materials and Solar Cells, 91*(12), 1137-1146.

Mallick, T. K., & Eames, P. C. (2007). Design and fabrication of low concentrating second generation PRIDE concentrator. *Solar Energy Materials and Solar Cells, 91*(7), 597-608.

Matweb. (2010). Carbon. Available: http://matweb.com (Accessed 16th January, 2010)

Masters, G. M. (2004). Renewable and efficient electric power systems. New Jersey: John Wiley and Sons.

Ma, J., Sun, W., Ji, J., Zhang, Y., Zhang, A., & Fan, W. (2011). Experimental and theoretical study of the efficiency of a dual-function solar collector. *Applied Thermal Engineering, 31*(10), 1751-1756.

McAdams, W. H., (1954), “Heat Transmission”, McGraw-Hill.

MET, The Irish Meteorological Service. Available: http://www.met.ie (Accessed 1st November, 2011)

Mittal, M. K., & Varshney, L. (2006). Optimal thermohydraulic performance of a wire mesh packed solar air heater. *Solar Energy, 80*(9), 1112-1120.

Moummi, N., Youcef-Ali, S., Moummi, A., & Desmons, J. Y. (2004). Energy analysis of a solar air collector with rows of fins. *Renewable Energy, 29*(13), 2053-2064.

Mondol, J. D., Yohanis, Y. G., & Norton, B. (2008). Solar radiation modelling for the simulation of photovoltaic systems. *Renewable Energy, 33,* 1109-1120.

Nilsson, J. (2005). *Optical Design and Characterization of Solar Concentrators for Photovoltics.* (PhD), Lund University, Sweden.

Norton, B., Prapas, D. E., Eames, P. C. and Probert, S. D. (1989). Measured performances of curved inverted-vee absorber compound parabolic concentrating solar energy collectors. *Solar Energy, 43(5),* 267-279.

Norton, B., Eames, P. C. and Yadav, Y. P. (1991). Symmetric and asymmetric linear compound parabolic concentrating solar energy collectors. *International Journal of Ambient Energy,12(4),* 171-190.

Norton, B., Kothdiwala, A. F., & Eames, P. C. (1994). Effect of inclination on the performance of CPC solar energy collectors. *Renewable Energy, 5*(1–4), 357-367.

Odeh, N., Grassie, T., Henderson, D., & Muneer, T. (2006). Modelling of flow in a photovoltaic driven roof slate-based solar ventilation air preheating system. *Energy Conversion and Management, 47(7-8),* 909-925.

O’Leary, F., Howley, M., & Gallachóir, B. Ó. (2008). Energy in the residential sector: Energy Policy Statistical Support Unit, Sustainable Energy Ireland. Available:

http://www.seai.ie/News_Events/Press_Releases/Energy_in_the_Residential_Sector_FNL.pdf (Accessed 7th May, 2010)

Ozgen, F., Esen, M., & Esen, H. (2009). Experimental investigation of thermal performance of a double-flow solar air heater having aluminium cans. *Renewable Energy, 34*(11), 2391-2398.

Palsun. Available: http://www.palramamericas.com/docs/upload/PALSUN_En_Brochure_805-01-07-11.pdf (Accessed 8th March, 2011)

Palz, W. (1978). *Solar electricity, an economic approach to solar energy,* . London: Butterworth Co. Ltd.

Peng, D., Zhang, X., Dong, H., & Lv, K. (2010). Performance study of a novel solar air collector. *Applied Thermal Engineering, 30*(16), 2594-2601.

Piao, Y., Hauptmann, E. G., & Iqbal, M. (1994). Forced convective heat transfer in cross-corrugated solar air heaters. *Journal of Solar Energy Engineering, Transactions of the ASME, 116*(4), 212-214.

Pilkington. Available: http://www.pilkington.com/en-gb/uk (Accessed 23rd April, 2013)

Plasticsintl. Available: http://www.plasticsintl.com/datasheets/Acrylic_PMMA%29_Extruded.pdf (Accessed 8th March, 2011)

Power, T., Walsh, S., & O'Meara, P. (2009). *Financial management: An Irish context* (Third ed.). Dublin: Gill and Mcmillan.

Pramuang, S., & Exell, R. H. B. (2005). Transient test of a solar air heater with a compound parabolic concentrator. *Renewable Energy, 30*(5), 715-728.

Prapas, D. E., Norton, B., Melidis, P. E., & Probert, S. D. (1987). Convective heat transfers within air spaces of compound parabolic concentrating solar-energy collectors. *Applied Energy, 28*(2), 123-135.

Rabl, A. (1976a). Comparison of solar concentrators. *Solar Energy, 18*(2), 93-111.

Rabl, A. (1976b). Optical and thermal properties of compound parabolic concentrators. *Solar Energy, 18*(6), 497-511.

Rabl, A., Goodman, N. B. & Winston, R. (1979). Practical design considerations for CPC solar collectors. *Solar Energy,* 22, 373-381.

Rabl, A., J. O'Gallagher & Winston, R. (1980). Design and test of non-evacuated solar collectors with compound parabolic concentrators. *Solar Energy,* 25, 335-351.

Rabl, A. (1985). *Active Solar Collectors and Their Applications*. New York: Oxford University Press.

Ramadan, M. R. I., El-Sebaii, A. A., Aboul-Enein, S., & El-Bialy, E. (2007). Thermal performance of a packed bed double-pass solar air heater. *Energy, 32*(8), 1524-1535.

Residensialsolarenergysystems. Available: http://www.residentialsolarenergysystems.net/facts-figures-and-information/all-about-collectors/ (Accessed 4th February, 2011)

Romdhane, B. S. (2007). The air solar collectors: Comparative study, introduction of baffles to favor the heat transfer. *Solar Energy, 81*(1), 139-149.

Seo, D. J., Krajewski, W. F., Azimi-Zonooz, A., & Bowles, D. S. (1990). Stochastic interpolation of rainfall data from rain gages and radar using cokriging, 2, results. *Water Resources Research, 26*(5), 915-915.

SEAI. (2011). Efficient home heating. Available: http://www.seai.ie/Publications/Your_Home_Publications/Efficient_Home_Heating_guide.pdf (Accessed 14th July, 2011)

SEAI Calculator. Available: http://forms.sei.ie/calc/seicalculator.html (Accessed 12 January, 2012)

SEAI. (2007). Government White Paper. Available: http://www.seai.ie/Renewables/Renewable_Energy_Policy/Policy_Drivers/1_EnergyWhitePaper12March2007.pdf (Accessed 1 January, 2010)

SEAI. (2008). SEAI energy in residential sector 2008 report. Available: http://www.seai.ie/News_Events/Press_Releases/Energy_in_the_Residential_Sector_FNL.pdf (Accessed 1 January, 2010)

Shukla, A., Nkwetta, D. N., Choa, Y. J., Stevenson, V. & Jones, P. (2012). A state of art review on the performance of transpired solar collector. *Renewable and Sustainable Energy Reviews, 16(6)*, 3975-3985.

Singh, V. K. and Ahmad, N. (2011). Forecasting performance of constant elasticity of variance model: Empirical evidence from India, Applied Economics and Finance, 5(1), 87-96.

Smyth, M., McGarrigle, P., Eames, P. C., & Norton, B. (2005). Experimental comparison of alternative convection suppression arrangements for concentrating integral collector storage solar water heaters. *Solar Energy, 78*(2), 223-233.

Solar-components. Fiberglass solar glazing. Available: http://www.solar-components.com/sun.htm

Solarwall, Conserval Engineering Inc. Available: http://www.solarwall.com/ (Accessed 2nd February, 2009)

Sopian, K., Alghoul, M. A., Alfegi, E. M., Sulaiman, M. Y., & Musa, E. A. (2009). Evaluation of thermal efficiency of double-pass solar collector with porous–nonporous media. *Renewable Energy, 34*(3), 640-645.

Sproul, B. A., (2007). Derivation of the solar geometric relationships using vector analysis. *Renewable Energy,* 32, 1187-205.

Sreekumar, A. (2010). Techno-economic analysis of a roof-integrated solar air heating system for drying fruit and vegetables. *Energy Conversion and Management, 51*(11), 2230-2238.

Struckmann, F. (2008). Analysis of a flat-plate solar collector. Project Report, MWK160 Heat and Mass Transport, May 08, Lund, Sweden.

STW. (2012). Solarthermalworld. Available: http://www.solarthermalworld.org/node/1288 (Accessed 12th June, 2012)

Sukhatme, S. P., (1996). *Solar Energy: Principles of Thermal Collection and Storage,* 2nd, Tata Mc Graw – Hill, New Delhi.

Tanda, G. (2011). Performance of solar air heater ducts with different types of ribs on the absorber plate. *Energy, 36*(11), 6651-6660.

Tchinda, R. (2008). Thermal behaviour of solar air heater with compound parabolic concentrator. *Energy Conversion and Management, 49*(4), 529-540.

Tedlar. Polyvinyl fluoride film. Available: http://www2.dupont.com/Tedlar_PVF_Film/en_US/assets/downloads/pdf/h49719.pdf (Accessed 18th June, 2012)

Thuesen, G. J., & Fabrycky, W. J. (2000). *Engineering Economy* (9th ed.). Englewood Cliffs, NJ: Prentice Hall.

Tiwari, G. N., & Suneja, S. (1997). *Solar thermal engineering systems*. UK: Narosa Publishing House.

Tripanagnostopoulos, Y., & Souliotis, M. (2004). Integrated collector storage solar systems with asymmetric CPC reflectors. *Renewable Energy, 29*(2), 223-248.

Van Decker, G. W. E., Hollands, K. G. T., & Brunger, A. P. (2001). Heat-exchange relations for unglazed transpired solar collectors with circular holes on a square or triangular pitch. *Solar Energy, 71*(1), 33-45.

Wasley, J. H., & Utzinger, M. (1996). Vital signs. Available: http://arch.ced.berkeley.edu/vitalsigns/res/downloads/rp/glazing/glaz1-bg.pdf (Accessed 17th July, 2009)

Wazed, M. A., Nukman, Y., & Islam, M. T. (2010). Design and fabrication of a cost effective solar air heater for Bangladesh. *Applied Energy, 87*(10), 3030-3036.

Watmuff, J. H., Charters, W.W.S, & Proctor, D. (1977). Solar and wind induced external coefficients for solar collectors, *COMPLES*, 2, 56.

Welford, W. T., & Winston, R. (1978). *The Optics of Non-imaging Concentrators: Light and Solar Energy*. New York: Academic Press.

Welford, W. T. & Winston, R. (1982). Upper bound on the efficiency of certain nonimaging concentrators in the physical optics model. V 72, 1244-1248.

Welford, W. T. & Winston, R. (1989). *High collection nonimaging optics*. San Diego, USA.: Academic Press.

Winston, R. (1974). Principles of solar concentrators of a novel design. *Solar Energy,* 16, 89-95.

Winston, R. & Welford, W. T. (1982). Efficiency of nonimaging concentrators in the physical optics model. *Journal of the Optical Society of America*, 72, 1564-1566.

Yeh, H. M., & Ting, Y. C. (1986). Effects of free convection on collector efficiencies of solar air heaters. *Applied Energy, 22*(2), 145-155.

Yeh, H. M., Ho, C. D., & Hou, J. Z. (1999). The improvement of collector efficiency in solar air heaters by simultaneously air flow over and under the absorbing plate. *Energy, 24*(10), 857-871.

Yeh, H. M., Ho, C. D., & Hou, J. Z. (2002). Collector efficiency of double-flow solar air heaters with fins attached. *Energy, 27*(8), 715-727.

Yildiz, C., Togrul, I. T., Sarsilmaz, C., & Pehlivan, D. (2002). Thermal efficiency of an air solar collector with extended absorption surface and increased convection. *International Communications in Heat and Mass Transfer, 29*(6), 831-840.

Youcef-Ali, S. (2005). Study and optimization of the thermal performances of the offset rectangular plate fin absorber plates, with various glazing. *Renewable Energy, 30*(2), 271-280.

Yousef, B. A. A., & Adam, N. M. (2008). Performance analysis for flat plate collector with and without porous media. *Journal of Energy in Southern Africa, 19*(November, 4), 10.

Zhao, D. L., Li, Y., Dai, Y. J., & Wang, R. Z. (2011). Optimal study of a solar air heating system with pebble bed energy storage. *Energy Conversion and Management, 52*(6), 2392-2400.

Zoltek. (2010). Carbon Fiber. Available: http://www.zoltek.com/(Accessed 26th March, 2010)

Zomorodian, A. and Zamanian, M. (2012). Designing and Evaluating an Innovative Solar Air Collector with Transpired Absorber and Cover, ISRN Renewable Energy, Article ID 282538, 5 pages.

3M. Radiant mirror film, Available: http://www.3m.com/product/information/Radiant-Mirror-Film.html (Accessed 14th June, 2009).

Appendix 1

Appendix 1.1: Properties of selective coatings

Coating	Substrate	Solar absorptance (α)	Solar emittance (ε)	Performance factor
[a]Silicon on silver	×	0.76	0.06	12
[a]Black chromium on bright nickel	×	0.93	0.19	4.8
[a]ZrNy on silver	×	0.85	0.03	24
[b]Black nickel on nickel	Steel	0.95	0.07	13.57
[b]Black chrome	Steel	0.91	0.07	13
	Copper	0.95	0.14	6.78
[b]Black chrome on nickel	Steel	0.95	0.09	10.55
[b]Black copper	Copper	0.88	0.15	5.87
[b]Iron oxide	Steel	0.85	0.08	10.63
[b]Manganese oxide	Aluminium	0.70	0.08	8.75
[b]Organic overcoat on iron oxide	Steel	0.90	0.16	5.625
[b]Organic overcoat on black chrome	Steel	0.94	0.20	4.7
[c]Coppersun plate	×	0.95	0.1	9.5
[d]Titanium-Oxy-Nitride with a proactive quartz coating	×	0.96	×	×

[a](Palz, 1978); [b](Goswami et al., 2000); [c](Moummi et al., 2004); [d](Residensial Solar Energy System, 2011)

Appendix 1.2: Properties of transparent glazing materials

Material	Refractive index	Max. Transmittance
[a]Glass (low iron with reflecting coating)	1.526	96%
[b]Clean polycarbonate	1.59	90%
Polymethyl methacrylate (PMMA)/Transparent Thermoplastics (Commercial Brands: [h]Acrylite FF, [b]Plexiglassk, [c]Optix)	1.49	92%
Polyethylene terephthalate (PET)(Commercial brand:[a]Mylar)	1.64	
[b, d]Tedlar (polyvinyl fluoride, PVF)	1.45	92%
[e]Fiberglass solar glazing	1.34	85-90%
[f,a]Polycarbonate (Commercial Brand:Palsun)	1.586	90%

[a](Koyuncu, 2006); [b](Goswami et al., 2000); [c](Plasticsintl); [d](Tedlar); [e](Solar_components); [f,g](Cansolar); [h](Acrylite, 2011); [i](pilkington)

Appendix 2

Appendix 2.1: One way ANOVA table

Newman-Keuls Multiple Comparison

Test	Mean Diff.	q	Significant? P < 0.05	Summary
100 mm 90 ref vs 0mm 95 ref	-14.53	6.692	Yes	***
100 mm 90 ref vs 100 mm 95 ref	-9.449	4.351	Yes	**
100 mm 90 ref vs 0mm 90 ref	-7.085	3.262	Yes	*
0mm 90 ref vs 0mm 95 ref	-7.448	3.429	Yes	*
0mm 90 ref vs 100 mm 95 ref	-2.364	1.089	No	ns
100 mm 95 ref vs 0mm 95 ref	-5.084	2.341	No	ns

Appendix 3

Design of transpired absorber

A circular hole with triangular pitch can be designed as follows:

Area of 1 perforation hole, $A_{hole} = \frac{\pi D^2}{4}$ A3.1

Area of 1 triangle, $A_{triangle} = \frac{\sqrt{3}P^2}{4}$ A3.2

The perforation in the perforated absorber can be defined by porosity which is the ratio of the perforated area within pitch area. For equilateral triangular pitch area and circular hole porosity can be calculated as equation A 3.3 (Duffie & Beckman, 2006)

$$\rho_p = \frac{A_{holes}}{A_{triangle}} = \frac{\left(\pi D^2 / 4\right)}{2} \times \frac{1}{\left(\sqrt{3}P^2 / 4\right)} = \frac{\pi D^2}{2\sqrt{3}P^2} \qquad \text{A3.3}$$

$$\rho_p = \frac{A_{holes}}{A_{triangle}} = \frac{\pi D^2}{2\sqrt{3}P^2} \qquad \text{A3.4}$$

Where,

P = Pitch length (m)

D = Diameter of the perforation (m)

ρ_p = Porosity of absorber plate

A_{holes} =Area of perforation hole (m^2)

$A_{triangle}$ =Area of equilateral triangle (m^2)

It is necessary to calculate the amount of perforation to find out the mass flow and velocity of air through the absorber plate. From the total area of the absorber plate, the number of equilateral triangles can be calculated as follows:

Area of absorber plate,

$$A_{absorber} = L_{length} \times W_{width} \qquad \text{A3.5}$$

Number of equilateral triangles in the collector area,

$$N_{triangle} = \frac{A_{absorber}}{A_{triangle}} \qquad \text{A3.6}$$

One equilateral triangle connects three perforation holes. Each triangle has half area of one hole.

So total area of hole, $A_{hole} = N_{triangle} \times \frac{A_{triangle}}{2}$ A3.7

Mass flow rate through the perforated holes can be calculated once the area of holes and velocity through the holes are known:

Mass flow rate per unit of collector area,

$$\frac{\dot{m}}{A_c} = \frac{V_{holes} \times \rho \times A_{holes}}{A_c} \qquad \text{A3.8}$$

Mass flow rate through the collector area,

$$\dot{m} = V_{holes} \times \rho \times A_{holes} \qquad \text{A3.9}$$

Figure 4.3 illustrates the effect of perforation diameter, pitch length and type of pitch on the percentage perforation of the absorber which is related with the pressure drop and the heat transfer coefficient. The effect of diameter and pitch is higher in the case of the equilateral triangular pitch compared to square pitch. As the diameter of the perforation is significantly low, the effect of pitch length is vital on the perforation for both types of pitch orientation.

If the pitch increases to 2 mm, the perforation diameter has to be approximately 200-300 µm, for approx. 1.5 mm pitch, the perforation diameter needs to be approximately. 300-500 µm and if the pitch is around 1 mm, the perforation diameter should be 500-600 µm.

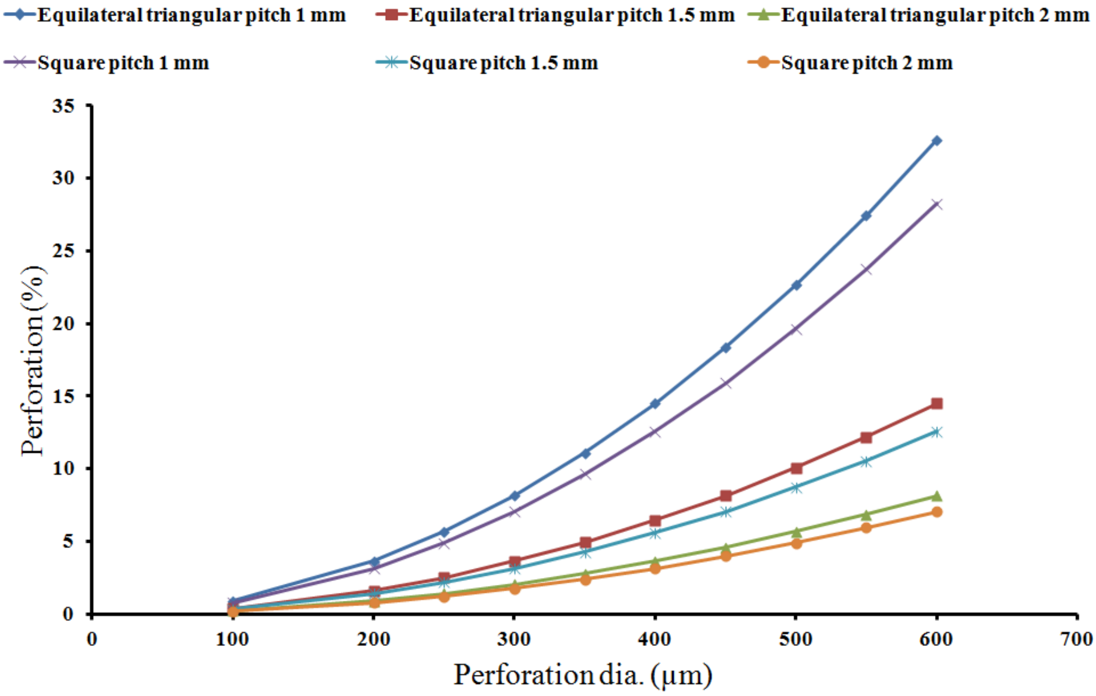

Figure A3.1: Calculated effects of pitch and diameter on absorber perforation

Lower section part numbers:

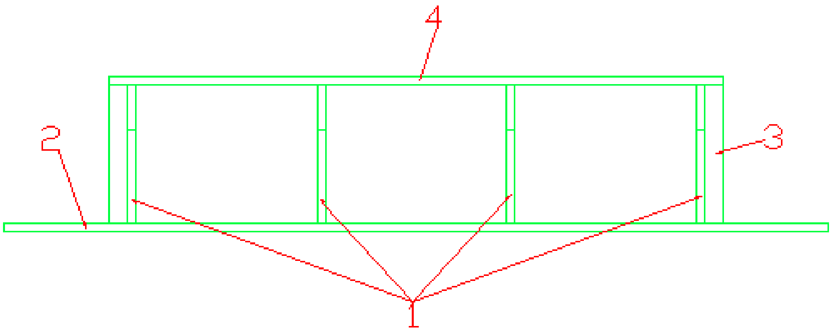

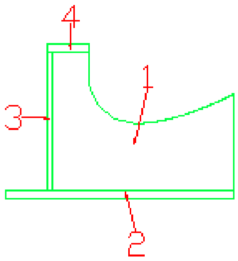

Lower section dimension:

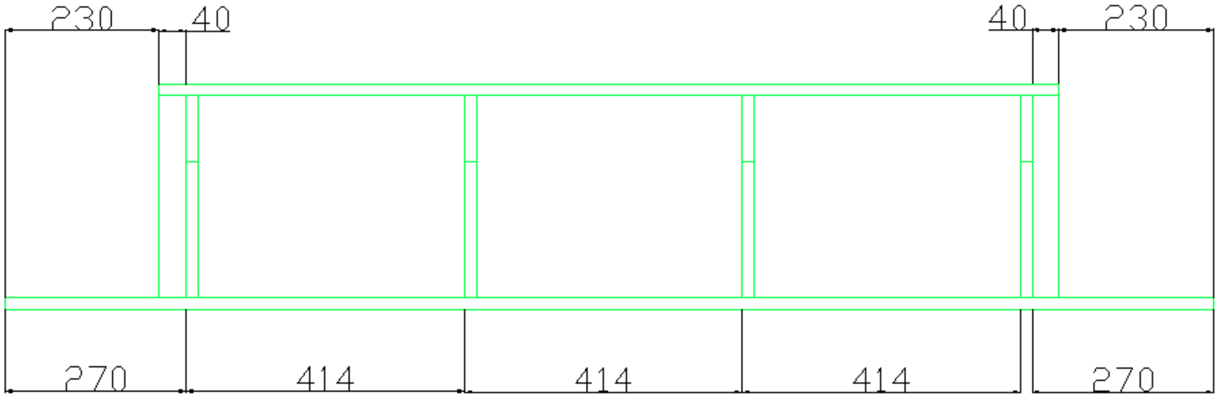

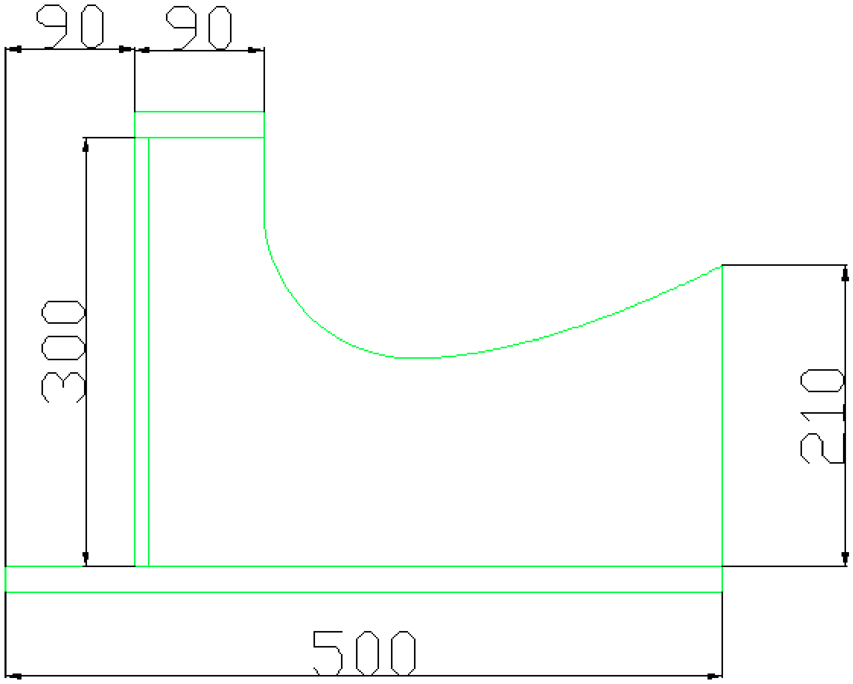

Upper section part numbers:

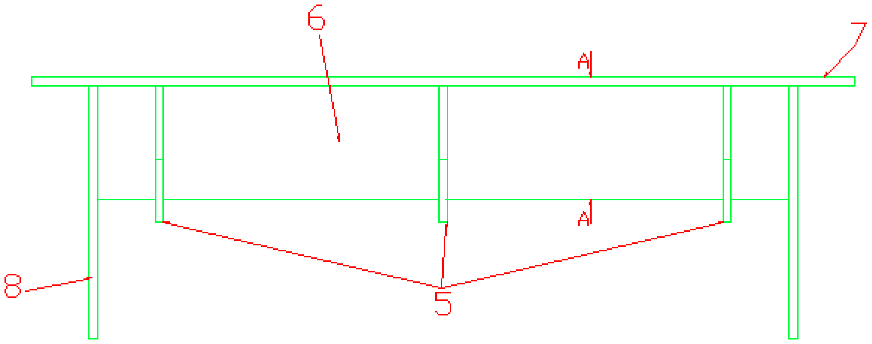

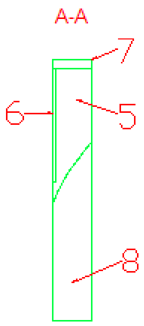

Upper section dimension:

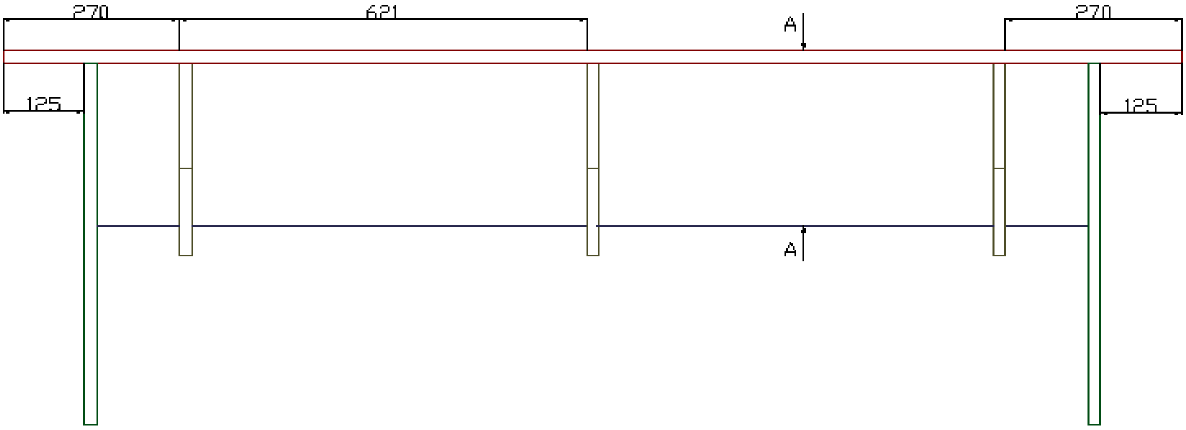

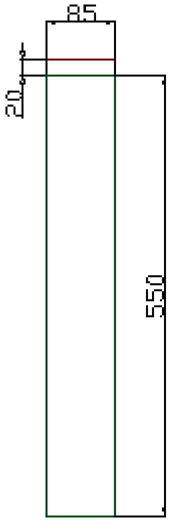

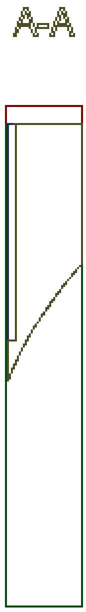

Part Number: 1

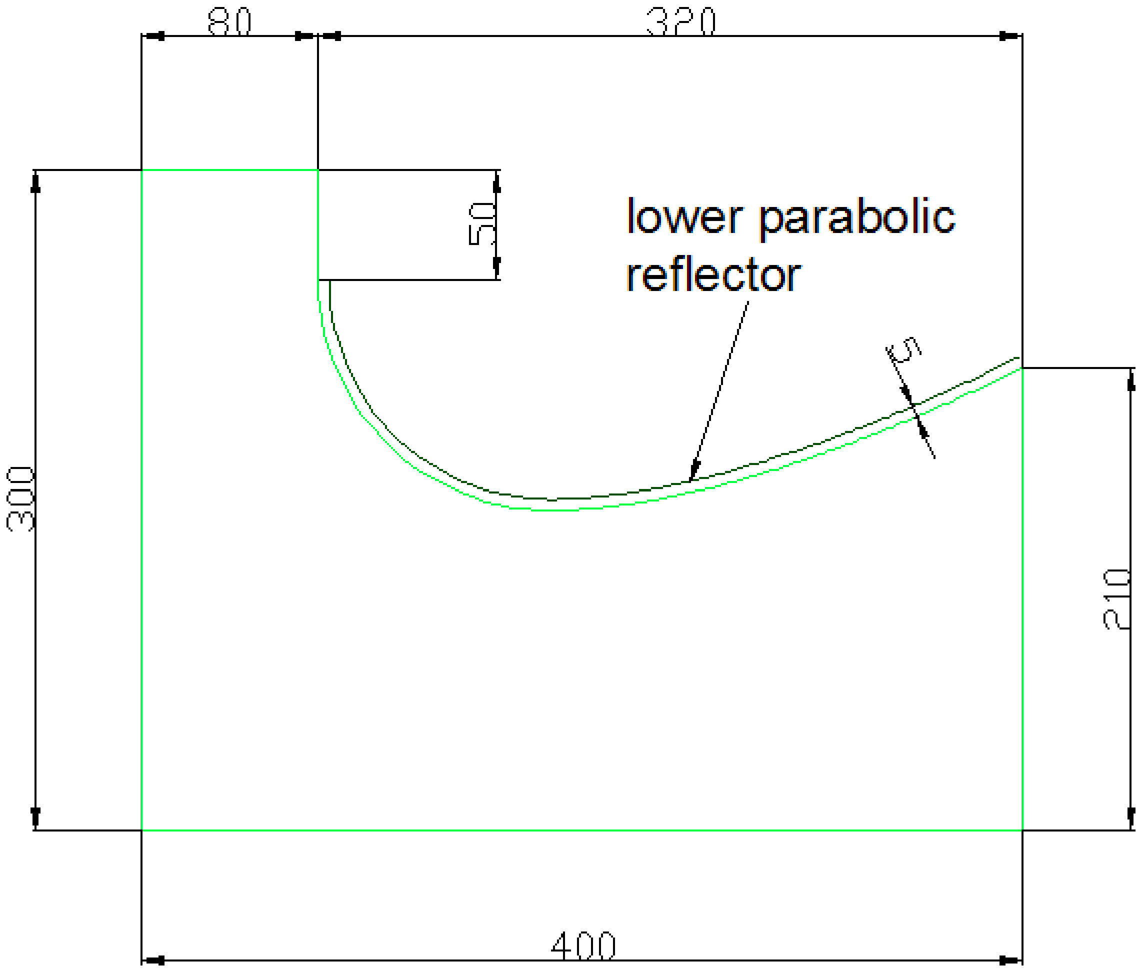

Part Number: 2

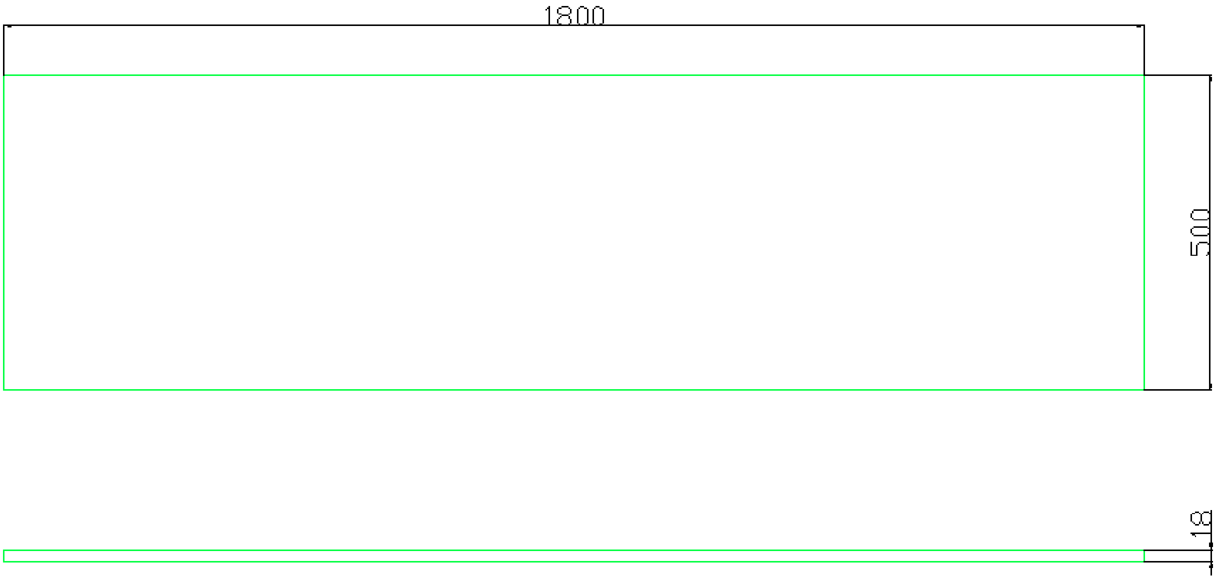

Part Number: 3

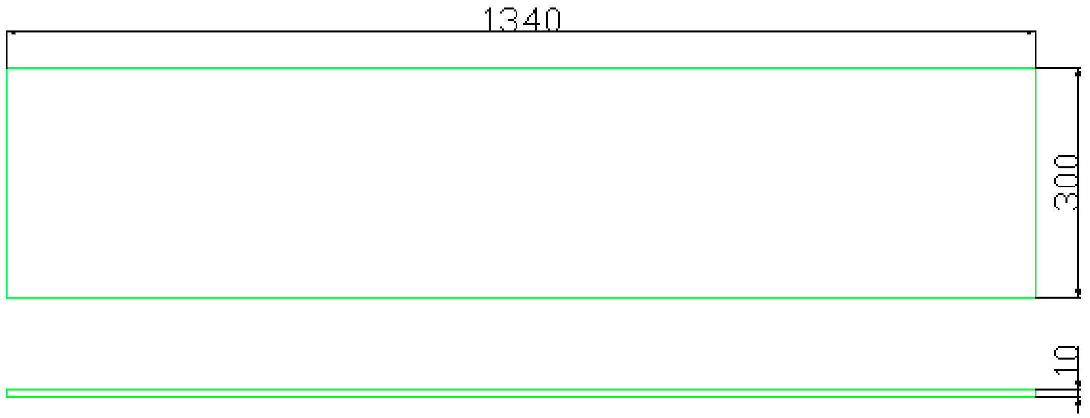

Part Number: 4

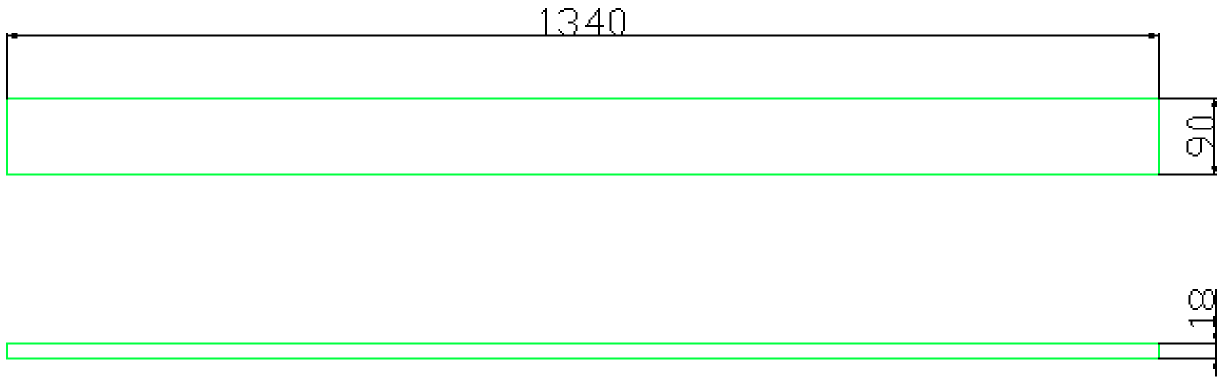

Part Number: 5

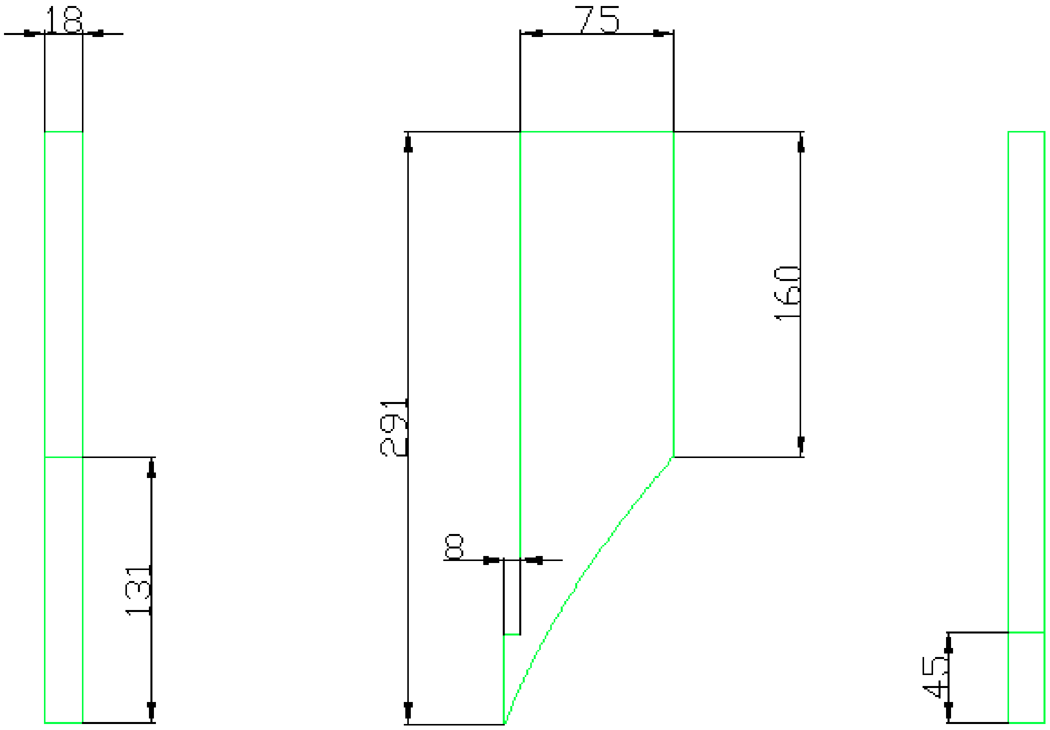

Part Number: 6

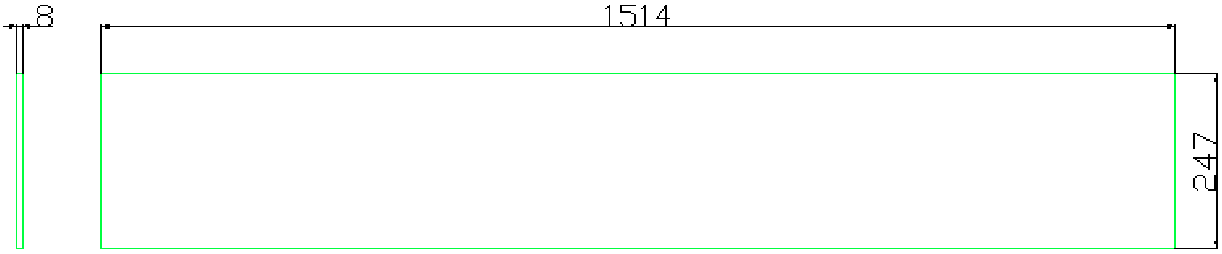

Part Number: 7

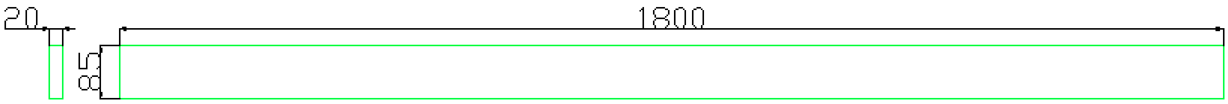

Part Number: 8

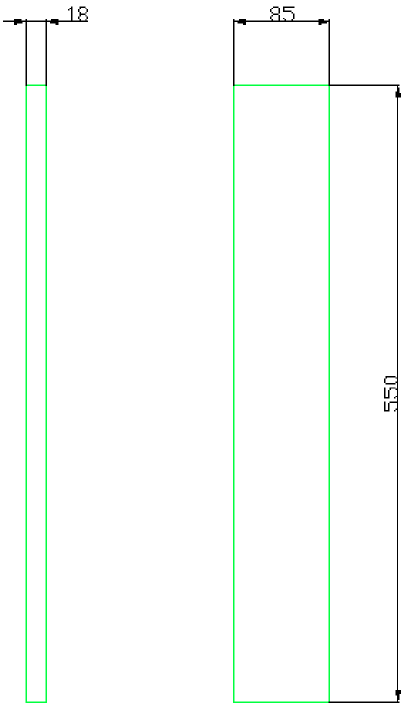

Appendix 4

Appendix 4.1: In-plane solar irradiation, modelled and measured energy output and efficiency on the 13th of July 2011

	Measured energy available (MJ/m^2)	Expt. energy out (MJ/m^2)	Simulated energy out (MJ/m^2)	Expt. thermal efficiency (%)	Simulated thermal efficiency (%)	Statistical validation	
10 am – 11 am	2.88	1.74	1.77	60.67	61.49	PME	-4.8
11 am – 12am	3.41	2.10	2.07	61.50	60.66	CE	-6.3
12 am – 1 pm	3.71	2.37	2.19	63.92	59.00	SMAPE	4.36
1 pm – 2 pm	3.76	2.51	2.24	66.94	59.61		
2 pm – 3 pm	3.54	2.47	2.10	69.63	59.32		
3 pm – 4 pm	3.08	2.12	1.91	68.89	62.13		
4 pm – 5 pm	2.43	1.39	1.50	57.43	61.68		
Average	3.26	2.10	1.97	64.14084	60.56		
Total	22.81	14.71	13.78				

Appendix 4.2: In-plane solar irradiation, modelled and measured energy output and efficiency on the 15th of July 2011

	Measured energy available (MJ/m^2)	Expt. energy out (MJ/m^2)	Simulated energy out (MJ/m^2)	Expt. thermal efficiency (%)	Simulated thermal efficiency (%)	Statistical validation	
10 am – 11 am	0.77	0.34	0.41	43.77	52.74	PME	3.4
11 am – 12am	1.25	0.57	0.67	45.18	53.08	CE	5.2
12 am – 1 pm	1.54	0.76	0.80	49.37	51.99	SMAPE	9.15
1 pm – 2 pm	1.34	0.66	0.67	48.87	50.05		
2 pm – 3 pm	0.83	0.48	0.40	57.52	48.94		
3 pm – 4 pm	0.48	0.34	0.25	70.31	52.44		
4 pm – 5 pm	0.63	0.27	0.33	42.83	52.78		
Average	0.98	0.49	0.50	51.12	52.74		
Total	6.84	3.40	3.53				

Appendix 4.3: In-plane solar irradiation, modelled and measured energy output and efficiency on the 27th of July , 2011

	Measured energy available (MJ/m^2)	Expt. energy out (MJ/m^2)	Simulated energy out (MJ/m^2)	Expt. thermal efficiency (%)	Simulated thermal efficiency (%)	Statistical validation	
10 am – 11 am	2.84	1.61	1.73	56.47	60.83	PME	6.3
11 am – 12am	3.39	1.99	2.09	58.65	61.57	CE	5.2
12 am – 1 pm	3.69	2.20	2.19	59.71	59.37	SMAPE	4.74
1 pm – 2 pm	3.74	2.23	2.21	59.48	58.96		
2 pm – 3 pm	3.55	2.01	2.14	56.55	60.23		
3 pm – 4 pm	2.79	1.62	1.72	58.02	61.63		
4 pm – 5 pm	2.48	1.26	1.51	50.81	60.97		
Average	1.94	1.84	3.21	57.1	60.5		
Total	13.58	12.91	22.48				

Appendix: 4.4

	Monthly avg. daily Insulation $MJ/m^2/day$	Monthly avg. daily energy out $MJ/m^2/day$	Total solar Insolation MJ/m^2	Total Energy out MJ/m^2
January	4.7	2.6	147.2	80.7
February	7.1	4.0	200.0	111.5
March	8.8	5.0	273.6	155.7
April	11.0	6.4	330.6	191.0
May	11.5	6.6	356.6	205.5
June	11.0	6.2	330.4	185.6
July	10.7	6.0	331.1	187.4
August	10.4	6.1	323.9	189.2
September	9.7	5.6	292.0	169.1
October	6.6	3.7	203.7	113.7
November	5.2	2.9	155.8	87.6
December	3.5	1.9	108.2	57.6
Average	8.4	4.8		
Annual total			3053.1	1734.6

Appendix 4.5

Time	January Monthly avg. daily insolation MJ/m^2/day	Monthly avg. daily energy out MJ/m^2/day	February Monthly avg. daily insolation MJ/m^2/day	Monthly avg. daily energy out MJ/m^2/day	March Monthly avg. daily insolation MJ/m^2/day	Monthly avg. daily energy out MJ/m^2/day	April Monthly avg. daily insolation MJ/m^2/day	Monthly avg. daily energy out MJ/m^2/day	May Monthly avg. daily insolation MJ/m^2/day	Monthly avg. daily energy out MJ/m^2/day	June Monthly avg. daily insolation MJ/m^2/day	Monthly avg. daily energy out MJ/m^2/day
10	0.93	0.51	1.13	0.64	1.47	0.84	1.84	1.08	1.75	1.03	1.78	1.04
11	0.92	0.50	1.40	0.79	1.50	0.86	1.72	1.00	1.86	1.06	1.93	1.08
12	**0.99**	**0.55**	1.48	0.84	1.44	0.82	1.86	1.09	**1.98**	**1.12**	1.91	1.05
13	0.90	0.50	1.12	0.63	1.58	0.91	1.76	1.03	1.73	0.98	1.60	0.86
14	0.74	0.41	1.01	0.56	1.30	0.75	1.41	0.81	1.64	0.98	1.40	0.80
15	0.26	0.13	0.65	0.35	0.84	0.47	1.07	0.60	1.36	0.80	1.16	0.67
16	0.00	0.00	0.36	0.18	0.51	0.28	0.71	0.39	0.80	0.46	0.79	0.44
17	0.00	0.00	0.00	0.00	0.19	0.10	0.30	0.16	0.38	0.20	0.44	0.24

Appendix 4.6

Time	July Monthly avg. daily insolation MJ/m^2/day	Monthly avg. daily energy out MJ/m^2/day	August Monthly avg. daily insolation MJ/m^2/day	Monthly avg. daily energy out MJ/m^2/day	Sept. Monthly avg. daily insolation MJ/m^2/day	Monthly avg. daily energy out MJ/m^2/day	Oct. Monthly avg. daily insolation MJ/m^2/day	Monthly avg. daily energy out MJ/m^2/day	Nov. Monthly avg. daily insolation MJ/m^2/day	Monthly avg. daily energy out MJ/m^2/day	Dec. Monthly avg. daily insolation MJ/m^2/day	Monthly avg. daily energy out MJ/m^2/day
10	1.72	1.01	1.52	0.89	1.58	0.91	1.09	0.60	0.95	0.52	0.71	0.37
11	1.80	1.01	1.62	0.95	1.75	1.03	1.30	0.74	1.08	0.62	0.76	0.41
12	1.82	1.01	**1.85**	**1.09**	1.84	1.08	1.27	0.72	1.03	0.59	**0.83**	**0.45**
13	1.64	0.91	1.75	1.04	1.55	0.90	1.11	0.62	0.94	0.53	0.63	0.33
14	1.45	0.83	1.49	0.89	1.31	0.76	0.83	0.46	0.83	0.46	0.47	0.25
15	1.08	0.62	1.11	0.63	0.96	0.55	0.71	0.39	0.36	0.20	0.09	0.05
16	0.74	0.42	0.73	0.41	0.57	0.31	0.26	0.14	0.00	0.00	0.00	0.00
17	0.43	0.24	0.39	0.21	0.18	0.10	0.00	0.00	0.00	0.00	0.00	0.00

Appendix 5

Appendix 5.1: Energy demand and energy generation for different aperture area of CTAH

Month	Energy Generation $1\ m^2$ kWh	Energy Generation $4\ m^2$ kWh	Energy Generation $8\ m^2$ kWh	Space Heating Demand kWh	Water Heating Demand kWh	Total Thermal Demand kWh
Jan	22.4	89.7	179.4	291.3	361.8	653.1
Feb	31.0	123.9	247.9	223.6	326.8	550.4
Mar	43.3	173.0	346.1	120.3	361.8	482.1
Apr	53.1	212.3	424.6	69.6	350.1	419.7
May	57.1	228.3	456.6	0.0	361.8	361.8
Jun	51.6	206.2	412.5	0.0	350.1	350.1
Jul	52.0	208.2	416.4	0.0	361.8	361.8
Aug	52.5	210.2	420.4	0.0	361.8	361.8
Sep	47.0	187.9	375.8	0.0	350.1	350.1
Oct	31.6	126.3	252.7	36.6	361.8	398.4
Nov	24.3	97.3	194.6	86.8	350.1	436.9
Dec	16.0	64.0	128.0	367.0	361.8	728.8
Total	481.8	1927.4	3854.7	1195.2	4259.6	5454.8

Table 5.2: NPV calculation of CTAH for 8% discount rate for domestic dwelling

Year	Primary cost	Installation cost	Maintenance cost	Fuel costs	Annual electricity cost	Contribution	Net annual cash flow	Discount factor	Discounted Cash Flow (DCF)	Cumulative DCF
0	-1800	0					-1,800	1	-1,800	-1,800
1			0	0.00	-10.88	289.10	278.22	0.93	257.61	-1,541.59
2			0	0.00	-11.21	297.78	286.57	0.86	245.69	-1,295.90
3			0	0.00	-11.55	306.71	295.17	0.79	234.31	-1,061.59
4			0	0.00	-11.89	315.91	304.02	0.74	223.46	-838.12
5			0	0.00	-12.25	325.39	313.14	0.68	213.12	-625.01
6			0	0.00	-12.62	335.15	322.54	0.63	203.25	-421.75
7			0	0.00	-12.99	345.21	332.21	0.58	193.84	-227.91
8			0	0.00	-13.38	355.56	342.18	0.54	184.87	-43.04
9			0	0.00	-13.79	366.23	352.44	0.50	176.31	133.27
10			0	0.00	-14.20	377.22	363.02	0.46	168.15	301.41
11			0	0.00	-14.63	388.53	373.91	0.43	160.36	461.78
12			0	0.00	-15.06	400.19	385.12	0.40	152.94	614.71
13			0	0.00	-15.52	412.19	396.68	0.37	145.86	760.57
14			0	0.00	-15.98	424.56	408.58	0.34	139.11	899.68
15			0	0.00	-16.46	437.30	420.84	0.32	132.66	1,032.34
16			0	0.00	-16.95	450.42	433.46	0.29	126.52	1,158.86
17			0	0.00	-17.46	463.93	446.46	0.27	120.67	1,279.53
18			0	0.00	-17.99	477.85	459.86	0.25	115.08	1,394.61
19			0	0.00	-18.53	492.18	473.65	0.23	109.75	1,504.36
20			0	0.00	-19.08	506.95	487.86	0.21	104.67	1,609.03
								NPV	1,609	

Table 5.3: NPV calculation of ETC for 8% discount rate for domestic dwelling

Year	Primary cost	Installation cost	Maintenance cost	Fuel costs	Annual electricity cost	Contribution	Net annual cash flow	Discount factor	Discounted Cash Flow (DCF)	Cumulative DCF
0	-5000	0					-5000	1	-5000	-5,000.00
1			0.00	0.00	0.00	256.86	256.86	0.93	237.83	-4,762.17
2			0.00	0.00	0.00	264.57	264.57	0.86	226.82	-4,535.34
3			0.00	0.00	0.00	272.50	272.50	0.79	216.32	-4,319.02
4			0.00	0.00	0.00	280.68	280.68	0.74	206.31	-4,112.72
5			0.00	0.00	0.00	289.10	289.10	0.68	196.76	-3,915.96
6			0.00	0.00	0.00	297.77	297.77	0.63	187.65	-3,728.31
7			0.00	0.00	0.00	306.70	306.70	0.58	178.96	-3,549.36
8			0.00	0.00	0.00	315.91	315.91	0.54	170.67	-3,378.68
9			0.00	0.00	0.00	325.38	325.38	0.50	162.77	-3,215.91
10			0.00	0.00	0.00	335.14	335.14	0.46	155.24	-3,060.67
11			0.00	0.00	0.00	345.20	345.20	0.43	148.05	-2,912.62
12			0.00	0.00	0.00	355.55	355.55	0.40	141.20	-2,771.43
13			0.00	0.00	0.00	366.22	366.22	0.37	134.66	-2,636.77
14			0.00	0.00	0.00	377.21	377.21	0.34	128.42	-2,508.34
15			0.00	0.00	0.00	388.52	388.52	0.32	122.48	-2,385.87
16			0.00	0.00	0.00	400.18	400.18	0.29	116.81	-2,269.06
17			0.00	0.00	0.00	412.18	412.18	0.27	111.40	-2,157.66
18			0.00	0.00	0.00	424.55	424.55	0.25	106.24	-2,051.41
19			0.00	0.00	0.00	437.29	437.29	0.23	101.32	-1,950.09
20			0.00	0.00	0.00	450.41	450.41	0.21	96.63	-1,853.45
								NPV	-1853	

Table 5.4: NPV calculation of FPC for 8% discount rate for domestic dwelling

Year	Primary cost	Installation cost	Maintenance cost	Fuel costs	Electricity cost	Contribution	Net annual cash flow	Discount factor	Discounted Cash Flow (DCF)	Cumulative DCF
0	-4400	0					-4400	1	-4400	-4,400.00
1			0.00	0.00	0.00	246.63	246.63	0.93	228.36	-4,171.64
2			0.00	0.00	0.00	254.03	254.03	0.86	217.79	-3,953.85
3			0.00	0.00	0.00	261.65	261.65	0.79	207.71	-3,746.14
4			0.00	0.00	0.00	269.50	269.50	0.74	198.09	-3,548.05
5			0.00	0.00	0.00	277.58	277.58	0.68	188.92	-3,359.13
6			0.00	0.00	0.00	285.91	285.91	0.63	180.17	-3,178.96
7			0.00	0.00	0.00	294.49	294.49	0.58	171.83	-3,007.13
8			0.00	0.00	0.00	303.32	303.32	0.54	163.88	-2,843.25
9			0.00	0.00	0.00	312.42	312.42	0.50	156.29	-2,686.96
10			0.00	0.00	0.00	321.80	321.80	0.46	149.05	-2,537.91
11			0.00	0.00	0.00	331.45	331.45	0.43	142.15	-2,395.76
12			0.00	0.00	0.00	341.39	341.39	0.40	135.57	-2,260.19
13			0.00	0.00	0.00	351.64	351.64	0.37	129.30	-2,130.89
14			0.00	0.00	0.00	362.18	362.18	0.34	123.31	-2,007.58
15			0.00	0.00	0.00	373.05	373.05	0.32	117.60	-1,889.98
16			0.00	0.00	0.00	384.24	384.24	0.29	112.16	-1,777.82
17			0.00	0.00	0.00	395.77	395.77	0.27	106.96	-1,670.86
18			0.00	0.00	0.00	407.64	407.64	0.25	102.01	-1,568.85
19			0.00	0.00	0.00	419.87	419.87	0.23	97.29	-1,471.56
20			0.00	0.00	0.00	432.47	432.47	0.21	92.79	-1,378.77
								NPV	-1379	